TECHNISCHE UNIVERSITÄT MÜNCHEN
Lehrstuhl für Raumfahrttechnik

TECHNICAL UNIVERSITY OF MUNICH
Institute of Astronautics

In-Situ Thermal Extraction of Volatiles from Lunar Regolith

Philipp Martin Reiß, M.Sc.

Vollständiger Abdruck der von der Fakultät für Maschinenwesen der Technischen Universität München zur Erlangung des akademischen Grades eines

Doktor-Ingenieurs (Dr.-Ing.)

genehmigten Dissertation.

Vorsitzender:		Prof. Dr.-Ing. Thomas Sattelmayer
Prüfer der Dissertation:	1.)	Prof. Dr. rer.nat. Dr. h.c. Ulrich Walter
	2.)	Prof. Dr.-Ing. Harald Klein

Die Dissertation wurde am 10.01.2018 bei der Technischen Universität München eingereicht und durch die Fakultät für Maschinenwesen am 01.06.2018 angenommen.

Acknowledgements

Thank you to all who helped me making this dissertation possible, for the inspiration, the motivation, the support, the questioning, and numerous discussions.

Through all highs and lows I enjoyed the past years at the 'Lehrstuhl für Raumfahrttechnik', and this was only possible because of the very friendly atmosphere among my colleagues. A special thank shall be addressed to all colleagues of the space exploration group, with whom I spend most of my time at the institute and who are probably among the few people that actually understand what this dissertation is about: Laura Grill, Matthias Killian, Janos Biswas, and Claas Olthoff. Furthermore I thank Matthias Tebbe for practicing the open door policy like no other, his valuable feedback on just any matter, and for endless entertaining hours setting up and repairing the thermal vacuum chamber. Many thanks to Martin Rott for supporting me in questions related to project finances and contracts, and for introducing me into the world of vacuum hardware. Thank you to all other colleagues for sharing a great time!

I enjoyed a great freedom at the institute and could always self-responsibly pursue my own research interests. From computer simulations to experimental work in the laboratory, from standing in the workshop machining parts to teaching students and giving talks at conferences, from acquiring and managing new research projects to floating in zero gravity on a parabolic flight – in the end it was the potpourri of different activities that made a great deal of my motivation to come to work every day. I am grateful to my supervisor Professor Ulrich Walter, who provided me these opportunities, who always supported me in my doings, and who gave me the freedom to develop my skills.

Thank you to my former colleagues and mentors Alex Hoehn and Philipp Hager, for introducing me into the world of lunar regolith, helping with project work and its bureaucracy, and providing the initial funding for my position. Thank you Philipp for your guidance during the first years and all the work that influenced my dissertation. Thank you Alex for always asking the right questions, sharing your great experience, all that proof-reading, and your continuous support. I would also like to thank my former colleague Stephan Parzinger for the contributions to our shared project and the valuable research which I was able to base my (thermal) work upon. A big thank-you shall be addressed to Simeon Barber for the very pleasant collaboration on ProSPA and for the always constructive feedback on my work. Thank you Lutz Richter for the valuable insights into current missions and the expert knowledge on planetary terramechanics. Many thanks to Professor Teja Reetz for sharing your expertise and practical knowledge on high-temperature materials. I would also like to thank my colleagues from TU Braunschweig for supporting our shared parabolic flight experiment and all other colleagues whom I had the pleasure to work with on various topics related to this dissertation. Thank you to all who reviewed my abstracts, papers, presentations, and finally this dissertation.

All the concept design and experimental work would not have been possible without the continuous support of my former student assistants Max Kellner, Natan Nudelis, Monty Mutschler, Alexander Schmitt, and the students I had the pleasure to supervise for their Bachelor's-, semester-, or Master's-theses.

A special thank shall be addressed to my friends and family, who supported me in any possible way. Thank you to all who share the curiosity and fascination about space, all the luna-tics out there, for keeping my motivation alive.

Finally I want to express my gratitude to my wife Andrea and my sons Emil and Carl. Thank you for supporting me, thank you for being there.

Abstract

The exploration of resources on the Moon focuses on the lunar regolith, which contains valuable oxides, metals, solar wind implanted particles, and highly volatile elements such as water. Up to now the latter has only been evidenced through remote sensing, and confirmation through ground truth remains to be delivered. Future resource prospecting missions will determine the volatile species, their abundance, and their bonding mechanisms through in-situ measurements.

The work presented here addresses technological and scientific questions that are relevant for the thermal extraction of volatiles from lunar regolith. A dynamic combined model for the heat and mass transfer inside a regolith sample, together with the desorption of volatile water molecules from the sample particles, was developed. This allows to investigate the interdependencies of different physical parameters and their effect on the overall extraction process. The model was implemented in the software COMSOL to study this process in the context of the currently developed gas analysis instrument ProSPA. For a representative cylindrical sample with 2.8 mm diameter and 4.5 mm height it was shown through simulations that temperature gradients up to 30 °C and gas pressures in the 10^{-2} to 10^{0} mbar range can occur for a typical water content between 0.1 wt% and 1 wt%. The studies presented here also illustrate the effects of bulk density and heating mode on the resulting temperature distribution, gas pressure, and process duration.

The simulations were extended to experimental studies on the extraction of volatiles from the lunar regolith simulant NU-LHT-2M. Samples with adsorbed water were conditioned in a humidity-controlled nitrogen atmosphere. A new test setup was developed to enable the controlled heating of these samples from -150 °C to 800 °C in a high vacuum of 10^{-7} mbar to 10^{-5} mbar. This setup was used to run parameter studies with differently conditioned samples and evaluate the effect of initial water concentration, sample mass, particle size, bulk density, and heating modes. The outgassing of volatiles, mainly water, showed significantly varying behaviour in a temperature range between -50 °C and 300 °C. Above 300 °C, the outgassing was attributed mainly to mineral decomposition with very similar outgassing features for all samples. In addition to the extraction of volatile compounds, the same test setup was used to demonstrate the feasibility of chemically reducing samples of ilmenite and NU-LHT-2M via heating in a hydrogen atmosphere. The best results were achieved with an operation in semibatch mode with ilmenite, where water in quantities between 1 wt% and 2 wt% were produced.

In the frame of the present thesis, a theoretical and experimental evaluation regarding the implications of an enlarged sample size and hence an enlarged sample oven was also performed. Several issues related to up-scaling were highlighted, including the occurrence of high temperature gradients inside the sample, increased power demands and insulation effort, as well as material incompatibilities.

Regarding the transport of lunar regolith samples, a study on the flow properties of the regolith simulants NU-LHT-2M and JSC-1A was conducted for the present thesis. This included the experimental evaluation of the sample flow in two-dimensional feed hoppers under reduced gravity and vacuum, as well as a parameter study regarding the gas pressure dependency of flow hindrance and the effect of vibration on the sample flow. It was found that gravity and hopper outlet width are linearly proportional to the flow rate. Further observations include the reduction of sample compaction under reduced gravity and a randomly occurring and variably strong disturbance of the flow.

In conclusion, this work presents a practically oriented evaluation of the process chain that enables the thermal processing of lunar regolith for the in-situ extraction of volatiles and the chemical reduction of the mineral compounds. It closes the gap between the engineering and design of instruments for the analysis of volatiles and the scientific objectives and interpretation of data gathered with such instruments.

Zusammenfassung

Die Exploration von Ressourcen auf dem Mond konzentriert sich auf das lunare Regolith, welches wertvolle Sauerstoffverbindungen, Metalle, vom Sonnenwind implantierte Partikel und hochvolatile Elemente wie Wasser enthält. Letztere wurden bis dato nur durch Fernerkundung nachgewiesen, und die Bestätigung durch Bodendaten steht noch aus. Zukünftige Erkundungsmissionen werden die volatilen Spezies, ihre Häufigkeit und ihre Bindungsmechanismen durch in-situ Messungen bestimmen.

Die vorliegende Arbeit adressiert technologische und wissenschaftliche Fragestellungen, die für die thermische Extraktion von Volatilen aus lunarem Regolith relevant sind. Ein dynamisches kombiniertes Modell für den Wärme- und Stofftransport und die Desorption von Wassermolekülen von der Partikeloberfläche innerhalb einer Regolithprobe wurde entwickelt. Dies ermöglicht, die Wechselwirkung verschiedener physikalischer Parameter und deren Effekt auf den gesamten Extraktionsprozess zu untersuchen. Das Modell wurde in der Software COMSOL implementiert, um diesen Prozess im Kontext des derzeit entwickelten Gasanalyse-Instruments ProSPA zu erforschen. Für eine repräsentative zylindrische Probe mit 2,8 mm Durchmesser und 4,5 mm Höhe wurde gezeigt, dass Temperaturgradienten von bis zu 30 °C und Gasdrücke im Bereich 10^{-2} bis 10^{0} mbar für eine typische Wasserkonzentration zwischen 0,1 wt% und 1 wt% auftreten können. Die hier vorgestellten Studien veranschaulichen zusätzlich den Effekt der Änderung des Wassergehalts, der Dichte und des Heizmodus auf die resultierende Temperaturverteilung, den Gasdruck und die Prozessdauer.

Die Simulationen wurden um experimentelle Studien zur Extraktion von Volatilen aus dem Regolithsimulat NU-LHT-2M erweitert. Proben mit adsorbiertem Wasser wurden in einer Stickstoffatmosphäre mit kontrollierter Feuchte konditioniert. Ein neuer Versuchsaufbau wurde entwickelt, um die geregelte Erhitzung dieser Proben von -150 °C bis 800 °C in Hochvakuum von 10^{-7} mbar bis 10^{-5} mbar zu ermöglichen. Dieser Aufbau wurde verwendet, um Parameterstudien mit unterschiedlich konditionierten Proben durchzuführen und den Effekt von anfänglicher Wasserkonzentration, Probenmasse, Partikelgröße, Dichte, und Heizmodi zu untersuchen. Das Ausgasen der Volatile, hauptsächlich Wasser, zeigte ein deutlich unterschiedliches Verhalten im Temperaturbereich von -50 °C bis 300 °C. Über 300 °C wurde das Ausgasen hauptsächlich auf den Zerfall von Mineralien zurückgeführt mit sehr ähnlichen Ausgasmerkmalen für alle Proben. Zusätzlich zu der Extraktion von volatilen Inhaltsstoffen wurde derselbe Testaufbau dazu verwendet, um die Machbarkeit der chemischen Reduktion von Ilmenit- und NU-LHT-2M-Proben durch Erhitzung in einer Wasserstoffatmosphäre zu demonstrieren. Die besten Ergebnisse wurden mithilfe eines Betriebs im Semibatch-Modus mit Ilmenit erzielt, wobei Wasser in Mengen von 1 wt% bis 2 wt% hergestellt wurde.

Im Rahmen der vorliegenden Arbeit wurde außerdem eine theoretische und experimentelle Untersuchung bezüglich der Implikationen einer vergrößerten Probe und damit eines vergrößerten Probeofens durchgeführt. Es wurden einige Probleme bezüglich des Hochskalierens aufgezeigt, darunter das Auftreten von hohen Temperaturgradienten in der Probe, ein erhöhter Energiebedarf und Isolierungsaufwand, sowie Materialinkompatibilitäten.

Bezüglich des Transports von lunaren Regolithproben wurde eine Studie zur den Fließeigenschaften der Regolithsimulate NU-LHT-2M und JSC-1A durchgeführt. Dies beinhaltete die experimentelle Untersuchung des Probenflusses in zweidimensionalen Fördertrichtern unter reduzierter Schwerkraft und Vakuum und eine Parameterstudie hinsichtlich der Gasdruckabhängigkeit von Fließhemmungen und des Effekts von Vibration auf den Probenfluss. Es wurde herausgefunden, dass Schwerkraft und Öffnungsweite des Trichters linear proportional zur Fließrate sind. Zusätzliche wurde eine Verringerung der Probenkompaktierung unter

reduzierter Schwerkraft und eine zufällig auftretende unterschiedlich starke Störung des Probenflusses beobachtet.

Zusammenfassend präsentiert die vorliegende Arbeit eine praktisch orientierte Betrachtung der Prozesskette die die thermische Prozessierung von Mondregolith zur in-situ Extraktion von Volatilen oder zur chemischen Reduktion der mineralischen Bestandteile ermöglicht. Sie schließt dabei die Lücke zwischen der ingenieurtechnischen Entwicklung und Konstruktion von Instrumenten zur Analyse von Volatilen und der wissenschaftlichen Zielsetzung und Interpretation der gewonnenen Daten mithilfe solcher Instrumente.

Contents

Abbreviations

ADM	Advective Diffusion Model
APXS	Alpha Particle induced X-ray Spectrometer
CAD	Computer Aided Design
CHACE	Chandra's Altitudinal Composition Explorer
CNES	Centre National d'Études Spatiales
CTE	Coefficient of Thermal Expansion
DGM	Dusty Gas Model
DLR	Deutsches Zentrum für Luft- und Raumfahrt
DLRE	Diviner Lunar Radiometer Experiment
DU	Dosing Unit
EGA	Evolved Gas Analysis
ESA	European Space Agency
EC	European Commission
EU	European Union
FDU	Field Demonstration Unit
COSAC	Cometary Sampling and Composition experiment
GAP	Gas Analysis Package
GC	Gas Chromatograph
HRI-IR	High-Resolution Instrument – Infrared Spectrometer
HTO	High Temperature Oven
ISECG	International Space Exploration Coordination Group
ISRU	In-Situ Resource Utilisation
IR	Infrared
JEPPF	Joint European Partial-g Parabolic Flight Campaign
LCROSS	Lunar Crater Observation and Sensing Satellite
LED	Light Emitting Diode
LEND	Lunar Exploration Neutron Detector
LIBS	Laser Induced Breakdown Spectroscopy
LLOX	Lunar Liquid Oxygen
LRO	Lunar Reconnaissance Orbiter
LUISE	Lunar In Situ Experiment
LUVMI	Lunar Volatiles Mobile Instrumentation
LVRAP	Lunar Volatile Resources Analysis Package
LVS	Lunar Volatiles Scout
M^3	Moon Mineralogy Mapper
MARVIN	Moon Advanced Resource Utilization Viability Investigation
MIP	Moon Impact Probe
MOMA	Mars Organic Molecule Analyser
MS	Mass Spectrometer
MSL	Mars Science Laboratory
MTO	Medium Temperature Oven
NASA	National Aeronautics and Space Administration
OVEN	Oxygen and Volatile Extraction Node
PDE	Partial Differential Equation
PID	Proportional-Integral-Derivative
PMMA	Polymethyl Methacrylate

ProSEED	PROSPECT Sample Excavation and Extraction Drill
ProSPA	PROSPECT Sample Processing and Analysis
PROSPECT	Platform for Resource Observation and in-Situ Prospecting for Exploration, Commercial exploitation and Transportation
PSDDS	Powdered Sample Dosing and Distribution System
PSR	Permanently Shadowed Region
PVC	Polyvinyl Chloride
RGA	Residual Gas Analyser
SAM	Sample Analysis at Mars
SD2	Sampler, Drill and Distribution System
SEM	Scanning Electron Microscope
SSIT	Solid Sample Inlet Tube
SPDS	Sample Preparation and Distribution System
TDS	Total Dissolved Solids
TEGA	Thermal and Evolved Gas Analyser
TPD	Temperature Programmed Desorption
TUM	Technical University of Munich
TVAC	Thermal Vacuum Chamber
VAPoR	Volatile Analysis by Pyrolysis of Regolith
VED	Volatiles Extraction Demonstration
VIMS	Visual and Infrared Mapping Spectrometer
XRD	X-Ray Diffraction
ZGS	Zirconium Grain Strengthened

Symbols

Symbol	*SI unit*	*Description*
α	$[m^2/s]$	Thermal diffusivity
α	$[rad]$	Angle
α_a	$[1]$	Accommodation index
β	$[1]$	Gas-specific constant
γ	$[1]$	Ratio of specific heat capacities
δ	$[rad]$	Angle of friction
θ	$[1]$	Surface coverage
λ	$[m]$	Mean free path
μ	$[Pa \cdot s]$	Dynamic viscosity
ν	$[1]$	Poisson's ratio
ρ	$[kg/m^3]$	Density
ρ_A	$[1/m^2]$	Areal density
σ	$[W/(m^2 \cdot K^4)]$	Stefan-Boltzmann constant
σ_c	$[N/m^2]$	Unconfined yield strength
τ	$[1]$	Tortuosity
ϕ	$[1]$	Porosity
φ_w	$[rad]$	Angle of wall friction
ψ	$[1]$	Volume ratio
a	$[m]$	Semi-major axis or distance
A	$[m^2]$	Area
A	$[1/s]$	Pre-exponential factor
b	$[m]$	Semi-minor axis
B	$[m]$	Hopper outlet width
c	$[mol/m^3]$	Concentration
c_p	$[J/(kg \cdot K)]$	Specific heat capacity
C	$[1]$	Constant
C_{cond}	$[W/(m \cdot K)]$	Constant for conduction
C_{rad}	$[W/(m \cdot K^4)]$	Constant for radiation
d	$[m]$	Diameter
D	$[m^2/s]$	Diffusion coefficient
E	$[J]$	Activation energy
E	$[kg/(m^2 \cdot s)]$	Condensation/sublimation rate
E	$[1/m]$	Extinction coefficient
f	$[1]$	Fraction/factor
ff	$[1]$	Flow factor
F	$[1]$	Shape factor
g	$[m/s^2]$	Gravitational acceleration
h	$[m]$	Height
I	$[A]$	Current

J	$[mol/m^2 \cdot s]$	Molar flux
k	$[W/(m \cdot K)]$	Thermal conductivity
k	$[1/s]$	Rate constant
k_B	$[J/K]$	Boltzmann constant
k_g	$[m^2]$	Gas permeability
Kn	$[1]$	Knudsen number
l	$[m]$	Length
L	$[m]$	Characteristic length
m	$[kg]$	Mass
M	$[kg/mol]$	Molar mass
n	$[1]$	Refractive index (real part)
n	$[mol]$	Amount of substance
N_A	$[1/mol]$	Avogadro constant
p	$[Pa]$	Pressure/load
p_t	$[Pa]$	Triple point pressure
p_v	$[Pa]$	Equilibrium vapour pressure
P	$[W]$	Power
Pe	$[1]$	Péclet number
q	$[m^3/s]$	Volumetric flow rate
Q	$[J/mol]$	Sublimation enthalpy
r	$[m]$	Radius
R	Ω	Electrical resistance
R	$[J/(mol \cdot K)]$	Universal gas constant
R_s	$[J/(kg \cdot K)]$	Specific gas constant
S	$[1]$	Sticking coefficient
S_0	$[1/m]$	Specific surface
t	$[s]$	Time
T	$[K]$	Temperature
T_t	$[K]$	Triple point temperature
u	$[m/s]$	Darcy velocity
U	$[V]$	Voltage
$\bar{v}$	$[m/s]$	Mean thermal velocity
V	$[m^3]$	Volume
Y	$[N/m^2]$	Young's modulus

1 Introduction

1.1 Motivation

Since the beginning of lunar exploration in the late 1950‘s there have been countless manned and unmanned lunar missions, including flybys, orbiters, landers, and rovers. Nevertheless, only a small fraction of the Moon has been accessed so far and there are still many good reasons to continue exploring our nearest neighbour, some of which are summarised by Neal (2009). After the first wave of lunar exploration in the 1960’s and 1970’s, including the prominent Apollo and Luna programmes, ‘*a consensus emerged that the Moon was primarily an anhydrous planetary body*’ (Jaumann *et al.*, 2012, p. 28). This conclusion was mainly drawn from the analysis of returned lunar regolith samples, which showed no evidence of hydrated minerals or altered metallic iron (Lucey, 2009). The interpretation of a ‘dry’ Moon however has been challenged in the last years, both due to more sensitive measurement methods that were applied to lunar samples, but even more due to the findings of orbital remote sensing missions of the late 1990’s and early 2000’s. The latter indicated ‘*that nearly the entire lunar surface, at least in the uppermost few micrometers to millimeters depth, is hydrated at least during some portions of the lunar day*’ (Jaumann *et al.*, 2012, p. 28). This discovery lead to the fact that the in-depth investigation of lunar volatiles, particularly water, is now one of the primary objectives of lunar exploration.

The results of several recent missions suggest the existence of hydroxyl and/or water at the lunar poles: Clementine (Nozette *et al.*, 1996), Lunar Prospector (Feldman *et al.*, 1998), Cassini (Clark, 2009), Deep Impact (Sunshine *et al.*, 2009), Chandrayaan-1 (Pieters *et al.*, 2009; Sridharan *et al.*, 2010), and the Lunar Crater Observation and Sensing Satellite LCROSS together with the Lunar Reconnaissance Orbiter LRO (Colaprete *et al.*, 2010). All current estimates for the abundance of lunar polar water are based on neutron spectroscopy (Neutron Spectrometer on Lunar Prospector, Lunar Exploration Neutron Detector LEND on LRO), visual and infrared spectroscopy (Moon Mineralogy Mapper M^3 on Chandrayaan-1, Visual and Infrared Mapping Spectrometer VIMS on Cassini, High-Resolution Instrument – Infrared Spectrometer HRI-IR on Deep Impact), mass spectrometry (Chandra’s Altitudinal Composition Explorer CHACE on Chandrayaan-1), and radiometry (Bistatic Radar Experiment on Clementine, Diviner Lunar Radiometer Experiment DLRE on LRO). Because of ambiguous interpretations of these indirect measurements of lunar water, ‘*confirming the interpretation of the remote sensing measurements, and obtaining accurate values for the concentration of polar ice and high latitude surficial OH/H_2O will require in situ measurements by suitably instrumented and landed spacecraft*’ (Crawford *et al.*, 2012, p. 6). Such in-situ measurements are also recommended in the Global Exploration Roadmap, developed by the International Space Exploration Coordination Group (ISECG), which describes the coordinated exploration strategies of currently 15 of the world's space agencies: ‘*To gain an understanding of whether lunar volatiles could be used in a cost effective and safe manner, it is necessary to understand more about the nature and distribution of the volatiles and whether they could be processed cost effectively. The first step is robotic prospecting to take measurements on the lunar surface. Several of the planned robotic missions can be considered prospecting missions.*’ (ISECG, 2013, p. 23) The rationale for further exploring lunar volatiles is not only driven by the scientific interest, but also by the fact that volatiles can be utilised as an important resource in the frame of In-Situ Resource Utilisation (ISRU) to enable long-term lunar exploration and human presence on the Moon. Water can be used as a consumable for life support or as a basis for propellant production. Other volatiles, such as hydrogen, can be used as a reactant to extract oxygen from lunar minerals, or for propellant production.

Based on remote sensing data, the search for water focuses on the exploration of the lunar poles, where solar illumination is rare. In permanently shadowed regions (PSR), temperatures can be as low as 40 K,

which is sufficient to hold water and other highly volatile elements over long periods of time in the near-perfect vacuum environment of the Moon. The two impactors that delivered evidence for lunar water, Moon Impact Probe MIP of Chandrayaan-1 and the Centaur upper stage of LCROSS, crashed into the lunar surface near the South Pole, and current plans for lunar volatiles prospecting missions also focus on this particular region: '*Recent discoveries of volatiles at the lunar South Pole regions make the Moon an ideal place for demonstrating the potential resulting from in-situ resources utilisation in support of human exploration'* (European Space Agency, 2015a, p. 9). To date, space agencies are planning the following relevant polar missions: Chandrayaan-2 (ISRO, launch 2018), Luna-27 (Roscosmos/ESA, launch early 2020's), Resource Prospector (NASA), and Lunar Prospecting Rover (ESA). The most advanced missions are the Indian Chandrayaan-2 and the Russian Luna-27, both including a 1000 kg class lander that aims at landing at a high-latitude non-PSR polar region. Chandrayaan-2 also carries a rover, equipped with two instruments for the analysis of volatiles (Mylswamy *et al.*, 2012): an Alpha Particle induced X-ray Spectrometer (APXS) and a Laser Induced Breakdown Spectrometer (LIBS). Luna-27 will carry the European payload PROSPECT (Platform for Resource Observation and in-Situ Prospecting in Support of Exploration, Commercial Exploitation and Transportation) with the instrument ProSPA (PROSPECT Sample Processing and Analysis) to release and analyse volatiles from lunar subsurface samples (Barber *et al.*, 2017; Carpenter *et al.*, 2017). The aforementioned missions are seen as precursors in a phase of prospecting for resources. Accessing and utilising these resources will be part of a later phase of lunar exploration which also involves bringing humans back to the lunar surface.

It is crucial to understand the nature of lunar regolith and lunar volatiles in order to design suitable hardware and develop appropriate procedures for the in-situ sampling of regolith and the extraction of volatiles. Lunar water for instance is assumed to be mainly loosely bound to the regolith and hence very sensitive to thermal variations. The regolith on the other hand is a very good thermal insulator, making it hard to introduce greater amounts of heat, such as required for ISRU applications. Heat and mass transfer are therefore of special interest regarding the design of instruments for the extraction and analysis of lunar volatiles, as the interaction of different physical effects generates several unknowns for such systems. For ProSPA this is of particular relevance, since it is currently the only instrument under development that specifically targets an in-situ analysis of lunar polar volatiles. ProSPA also aims at performing an ISRU-style reduction of the lunar regolith to demonstrate the in-situ production of water. The instrument therefore needs to cover a very broad temperature range and needs to handle processing pressures that extend over many orders of magnitude. Furthermore it is unclear what kind of sample is to be expected, since there has not been any polar regolith sampling yet. It is therefore important to analyse the general feasibility of the planned operating modes with the instrument configuration and hardware, and with different types and conditions of regolith.

1.2 State of the Art

1.2.1 The Lunar Volatiles Sampling Chain

There are a number of different approaches to realise a 'sampling chain' for lunar volatiles, that is, to access, extract, and analyse lunar resources in-situ. Table 1-1 provides an overview of the methods and technologies required in a lunar mission for this purpose. It can be seen from the table that there are manifold possibilities to combine existing approaches, depending on the mission context and the scientific goals. However, not all of the presented methods are suitable when it comes to lunar volatiles as a resource, as discussed in the following.

According to the current knowledge, as described in the previous section, lunar volatiles exist only in permanently shadowed regions with an extremely cold ambient temperature. This makes it difficult to access any volatiles-bearing samples to begin with. A mobile element (rover) is desirable to have because of higher flexibility, the possibility of taking measurements of volatiles at different times and locations, as well as outside the contaminated landing area (Reiss, Hoehn and Henn, 2015). However, a mobile platform is technically difficult to operate in such an extreme environment. The choice between a stationary lander and a mobile rover also determines the complexity of an instrument for the analysis of extracted volatiles. On a

mobile element quick but only simple analysis can be performed, whereas on a stationary lander a more complex instrument or a combination of different instruments could be accommodated.

A main constraint for the exploration of lunar volatiles is sample preservation. Since volatiles by definition are only loosely bound to the regolith, it requires extremely careful handling to avoid an alteration of the sample's pristine character. Regarding acquisition, transfer, pre-treatment, and processing, any thermal or mechanical loads on the sample therefore need to be avoided. In this regard, drilling into regolith is to be seen critically, since even a low rotational speed can cause an increase in sample temperature through friction. Static penetrators (corers) and scoops can mitigate this problem, but are more limited in depth. An instrument that only needs to be applied to the topmost layer of the lunar surface minimises sample disturbance but is limited in the sample mass that can be collected.

Sample transfer can be realised using standard conveying devices or robotic elements, but for all approaches the exposure of the sample to heat sources (solar, albedo, and infrared radiation) needs to be avoided and distances need to be kept short (Hager *et al.*, 2015). For larger sample sizes that require conveying devices of some kind, mechanical clogging or hindered sample transfer might be a problem (Reiss *et al.*, 2014), which can either lead to the complete loss of a sample, or the longer exposure to external heat sources.

Depending on the type of regolith, the sample acquisition tool, and the sample processing container, a certain degree of pre-treatment or sorting might be required. This includes crushing or sieving the sample to a particular fraction of grain sizes or separation of different minerals in the regolith through electrostatic charging or mass separation. However, this introduces mechanical loads to the sample which could also lead to a loss of volatiles (Carrier, Bromwell and Martin, 1973).

The most common way of heating a sample is to fill it into a crucible and let it sit there during heating until the experiment is completed. In terms of heat transfer this might not be ideal, since high thermal gradients can occur across the sample. Mechanical agitation can help to introduce heat more uniformly and hence more efficiently into the sample, be it by fluidisation using a carrier gas, vibrofluidisation without carrier gas, or by using a rotary kiln or similar rotating device. Compared to the static sample in a crucible, the improved heat input for all these approaches comes at the cost of a more complex mechanical design.

For the actual extraction of lunar volatiles, the method of choice most often is to heat the sample by electrical heating (compare chapter 1.2.2). Other methods such as microwave heating, laser heating, or solar heating have been addressed in the past, but for scientific instruments in the scope of planetary exploration these have not found any application so far with the exception of LIBS for mineralogical analysis (Thomas *et al.*, 2017). Electrical heating can be applied to any sample, be it via conduction or radiation. Microwave heating generally is a much faster and more energy efficient process (Taylor and Meek, 2005), but it is more challenging to achieve a controlled heating of the regolith. There are also controversial opinions regarding what actually causes the regolith to couple with microwave radiation: ilmenite content (Vaniman, Meek and Blake, 1986; Wright *et al.*, 1986), nanophase iron (Taylor and Meek, 2004, 2005), and particle shape (Barmatz *et al.*, 2013) are possible explanations. Because of the difficulties in controlling the heat, microwave heating is more applicable where only high temperatures need to be achieved in one single step, for instance for 3D printing, which includes sintering and melting of the regolith (Barmatz *et al.*, 2014; Cowley *et al.*, 2016). The same is true for solar heating, with the advantage that no power supply is required. Additionally an increased system complexity might have to be taken into account, because solar light needs to be focussed with lenses or mirrors, which are difficult to maintain dust-free in the lunar environment. Solar heating is also considered for 3D printing, respectively solar sintering (Fateri, Meurisse and Sperl, 2017), or high temperature ISRU processes that require a regolith melt (Senior, 1993; Sauerborn, 2005). Laser heating also only applies to the top surface of a sample and hence requires mixing if the bulk sample shall be heated. Gustafson et al. (2010) have applied laser heating as a precursor for solar heating on regolith for the demonstration of the ISRU process of carbothermal reduction.

Once the volatile gases are extracted from the sample, they can either be continuously analysed as they evolve (evolved gas analysis, EGA) or collected (for instance by a cold finger) and analysed in batches by stepwise desorption of the collected gases. Both approaches require different operational aspects, oven or

reactor designs, and heating modes, which in turn might require different heating methods as described before. The decision on which process type to be used is mainly driven by the scientific or mission objectives.

The extracted volatiles can be analysed with standard instrumentation, including mass spectrometry (MS), gas chromatography (GC), LIBS spectroscopy, Raman spectroscopy, or infrared spectroscopy. Mass spectrometry requires the collection of a sample and access to the evolved volatiles for ionisation and analysis of the molecular masses. The same is true for gas chromatography, while both methods can be combined (GC-MS) to improve the separation of molecular masses. The remaining technologies can be applied remotely with line of sight contact to a sample that is up to several meters apart. LIBS and Raman laser spectroscopy are complementary and can be combined to gain both the elemental and the molecular composition of the sample (Wiens *et al.*, 2005), as well as get insight into subsurface compositions by ablating the surface of the sample. Because in the latter only the scattering of the impacting laser is measured, it can be of advantage to combine these with spectroscopy in the visible (VIS), near infrared (NIR) or mid infrared (IR) wavelengths (Adar, 2011).

Table 1-1: Methods to access, extract, and analyse lunar volatiles

	Alternative A	Alternative B	Alternative C	Alternative D	Alternative E
Platform	stationary (lander)	semi-mobile (robotic arm)	mobile (rover)	n/a	n/a
Sample acquisition	drill	penetrator	scoop	surface cover	none (remote inspection)
Sample transfer	robotic arm container	feed hopper/ feed tube	pneumatic tube	vibration transport	none
Sample pre-treatment	crushing	sieving	none	n/a	n/a
Sample processing	crucible	gas fluidisation	vibrofluidisation	rotary kiln/ tumbling mixer	none
Volatiles extraction	electrical heating (contact, conduction)	electrical heating (contactless, radiation)	microwave heating	laser heating	solar heating
Volatiles transfer	continuous transfer	batch collection	n/a	n/a	n/a
Volatiles analysis	mass spectrometry	LIBS spectroscopy	Raman spectroscopy	VIS/NIR/IR spectroscopy	gas chromatography

1.2.2 ExoMars and MSL Feed Hoppers

Before it comes to processing of a volatiles-bearing regolith sample, it must be excavated and handled in a way that ideally does not alter its pristine state in terms of composition and temperature. A crucial part of the sample handling is the transfer to the location where it is processed – in the present context being the sample oven of the instrument where the thermal extraction of gases is conducted. The transfer often involves the use of a conveying device, such as a feed hopper, to guide the sample into the oven. Figure 1-1 depicts the Dosing Unit (DU) of the ExoMars Powdered Sample Dosing and Distribution System (PSDDS, part of the Sample Preparation and Distribution System SPDS), which is used to dose the sample into the ovens (Paul *et al.*, 2017). The DU includes two sets of an inlet funnel and an outlet funnel with a rotating dosing mechanism in between. The outlet diameter of the lower funnel is 4 mm, as defined by the internal diameter of the sample ovens. For the material of the inlet funnels, polished stainless steel was chosen because it is generates less triboelectric charging compared to aluminium or titanium (Anderson *et al.*, 2009; Paul *et al.*, 2017). To enhance the sample flow a piezoelectric vibration actuator is included, which provides a square profile of frequencies from 0 Hz to 500 Hz. It was found that 150 Hz is an optimum frequency for this system to ensure reliable dosing (Paul *et al.*, 2017).

A similar funnel was designed for the Beagle-2 GAP (Gas Analysis Package) instrument (Pullan *et al.*, 2004) and the derived concept L-VRAP (Lunar Volatile Resources Analysis Package) (Wright *et al.*, 2012). The concept design for the instrument VAPoR (Volatile Analysis by Pyrolysis of Regolith) foresees a Solid Sample Inlet Tube (SSIT) for sample dosing (ten Kate *et al.*, 2010), which is inherited from the instrument SAM (Sample Analysis at Mars) on the MSL (Mars Science Laboratory) rover. The SAM SSIT implies two asymmetrical funnels that are joined with a tube at the bottom end. The inside diameter of the tubes is 4.1 mm and the overall height of the SSIT is 254 mm. To make sure that at least 98 % of the sample are reliably transported through the SSIT, a redundant piezoelectric vibration mechanism is included in the assembly, driving a frequency sweep from 100 Hz to 500 Hz over 15 s with a peak amplitude of 0.22 mm (Mahaffy *et al.*, 2012).

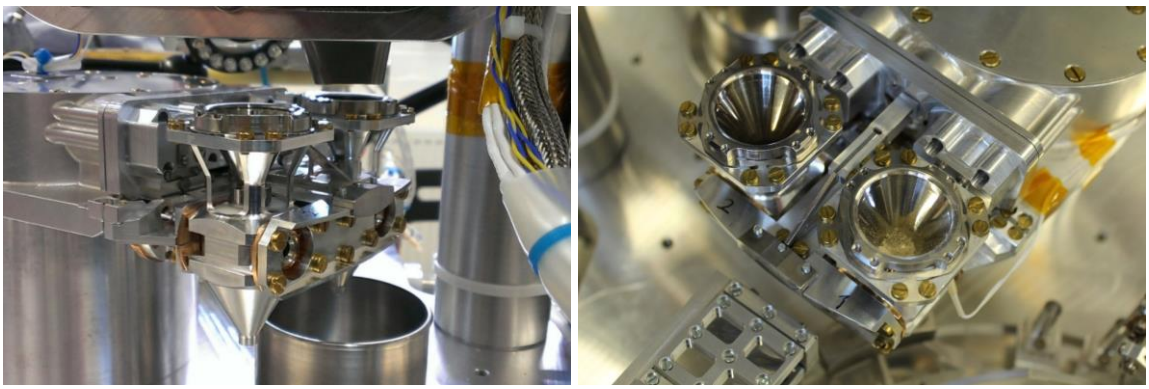

Figure 1-1: Engineering prototype of the ExoMars SPDS sample dosing unit (European Space Agency, 2017, Credit: Kayser-Threde GmbH)

1.2.3 Relevant Sample Oven Designs

This section is an adapted and updated excerpt from Reiss et al. (2017)*, written by the author of the present thesis.*

As a key element for the processing of a lunar soil sample and the subsequent extraction of volatile content, the sample container, or oven/crucible, and the heating methods will further be reflected in this thesis. To create a basis for later discussions, a review of existing relevant instrument designs is presented in the following, focusing on the sample oven and the heating method. Table 1-2 summarises the result of this review. Relevant instruments for the extraction and analysis of volatiles include: Rosetta SD2 (Sampler, Drill and Distribution System) with Ptolemy/COSAC (Cometary Sampling and Composition experiment), ExoMars SPDS with MOMA (Mars Organic Molecule Analyzer), Beagle-2 GAP, Viking GCMS (Gas Chromatograph Mass Spectrometer), Phoenix TEGA (Thermal and Evolved Gas Analyzer), Mars Science Laboratory SAM, Resource Prospector OVEN (Oxygen and Volatile Extraction Node), Lunar Lander L-VRAP, and VAPoR.

While all of these instruments are designed to heat a regolith sample (of martian, lunar, or cometary origin), they mainly differ in temperature ranges, sample size, number of ovens, and oven materials. Most of them are designed to achieve temperatures between 1000 °C and 1400 °C in order to release gases (for instance oxygen) by pyrolysis of the sample material. These ovens use crucibles made of platinum (SD2, GAP), ceramics (Viking), nickel (TEGA), Inconel (SAM, OVEN), alumina (VAPoR), or steel (MOMA). The sample ovens of SAM are made of Inconel 693, which offers improved resistance to high temperature corrosion mechanisms compared to common nickel-based alloys (Special Metals Corporation, 2005). The sample cups that are inserted into this oven are made of quartz glass, which adds chemical inertness. Another concept is used for the sample ovens of SAM's successor VAPoR, which is designed to achieve maximum temperatures of 1400 °C, compared to 1000 °C on SAM. VAPoR uses alumina crucibles together with quartz sample cups. OVEN utilises six reusable Inconel crucibles that are inserted into a reactor, consisting of two 17-4 stainless steel clamshells that are insulated with alumina in the inside.

All reviewed instruments use resistance wires to heat the oven. Most of them use a platinum wire, whereas on SAM and VAPoR, a zirconium grain strengthened (ZGS) 90 % platinum / 10 % rhodium wire was chosen. This alloy offers high creep resistance and rupture strength at high temperatures for prolonged periods, such

as around 150 h at an applied stress of about 1 kg/mm² and a temperature of 1400 °C (McGrath and Badcock, 1987), and is often used to contain molten glass. Alternatives to this resistance wire are standard high-resistivity FeCrAl alloys for use up to 1400 °C (for instance Kanthal A or Kanthal APM). On SD2, GAP, and TEGA, the resistance wire is wound around the cylindrical oven and affixed as well as insulated with ceramics. MOMA uses a platinum heating filament that is embedded in ceramics. On SAM and VAPoR, the resistance wire is threaded up and down through small channels in an alumina crucible, whose complex geometry is additively manufactured with ceramic stereolithography. OVEN contains three segments of coiled NiCr wire heaters on each half of the clamshells that surround the crucible.

The sample sizes of the above listed instruments range from around 40 mm³ to 789 mm³. This corresponds to oven dimensions in the range of 2 mm to 7 mm in diameter and 5 mm to 20 mm in height, respectively. The exception here is OVEN with a sample core of diameter 16 mm and height 125 mm, which allows a sample size of approximately 25 cm³. SAM draws an average of 36 W to reach 950 °C (measured at the outside of the oven), whereas VAPoR needs about 60 W to heat a sample up to 1300 °C and maintain this temperature. OVEN even uses a maximum of 150 W for its six heating segments to reach 900 °C. GAP on the other hand only needed 6 W to heat a sample up to 1000 °C, but the sample size with less than 20 mm³ is considerably smaller. Thermal conductivity strongly depends on gas pressure and temperature, facilitating heating of samples on Mars (SAM, GAP) when compared to Moon (VAPoR, OVEN) with its ultra-high vacuum and extremely low temperatures.

Table 1-2: Summary of the main oven parameters of relevant instrument designs, based on Reiss et al. (2017)

Mission/ Instrument/ Target	Number of ovens	Maximum oven temp.	Oven/ sample size	Sample volume/ mass	Oven material	Heating method/ material	Power demand
Rosetta/ SD2/ 67P-CG	10 MTO, 16 HTO [a]	180 °C, 600 °C, [b] 800 °C [a,c]	Ø5 outside, Ø3 inside x 6 mm, ~16 x 8.5 mm overall[a,c]	42 mm³	MTO: Platinum, Sapphire crystal for inspection[a]	Platinum resistance wire enamelled on oven (encased in glass)[b,c]	n/a
ExoMars/ MOMA/ Mars	20 for EGA, 12 for derivatisation [d]	850 °C, 600 °C [d]	Ø6 x 8 mm [d]	50 to 100 mg[e], ~200 mm³ [d]	High-temperature steel[d]	Platinum heating element embedded in ceramics[d]	n/a
Beagle-2/ GAP/ Mars	12 [f]	1000 °C [f]	Ø3 mm, sample filled up to 5 mm height	50 to 100 mg [f]	Platinum liner, 2 g oven mass, radiation shield and ceramic support structure[f]	Wound Pt-Rh filament, electrical insulation with layer of aluminum oxide[f]	6 W
Viking/ GCMS/ Mars	3 [g]	50 °C, 200 °C, 350 °C, 500 °C [g]	Ø2 x 19 mm [g]	60 mm³ [g]	Ceramic[g]	n/a	n/a
Phoenix/ TEGA/ Mars	8 thermal analysers with each two ovens (one with and one without sample)[h]	950 °C [h]	Ø7.2 x 21.6 mm [h]	38 mm³ [h]	Nickel, two radiation shields (multiple layer platinum sheet around each oven, second multiple layer nickel sheet around pair of two ovens)[h]	Platinum resistance wire (Ø0.075 mm) and resistance thermometer (Ø0.05 mm) wound around oven and insulated with ceramics coating (alumina) [h]	78 W with all heaters on[h]

MSL Curiosity/ SAM/ Mars	2 ovens, 74 sample cups, 60 sample cups[i,j]	1100 °C [j]	Ø7 x 20.5 mm [j,k]	789 mm³ [k]	Inconel 693 tube surrounded by alumina sleeve, quartz sample cups[i]	Ø0.51 mm platinum-zirconium alloy resistance wire[j]	36 W at 950 °C [k]
Resource Prospector/ OVEN/ Moon (FDU)	6 crucibles, 1 heating reactor[l]	150 °C, 900 °C (H_2 red.) [l]	Ø 16 x 125 mm [l]	25133 mm³, 38 g [l]	Inconel crucibles, 17-4 stainless steel oven with internal alumina fabric insulation[l]	Two clamshell halves with three heating segments (coiled NiCr wire) each[l]	25 W for each heating segment to reach 150 °C[l]
Lunar Lander/ L-VRAP/ Moon (Concept)	24 [m,n]	1000 °C	Ø3 mm, sample filled up to 5 mm height	50 to 100 mg [m]	n/a (2 g oven mass)	Resistance wire	n/a
VAPoR/ Moon (Concept)	6 [k]	1400 °C [k,o]	Oven Ø6.2 x 18.2 mm, quartz sample cup Ø3 inside, Ø5 outside x 25 mm[k]	539 mm³ [k]	Alumina crucible[k]	ZGS Platinum-10% Rhodium resistance wire[k]	64 W (reach 1300 °C), 60 W (hold 1300 °C), 70 W (10 mg silicate powder)[k]

Note: MTO = Medium Temperature Oven; HTO = High Temperature Oven; FDU = Field Demonstration Unit
References: [a](Finzi *et al.*, 2007), [b](Goesmann *et al.*, 2007),[c](Wright *et al.*, 2007), [d](Goesmann *et al.*, 2017), [e](Buch *et al.*, 2011), [f](Pullan *et al.*, 2004), [g](Biemann *et al.*, 1977), [h](Boynton *et al.*, 2001), [i](Mahaffy, 2008), [j](Mahaffy *et al.*, 2012), [k](Glavin *et al.*, 2012), [l](Paz *et al.*, 2013), [m](Morse *et al.*, 2012), [n](Wright *et al.*, 2012), [o](ten Kate *et al.*, 2010)

1.2.4 ProSPA Sample Oven

Many of the studies presented in this thesis were done in the context of the ProSPA sample analysis instrument, which is currently under development by ESA and planned to fly on board the Luna-27 mission (see chapter 1.1). To provide a better understanding of the relevant parts of the system, a brief description with focus on the sample ovens is given in the following. ProSPA strongly builds upon the heritage of earlier instruments (Carpenter *et al.*, 2017), such as GAP, COSAC, and MOMA, and directly evolves from the L-VRAP concept study, as described in the previous section. Similar to these systems, ProSPA contains a rotating carousel-like structure, on which a number of sample ovens are mounted. A drill that is part of a separate subsystem called PROSEED (PROSPECT Sample Excavation and Extraction Drill) is used to acquire a sample from a depth of up to 1.2 m below the lunar surface. After the sample is excavated the drill moves over one of the ovens on the carousel and drops the sample into an oven. The latter is then moved under a so-called tapping station, where it is sealed and connected to the power supply of the instrument to be subsequently heated. Evolved gases are guided through a pipe at the top of the oven to be analysed by one of two mass spectrometers. The instrument features three different analysis modes (Barber *et al.*, 2017):

- Evolved gas analysis: The sample is heated from ambient temperature (around -150 °C) up to 1200 °C at a defined temperature rate (for instance 6 °C/min) and the evolved gases are continuously analysed with an ion trap mass spectrometer similar to the one of the Ptolemy instrument (Wright *et al.*, 2007). This analysis mode is also referred to as Volatiles Extraction Demonstration (VED).
- Stepped pyrolysis or combustion: The sample is heated to defined temperatures and the evolved gases are collected with a cold finger before they are further processes for isotopic analysis with a magnetic sector mass spectrometer similar to the one of the GAP instrument (Pullan *et al.*, 2004).
- ISRU demonstration: The sample is heated to a defined reaction temperature (for instance 900 °C, held for 3 h) in the presence of hydrogen to reduce the iron oxides and produce water.

The baseline design of the cylindrical sample ovens was derived from COSAC and GAP and has an internal diameter of 2.8 mm and a height of 4.5 mm. Similar to the heritage systems, the sample is heated by a resistive wire that is wound around the outside of the cylindrical ovens and fixed with ceramic paste. A

thermocouple is mounted on the outside of the ovens to measure the sample temperature. Figure 1-2 shows some of the heritage designs relevant for ProSPA.

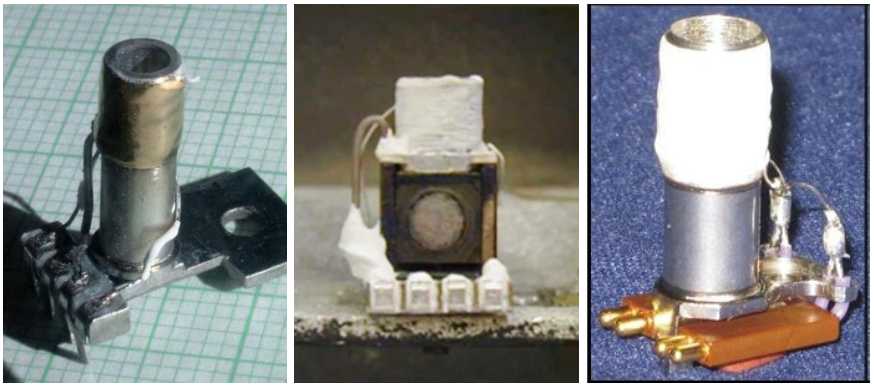

Figure 1-2: Heritage designs for the ProSPA sample ovens. From left to right: COSAC high temperature oven (Goesmann *et al.*, 2007), COSAC medium temperature oven (Finzi *et al.*, 2007), and early MOMA oven (European Space Agency, 2015b, Copyright: Max Planck Institute for Solar System Research).

1.3 Lunar Regolith Simulants

The availability of real lunar regolith on Earth is very limited and hence all experimental studies relevant to this thesis were done with analogue materials, referred to as lunar regolith simulants. Since the first simulant was produced in the early 1970's, there have been many attempts to mimic lunar regolith, be it in its particle size distribution, its geotechnical or chemical properties or its glass or (nanophase) metallic iron content. Taylor, Pieters and Britt (2016) list almost 30 different lunar regolith simulants that have been produced over the past decades and critically discuss their actual purpose. Regarding the latter, a comprehensive list of recommendations for the applicability of the most common simulants was published by Schrader et al. (2010).

In the scope of the experimental studies presented in this thesis, the two simulants JSC-1A (Orbital Technologies Corporation, 2007) and NU-LHT-2M (U.S. Geological Survey, 2008) were repeatedly utilised. JSC-1A resembles a mare type lunar regolith and consist of volcanic ash of basaltic composition from a quarry near Flagstaff, Arizona (Street *et al.*, 2010). It is one of the most widely used lunar simulants and actually describes a simulant family with the variations JSC-1AF (particles <50 µm), JSC-1A (particles <1 mm), and JSC-1AC (particles <5 mm). The second simulant NU-LHT-2M resembles a highland type lunar regolith and is a mixture of anorthosite and norite from the Stillwater Complex near Nye, Montana, and glass produced from the same feedstock (Street *et al.*, 2010). Particle sizes of both simulants extend below 25 µm (approximately 10 % for NU-LHT-2M). Various geotechnical and chemical analyses of both simulants are available in literature and referred to as required in the following chapters.

For a better understanding of all issues related to the transport phenomena discussed in the following chapters, it is beneficial to visualise the particle sizes and shapes of the simulants. Figure 1-3 and Figure 1-4 show selected microscopic images of the JSC-1A and NU-LHT-2M samples that were used in the experiments presented in this thesis. The difference in colour, as well as the broad particle size distribution becomes evident from these pictures, especially the large number of very fine-grained and clustered particles. Figure 1-5 shows a comparison of 70 µm glass beads and a sieved 70 µm to 80 µm fraction of NU-LHT-2M, which was intensively used for the volatiles extraction experiments.

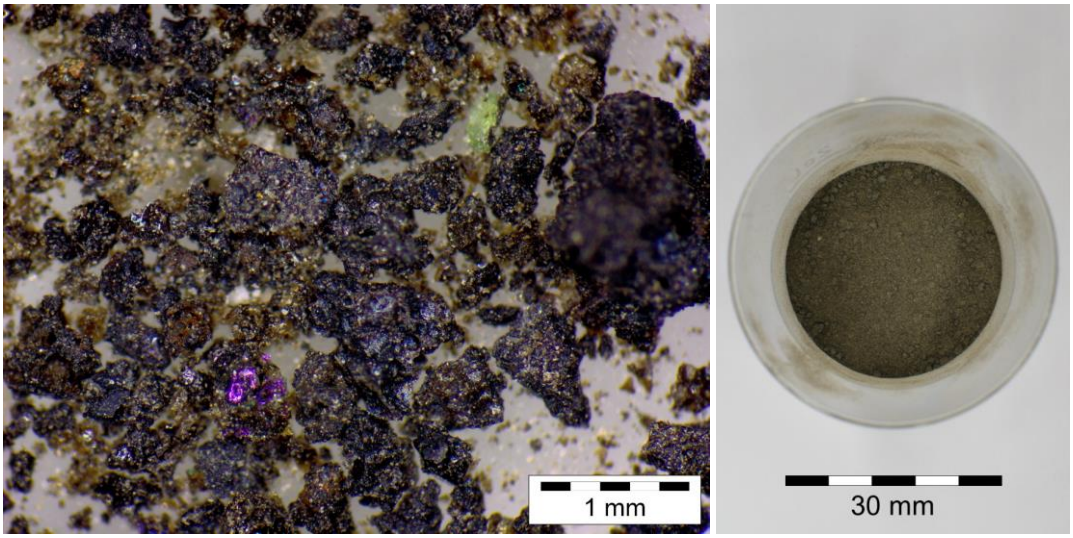

Figure 1-3: Microscopic image (left) and picture (right) of JSC-1A

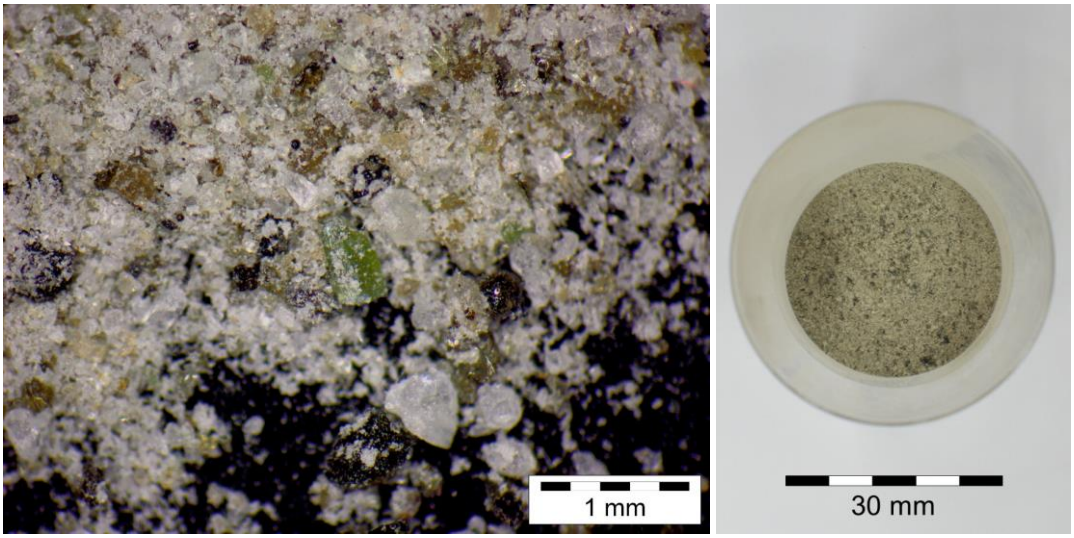

Figure 1-4: Microscopic image (left) and picture (right) of NU-LHT-2M

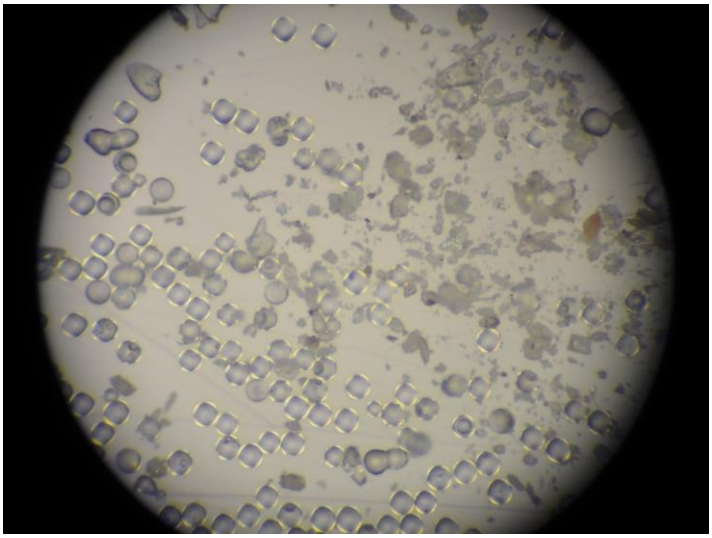

Figure 1-5: Microscopic image of 70 µm glass beads and the 70 µm to 80 µm fraction of NU-LHT-2M

1.4 Hydrated Lunar Regolith Simulants

Several approaches have been developed for laboratory studies to create lunar regolith simulants that contain water. The goal is to add water to a dry regolith sample in a controlled and reproducible way while avoiding contamination of the sample with other species. Ideally the bonds between water and regolith should be established in the same way as they are expected to form under lunar conditions. The following possible approaches to this problem have been examined and published to date:

A) Mixing the regolith with liquid water (Kleinhenz and Linne, 2013)

Probably the most straightforward method is to pour liquid water over regolith or spray liquid water onto regolith and stir the mixture until a uniform distribution of the water is achieved. It can subsequently be frozen to fix the water in the mixture and prevent that the liquid water either evaporates or accumulates due to gravity. Kleinhenz and Linne (2013) used this technique to add between 2 wt% and 11 wt% water to a 20 kg to 25 kg batch of lunar regolith simulant GRC-3 and Chenobi.

B) Mixing the regolith with a hydrated mineral salt (Kleinhenz, Sacksteder and Nayagam, 2008)

This is a simple way to add a known amount of water to the sample, but inherits the problem that the mineral composition and particle size of the bulk sample is altered. It was also observed that the mineral salt borax for instance strongly increases in size during dehydration. Since these problems all lead to significantly different physical properties, mixing the regolith with salt does not appear to be a viable solution to simulate hydrated regolith. Additionally the bonding mechanisms between water and regolith that are relevant in a lunar environment cannot be simulated and as a result the activation energy is not representative as well.

C) Adding water vapour to regolith (Pitcher *et al.*, 2016)

This method is based on introducing gaseous water into regolith by evaporating water in the direct presence of regolith. This technique was employed by Pitcher et al. (2016) in two different approaches. First they used a cooking pot with a second open container inside that holds the sample (15 cm diameter and ~16 cm height). Water was filled into the pot and boiled for 3 h. With this method, water concentrations of 1 wt% to 12 wt% for the regolith simulant UK4, 1 wt% to 9 wt% for JSC-1A, and 1 wt% to 5 wt% for NU-LHT-2M were achieved. Nevertheless, the distribution across the cylindrical sample was not uniform but strongly decreased towards its lateral and top boundary. As an improvement, the cooking pot was replaced with a pressurised cooking pot in the expectation that higher water concentrations can be realised. The sample size was changed to 11 cm in diameter and 12 cm in height. The result however showed lower water concentrations for UK4 (1 wt% to 6 wt%), similar concentrations for JSC-1A (1 wt% to 8 wt%), and only increased concentrations for NU-LHT-2M (6 wt% to 9 wt%). For the latter simulant the higher gas pressure produced a far more uniform distribution of water throughout the sample.

D) Adding dispersed water to regolith (Pitcher *et al.*, 2016)

In an approach to improve the previously described technique, Pitcher et al. (2016) used a water disperser with a tube connected to a sample container to wet the sample with water droplets. A NU-LHT-2M sample with diameter 15 cm and ~10 cm height was wetted for 3 h, which resulted in water concentrations of 7 wt% to 14 wt% across the sample. To achieve a more uniform distribution of the water, another sample was build up in layers, each being wetted for 1 h before adding a new layer. This lead to a very uniform water distribution with concentrations between 10 wt% and 14 wt% for different repetitions of the experiment. These values were close to the saturation level of NU-LHT-2M, which was determined to be between 13 wt% and 17 wt%.

E) Exposing regolith to a humidified carrier gas (Holmes and Gammage, 1975; Fuller and Agron, 1976; Robens *et al.*, 2007)

So-called gravimetric sorption analysers are commonly used for adsorption/desorption studies and allow the controlled humidification and weighing of a sample using a microbalance. The system continuously

guides a carrier gas over the sample, while the humidity level is controlled by combining a dry gas stream with a stream that is passed through a solvent to get saturated with the gas phase of the solvent (water vapour). The sample mass is in the range of several grams, while the final water content of the sample depends on the adsorption properties. The system is temperature controlled, and includes the capability to heat the sample for desorption. (Robens *et al.*, 2007) used such a device (DVS1 Advantage, by the company Surface Measurement Systems) to study water vapour adsorption on the Apollo 12 sample 12001,922. For relative humidity levels up to 96 %, the resulting mass gain of the sample was found to be around 0.1 wt% at maximum. In a similar apparatus, (Holmes and Gammage, 1975; Fuller and Agron, 1976) have also studied the adsorption of water on lunar regolith and found similar results, as summarised in Table 1-3. Although not specified any further, it was reported that the time required to achieve equilibrium could be *'…days to weeks if necessary'* (Fuller and Agron, 1976, p. 3). It was also observed that in particular the adsorption of water vapour *'at high relative pressures, required an overnight waiting period, or longer, for equilibration with the fines.'* (Holmes and Gammage, 1975, p. 3344)

F) Injecting water vapour into an evacuated chamber with regolith (Beck *et al.*, 2010; Poston *et al.*, 2013)

In order to create environmental conditions that are relevant to the adsorption of water on lunar or martian regolith, another method was applied that allows evacuation the sample. For studies on JSC-1A, (Poston *et al.*, 2013) used an apparatus to run temperature programmed desorption (TPD) experiments for samples dosed with different amounts of water. The apparatus includes a vacuum chamber with mass spectrometer, a sample holder (oxygen-free copper bar, chemically plated with nickel and capped with gold) with heating filament and cooling stage. The dosing with water was realised with a leak valve, which allowed exposures from 0.2 Langmuir to 500 Langmuir. Although the mass gain of the sample cannot directly be measured with this apparatus, the resulting desorption profile measured by the mass spectrometer allows a qualitative assessment of the adsorbed amount of water. A similar setup was employed by (Beck *et al.*, 2010) to study the adsorption of water on different martian minerals and the simulant JSC-Mars-1. The sample mass and its change during the course of the experiment was derived from reflectance spectroscopy in the near infrared. The amount of adsorbed water could be calculated from the strength of the spectral absorption, if a calibration to the individual samples was done beforehand. However, it needs to be noted that only the topmost grains of the sample (few tens of microns) can actually be measured with this technique, since the utilised wavelengths are subject to high absorption by the regolith. Generally, this study revealed comparably high values for the adsorption of water. For a relative humidity of 25 % to 30 %, the adsorbed water was found to be up to 5 wt% for JSC-Mars-1, volcanic tuff, and ferrihydrate, and 0.1 wt% for dunite. The authors state that *'The time scale for the adsorption process to reach equilibrium ranges from a few tens of seconds to a few tens of minutes for the samples studied.'* (Beck *et al.*, 2010, p. 4).

For larger sample quantities in combination with higher quantities of water above 1 wt%, the previously described methods A - D are a reasonable approach if for instance only the mechanical characteristics of moist or icy regolith shall be resembled. For smaller sample sizes it is questionable how well a uniform distribution of the water can be achieved with these methods. The methods E and F are of particular interest for the preparation of small samples with well-known quantities of water (primarily <1 wt%) under vacuum and in a clean environment, which is more representative of lunar conditions (Table 1-3).

Table 1-3: Literature values for humidity-driven adsorption of water on regolith (approximate values as read from diagrams in the respective references)

Sample	Maximum relative humidity (approx.) [%]	Maximum weight gain (approx.) [%]	Reference
12001,922	96	0.10	(Robens *et al.*, 2007, 2008)
10084,66	95	0.08	(Holmes and Gammage, 1975)
14003	40	0.012	(Fuller and Agron, 1976)
14003	98	0.15	(Fuller and Agron, 1976)
JSC-Mars-1	27	5	(Beck *et al.*, 2010)

1.5 Research Gaps

1.5.1 Regolith Flow

This section is an adapted and updated excerpt from Reiss et al. (2014)*, written by the author of the present thesis.*

Regolith transport shall be discussed for the example of feed hoppers, such as the ones used for ExoMars or MSL (chapter 1.2.2). The main indicator for the quality of sample transport in this case is the type of flow and the flow rate. Both are influenced by environmental factors such as gravity and gas pressure, and inherent physical properties of the sample such as particle shape and size and according friction angles. Design parameters of the respective hopper, such as inclination angles of the walls, outlet size, and surface materials also play a major role and should be chosen according to the desired sample flow. Common problems with hopper design include hindered sample flow, full clogging of the hopper, and residual sample material and therefore cross-contamination. Especially in a lunar environment with reduced gravity, there might be an increased risk that these problems occur: '*Flow of granular material at reduced gravity is not well understood, so predicting and designing for this behavior will be challenging.*' (Kleinhenz *et al.*, 2009, p. 3). A common approach to reduce the risk of restricted sample flow is to apply vibration to the hopper, as in the case of the ExoMars DU: '*Various breadboard tests showed that depending on the powder and the storage duration of sample inside the inlet funnel, a dosing is only reliable when the DU is vibrated'* (Paul *et al.*, 2017, p. 6).

Several experiments have been conducted in the past to understand the flowability of lunar regolith using the analogue materials JSC-1A and NU-LHT-2M (Mueller and Townsend, 2009; Ramé, Aguí and Wilkinson, 2010; Walton, 2012). Only few of them were realised in a representative environment with reduced gravity and none is known to have been conducted in vacuum. Mueller and Townsend (2009) performed experiments on board a partial-*g* parabolic flight to determine the flowability of the lunar regolith simulants JSC-1A, NU-LHT-2M, and OB-1 through a hopper for the ROxygen system. Due to a relatively large sample size it took up to 15 parabolas or 300 s under Moon-*g* to empty the experiment container and it required the application of hammer taps on the hopper to improve the material flow. Walton (2012) discusses the minimum outlet diameter for hopper-like containers to avoid cohesive arches. His laboratory tests under terrestrial conditions with JSC-1A and NU-LHT-2M resulted in a minimum outlet size of approximately 5 cm to 6 cm, without defining geometry and sample mass. The onset of material flow in a hopper is dependent on the major stress at the outlet, which is a linear function of the outlet size, bulk density of the sample, and gravity (Schulze, 2008). To reproduce a comparable flow, the outlet size therefore scales inversely with gravity. Under lunar gravity the minimum outlet size of a hopper would therefore be approximately six times larger. However, the resulting size appears to be largely overestimated if applied to smaller sample quantities in the range of several grams or milligrams, as relevant for sample analysis instruments such as MOMA, SAM, or ProSPA (compare chapter 1.2.2).

It can be concluded that sample flow is an issue also for smaller conveying hoppers, and that a common measure is to apply vibration to enhance the flow and make sure the sample does not get stuck. However, the exact influence and interplay of environmental conditions and material properties seems not to be fully understood, which is why a more detailed study on the overall process would:

1. Support design optimisations of existing concepts.
2. Provide new or confirm existing scaling laws for the design of such systems at different gravities.
3. Raise the attention and understanding of reduced gravity effects on the overall sampling chain.

1.5.2 Oven Design

For the oven design of ProSPA, certain deviations from the baseline oven size (chapter 1.2.4) are possible, depending on the interfaces to other subsystems and changing instrument requirements. In this regard several questions arose during the first phases of the instrument development. One consideration was to enlarge the sample ovens to accommodate larger samples. However, it was unclear to which extent this would affect the power demand and the heating duration, if additional thermal insulation would be required, as well as what the consequences would be from the perspective of volatiles analysis. At the same time it

was suggested that the ovens should be operated at temperatures up to 1200 °C, which is more than all of the heritage designs on which the ProSPA ovens are based upon were designed for (compare Table 1-2). Besides the question of energy demand and heating method, it was also unclear if there were any material incompatibilities or if contamination of the extracted volatiles with outgassing from oven materials was to be expected when using the heritage oven designs at higher temperatures. In particular for the envisaged ISRU operation mode (compare chapter 1.2.4), where a reactant gas would have to be kept inside the oven for longer periods, the material compatibility is a crucial factor. Finally, an upscaled oven would also mean an increase in sample diameter and hence a less homogeneous temperature distribution in the sample. It was not known to which extent this would affect the release of volatiles.

A thorough evaluation of the above problems through review, analysis, and test would:

1. Support the development of sample ovens for the ProSPA instrument or similar applications.
2. Inform trade-off studies for the design of the ProSPA sample ovens or comparable systems.
3. Support the design optimisation of sample ovens and mechanical/electrical/thermal interfaces.
4. Identify possible incompatibilities that have an effect on the viability of the analysis of volatiles or ISRU demonstration.

1.5.3 Regolith Processing

From the previous section it becomes clear that relevant past and current instruments strongly build upon heritage of earlier instruments and well-established technologies. It may seem likely to assume that heating a sample and analysing the extracted volatiles is a straightforward and well-understood process. However, reality often shows that especially the combination of the involved thermal and chemical processes is more complex and that the results are difficult to interpret.

Table 1-4 illustrates the interdependencies between environmental parameters (pressure, temperature, gravity), physical parameters of the sample (mineral composition, density, porosity, particle size), molecular kinetics and transport processes in the sample (heat transfer, sorption, mass transfer), and instrument- or mission-relevant parameters (power, energy, process duration, outgassing of released volatiles). It becomes clear that the measurement of the outgassing volatiles as the major scientific output is a result of many different interactions. If an instrument is able to measure the outgassing alone, it can only provide basic information about the volatile contents of the sample. If the sample temperature can be measured in conjunction with the outgassing, this provides substantially more information since actual desorption temperatures can be determined, which are an indicator for how the volatile element is bond to the regolith. However, the major problem with measuring the sample temperature is that there is no single ‘sample temperature’, but rather a range of temperatures across the sample due to the highly insulating character of porous media in general and lunar regolith in particular. From Table 1-4 it can be seen that temperature is a result of heat transfer, which in turn strongly depends on a variety of other parameters which themselves can differ across the entire sample volume, for instance particle size or mineral composition. Also volatiles-rich regions within the sample might create higher gas pressures locally after the volatiles are desorbed. As gas pressure is a major contributor to the effective heat transfer, this in turn can lead to a significantly different temperature in these regions. In conclusion it is more precise to use the term ‘sample temperatures’ or refer to an average sample temperature instead of a single sample temperature only. This is even more relevant when considering that temperature measurement implies several errors, among which the biggest is the thermal disturbance that is introduced by the temperature sensor itself. Especially at very low or very high temperature, the heat transfer through the (metallic) sensor is higher than through the regolith sample, so that either heat is removed from or added to the sample by the sensor. In this sense, the sensor can only measure its own temperature, which can be significantly different from the ‘sample temperature’. A model that includes a correct representation of the physical processes during the extraction of volatiles can help to understand the effect of the aforementioned influencing factors. It can also be used to get a closer look beyond experimentally measured data through model correlation. To this date, there is no comprehensive model that takes into account all of the factors described in Table 1-4 for the thermal extraction of volatiles from lunar regolith over a broad range of temperatures.

Table 1-4: Interdependencies between elements of the thermal extraction process

influences	Mineral composition	Gravity	Density/porosity/particle size	Gas pressure	Temperature	Heat transfer	Sorption	Mass transfer	Power demand	Process duration	Energy demand	Outgassing
Mineral composition			■			■	■					
Gravity						■						
Density/porosity/particle size				■		■		■				
Gas pressure						■	■	■				
Temperature				■		■	■	■				
Heat transfer					■				■	■		
Sorption				■								■
Mass transfer				■						■		■
Power demand					■						■	
Process duration											■	
Energy demand												
Outgassing												

From the perspective of gas analysis, the interplay of the aforementioned factors are relevant because the combination of temperature and outgassing signal most often is the only information that is available from in-situ measurements. If it is known how the sample properties influence the outgassing that is measured by a gas analyser, these properties could potentially be derived from the outgassing measurements. If for instance sample density affects the volatiles outgassing in a way that the measured gas pressure is delayed or shows distinctly different peaks, those characteristics can be used to derive the actual sample density. It is therefore advantageous to identify and assess such possible connections and verify them using combined models and experimental studies.

Theoretical models and experimental analyses can also help to estimate technical requirements for the respective instrument, which are mission-relevant. As heat and mass transfer within the sample dictate the duration of the extraction and hence the heating process, they also determine the energy requirement for the instrument. A better understanding of heat transfer in the sample can further be applied to an optimisation of the heating modes, which determine both the required power and the duration. If for instance from a scientific perspective it is desirable to reach a certain temperature in the sample in a certain time or hold the temperature over a certain period of time, it can be estimated beforehand how this affects the energy budget of the instrument. Thermal analysis on this level of detail is mostly neglected in the context of the overlying thermal analysis of the instrument. In this regard, a better understanding of the extraction process helps to connect the scientific requirements of an instrument with its technical, functional, or operational requirements.

In conclusion, a better understanding of the processes involved in the thermal extraction of volatiles from lunar regolith samples would:

1. Support and improve the scientific analysis of the data gathered from an in-situ experiment.
2. Provide an insight beyond measured or measurable data through model correlation.
3. Support the design and optimisation of the instrument and its operational modes.
4. Make the connection between scientific, technical, functional, and operational requirements.

1.6 Scope of this Thesis

1.6.1 Objectives

From the existing research gaps outlined in the previous section, the primary objective of this thesis is to enhance the current understanding of the thermal extraction process and the release of volatiles from lunar regolith samples. This objective shall be fulfilled by applying theoretical considerations, parameter studies, and an experimental proof of concept demonstration of the extraction of volatiles from lunar regolith analogues in a relevant environment. As a secondary objective, the feasibility of a chemical reduction process relevant to ISRU shall be investigated. To account for the sampling chain that precedes the thermal processing, the impact of environmental factors on the flow or transport of a sample shall be evaluated. In order to achieve these objectives, the following steps shall be covered:

1. Provide a theoretical assessment of the processes involved in the thermal extraction of volatiles from lunar regolith.
2. Assess the relevance and interdependency of heat and mass transfer for the thermal extraction of volatiles from lunar regolith.
3. Implement the theoretical basics of the thermal extraction of volatiles into a simulation model.
4. Perform parameter studies to get an insight into the sensitivity of the thermal extraction process to different environmental and material properties.
5. Develop and experimentally validate a method to add water to a lunar regolith analogue material.
6. Perform a proof of concept for the experimental extraction of volatiles from a lunar regolith analogue material in a relevant environment.
7. Perform a proof of concept for the experimental reduction of a lunar regolith analogue with hydrogen in a relevant environment.
8. Investigate the material flow of lunar regolith analogues through feed hoppers in a relevant environment.

1.6.2 Approach

To achieve the aforementioned objectives of this thesis, a stepwise approach was taken where different studies that investigate individual aspects were performed and sequentially combined to fulfil the overlying objective. In this thesis, chapter ‘2 Thermal Processing of Lunar Regolith‘ covers the theoretical basics of sorption, heat transfer and mass transfer, as well as hydrogen reduction, to create a basis for the following simulations and experimental studies. Chapter ‘3 Combined Model for Heat and Mass Transfer’ describes the implementation of these theoretical considerations into a simulation model and the parameter studies that were performed with this model. The following chapters present experimental studies that were performed as part of this thesis, together with the individually required preparatory studies. In chapter ‘4 Experimental Extraction of Volatiles’, the experimental parameter studies on the thermal extraction of volatiles are presented. Chapter ‘5 Experimental Reduction with Hydrogen’ describes the experiments on hydrogen reduction of lunar regolith analogues to produce water. Chapter ‘6 Sample Oven Scalability’ describes the trade studies to investigate the scalability of sample ovens and experiments on sample heating. In chapter ‘7 Flow Properties of Lunar Regolith Simulants’ the flowability of lunar regolith through feed hoppers under reduced gravity is addressed.

Several research projects were involved in the context of this thesis and delivered a large part of its motivation and justification. Relevant projects are therefore briefly described in the following.

ProSPA

From 2014 to 2016, the author of the present thesis was involved in the Phase A study of the ESA instrument study PROSPECT as part of the consortium assigned for the development of the ProSPA gas analysis instrument, which is planned to fly on the Russian Luna-27 mission. The author was tasked with the thermal analysis of the sample oven and a feasibility study that aimed to determine the implications of accepting a larger sample size and increasing the process temperatures. From 2016 to 2018, the author was involved in Phase B+ of the same study with the task to, among others, study and experimentally determine the

feasibility of volatiles extraction from lunar regolith and hydrogen reduction of lunar regolith with a ProSPA-like setup. The simulations, trade studies, and experiments presented in chapters 4, 5, and 6 were done in conjunction with the project tasks for ProSPA.

LUISE-2

Between 2012 and 2016, the author of the present thesis was executive project manager for the research project LUISE-2 (Lunar In-Situ Experiments), funded by the German Aerospace Centre DLR. The main activity was to perform preparatory studies for the thermal extraction of volatiles from lunar regolith. This primarily involved the development of the so-called LVS (Lunar Volatiles Scout), a probe that allows in-situ heating and analysis of a lunar soil sample with minimum sample manipulation. LUISE-2 enabled the participation in the partial-g parabolic flight campaign and the related experiments on sample transfer presented in chapter 7.

LUVMI

Between 2016 and 2018, the author of the present thesis was a member of the management board and involved in the scientific and technical work on the project LUVMI (Lunar Volatiles Mobile Instrumentation), funded by the European Commission within the European Union's Horizon 2020 framework. The relevant work in this project includes the further development of the LVS instrument concept and the supervision of breadboarding activities to raise the instrument's technology readiness level.

MARVIN

In this Phase 0 study from 2016 to 2017, funded by DLR, the author of the present thesis was responsible for developing a payload concept for the technological demonstration of ISRU on the Moon. This included the assessment of possible methods to produce oxygen from lunar regolith and the conceptual design and layout of an ISRU payload with a reactor that uses hydrogen to reduce lunar regolith and produce water, and subsequently oxygen.

2 Thermal Processing of Lunar Regolith

Chapters 2.1 to 2.3 are an adapted and updated excerpt from Reiss (2018)*, written by the author of the present thesis.*

This chapter describes the basics of molecular sorption and heat and mass transfer, which are relevant for the thermal processing of lunar soil samples that contain volatile species, in particular volatile water. The presented equations and theoretical models provide a basis for the understanding of the combined simulation model that was established within this thesis and the interpretation of results that were obtained from simulations and experimental studies. In chapter 2.1 relevant theoretical models are presented for the desorption and adsorption of water on lunar regolith particles together with estimates on the residence time and adsorption probability. In chapter 2.2 basic transient heat transfer equations are introduced with different models and curve fits for the specific heat and efficient thermal conductivity of lunar regolith and the lunar highland simulant NU-LHT-2M. An insight into the mechanisms of heat transfer at varying temperature and gas pressure is given for an Apollo 16 type regolith and the resulting thermal diffusivity as a combination of variable specific heat and thermal conductivity is presented. In chapter 2.3 the basics of mass transfer inside a lunar regolith sample are described, which is relevant for the outgassing of released volatile species. Models for the mass transfer at different flow regimes, including both diffusion and convection, are discussed in this context. Finally chapter 2.4 introduces the chemical process of reducing the oxides of lunar regolith with hydrogen, which is relevant for ISRU applications and further addressed by the experimental studies presented in this thesis.

2.1 Sorption of Lunar Volatiles

2.1.1 Desorption

Lunar volatile water as referred to in this study, is bound to the regolith by means of physisorption with a bond energy <0.35 eV or chemisorption with a bond energy >0.35 eV (Dyar, Hibbitts and Orlando, 2010). Both types of bonds are strongly sensitive to temperature and more stable for charged surfaces, more porous surfaces, and surfaces with defects. At temperatures below 100 K adsorbed monomers can be present, which cluster to form amorphous solid water at 110 K to 140 K, and crystalline water ice with cubic structure above 140 K to 150 K (glass transition happens at approximately 135 K). Near 200 K, this crystalline water with cubic structure can transform to hexagonal water. Above 150 K, only chemisorbed water is stable up to approximately 400 K (Dyar, Hibbitts and Orlando, 2010; Hibbitts *et al.*, 2011). A review of adsorption phenomena on materials relevant to lunar regolith can be found in (Goering *et al.*, 2008).

The desorption of an adsorbed molecule from a particle surface can be described by the desorption rate according to the Polanyi-Wigner equation:

$$\frac{d\theta}{dt} = -k_d \theta^n \tag{2-1}$$

with the rate constant k_d, the surface coverage θ (ratio of occupied sites on the particle surface), and the order of desorption n. For a first-order process, such as the gaseous desorption of adsorbed molecular water, $n = 1$ (Poston *et al.*, 2013). For the desorption of clusters or multi-layers of adsorbate, $n = 0$. For a recombinative molecular desorption, such as the desorption of two hydrogen atoms that form a gaseous H_2 molecule, the process would be of second order (Hibbitts *et al.*, 2011). The unit of k depends on the order of the reaction and is $[s^{-1}]$ for a first-order process. The rate constant can be calculated with the Arrhenius equation:

$$k_d = Ae^{\frac{-E_d}{k_B T}} \tag{2-2}$$

where A is the pre-exponential factor, E_d is the activation or desorption energy, k_B is the Boltzmann constant, and T is the temperature. For thermal desorption studies of water ice, Hibbitts et al. (2011) and Poston et al. (2013) chose the pre-exponential factor to be $A = 10^{13}\ \mathrm{s}^{-1}$. In the same study, isothermal desorption measurements were performed to determine the desorption energy of water on micronised lunar regolith simulant JSC-1A and albite. Desorption energies found in this study range from 0.45 eV (Poston *et al.*, 2013) and 0.50 eV for water ice clusters to 1.20 eV for strongly chemisorbed water (Hibbitts *et al.*, 2011). More than 90 % of the bindings are reported to have desorption energies less than 0.90 eV. The desorption of water from JSC-1A was observed at temperatures between 120 K and approximately 400 K. A desorption peak appeared at 170 K which was attributed to the formation of ice or water clusters at higher exposures with water.

Figure 2-1 shows the residence time of a single molecule on a lunar regolith particle (residence time equals the inverse of the desorption rate), depending on the desorption energy. It can be seen that for low-energy bonds and temperatures above 175 K the desorption takes place in less than a second. For the strongest bonds however the timescales are much longer. Even the duration of an entire lunar day (see dotted line in Figure 2-1) is not enough for a water molecule to desorb at temperatures below 320 K.

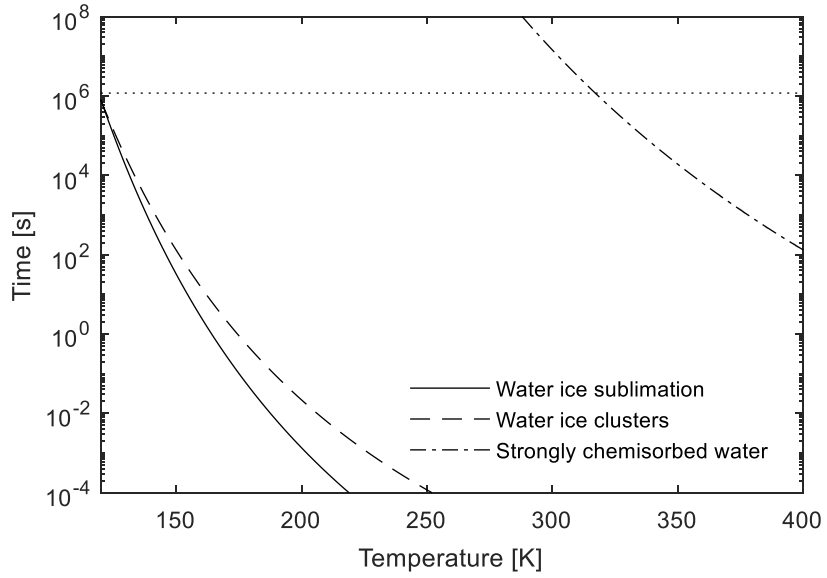

Figure 2-1: Residence time of a water molecule adsorbed on lunar regolith in the form of water ice clusters ($E_d = 0.45\ eV$) or strongly chemisorbed water ($E_d = 1.20\ eV$), as calculated on the basis of the desorption rate (Hibbitts *et al.*, 2011; Poston *et al.*, 2013). The sublimation curve is calculated on the basis of the sublimation rate at a given equilibrium vapour pressure (Schorghofer and Taylor, 2007). The dotted line marks the duration of a lunar day for reference.

Schorghofer and Taylor (2007) estimated the residence time of water molecules adsorbed on a solid layer of water ice based on the sublimation model. If the water vapour is in equilibrium with water ice, the sublimation rate equals the condensation rate. The residence time t_{res} can then be calculated with:

$$t_{res} = \frac{\rho_A}{S \cdot E} \tag{2-3}$$

Here $\rho_A = (\rho/m)^{2/3}$ is the areal density in molecules/m² with the density of water ice ρ and the mass of a single water molecule m. S is the dimensionless sticking coefficient that determines the ratio of molecules that condense on the surface. In the case considered here, $S = 1$, which means that all incident molecules stick to the surface and the up-going molecular flux from the particle surface only results from sublimation or evaporation (Andreas, 2007). The condensation rate or sublimation rate E is (Watson, Murray and Brown, 1961; Andreas, 2007):

$$E = p_v \sqrt{\frac{M}{2\pi RT}} \tag{2-4}$$

with the equilibrium vapour pressure p_v , the molar mass of water M, the universal gas constant R, and the temperature T. Schorghofer and Taylor (2007) use another form of equation (2-4) to calculate the sublimation rate in the unit molecules/(m²·s) using the molecular mass of water $m = M/N_A$ with Avogadro's constant N_A and the Boltzmann constant k_B:

$$E = \frac{p_v}{\sqrt{2\pi k_B T m}} \tag{2-5}$$

For calculating the equilibrium vapour pressure there are a number of semi-empirical models that extend into the lower temperatures between 110 K and 190 K (Buck, 1981; Wagner, Saul and Pruss, 1994; Murphy and Koop, 2005). In particular, the models by Buck (1981) and Murphy and Koop (2005) show good agreement even at very low temperatures below 100 K and are recommended by (Andreas, 2007) for the estimation of sublimation rates in a lunar cold trap environment. Schorghofer and Taylor (2007) use another simple form for the equilibrium vapour pressure that uses the triple point pressure $p_t = 611.657\ Pa$, the triple point temperature $T_t = 273.16\ K$, and the sublimation enthalpy $Q = 51.058\ kJ/mol$. The latter also matches well with the other two models and is further used here. Table 2-1 shows the three preferred models for the equilibrium vapour pressure. As depicted in Figure 2-1, the residence time of water ice based on the sublimation model, and a sublimation enthalpy of 51.058 kJ/mol (equals 0.53 eV), matches well with the time determined for the desorption model of water ice clusters with desorption energies around 0.45 eV.

Table 2-1: Calculation models for the equilibrium vapour pressure

Equation	Original validity range	Reference
$p_v = 611.15 exp\left[\frac{22.542(T-273.15)}{273.48+(T-273.15)}\right]$	193.15 K < T < 273.15 K	(Buck, 1981)
$p_v = exp\left[9.550426 - \frac{5723.265}{T} + 3.53068 ln(T) - 0.00728332T\right]$	T > 110 K	(Murphy and Koop, 2005)
$p_v = p_t exp\left[-\frac{Q}{R}\left(\frac{1}{T}-\frac{1}{T_t}\right)\right]$	n/a	(Schorghofer and Taylor, 2007)

The variation of surface coverage over time t for water adsorbed on lunar regolith can be calculated by solving equation (2-1). For the isothermal case this results in the following equation (2-6) with the initial surface coverage θ_0. For a non-isothermal sample, the integration of equation (2-1) is somewhat more complex due to the time-dependency of the temperature.

$$\theta = \theta_0 e^{-k_d t} \tag{2-6}$$

The specific surface area of lunar regolith ranges between 0.02 m²/g and 0.78 m²/g with a typical value of 0.50 m²/g (Carrier, Olhoeft and Mendell, 1991). The values are relatively high compared to the surface area of spheroidal particles with the same size, which is an indicator for the very irregular shape of lunar regolith. Analogue materials, such as the highland simulant NU-LHT-1M have comparable surface areas, as determined by Malvern Instruments (2007). Table C-1 in the appendix gives a summary of the values found for relevant particles. Assuming the effective surface area for an adsorbed water molecule with a molecular diameter of 2.75 Å to be approximately 6 Å², the surface coverage for a monolayer of molecular water can be calculated and translated into a mass fraction of the sample. As depicted in Table C-1, a monolayer of water on typical unaltered lunar regolith with a surface area of 0.50 m²/g would have a water concentration of $14 \cdot 10^{-6}$ mol/g, or 0.025 wt% respectively.

2.1.2 Resorption

If a molecule hits the surface of a sample particle, it will either scatter, trap, or stick (Masel, 1996). In contrast to sticking, trapping usually depends on the gas temperature and occurs more often at lower temperatures. Trapped molecules are in a weakly stable bond and can easily desorb if the surface temperature of the adsorbent is high enough. If the molecule forms a stronger bond with the adsorbent, it sticks and remains there for a reasonable time. Sticking is constrained by the ability of the molecule to form a bond with the surface and the rate of the energy transfer at collision. The sticking probability $S(\theta)$, which is a function of the surface coverage θ, may be used to determine whether a molecule sticks to the surface or not. The sticking probability is defined by the quotient of the number of molecules that adsorb, divided by the number of molecules that impinge on the surface, and can reach values between 0 and 1. With the incident flux of molecules E, the rate of adsorption can be described as:

$$\frac{d\theta}{dt} = S(\theta)E \tag{2-7}$$

Usually, experiments are performed to determine the initial sticking probability $S(0)$ at zero coverage and the variation of the sticking probability over surface coverage to find the term $S(\theta)/S(0)$. Values for $S(0)$ typically range from 0.1 to 1 and gases with $S(0) < 0.0001 \dots 0.01$ are said to not stick (Masel, 1996). $S(0)$ depends on the temperature, composition, and topology of the surface. The variation of the sticking coefficient over surface coverage can show different forms, ranging from a linear decrease (Type A) over an exponential decrease (Type B) to various other forms described by Morris, Bowker and King (1984). The simplest approach to obtain the sticking probability is to assume the probability that a molecule hits a free site is $(1-\theta)^n$ with n being the number of sites that are required to hold the adsorbate. This assumption leads to Langmuir's adsorption law, which uses the following sticking probability:

$$S(\theta) = S(0)(1-\theta)^n \tag{2-8}$$

The sticking probability shows Type A behaviour with $n = 1$ and Type B behaviour with $n > 1$. However, this approach is limited as Type A behaviour does not occur very often in reality. In fact, the majority of adsorption processes deviates from this model because there are more than only one adsorption site and there is interaction between the adsorbates. Additionally, a molecule that hits an occupied site does not necessarily desorb instantaneously, but can diffuse across the surface and adsorb at a free site. New models for so-called precursor-moderated adsorption account for such phenomena and include the probabilities for trapping at both free and occupied sites (Masel, 1996). Consequently, the sticking coefficient is a combination of different probabilities depending on the surface coverage and can become very complex.

The sticking probability of water on lunar regolith is poorly known with no sufficient data available in the literature. A study by Goering et al. (2008) investigated the sticking probability of water on JSC-1A in dependence of the monolayer surface coverage. For a zero coverage an initial sticking probability of $S(0) = 0.92 \pm 0.05$ was measured at 153 K and 10^{-9} mbar. For the adsorption of water on water ice there are multiple studies available that empirically determined the sticking probability (Crotts and Hummels, 2009). A study by Haynes, Tro and George (1992) found that for water on water ice, the sticking probability varies from $S(\theta) = 1.06 \pm 0.10$ at 20 K to $S(\theta) = 0.65 \pm 0.08$ at 185 K. They developed a precursor-moderated adsorption model that was correlated with the measured sticking coefficient:

$$S = \sigma\left(1 + \frac{k_d^0}{k_r^0} e^{\frac{-(E_d - E_r)}{RT}}\right)^{-1} \tag{2-9}$$

Values of $\sigma = 1.06$, $k_d^0/k_r^0 = 1.0$, and $(E_d - E_r) = 0.23\ kcal/mol$ delivered the best fit to the experimental data and showed an exponential decay with temperature, as depicted in Figure 2-2. For reference, a model developed by Matar et al. (2010) for the sticking coefficient of hydrogen on water ice is also illustrated in Figure 2-2. Even at higher temperatures the sticking probability for water on ice is above 0.6. However, it is questionable for how long these bonds remain, since the residence times rapidly decay to values below 1 s with temperature, as illustrated by Figure 2-1.

At equilibrium the incident flux of molecules in equation (2-7) equals the condensation rate described by equation (2-5) (Do, 1998; Beck *et al.*, 2010). This relation can be used when sublimation takes place in an undisturbed sample. According to Langmuir theory and in agreement with equation (2-7), the rate of adsorption is:

$$\frac{d\theta}{dt} = S(\theta)(1-\theta)\frac{p}{\sqrt{2\pi k_B T m}} \tag{2-10}$$

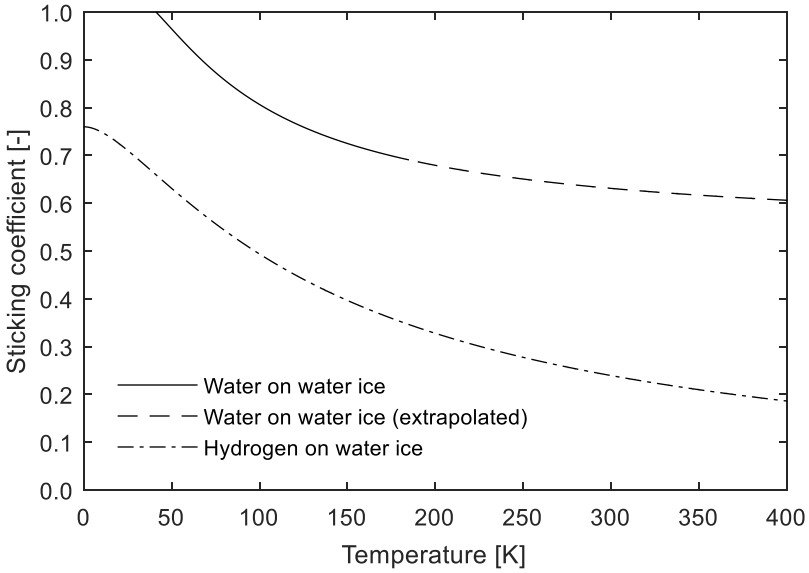

Figure 2-2: Sticking coefficients for water on water ice (Haynes, Tro and George, 1992) and hydrogen on water ice (Matar *et al.*, 2010), based on experimentally correlated models (dashed line is extrapolated)

2.2 Heat Transfer in Lunar Regolith

The general equation relevant for heat transfer in the sample is:

$$\left(\rho c_p\right)_{sg}\frac{\partial T}{\partial t} + \nabla\left(-k\nabla T - \left(\rho c_p\right)_g uT\right) = Q \tag{2-11}$$

The first term on the left-hand side of equation (2-11) describes the temperature change over time of the mixture of solid particles and gas in the voids. The second term describes conductive heat transfer through the solid-gas mixture with the thermal conductivity k, and the third term is the convective heat transfer via the gas phase with the Darcy velocity u. The right-hand side of the equation describes the source term. The product of density ρ and specific heat capacity c_p for the solid-gas mixture can be calculated with:

$$\left(\rho c_p\right)_{sg} = (1-\phi)\rho_s c_{p,s} + \phi\rho_g c_{p,g} \tag{2-12}$$

where ϕ is the porosity, $\rho_s c_{p,s}$ the product of density and specific heat capacity of the solid, and $\rho_g c_{p,g}$ the product of density and specific heat capacity of the gas. For the specific heat capacity of lunar regolith, a model by Schreiner et al. (2016) is considered best suitable as it combines earlier models by Robie, Hemingway and Wilson (1970) and Hemingway, Robie and Wilson (1973) for Apollo 14, 15, and 16 soils between 90 K and 350 K, and models by Stebbins, Carmichael and Moret (1984) for silicate minerals above 350 K and molten regolith above 1500 K. Figure 2-3 illustrates the resulting specific heat capacity over temperature, where values below 100 K were extrapolated with a cubic fit through the origin. The specific heat capacity of the gas phase is also temperature-dependent, for the case of water vapour there is a comprehensive list provided by Chase (1998). The effective thermal conductivity of the solid-gas mixture is discussed in more detail in the following section.

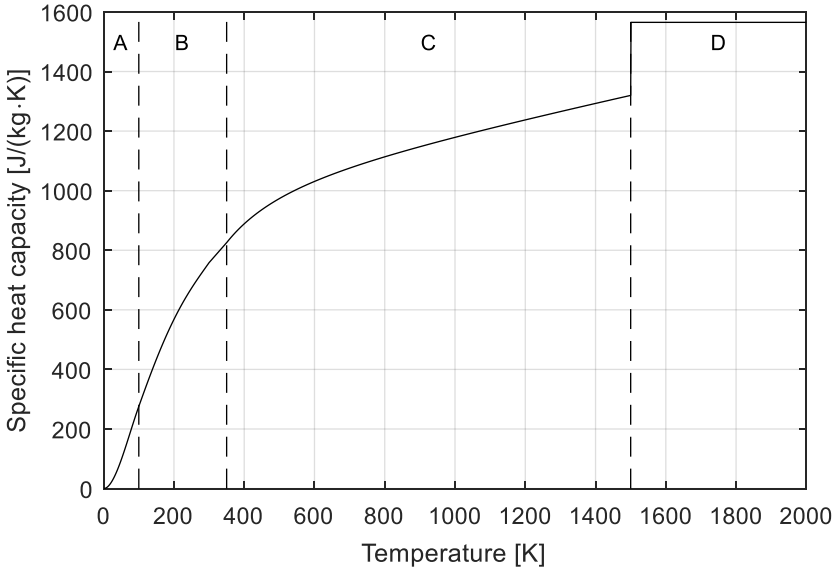

Figure 2-3: Specific heat capacity of lunar regolith, based on a model by (Schreiner *et al.*, 2016) with A) extrapolated values, B) data of Apollo 14/15/16 (Hemingway, Robie and Wilson, 1973), C) data of highland regolith (Stebbins, Carmichael and Moret, 1984), and D) data of molten regolith (Stebbins, Carmichael and Moret, 1984).

2.2.1 Thermal Conductivity Standard Model

The common simplified model used to fit all measurements of the thermal conductivity of lunar samples is described by the following equation (2-13) (Watson, 1964). It is assumed in this model, that the effective thermal conductivity k consists of a temperature-independent term with the constant C_{cond}, which accounts for conduction through the particle, as well as a temperature-dependent term with the constant C_{rad}, which accounts for radiation between the particles.

$$k = C_{cond} + C_{rad} \cdot T^3 \tag{2-13}$$

Various studies experimentally determined the thermal conductivity of regolith samples that were returned by the Apollo missions. Table 2-2 presents the boundary conditions for these measurements as well as the resulting constants that were used to fit equation (2-13) to this data.

Table 2-2: Parameters for the experimentally determined thermal conductivity of Apollo samples

Mission/ Sample	Origin	Rock type	Density [g/cm³]	C_{cond} [W/(m·K)]	C_{rad} [W/(m·K⁴)]	T [K]	P [Torr]	Reference
Apollo 11/ 10084-68	Mare	basaltic lava	1.265	$1.42 \cdot 10^{-3}$	$1.73 \cdot 10^{-11}$	203 - 405	10^{-2} - 10^{-7}	(Cremers, Birkebak and Dawson, 1970; Cremers and Birkebak, 1971)
Apollo 12/ 12001,19	Mare	basaltic lava	1.300	$9.22 \cdot 10^{-4}$	$3.19 \cdot 10^{-11}$	169 - 349	~10^{-6}	(Cremers and Birkebak, 1971)
Apollo 14/ 14163,133	Highland	ejecta	1.100	$8.36 \cdot 10^{-4}$	$2.09 \cdot 10^{-11}$	122 - 353	~10^{-6}	(Cremers, 1972b)
Apollo 14/ 14163,133	Highland	ejecta	1.300	$6.19 \cdot 10^{-4}$	$2.49 \cdot 10^{-11}$	109 - 404	~10^{-6}	(Cremers, 1972a)
Apollo 15/ 15031,38	Mare/ Highland	breccia, basalt	1.300	$6.25 \cdot 10^{-4}$	$1.19 \cdot 10^{-11}$	95 - 406	~10^{-6}	(Cremers and Hsia, 1973)
Apollo 16/ 68501	Highland	anorthosite	1.500	$4.84 \cdot 10^{-4}$	$1.11 \cdot 10^{-11}$	~100 - 400	n/a	(Cremers and Hsia, 1974)

The variation of thermal conductivities over their respective temperature range is given in Figure 2-4. Although the soil types vary strongly between the different samples, the resulting conductivities are in a similar order of magnitude. It is noteworthy that the highland type samples have the lowest thermal conductivity although their bulk density is the highest.

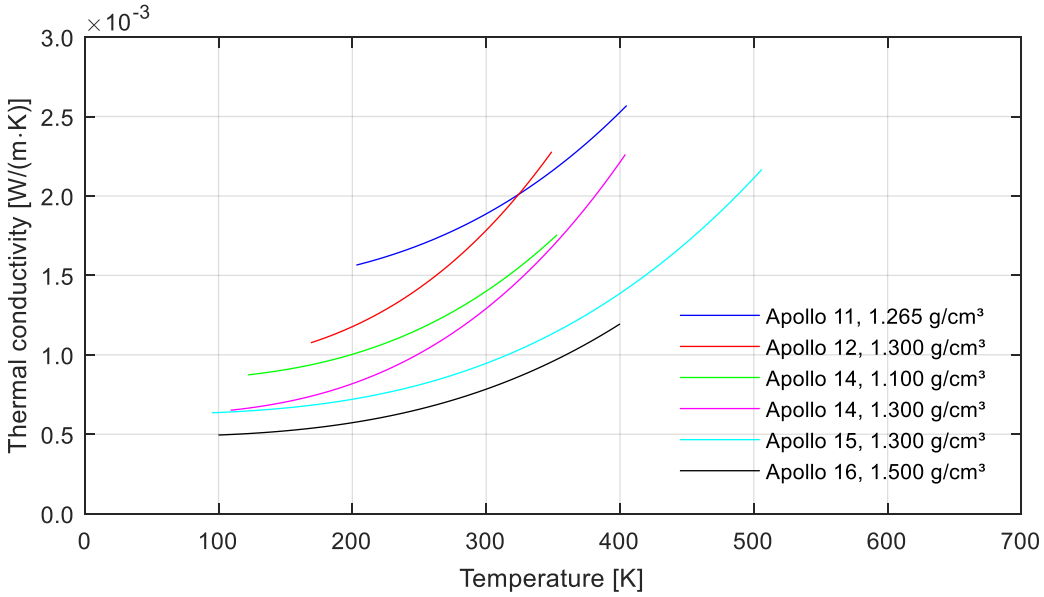

Figure 2-4: Thermal conductivities of Apollo samples plotted with the curve fit values taken from Table 2-2

2.2.2 Thermal Conductivity Coupled Model

The previously described standard model does not take into account the temperature dependency of the particle conductivity, the influence of the contact zone between particles, and the gas conductivity between the particles. To study the variation of thermal conductivity during a gas extraction process over a wide range of temperatures and gas pressures, a more sophisticated model is required. So-called coupled models can be used to combine these effects to an effective thermal conductivity. Parzinger (2014) compared 59 models for the thermal conductivity and found that only 10 are suitable for the application with lunar regolith in a lunar environment, because they incorporate particle contact conductivity, radiation, and gas conductivity. However, none of these remaining models covers the entire range of temperatures and gas pressures required for the present problem of gas extraction from lunar samples. Parzinger (2014) therefore developed a semi-empirical model that combines the most appropriate models and covers a wider range. It assumes a parallel connection of the following heat transfer mechanisms: conduction through the physical contact between solid particles k_{sc}, radiation between the particles k_{rad}, conduction through gas in the void spaces between the particles k_{gas}, and the coupling of solid and gas conduction k_{sg}. All of these add up to form the effective thermal conductivity k:

$$k = k_{sc} + k_{rad} + k_{gas} + k_{sg} \tag{2-14}$$

The first term takes into account the contact area between particles, through which heat is transferred, and hence mainly depends on the mechanical properties of the particles (Kaganer, 1969; Parzinger, 2014):

$$k_{sc} = 3.44 \cdot (1-\phi)^{\frac{4}{3}} \left(\frac{1-\nu^2}{Y}\right)^{\frac{1}{3}} k_s p_s^{\frac{1}{3}} \tag{2-15}$$

Here ν is Poisson's ratio and Y the Young's modulus of the solid particle, k_s is its thermal conductivity, and p_s is the load that compresses the particles.

The second, radiative, term is calculated with the following relation, based on a model for absorption and scattering of the radiation after Caps, Fricke and Reiss (1985) and Verein Deutscher Ingenieure (2010):

$$k_{rad} = \frac{16\sigma n^2}{3E} T^3 \tag{2-16}$$

With the Stefan-Boltzmann constant σ, the extinction coefficient E, and the real part of the complex effective refractive index n (Reiss, 1985; Parzinger, 2014):

$$n^2 = {n_f}^2 \left(1 + \frac{3(1-\phi)\frac{{n_s}^2 - {n_f}^2}{{n_s}^2 + 2{n_f}^2}}{1 - (1-\phi)\frac{{n_s}^2 - {n_f}^2}{{n_s}^2 + 2{n_f}^2}} \right) = {n_f}^2 \left(1 + \frac{3(1-\phi)({n_s}^2 - {n_f}^2)}{3{n_f}^2 + \phi({n_s}^2 - {n_f}^2)} \right) \tag{2-17}$$

where n_f and n_s are the refractive indices of the fluid and the solid respectively. Experimentally determined values of n for terrestrial rocks are described by Pollack, Toon and Khare (1973).

The gas conductivity is mainly dependent on the gas pressure, which determines the flow regime. In free molecular flow, for $Kn > 10$, the heat flux between two parallel surfaces can be calculated with the following relation (Verein Deutscher Ingenieure, 2013):

$$k_{gas,Kn>10} = \frac{1}{2} \alpha_a (\gamma + 1) c_p \frac{p}{\sqrt{2\pi R_s T}} \tag{2-18}$$

Note that this term is not an actual thermal conductivity in the unit W/(m·K), but a heat flux with the unit W/(m²·K). This is because the heat transferred by the gas molecules in the free molecular flow is no longer dependent on the gap size between the surfaces. There is no contact between gas particles in the gap and heat transfer only depends on the number of molecules that move between the surfaces. In equation (2-18), γ is the ratio between the specific heat capacities of both surfaces, R_s is the specific gas constant, and:

$$\alpha_a = \frac{\alpha_{a,i}\alpha_{a,j}}{\alpha_{a,i} + \alpha_{a,j} - \alpha_{a,i}\alpha_{a,j}} \tag{2-19}$$

where $\alpha_{a,i}$ and $\alpha_{a,j}$ are the accommodation coefficients of the surfaces. The latter are difficult to determine, but the values tend to be closer to 0 for light molecules like hydrogen and helium and closer to 1 for heavier molecules like nitrogen and oxygen. Although they also depend on temperature and the state and cleanliness of the surface, they can be estimated using the following equation (Kaganer, 1969):

$$\alpha_{a,i} = 1 - \left(\frac{m_s - m_g}{m_s + m_g} \right) \tag{2-20}$$

where m_s is the mass of the molecules of the solid surface and m_g is the mass of the gas molecules. In case there is already an adsorbed layer of molecules on the solid surface, the accommodation coefficient comes close to 1.

Due to the Smoluchowski effect, the gas conductivity k_g is low in the free molecular flow regime and increases in an s-shape manner with increasing pressure, or decreasing Knudsen number respectively, according to the following equation (Kaganer, 1969; Griesinger, Spindler and Hahne, 1999):

$$k_{gas,Kn<10} = \frac{k_{gas,0}}{1 + 2\beta \cdot Kn} \tag{2-21}$$

where $k_{gas,0}$ is the thermal conductivity of the gas at atmospheric pressure and β is a gas-specific constant ($\beta = 1.41$ for water vapour at 373.2 K (Verein Deutscher Ingenieure, 2010)). For pressures close to atmospheric, the gas conductivity reduces to the ordinary equation of conduction (Kaganer, 1969).

Since the conductivity for high Knudsen numbers actually is a thermal transmittance in the unit W/(m²·K), it cannot simply be added to the other terms that form the effective thermal conductivity in equation (2-14). To address this issue and get an estimation of the order of magnitude for the free molecular gas conductivity, a comparison of both cases for the thermal transmittance through the gas-filled void between two particles with $k_{gas,Kn>10}$ and $k_{gas,Kn<10} \cdot 1/d$ was made (d is the gap size between the particles, equal to the mean particle diameter for a worst case scenario). From Figure 2-5 it can be seen that the values are mostly similar

especially in the free molecular flow regime with $Kn > 10$. For convenience, it is therefore decided that for the applications relevant to this thesis, equation (2-21) can be used to calculate the gas conductivity over the entire range of Knudsen numbers.

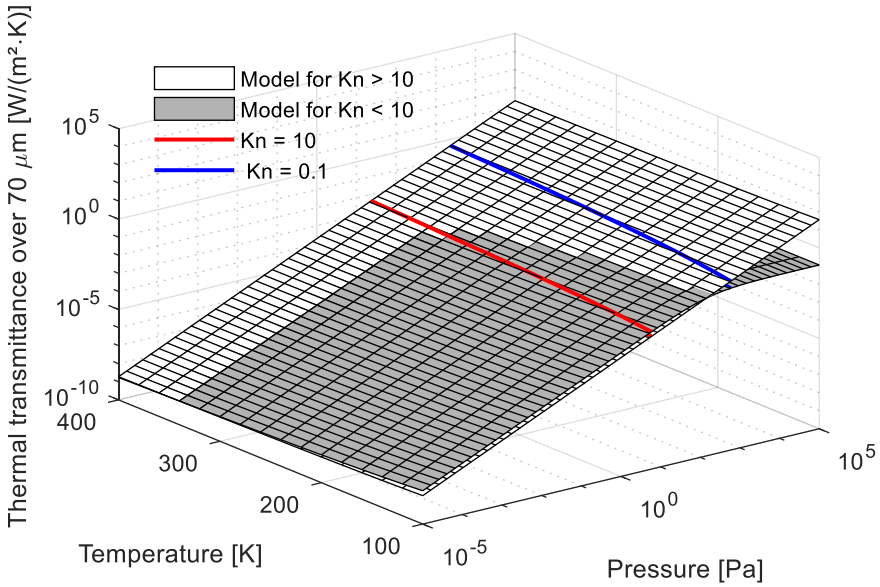

Figure 2-5: Comparison of the thermal transmittance over a particle gap of 70 µm , using equation (2-18) for $Kn > 10$ and equation (2-21) for $Kn < 10$

The last term in equation (2-14) represents the coupling between solid and gas in the vicinity of the contact between particles. The heat transfer in this area can be calculated using an extended model of the unit cell by Swimm et al. (2009), which discretises the contact area of two hemispheres with 1000 hollow cylinders. The extension of this standard model includes an additional shape factor that takes into account the deviation of the particle shape from the ideal sphere. The thermal conductivity for the solid-gas coupling is given by:

$$k_{sg} = (1 - \phi_{uc}) \frac{2r}{r^2 \pi} \sum_{i=1}^{1000} \left(\frac{h_{g,i}}{k_{gas,i} A_i} + \frac{h_{s,i}}{k_s A_i} \right)^{-1} \tag{2-22}$$

With the particle radius r, the area of the cylinders A_i, $\bar{\delta}_i$ and δ_i the heights of the solid particle and the gas at position r respectively, the porosity of the unit cell ϕ_{uc}, and the elliptical shape factor F_{ell}. The parameters of the unit cell can be calculated with the following relations, using the semi-major axis a, the semi-minor axis b, and the particle diameter d:

$$\phi_{uc} = \frac{1}{2}(3\phi - 1) \tag{2-23}$$

$$a = \frac{d}{2} {F_{ell}}^{-\frac{1}{3}} \tag{2-24}$$

$$b = \frac{d}{2} {F_{ell}}^{\frac{2}{3}} \tag{2-25}$$

$$h_{s,i} = d - 2b \left(1 + \sqrt{1 - \left(\frac{i}{a} \frac{r}{1000} \right)^2} \right) \tag{2-26}$$

$$h_{g,i} = d - h_{s,i} \tag{2-27}$$

$$A_i = \pi \left(\frac{r}{1000} \right)^2 (2i - 1) \tag{2-28}$$

Parzinger (2014) compared the particle shapes of the lunar soil simulant JSC-1A and the Apollo 17 sample 70009 and concluded that a shape factor of $F_{ell} = 0.6$ can be assumed for both materials. It shall be noted that the gas conductivity $k_{gas,i}$ at each cylinder has to be calculated individually depending on the Knudsen number at each position as the quotient of mean free path and gap size.

2.2.3 Parameter Fit for the Apollo Sample 68501

As described in section 2.2.1, Cremers and Hsia (1974) measured the thermal conductivity of the Apollo 16 sample 68501 in the range of approximately 100 K to 400 K and fitted the data to equation (2-13) with the constants $C_{cond} = 4.84 \cdot 10^{-4}\ W/(m \cdot K)$ and $C_{rad} = 1.11 \cdot 10^{-11}\ W/(m \cdot K^4)$. To predict how the thermal conductivity of an Apollo 16 like sample varies with temperature and pressure, the model described in the previous section (equation (2-14)) was fitted to the above curve. The constant for radiation, according to the previously introduced equation for the radiation term (2-16), is:

$$C_{rad} = \frac{16\sigma n^2}{3E} \tag{2-29}$$

The above equation can be solved to find the extinction coefficient $E = 40805\ m^{-1}$ when using $n^2 = 1.5$ (with $n_f = 1$ for vacuum and $n_S = 1.5$ for basalt, based on Pollack, Toon and Khare (1973), a porosity of 0.5 as calculated with a bulk density of 1.5 g/cm³ and particle density of 3.1 g/cm³ (Carrier, Olhoeft and Mendell, 1991) according to equation (2-42)). It was assumed from Cremers (1971) that the gas pressure during these measurements was in the range of 10^{-4} Pa, and that the sample size was 25 mm × 13 mm × 13 mm (width × length × height) with a bulk density of 1.5 g/cm³. These parameters were therefore fed into the theoretical model. The constant C_{cond} can be set equal to the solid contact conductivity k_{sc}, but this does not allow the modification of any of the (temperature-dependent) sample properties for subsequent parameter studies. To maintain a full parametrical model, the solid contact conductivity as derived in the previous section was tuned to fit the measurements of Apollo sample 68501. In fact, only the conductivity of the solid k_s had to be modified, since this is dependent on the actual sample properties. As a basis, the general equation by Zoth and Haenel (1988) and Vosteen and Schellschmidt (2003) for the thermal conductivity of rocks was used:

$$k_s = \frac{C_1}{350 + T} + C_2 \tag{2-30}$$

The temperature is to be inserted in °C in equation (2-30). The factors C_1 and C_2 depend on the rock type, whereas typical values are $C_1 = 750$ and $C_2 = 0.75$ for metamorphic rocks, $C_1 = 807$ and $C_2 = 0.64$ for acid rocks, $C_1 = 474$ and $C_2 = 1.18$ for basic rocks, $C_1 = 1293$ and $C_2 = 0.73$ for ultrabasic rocks, and $C_1 = 1073$ and $C_2 = 0.13$ for limestone. These values lead to thermal conductivities in the range of 2 W/(m·K) to 10 W/(m·K) between 100 K and 400 K. The best fit for the Apollo 16 sample 68501 however resulted with $C_1 = 0.50$ and $C_2 = 0.38$. The latter factors yield a thermal conductivity that is about one order of magnitude lower than the ones stated above, which can be explained with the rock composition. According to (Morris *et al.*, 1983), the Apollo sample mainly consists of breccia (38.5 %), agglutinates (38.6 %), and feldspar (12.3 %), with the major elements being 45.18 % SiO_2, 26.65 % Al_2O_3, and 15.35 % CaO. It is assumed that especially the high agglutinate content, being glassy breccia with vesicles that formed by melting and outgassing of solar wind implanted particles, is responsible for the significantly low thermal conductivity of the solid particles. Furthermore, the model used by Cremers and Hsia (1974) assumes a constant particle conductivity, whereas the model adapted here takes into account a certain temperature dependency, for instance an increasing thermal conductivity towards absolute zero temperature due to a change in the lattice of the solid material. Since the measurements of the Apollo sample only extend down to 100 K, it is not clear how the conductivity actually changes towards 0 K.

Having tuned all required parameters to fit the values of the Apollo 16 sample 68501, the effective thermal conductivity was calculated with the result illustrated in Figure 2-6. The green line indicates the result of equation (2-13) for the fit by (Cremers and Hsia, 1974). The red line indicates the combination of temperature and pressure where the Knudsen number is 10 to mark the approximate beginning of the free molecular flow regime. The blue line indicates a Knudsen number of 0.1 to mark the approximate start of the viscous flow

regime. Because the measurements by (Cremers and Hsia, 1974) were performed under terrestrial gravity, the model needs to be modified for lunar gravity. This is possible through equation (2-15), which contains the load p_s that compacts the particles and hence affects the solid contact conductivity k_{sc}. The load is calculated as the quotient of average weight force over cross sectional area of the sample. The weight scales linearly with gravity and so does the load. According to equation (2-15), the solid contact conductivity therefore scales with factor 0.55 when gravity is reduced from 9.81 m/s² for Earth to 1.63 m/s² for Moon. Figure 2-7 shows the resulting thermal conductivity at lunar gravity at selected temperatures. The transition from the free molecular flow regime with negligible gas conductivity to the viscous flow regime with dominating gas conductivity can be clearly seen through the s-shaped curves at constant temperatures. Near atmospheric pressure the effective thermal conductivity reaches values that are about two orders of magnitude higher than at high vacuum. In the low pressure region with dominating radiation, the effective thermal conductivity is higher for higher temperatures. This relation is opposite for the transition region and at high gas pressures where gas conductivity dominates. The latter is due to a decrease of the gas density and hence less molecule to molecule interactions when temperature is increased, assuming an open system where the gas can expand. In a closed system however, an increasing temperature would cause an increase of gas pressure and hence lead to a higher effective thermal conductivity.

To highlight the influence of the different conduction terms on the effective thermal conductivity, the relative contribution of solid contact, radiation, gas, and solid-gas coupling are depicted in Figure 2-8. It can be seen that at pressures lower than 10^{-2} Pa to 10^{0} Pa the heat transfer is governed by the solid contact conductivity and radiation between the particles, whereas the latter is more dominant at higher temperatures. This corresponds well with measurements of Horai (1981), who found that the effect of gas conductivity for simulated Apollo 12 soil becomes significant above approximately 1 Pa.

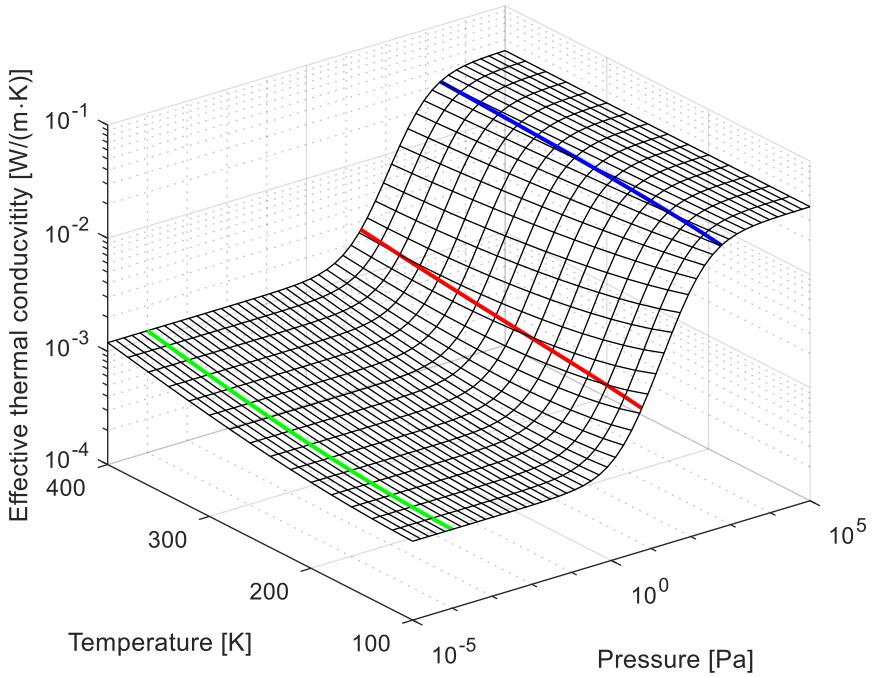

Figure 2-6: Effective thermal conductivity fitted for Apollo sample 68501 (green line). The red line indicates $Kn = 10$ and the blue line indicates $Kn = 0.1$.

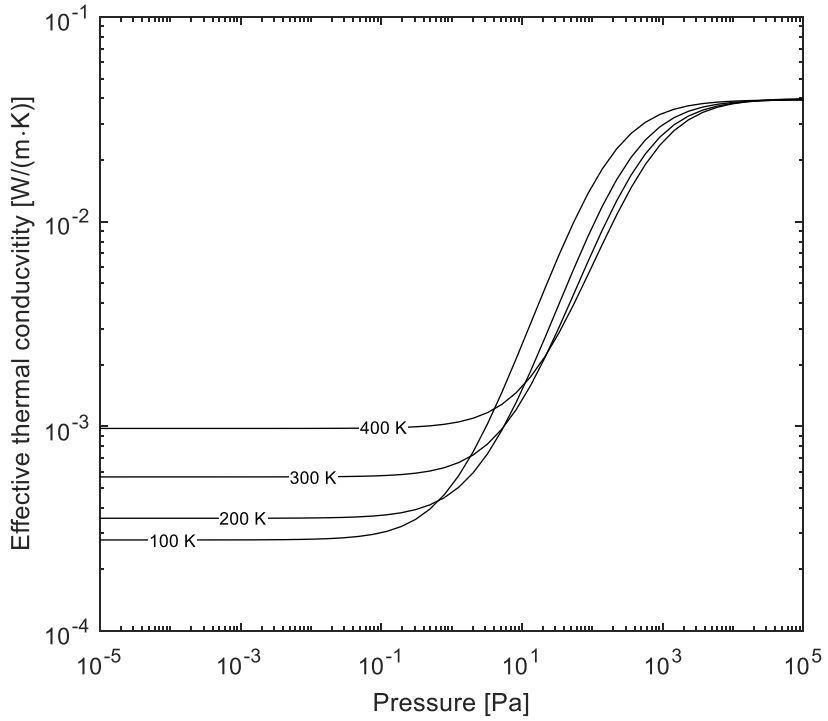

Figure 2-7: Effective thermal conductivity fitted for the Apollo sample 68501 and modified for lunar gravity

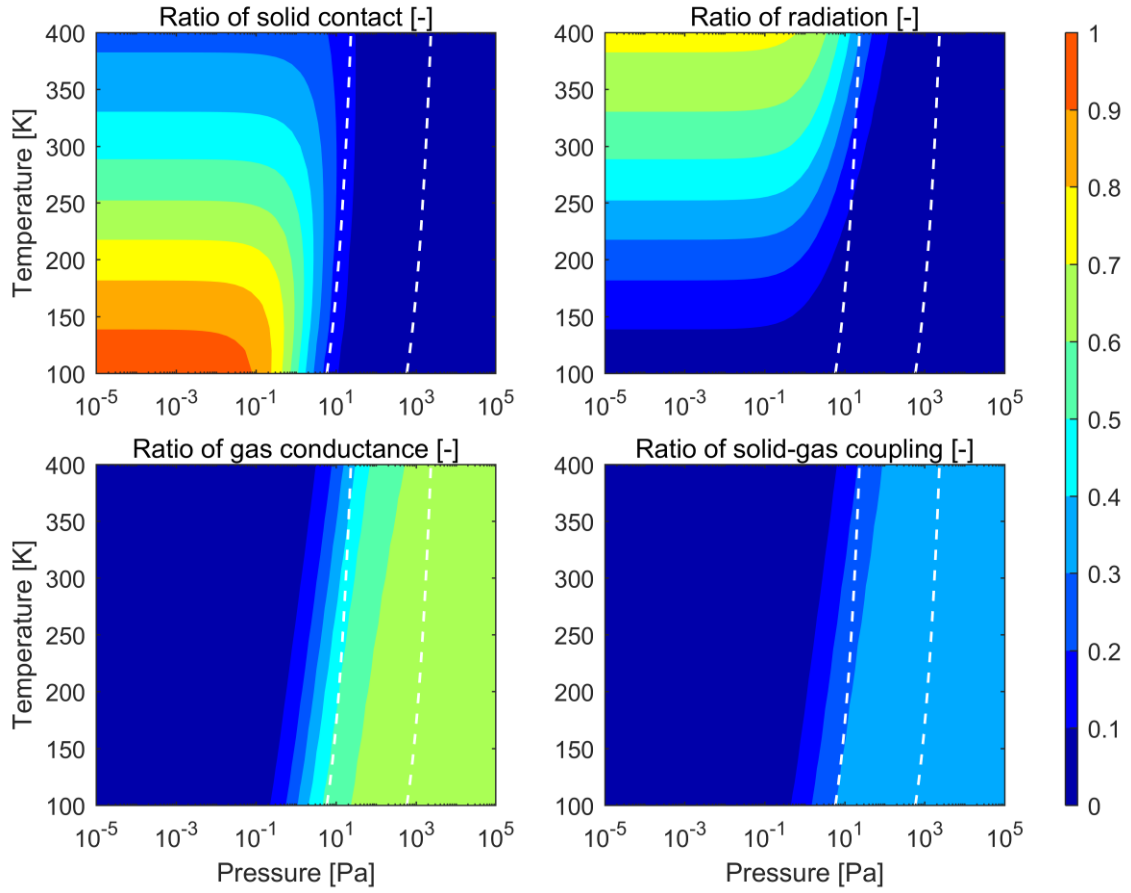

Figure 2-8: Ratio of solid contact, radiation, gas, and solid-gas coupling for the effective thermal conductivity. The left dashed line indicates $Kn = 10$ and the right dashed line indicates $Kn = 0.1$.

2.2.4 Parameter Fit for the Simulant NU-LHT-2M

As no data for the thermal conductivity of the simulant NU-LHT-2M was available, a set of measurements was carried out by the 'Bayerisches Zentrum für Angewandte Energieforschung' (ZAE) for the research project LUISE-2. This included the measurement of the effective thermal conductivity of a loosely packed sample from -150 °C to 100 °C in steps of 50 °C in the guarded hot-plate measurement apparatus LOLA 3 and LOLA 4 (Bayerisches Zentrum für Angewandte Energieforschung, 2015). Both are capable of measuring conductivities from 10^{-4} W/(m·K) to 10^{-1} W/(m·K) at temperatures from -200 °C to 200 °C and gas pressures from 10^{-5} mbar to 10^{3} mbar. Similar as for the Apollo 16 sample, as previously described, the simulation model for the effective thermal conductivity (equation (2-14)) was fitted to the experimental results produced by ZAE. The best fit was found with the parameters $C_{rad} = 1.15 \cdot 10^{-10}\, W/(m \cdot K^4)$ (equation (2-29)) and $C_1 = 0.20$ and $C_2 = 0.28$ for equation (2-30). This resulted in a coefficient of determination of 0.99. The extinction coefficient with $E = 4154\, m^{-1}$ is one order of magnitude lower than for the Apollo sample, but in a similar region as the one determined by Parzinger (2014) for 75 µm particles of the simulant JSC-1A ($E = 5864\, m^{-1}$), 100 µm particles of SiO_2 ($E = 3193\, m^{-1}$), and 75 µm particles of Al_2O_3 ($E = 7482\, m^{-1}$). Figure 2-9 shows the resulting effective thermal conductivity for NU-LHT-2M. A significant difference to the one of the Apollo sample is the stronger temperature dependency, as a result of the lower extinction coefficient. This leads to a thermal conductivity that is about one order of magnitude higher for low pressures. For higher gas pressures the thermal conductivity is approximately equal to the one of the Apollo sample.

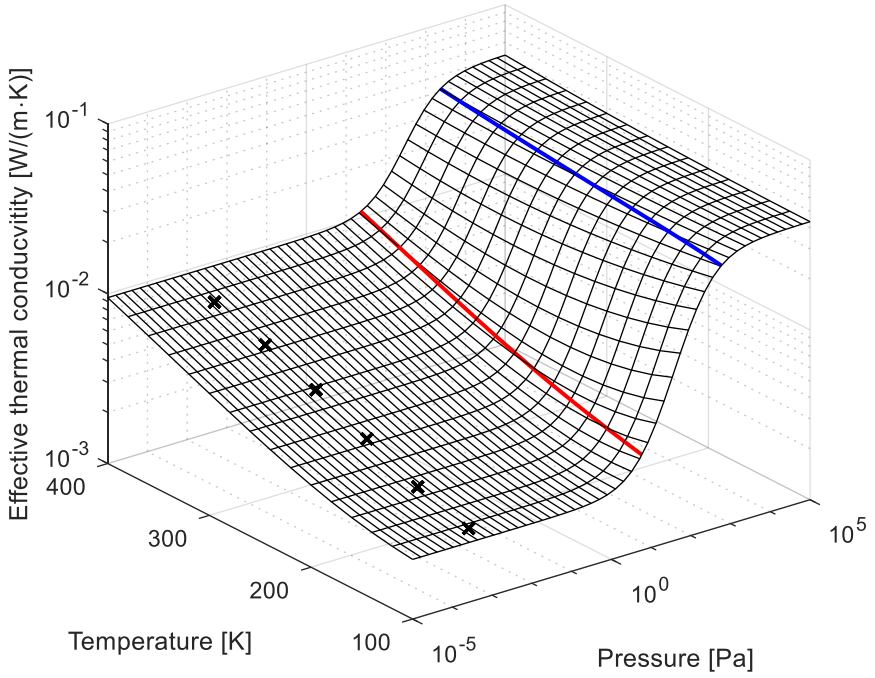

Figure 2-9: Effective thermal conductivity fitted for NU-LHT-2M (black crosses). The red line indicates $Kn = 10$ and the blue line indicates $Kn = 0.1$.

2.2.5 Extension for Icy Regolith

The effective thermal conductivity may vary by orders of magnitude if water ice is contained within the void spaces between the particles. This can mainly be attributed to the increased cross-sectional area for conductive heat transfer. Three types of models exist in literature to address this topic (Siegler *et al.*, 2011), based either on the assumption that 'ice necks' form between particles, based on empirical data of terrestrial soils, or based on the simplification that the ice content contributes proportionally to the overall thermal conductivity, just as it is the case for the specific heat capacity of icy regolith. The latter approach of 'volumetric mixing' is favoured by Siegler et al. (2011), since it matches well with experimental data of icy

martian regolith. The effective thermal conductivity according to this approach can be calculated with the thermal conductivity of dry soil k_{dry}, the thermal conductivity of water ice k_{ice}, and the filling fraction $f = V_{ice}/(\phi V_{dry})$ of the void between the particles:

$$k = k_{dry} + \phi k_{ice} f \tag{2-31}$$

Hudson, Aharonson and Schorghofer (2009) use the 'ice neck' model described by Mellon, Jakosky and Postawko (1997) for the estimation of water ice deposits in martian regolith. The thermal conductivity in this model strongly depends on the square root of the filling fraction, resulting in a particularly high gradient at low filling fractions:

$$k = \left(1 - \sqrt{F}\right) k_{dry} + \sqrt{f} k_{ice} \tag{2-32}$$

These models however can only be rough estimates, since they fail to sufficiently describe the effect of inter-granular ice on radiation (extinction and refractive index), gas conductivity (accommodation coefficient and Knudsen number), and solid-gas interaction (applicability of the unit cell model). Those contributions to the effective thermal conductivity strongly depend on the way ice is formed on the particle surface (ice clusters versus monolayer coverage), the amount of ice (reduced size of inter-granular voids), and the change of ice layers over time. For an ice content of 1 wt%, a porosity of $\phi = 0.5$, a density of the dry sample of $\rho_{dry} = 1.3 g/cm^3$, and a density of water ice of $\rho_{ice} = 0.9\, g/cm^3$, the filling fraction is $F = V_{ice}/(\phi V_{dry}) = (0.01 m_{dry})/(\rho_{ice} \phi V_{dry}) = (0.01 \rho_{dry})/(\rho_{ice} \phi) = 0.029$. Following equation (2-32) with a thermal conductivity of ice $k_{ice} \approx 2\, W/(m \cdot K)$, the thermal conductivity of the icy regolith would increase about two orders of magnitude from approximately 10^{-4} W/(m·K) for dry Apollo sample 68501 type regolith (compare section 2.2.3) to approximately 10^{-2} W/(m·K).

2.2.6 Thermal Diffusivity

For a qualitative measure of how fast heat is spread through the sample, the thermal diffusivity is more applicable than thermal conductivity, because is also takes into account the storage of heat, or thermal inertia of the sample. The thermal diffusivity α is defined by the following equation:

$$\alpha = \frac{k}{\rho c_p} \tag{2-33}$$

Figure 2-10 and Figure B-1 (in the appendix) show the thermal diffusivity of an Apollo 16 type sample with the parameter fit for the thermal conductivity described in chapter 2.2.3 at lunar gravity, the specific heat depicted in Figure 2-3, and a bulk density of 1.5 g/cm³. A similar shape as for the thermal conductivity is seen, with an increase of thermal diffusivity about two orders of magnitude between 10^{-5} Pa and 10^{5} Pa. In the depicted temperature and pressure range most of the values of the thermal diffusivity lie between 10^{-9} m/s² and 10^{-7} m/s². The temperature dependence at constant pressure is different at different pressure levels. At the lower range of the depicted pressures the thermal diffusivity decreases with temperature up to approximately 200 K, from where it increases again. This is partly caused by the solid particle properties, where changes in the lattice lead to an increase in conductivity towards absolute zero temperature. The effect is further amplified by the term $1/c_p$ in the thermal diffusivity, which decreases with temperature. At higher pressures above 10 Pa, there is a continuous decrease of thermal diffusivity with temperature.

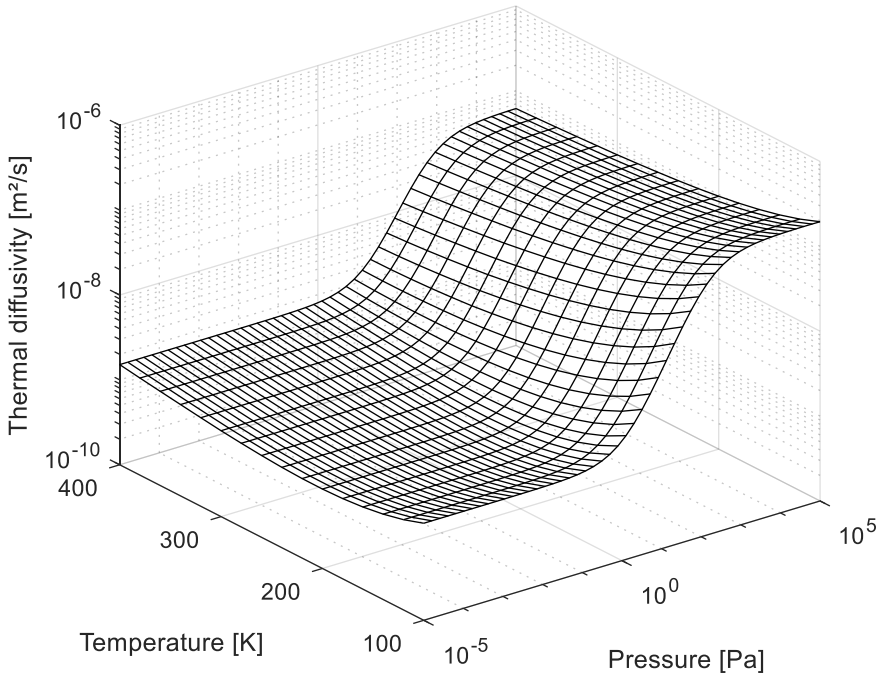

Figure 2-10: Calculated thermal diffusivity of the Apollo sample 68501

2.3 Mass Transfer in Lunar Regolith

The transport of gas in a porous medium can be divided into the following mechanisms: free molecular or Knudsen diffusion, bulk or continuum or ordinary diffusion, and viscous or convective flow (Gunn and King, 1969; Webb, 1996; Reinecke and Sleep, 2002; Ho and Webb, 2006; He, Lv and Dickerson, 2014). The former two are driven by a concentration gradient, whereas the latter is driven by a pressure gradient. Other minor transport mechanisms include surface diffusion, configurational diffusion, and pseudo-Knudsen flow (Reinecke and Sleep, 2002). If there is a thermal gradient, thermal transpiration and thermal diffusion also have to be considered, although in most cases these are negligible (Webb, 1996).

Knudsen and ordinary diffusion that are relevant for low pressure and small voids between particles are considered here, as well as convective flow, which is relevant when a sufficiently high pressure is present in the void spaces. Different models describe the combination of these mechanisms, the most popular being the Advective Diffusion Model (ADM) and the Dusty Gas Model (DGM). The DGM is recommended especially for the application with porous media where Knudsen diffusion occurs, and provides high accuracy for problems that incorporate all of the aforementioned transport mechanisms (Webb, 1996; Ho and Webb, 2006; He, Lv and Dickerson, 2014). It is further mainly suitable for single-component diffusion and becomes more inaccurate for multi-component diffusion. A detailed derivation of the above mentioned transport mechanisms and their combination is described in the following sections.

2.3.1 Knudsen and Ordinary Diffusion

The diffusion of released volatiles through a porous sample depends on the Knudsen number, which is defined as the ratio between the mean free path λ and the diameter of the inter-granular pores, or the void space between the particles respectively, d_v:

$$K_n = \frac{\lambda}{d_v} \tag{2-34}$$

The mean free path is calculated with the gas pressure p, the effective diameter of a gas molecule d_g, the Boltzmann constant k_B, and the gas temperature T:

$$\lambda = \frac{k_B T}{\sqrt{2} p \pi {d_g}^2} \tag{2-35}$$

For $d_v \gg \lambda$, collisions and interactions between gas molecules are dominant, which results in ordinary diffusion. For $d_v \ll \lambda$, collisions between the gas molecules and the particle surfaces are more dominant, resulting in Knudsen diffusion. In the transition region there is a combination of Knudsen diffusion and ordinary diffusion. There is no exact definition of the boundaries for the Knudsen number that determines the flow regime, but a common understanding in literature is that ordinary diffusion is dominant at $Kn \ll 0.1$ and Knudsen diffusion is dominant at $Kn \gg 10$ or $Kn \gg 1$ (Gunn and King, 1969; Kaganer, 1969; Clifford and Hillel, 1986; Clifford and Marshall, 1999; He *et al.*, 2013). For voids in the lower nanometre range, surface diffusion along the particles should also be considered (Schwister and Leven, 2014). With a molecular diameter of 2.75 Å for water and a mean size of $d_v = 70\ \mu m$ for the sample (in a worst-case scenario where the mean size of void spaces equals the mean particle diameter), $Kn > 10$ for pressures below 5 Pa and temperatures above 100 K. In a lunar environment with ultra-high vacuum, the particle transport will therefore be governed by Knudsen diffusion, even at elevated temperatures relevant to sample processing. If the gas pressure however increases due to outgassing of volatile components in the sample, Knudsen numbers in the transition region or even lower might occur. Hence, for the extraction of volatiles the gas diffusivity through the sample needs to be calculated dynamically with changing temperature and pressure.

Gaseous diffusion is described according to Fick's first law for the diffusive flux along a concentration gradient ∇c:

$$J_D = -D \nabla c \tag{2-36}$$

The coefficient for ordinary diffusion $D = D_O$ is defined by the following equation (Jackson, 2010):

$$D_O = \frac{\lambda}{3} \bar{v} \tag{2-37}$$

with the mean free path λ and the mean thermal velocity $\bar{v}$. The latter is defined as:

$$\bar{v} = \sqrt{\frac{8RT}{\pi M}} = \sqrt{\frac{8 k_B T}{\pi m}} \tag{2-38}$$

using either the molar mass of the gas M and the universal gas constant R, or the molecular mass $m = M / N_A$ with the Avogadro constant N_A and the Boltzmann constant k_B.

Knudsen diffusion of water molecules through a sample occurs by particle to particle diffusion, a process that implies repeated breaking and reestablishment of bonds (Hibbitts *et al.*, 2011). The transport of a molecule can either take place through hopping between particles or through movement along a particle surface to another particle. The former requires full desorption of the molecule, and hence approximately twice the thermal energy compared to the movement of a molecule along the particle surface. Knudsen diffusion can be described in the same manner as molecular diffusion, using Fick's first law for the molecular flux as defined in equation (2-36). The diffusion coefficient $D = D_K$ is similar to the molecular diffusivity, where the mean free path is replaced with the mean void size d_v:

$$D_K = \frac{d_v}{3} \bar{v} \tag{2-39}$$

Equations (2-37) and (2-39) are only valid for parallel cylindrical voids with an unobstructed diffusion path for the molecules. For diffusion through voids with a more complex shape, the effective diffusivities $D_{O,eff}$ and $D_{K,eff}$ are found by multiplying the respective terms with an obstruction factor, which is formed by the quotient of porosity ϕ and tortuosity τ (equations (2-40) and (2-41)). This factor hence accounts for deviations of the diffusion path of an individual molecule from a straight line.

$$D_{O,eff} = \frac{\phi}{\tau} D_O \tag{2-40}$$

$$D_{K,eff} = \frac{\phi}{\tau} D_K \tag{2-41}$$

The porosity can be calculated using the bulk density ρ_{bulk} and the specific gravity, or particle density, $\rho_{particle}$:

$$\phi = 1 - \frac{\rho_{bulk}}{\rho_{particle}} \tag{2-42}$$

The recommended value for $\rho_{particle}$ of lunar regolith is 3.1 g/cm³ (Carrier, Olhoeft and Mendell, 1991). Typical values of ϕ for lunar regolith range from 0.44 ± 0.02 to 0.52 ± 0.02, including both inter- and intra-granular porosity, as calculated from the depth-dependent bulk density measured in-situ during the Apollo missions (Carrier, Olhoeft and Mendell, 1991). Values for the tortuosity τ of related materials are provided in Table 2-3.

Table 2-3: Values and models for the tortuosity of porous media

Material	Tortuosity (porosity)	Reference
n/a ('typical pore')	3 to 7	(Schwister and Leven, 2014)
Chemical catalysts	1 to 10	(Reschetilowski, 2015)
Pelletised catalysts (various types)	1.7 ($\phi = 0.7$) to 7.5 ($\phi = 0.3$)	(Satterfield, 1970)
Martian soil	1 ($\phi = 0.8$), 5 ($\phi = 0.5$), 10 ($\phi < 0.5$)	(Smoluchowski, 1968)
JSC Mars-1	2.6 ± 0.4	(Hudson *et al.*, 2007)
40-70 µm glass beads	1.5 ± 0.6 to 2.6 ± 0.2	(Hudson *et al.*, 2007)
1-3 µm silicate mineral dust	5.3 ± 1.9 (loose), 12.1 ± 5.0 (packed)	(Hudson *et al.*, 2007)
1-1.25 mm glass spheres	1.4 ($\phi = 0.43$)	(Hoogschagen, 1955)
Spheres (Millington model)	$\phi^{-1/3}$	(Millington, 1959)
Spheres (Bruggeman model)	$\phi^{-1/2}$	(Tjaden *et al.*, 2016)
Cylinders (Bruggeman model)	ϕ^{-1}	(Tjaden *et al.*, 2016)

For a sequential combination of Knudsen diffusion and ordinary diffusion in the transition region, the effective diffusion coefficient D_{eff} is found according to the 'resistance in series' approach (Satterfield, 1970; Clifford and Hillel, 1986; He, Lv and Dickerson, 2014):

$$\frac{1}{D_{eff}} = \frac{1}{D_{K,eff}} + \frac{1}{D_{O,eff}} \tag{2-43}$$

A comparison of equations (2-37) and (2-39) shows that $D_{O,eff} = D_{K,eff}$ for $\lambda = d_p$, or $Kn = 1$ respectively. Figure 2-11 illustrates the relations between both diffusivities and the shape of the combined diffusivity according to equation (2-43). A porosity of 0.5 and a tortuosity of 5 were chosen in this case. The effective combined diffusivity D_{eff} results a smooth transition from Knudsen diffusion to ordinary diffusivity and approximates both very good towards lower and higher Knudsen numbers respectively. For $Kn > 10$ (left of the red line) and $Kn < 0.1$ (right of the blue line), the relative error is less than 10 %. For $Kn > 100$ and $Kn < 0.01$, the relative error is less than 1 %. It is concluded that equation (2-43) may be used over the entire range of Knudsen numbers with an acceptable error towards lower and higher Knudsen numbers.

The absolute values for the gas diffusivity lie between 10^{-7} m²/s and 10^{-3} m²/s in the investigated range of temperature and pressure. As illustrated by Figure B-1 in the appendix, this is up to six orders of magnitude higher than the thermal diffusivity expected for an Apollo 16 type sample (compare Figure 2-10). Only at gas pressures near 10^5 Pa and temperatures near 100 K both diffusivities are of similar order.

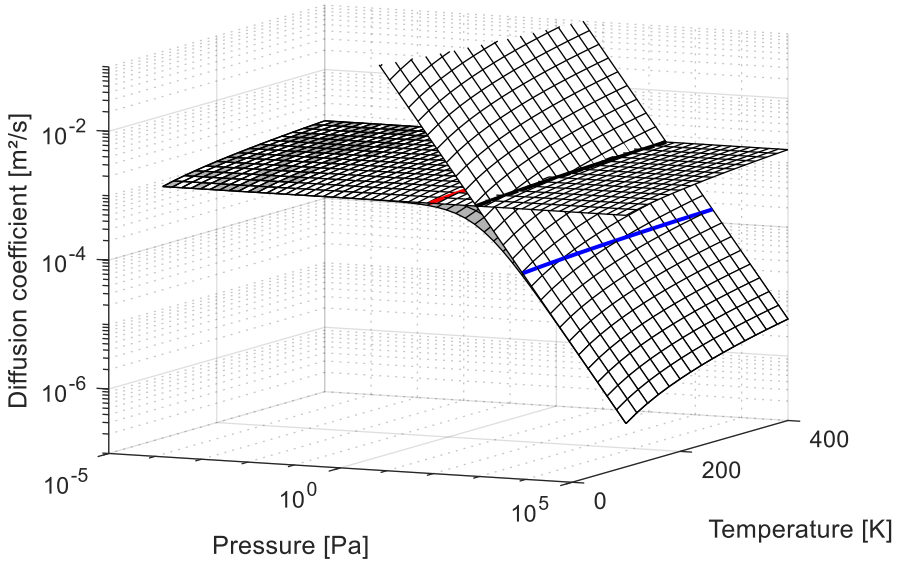

Figure 2-11: Gas diffusivity versus temperature and pressure. The coloured lines indicate $Kn = 10$ (red), $Kn = 1$ (black), $Kn = 0.1$ (blue). The grey curve illustrates the effective diffusivity according to equation (2-43).

2.3.2 Convective Flux

The convective flux J_C is directly related to the pressure gradient via the Darcy velocity u, as expressed by the following equation (Webb, 1996; Reinecke and Sleep, 2002; Ho and Webb, 2006):

$$J_C = -c \cdot u = -c \frac{k_{g,a}}{\mu} \nabla p \tag{2-44}$$

where c is the concentration, which for an ideal gas can also be expressed as $c = p/(RT)$, $k_{g,a}$ is the apparent gas permeability, μ is the dynamic viscosity of the gas, and p the gas pressure in the voids. The apparent gas permeability includes the effects of gas saturation and slip flux in a porous medium, and hence is larger than the corresponding permeability determined from liquid flow. The relation between apparent and effective gas permeability in a partially saturated medium can be determined with the help of the Klinkenberg parameter b (Reinecke and Sleep, 2002):

$$k_{g,a} = k_{g,e} \left(1 + \frac{b}{\bar{p}}\right) \tag{2-45}$$

The gas permeability of lunar soil was determined from firing of the Surveyor 5 Vernier engine to be in the range of $1 \cdot 10^{-12}$ m² to $7 \cdot 10^{-12}$ m², which is comparable to terrestrial silts with particle sizes between 2 µm and 60 µm (Choate *et al.*, 1969). Measurements with lunar soil simulants at varying bulk densities between 1.5 g/cm³ and 2.0 g/cm³ revealed permeabilities from approximately $3 \cdot 10^{-13}$ m² to $2 \cdot 10^{-12}$ m² for JSC-1A and $9 \cdot 10^{-14}$ m² to $1 \cdot 10^{-12}$ m² for NU-LHT (Toutanji *et al.*, 2012). In the latter experiments, a linear relationship between bulk density and permeability was observed, as well as an exponential decrease of permeability up to gas pressures around 40 kPa and a relatively constant dependency thereafter. LaMarche, Curtis and Metzger (2011) performed experiments on the permeability of JSC-1A and found values ranging from $1 \cdot 10^{-12}$ m² to $6 \cdot 10^{-12}$ m², which compares well with the estimates from the Surveyor 5 experiment. It was also found that for JSC-1A the permeability can be reliably determined via the Carman-Kozeny equation, using only the geometrical properties of voids or capillaries and particles:

$$k_{g,e} = \frac{1}{\tau^2 F_0} \frac{\phi^3}{{S_0}^2 (1-\phi)^2} \tag{2-46}$$

For JSC-1A the first term that accounts for tortuosity and the shape factor F_0 is $1/(\tau^2 F_0) = 0.18$. The specific surface of JSC-1A is $S_0 = 1026 \cdot 10^{-2}\ \mathrm{m}^{-1}$ and porosity can be calculated using equation (2-42).

The gas viscosity μ depends on the flow regime where two cases need to be distinguished: flow in the viscous regime for $Kn < 1$ and flow in the free-molecular regime for $Kn > 1$ (Kennard, 1938; O'Hanlon, 2003). As explained before, the Knudsen numbers where significant pressure gradients could cause a convective flux in a lunar regolith sample are more likely below 1. In this case the gas viscosity is independent of pressure and defined as:

$$\mu_{Kn<1} = \frac{1}{3} \frac{(4 m k_B T)^{\frac{1}{2}}}{\pi^{\frac{3}{2}} {d_g}^2} \tag{2-47}$$

The coefficient $1/3$ in equation (2-47) may also be replaced with 0.499 to account for velocity spread (mean free path is not equal for all velocities) and non-constant collision rate, using a rigorous molecular model with hard elastic spheres (Kennard, 1938).

2.3.3 Tortuosity of NU-LHT-2M

As described in chapter 2.3.1, there is a variety of models to calculate tortuosity for different particle types and shapes. From Table 2-3 it is estimated that tortuosity values relevant for NU-LHT-2M would lie in the range of 1 to 10. To further narrow this range down, a series of experiments was conducted to determine the tortuosity of the actual simulant and according particle size distribution that was used in the volatiles extraction experiments presented in this thesis. After a thorough assessment of possible methods to experimentally determine the tortuosity of porous media, the approach suggested by Delgado (2008) and Coutelieris and Delgado (2012) was realised. Here the sample is placed into a container and filled with distilled water up to its surface to fill all void spaces (inter- and intra-porous space). On top of the sample, a saline solution is filled and constantly stirred to achieve a homogeneous salinity above the sample. The electrical conductivity as well as the temperature of this solution is constantly measured and recorded. Due to the gradient of salt concentration above and within the sample, the salt slowly diffuses into the sample until equilibrium is reached. The ratio of the amount of salt in the sample n_t over time and its equilibrium value n_∞ can be approximated with the following series expansion derived by Wilson (1948) and Williams (1977):

$$\frac{n_t}{n_\infty} = 1 - \sum_{n=0}^{\infty} \frac{2\psi(1+\alpha_V)}{1+\psi+\psi^2 q_n^2} \cdot \exp\left(-\frac{D_{eff} \cdot q_n^2 \cdot t}{l^2}\right) \tag{2-48}$$

This approximation is valid for the one-dimensional diffusion from a stirred solution with limited volume and height $2a$ into a 'lamina' with thickness $2l$ that is suspended in the solution. The model does not take into account radial diffusion, and was originally derived for a situation where diffusion into the lamina is from both sides. Nevertheless it is thought to be appropriate for the present problem, where the concentration gradient is mainly along the vertical direction of the sample, and where the solution and sample and represent only one half of the originally described mathematical model.

In the above equation, ψ is the volume ratio of liquid solution and sample:

$$\psi = \frac{a}{l} \tag{2-49}$$

The term q_n represents the non-zero positive roots of the following equation:

$$tan(q_n) = -\psi q_n \tag{2-50}$$

The amount of salt in the sample can be derived from the concentration in the solution, c_t, which is measured over time:

$$n_t = V_{solution}(c_0 - c_t) \tag{2-51}$$

The equilibrium amount of salt in the sample is:

$$n_\infty = V_{solution}(c_0 - c_\infty) \tag{2-52}$$

The initial concentration c_0 and the equilibrium concentration c_∞ is calculated from the amount of salt that is added to the solution and the respective volumes of solution and sample. Applying the above equations, the term n_t/n_∞ can be calculated and equation (2-48) solved numerically for the term $D_{eff}t/l^2$ for each data point acquired for the concentration c_t over time. The discrete values of $D_{eff}t/l^2$ can then be arranged in a plot over time to determine the best linear fit through the origin to derive the term D_{eff}/l^2, and subsequently the effective diffusion coefficient D_{eff}. Using the relation between the molecular and effective diffusion coefficient provided in the following equation (compare equations (2-40) and (2-41)), the obstruction factor ϕ/τ and subsequently the tortuosity τ can be determined.

$$D_{eff} = \frac{\phi}{\tau} D \tag{2-53}$$

It should be noted that in their presentation of this derivation Delgado (2008) and Coutelieris and Delgado (2012) do not take into account the porosity ϕ, but call the obstruction factor itself 'tortuosity factor'.

In the frame of a semester thesis (Ciadamidaro, 2017), initiated and supervised by the author of the present thesis, an experimental setup was developed to apply the previously described method for the determination of the tortuosity of NU-LHT-2M. The setup depicted in Figure 2-12 features a glass beaker that holds the sample and the saline solution, a self-designed stirring rod, and a measurement equipment including a conductivity probe with measurement circuit (Atlas Scientific Conductivity K 1.0 Kit, range 5 µS/cm to 200,000 µS/cm), a DS18B20 temperature sensor coated in an epoxy resin (range -55 °C to +125 °C with accuracy ±0.5 °C from -10 °C to +85 °C), and an Arduino UNO R3 microcontroller connected to a computer for data logging. For the experiments NU-LHT-2M was sieved to produce one batch with particle sizes between 70 µm and 80 µm and one batch with particle sizes between 110 µm and 120 µm. The saline solution for the experiments was made from potassium chloride, since the two calibration solutions delivered with the conductivity probe were also made from potassium chloride. The molecular diffusion coefficient in the solution at 25 °C was taken from Lobo, Ribeiro and Verissimo (1998), where $1.891 \cdot 10^{-9}$ m²/s is suggested for a concentration of 1 mol/dm³.

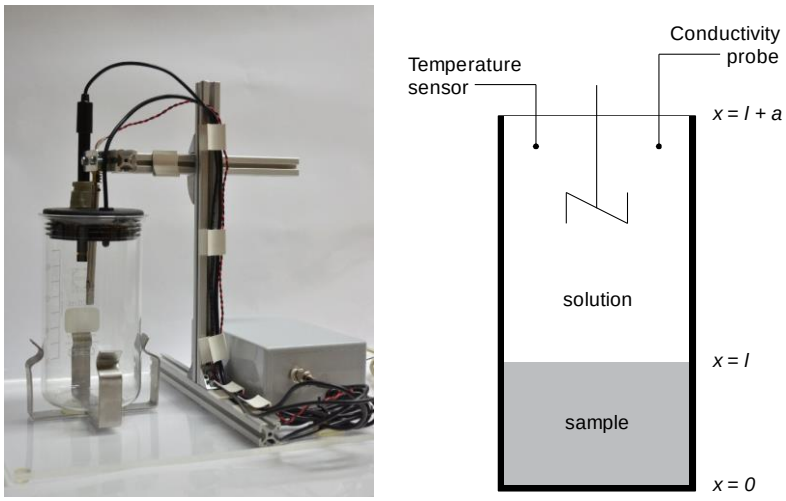

Figure 2-12: Picture and schematic depiction of the experimental setup for the determination of tortuosity

Three selected test runs are presented in the following, of which two used the smaller fraction and one the larger fraction of NU-LHT-2M. The sample mass in both cases was 560 g and the sample height 5.6 cm, which leads to a bulk density of 1.57 g/cm³ and to a porosity of 0.46, applying equation (2-42) with a particle

density of 2.9 g/cm³ (U.S. Geological Survey, 2008). There was no difference between the values for the smaller and the larger fraction because such would lie within the measurement error. The void volume of the sample was determined to be 137 ml and the volume of the solution was 210 ml. The latter was mixed with 16 g potassium chloride, which leads to a value of 76190 ppm total dissolved solids (TDS). The equilibrium value after diffusion into the sample should be 46110 ppm. Because these values strongly depend on the measurement accuracy for volume and mass, the actual maximum TDS values measured by the conductivity probe in each test run were taken as initial values and the equilibrium calculated accordingly. Table 2-4 lists the parameters for all three test presented here, the resulting curves for n_t/n_∞ and $D_{eff}t/L^2$ are shown in Figure 2-13 to Figure 2-15.

Table 2-4: Test parameter and resulting tortuosity for three test runs with NU-LHT-2M

	Test run 1	Test run 2	Test run 3
Particle size	70-80 µm	70-80 µm	110-120 µm
Initial TDS	77262 ppm	74698 ppm	71640 ppm
Equilibrium TDS	46758 ppm	45206 ppm	43356 ppm
D_{eff}/l^2 (fitted)	$1.411 \cdot 10^{-7}$ s^{-1}	$2.665 \cdot 10^{-7}$ s^{-1}	$4.925 \cdot 10^{-7}$ s^{-1}
Obstruction factor D_{eff}/D	0.06	0.11	0.20
Tortuosity	7.84	4.15	2.25

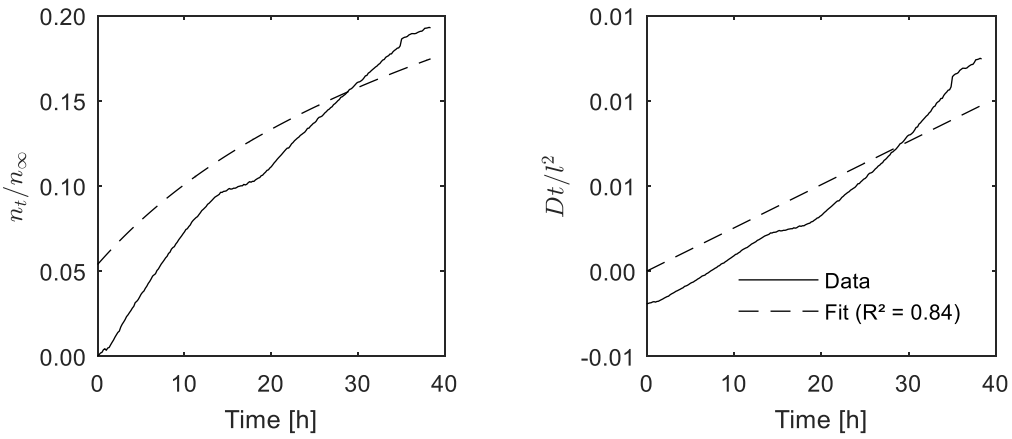

Figure 2-13: Experimental data and curve fits for test run 1 (70 – 80 µm)

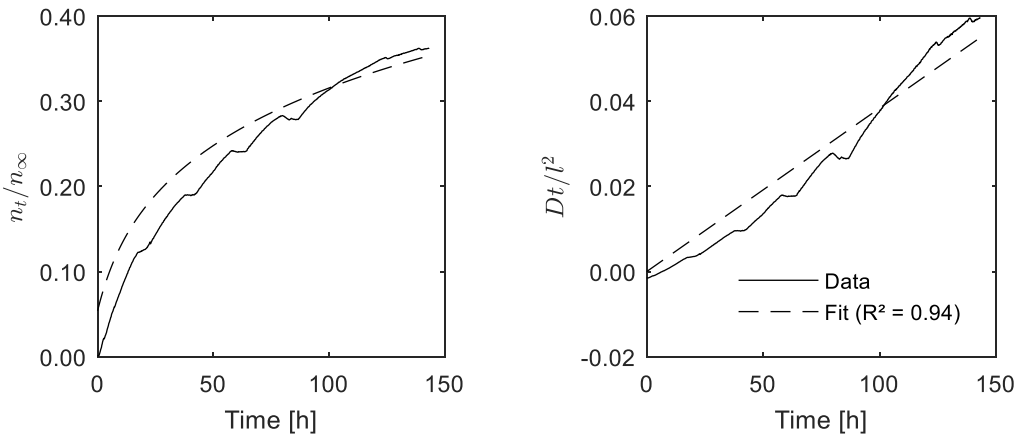

Figure 2-14: Experimental data and curve fits for test run 2 (70 – 80 µm)

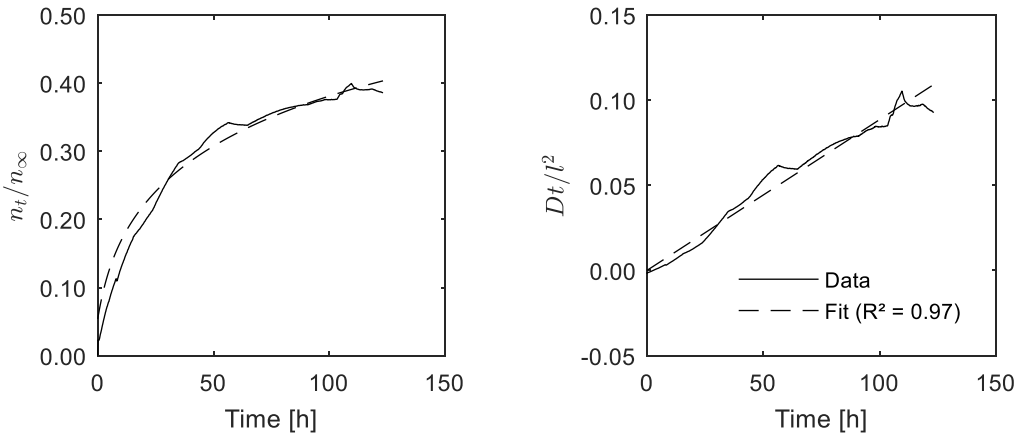

Figure 2-15: Experimental data and curve fits for test run 3 (110 – 120 µm)

Test run 3 with the larger particle fraction provides the most reasonable results with a clear exponential decay of the concentration in the solution and hence an exponential growth of the ratio n_t/n_∞. Equation (2-48) can be applied to this curve very well, which is expressed in a good coefficient of determination of 0.97. This is also due to the fact that this experiment was run for more than 120 h, which provides a good basis for the mathematical approximation. Test run 2 yields less conclusive results, because the duration of the experiment was much less and hence the decay of concentration was still in the rapid phase at the beginning, far from the asymptotic convergence to the equilibrium value. Test run 1 has a duration of approximately 145 h, but due to the smaller particle size the final recorded concentration is still far away from the equilibrium value. The calculated obstruction factor D_{eff}/D after curve fitting is most meaningful for test run 3. The obstruction factor for this sample was calculated to be 0.20, which means that the effective diffusivity through the sample is only one fifth of the molecular diffusivity. With a calculated porosity of 0.46 the tortuosity was determined to be 2.25. The finer grained samples expectedly have a higher tortuosity of 4.15 and 7.84, but given the insufficient experiment duration, the notably high value of test run 2 needs to be treated with caution. Nevertheless, values between 2 and 4 as resulted from test run 1 and 3 seem reasonable in the light of the researched values for comparable porous media listed in Table 2-3. In conclusion, this empirical method proofed to be applicable for determining the tortuosity of the lunar regolith simulant NU-LHT-2M. The time needed for the saline solution to equilibrate with the sample lies in the range of several days if not weeks and it is recommended to collect more data over a longer duration to enable a reasonable mathematical approximation of the problem.

2.4 Reduction of Lunar Regolith with Hydrogen

Hydrogen reduction or lunar regolith was selected by ESA as one of the candidate processes for ISRU demonstration with the ProSPA instrument. Among over 20 processes suggested for the in-situ production of oxygen from lunar regolith (Taylor and Carrier, 1993; Schwandt *et al.*, 2012), this process was evaluated several times as one of the most simple and promising, because it requires relatively low temperatures and yields water in a single reaction step with only a few by-products. The basic principle is the chemical reduction of ferrous iron (FeO) in the regolith, which for instance is contained in the mineral ilmenite ($FeTiO_3$). Other sources can be titanium dioxide (TiO_2) and silicon dioxide (SiO_2). The oxygen is released from the mineral phase and combines with hydrogen to form water, as described by equation (2-54). In a subsequent electrolysis, the water can be split into oxygen and hydrogen and hydrogen can potentially be recycled and fed back to the initial reaction (equation (2-55).

$$\mathrm{FeTiO_3 + H_2 = Fe + TiO_2 + H_2O} \tag{2-54}$$

$$\mathrm{2H_2O = 2H_2 + O_2} \tag{2-55}$$

Hydrogen reduction of lunar regolith requires process temperatures between 700 °C and 1000 °C, just below the sintering temperature of lunar regolith around 1100 °C. At 1000 °C the reaction will stop when the mole fraction of water exceeds 10 %. Therefore, it is very important to keep the water mole fraction low in the reacting gas (Taylor *et al.*, 1993). Oxygen yield from lunar soils strongly depends on the initial iron content of the sample, but generally lies in the range of 1 wt% to 5 wt% for lunar regolith (Allen, 1997). Allen, Morris and McKay (1996) found that the susceptibility of Fe^{2+} in mineral phases to reduction can be arranged as follows: ilmenite > glass > olivine > pyroxene. Gibson and Knudsen (1985) found that the reduction is mildly endothermic (ΔH = 9.7 kcal/(g·mol) at 900 °C for ilmenite), reversible, and strongly equilibrium-limited (at 900 °C the per-pass conversion of hydrogen cannot exceed 7.4 %). As a result, hydrogen circulation rates are large compared to oxygen production rates. Briggs and Sacco (1988) and Vijay, Venugopalan and Sathiyamoorthy (1996) found that preoxidation of the ilmenite by either oxygen, carbon dioxide, or water increases the rate of reduction and reduces the reduction temperature, so that the risk of sintering at higher temperatures can be mitigated. The presence of carbon monoxide can also lead to a reduction of the ilmenite to produce carbon dioxide:

$$\mathrm{FeTiO_3 + CO = Fe + TiO_2 + CO_2} \tag{2-56}$$

However, the reduction rate with hydrogen is *'much faster and less sensitive to temperature'* (Zhao and Shadman, 1993, p. 176) than with carbon monoxide. On the other hand, the presence of carbon monoxide can lead to decreased reduction rates, due to the water gas shift reaction, which forms hydrogen and carbon dioxide from water and carbon monoxide (Zhao and Shadman, 1993):

$$\mathrm{CO + H_2O = CO_2 + H_2} \tag{2-57}$$

According to Bardi, Gozzi and Stranges (1987), Zhao and Shadman (1993), and Dang, Zhang and Chou (2015), a higher temperature, a higher hydrogen partial pressure, as well as a higher hydrogen flow rate lead to an increased reduction rate.

In terms of reactor design, one of the most complete concepts was developed by the company Carbotek, Inc., who patented a technique to reduce ilmenite with hydrogen to produce Lunar Liquid Oxygen (LLOX) (Taylor and Carrier, 1993). The reactor consists of three stacked fluidised beds. Hydrogen passes upwards, whereas the feedstock passes downwards. Hydrogen is recycled and water is electrolysed into oxygen and hydrogen.

Several proof of concept experimental studies on hydrogen reduction of lunar regolith have been performed during the last century. Brecher et al. (1975) conducted reduction experiments on Apollo 17 samples at a reaction temperature of 800 °C and demonstrated a partial reduction over a period of 3 h in a continuous hydrogen flow. Mössbauer spectroscopy was used to determine that mainly the ilmenite was susceptible to reduction. Experiments by Bardi, Gozzi and Stranges (1987) showed that a stoichiometric reduction of ilmenite was reached between approximately 60 min and 200 min, depending on the hydrogen partial pressure and flow rate. It was concluded that it is sufficient to heat the sample up to just below 1000 °C to obtain high yields, for instance at 900 °C a 90 % separation between the iron and titanium dioxide was observed after 60 min. The same study investigated reduced ilmenite grains with an optical microscope and found segregated iron phases in the form of spheroidal nodules and TiO_2 phases in the form of vein-like arrangements. Similar morphologies were found by Gibson et al. (1994) and Dang, Zhang and Chou (2015). Briggs and Sacco (1991) demonstrated the complete reduction of ilmenite on a microbalance furnace after about 20 min at 1000 °C, 25 min at 900 °C, and 73 min at 800 °C. At 700 °C only a 20 % conversion of the ilmenite could be achieved after about 77 min. Studies by Zhao and Shadman (1993) investigated the reduction of ilmenite by carbon monoxide and hydrogen. The chemical reduction was characterised as a shrinking core type process with the following steps: diffusion of the reactant through a product TiO_2 layer, reaction with the ilmenite core, diffusion of iron out of the TiO_2 pores, and formation of metallic iron outside the ilmenite grains. The reduction process exhibits three stages, resulting in a sinusoidal shape of the conversion-time curves (or mass loss over time curves): induction due to slow transport of the iron out of the pores, followed by acceleration and deceleration until the reduction is complete (Briggs and Sacco, 1988, 1991; Zhao and Shadman, 1993). Preoxidation experiments by Vijay, Venugopalan and Sathiyamoorthy

(1996) in a fluidised bed reactor demonstrated that a sample that was oxidised at temperatures up to 800 °C can subsequently reach an optimum reduction with hydrogen at around 750 °C.

The first actual experimental demonstration of oxygen production from lunar regolith was claimed by Gibson et al. (1994). They reduced the crushed Apollo sample 70035 in quantities up to 2 g at temperatures between 900 °C and 1050 °C and reported on an oxygen yield between 2.93 wt% and 4.61 wt%. Taylor et al. (1993) developed a laboratory-scale demonstrator to produce LLOX from ilmenite via hydrogen reduction. 20 mg of pure ilmenite was placed into a silica-glass tube and heated to 1000 °C in a hydrogen flow. The resulting water was either condensed or scrubbed with Drierite. Within 1.5 h, more than 95 % of the ilmenite was reduced, resulting in an oxygen yield of 10 wt%. Hydrogen reduction was also addressed by NASA's ROxygen project (Lee *et al.*, 2013). After initially constructing a small-scale reactor for ilmenite hydrogen reduction with a sample size of 10 g to 100 g, the reactor was upscaled and the design was adapted to obtain a closed-loop system with the aim to be able to produce 1000 kg of oxygen in one year. To avoid sintering of the regolith, a mechanical mixing device was added. Water was condensed and stored in a water reservoir and hydrogen was processed and fed back to the reactor. For the small-scale demonstrator, the achieved oxygen yield at a process temperature of 1050 °C was between 1 wt% and 2 wt%. For the large-scale demonstrator 0.2 wt% to 0.5 wt% oxygen was released at temperatures between 800 °C and 900 °C. The observed reaction took more than 5 h to be considered complete. In a similar system, Yoshida et al. (2000) studied the hydrogen reduction of the simulant JSC-1A. 40 g were reacted at 900 °C to 1050 °C, while the highest water production rate as well as the highest cumulative amount of produced water was achieved at 1000 °C. It was shown that Fe_2O_3 was reduced almost completely and FeO only partially.

In the context of this thesis, the reduction of the simulant NU-LHT-2M is of particular interest since it is the analogue material of choice to resemble lunar highland regolith. Table 2-5 lists the major oxides found in NU-LHT-2M in comparison to an average of different Apollo 16 highland samples. Compared to mare regolith with FeO contents around 10 % to 22 % (Haskin and Warren, 1991), the highland type soil contains considerably less FeO. This is also true for TiO_2, of which mare regolith in contrast contains around 2 % to 12 %. As stated before, the oxygen yield by hydrogen reduction of lunar regolith strongly depends on the iron content. This relation is directly proportional according to experiments by Allen (1997), where the highland sample 62241 only reached an oxygen yield just over 1 wt%, while the mare soils 12032 and 71131 yielded 1.5 wt% and 3.5 wt% oxygen respectively. It is therefore to be expected that NU-LHT-2M would yield similar amounts of oxygen, well below 2 wt%.

Table 2-5: Major oxides in Apollo 16 regolith and the simulant NU-LHT-2M

Oxide	Apollo 16 soils and breccia (Haskin and Warren, 1991)		NU-LHT-2M certificate of information (not published, delivered with the simulant)		NU-LHT-2M (U.S. Geological Survey, 2008)	
	Average [wt%]	Standard deviation [wt%]	Average [wt%]	Standard deviation [wt%]	Average [wt%]	Standard deviation [wt%]
SiO_2	44.89	0.51	47.62	0.21	46.70	0.11
Al_2O_3	27.23	1.84	27.4	0.48	24.40	0.07
CaO	14.56	3.64	13.6	0.41	13.60	0.05
MgO	6.00	1.76	8.50	0.48	7.90	0.04
FeO	4.98	1.08	2.15	0.09	-	-
Fe_2O_3	-	-	-	-	4.16	0.03
TiO_2	0.53	0.14	0.33	0.02	0.41	0.02
Na_2O	0.47	0.08	1.43	0.03	1.26	0.02

3 Combined Model for Heat and Mass Transfer

This chapter is an adapted and updated excerpt from Reiss (2018)*, written by the author of the present thesis.*

To evaluate the effect of dynamically changing parameters during the heating of a lunar regolith sample and the respective volatiles extraction process, a simulation model was created with the software COMSOL Multiphysics. It takes into account all of the relevant reactions and transport kinetics discussed in chapter 2, except resorption. It therefore allows monitoring the actual variation of gas concentration, thus gas pressure, and temperature within the sample over time and space. This chapter describes the mathematical form and boundary conditions for the simulation model and the results of a parameter study to highlight the effect of different sample conditions and boundary conditions.

3.1 COMSOL Simulation Model

Heat and mass transfer were modelled in COMSOL using the coefficient form of the diffusion-convection equation with COMSOL's partial differential equation (PDE) module. The respective formulation for the heat transfer can be found in equation (2-11). The diffusive and convective terms for the transport of desorbed species, as derived in the previous chapters 2.3.1 and 2.3.2, can be combined in an additive manner to find the total gas flux for a single-component gas (Mason, Malinauskas and Evans, 1967; Webb, 1996; Krishna and Wesselingh, 1997; Kast and Hohenthanner, 2000; Pant, Mitra and Secanell, 2012) with the relations for J_D and J_C from equations (2-36) and (2-44):

$$J_T = J_D + J_C = -D\nabla c - cu \tag{3-1}$$

In the case of icy regolith, the diffusivity and permeability tend to decrease mainly due to the effect of the inter-particular ice deposits on porosity, tortuosity, and void size (Hudson, Aharonson and Schorghofer, 2009). As the voids are effectively reduced, the regime for molecular transport shifts towards Knudsen diffusion. The exact implications for the transport of desorbed molecules through icy regolith however are difficult to quantify, since the ice layer on particles can take different shapes from clusters to monolayers and because the amount of ice is changing over time. The influence of ice deposits it therefore neglected in the simulation model.

The change of concentration (for $c = \theta c_{sat}$ with the saturated concentration c_{sat}) due to a combination of sorption and gas transport is described according to the previous considerations with the following equation in the conservative form:

$$\frac{\partial c}{\partial t} + \nabla(-D\nabla c - uc) = -k_d c + k_a S(c_{sat} - c) \tag{3-2}$$

The second term on the left-hand side of equation (3-2) describes the diffusion and the third term is convection. The right-hand side is the source term that accounts for both adsorption and desorption. To distinguish between desorbed and adsorbed species in the model, two gas species with the concentrations c_d and c_a were defined. The desorption process was implemented as a reaction via the source term, where the adsorbed species decreases according to equation (2-1) and the desorbed species increases with the complementary negative rate (surface coverage is replaced with concentration in the aforementioned equation). While the diffusive and convective transport is applied to the desorbed species, the adsorbed species remains immobile. The specific transport equations for both species and the above transport kinetics hence are (compare with equation (3-2)):

$$\frac{\partial c_d}{\partial t} + \nabla(-D\nabla c_d - uc_d) = kc_a \quad (3\text{-}3)$$

$$\frac{\partial c_a}{\partial t} = -kc_a \quad (3\text{-}4)$$

The temperature- and pressure dependent values for the thermal conductivity and the gas diffusivity were computed externally with MATLAB in each time step, since the computation methods are too complex to be implemented directly in COMSOL.

As a role model, the baseline sample size of the ProSPA instrument was chosen, being a cylindrical volume with diameter 2.8 mm and height 4.5 mm (Figure 3-1, compare chapter 1.2.4). The sample is thermally insulated at all boundaries and heated at the outer circumference and the bottom surface. The upper boundary is thermally insulated and open for gas transport to the simulated lunar atmosphere. The latter has a concentration of $2 \cdot 10^{-5}$ molecules/cm^3, or $3.3 \cdot 10^{-13}$ mol/m^3 in accordance with the estimates for an undisturbed lunar atmosphere at night (Vaniman *et al.*, 1991). A sample density of 1.3 g/cm³ was selected, which is the experimentally determined density of loosely poured lunar regolith simulant NU-LHT-2M in a respective volume at terrestrial gravity. The model uses lunar gravity as an input, but it is assumed that the low bulk density would not change significantly for such a small sample volume. Additionally, a tortuosity of 5 and a mean void size of 70 µm were chosen (see chapter 2.3.3 for the experimental determination of the tortuosity). The activation energy was set to 0.45 eV to represent loosely bound water molecules on lunar regolith. This configuration represents a worst case scenario with slow heat transfer and quick diffusion due to low bulk density and fast desorption due to a low desorption energy. In such a scenario the highest gas pressure within the sample is expected. The thermal properties adapted to the Apollo 16 sample 68501, as described in chapter 2.2.3, were applied to the sample. The rate of desorption and the diffusion coefficient were calculated as temperature-dependent variables across the sample volume. A temperature ramp was applied to the outer circumference of the sample to simulate a heating profile with 6 °C/min in accordance with Apollo 14 and 15 sample analysis performed by Gibson and Moore (1972). The end of the extraction process was defined as the time when the concentration of molecules in the sample equalled the initial value, that is, the concentration of the lunar atmosphere as described above.

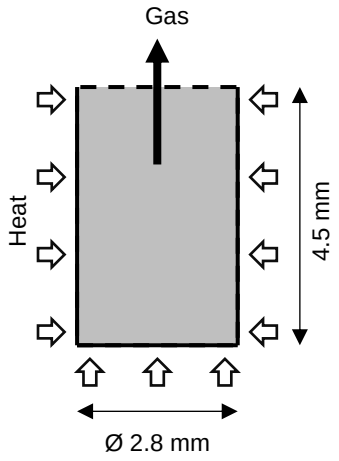

Figure 3-1: Sample dimensions for the COMSOL simulation model with heated sides and upper boundary open for gas transport

3.2 Parameter Study

3.2.1 Initial Water Concentration

The effects of two different water contents of 0.1 wt% and 1.0 wt% were evaluated, in conjunction with expected water contents based on estimates from remote sensing data (Hayne *et al.*, 2015). The temporal change of adsorbed (bond to the sample), desorbed (released from the sample and located in the voids), and outgassed (removed from the sample) molecules over time is shown in Figure 3-2. The amount of water

molecules present in desorbed form in the voids of the sample, n_d, is about three to four orders of magnitude lower than the number of adsorbed, n_a, or outgassed water molecules, n_o. This is due to a relatively quick gas transport to the environment, so that no greater accumulation of gas molecules can take place in the sample voids. A lower water content leads to a longer duration of the extraction (approximately 21 min versus 14 min) and a lower maximum gas pressure in the sample (approximately 6 Pa versus 566 Pa). Due to the higher gas pressure in the case of 1.0 wt% initial water concentration, the desorbed molecules are transported out of the sample at a similar rate after the pressure peak as they accumulate in the voids before the pressure peak. For the 0.1 wt% initial water concentration the amount of desorbed molecules decreases at a significantly slower rate after the pressure peak, because the pressure gradient to the environment is smaller. A comparison of both maximum temperature (at the sample boundary) and average temperature of the sample shows that the higher gas pressure significantly enhances thermal diffusivity, so that the heat is introduced more uniformly into the sample. Without the respective gas pressure at 0.1 wt% initial water content, there is a difference of about 30 K between maximum and average temperature at the end of the extraction process. In the case of 1.0 wt% initial water, the temperature even temporarily reaches a uniform temperature distribution when the gas pressure is at its maximum.

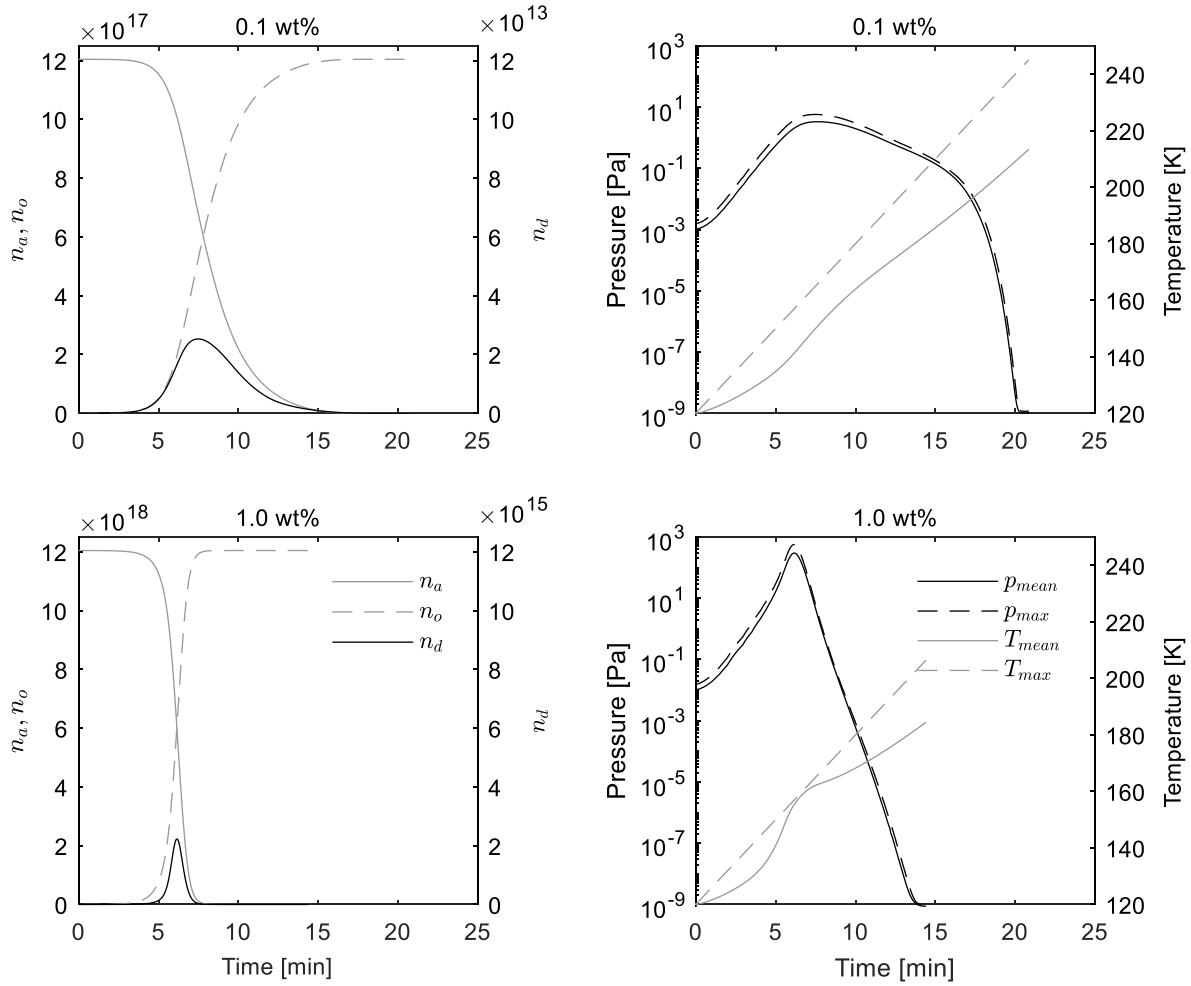

Figure 3-2: Amount of adsorbed (n_a), desorbed (n_d), and outgassed (n_o) water molecules and mean and maximum gas pressure and temperature for different water contents in the sample, as calculated with the COMSOL model.

As discussed in section 2.3.3, the tortuosity is one of the major unknowns and was found to vary between approximately 4 to 8 for the relevant fraction of NU-LHT-2M (compare Table 2-4), which is assumed to be representative of the Apollo 16 type sample simulated here. The default value for the simulation was chosen

to be 5, but it is unclear how a higher tortuosity would affect the outgassing pressure. The same is true for the mean diameter of void space, which in the default case was chosen to be 70 µm, equal to the mean particle size. To determine the actual influence of both parameters, a sensitivity analysis was performed for the sample with 0.1 wt% initial water content. It was shown that when increasing the tortuosity from 5 to 7 to 10 while decreasing the mean diameter of voids from 70 µm to 50 µm to 20 µm respectively, the shape of the gas pressure curve transforms more towards the one of the sample with 1.0 wt% initial water content. This means that the broad maximum of the pressure curve becomes a sharper peak with higher amplitude (from 6 Pa to 15 Pa to 83 Pa respectively), while the total duration of the process is slightly reduced (from 21 min to 20 min to 19 min). The resulting curves are depicted in Figure B-2 in the appendix.

The simulation allows a closer insight into the transport mechanisms that take place in the sample. To get an impression of the governing transport mechanisms during the extraction process, the Péclet number Pe was calculated. This dimensionless number can be used to assess whether the transport is dominated by convection ($Pe \gg 1$) or diffusion ($Pe \ll 1$). The Péclet number for gas transport and heat transport is generally defined as:

$$Pe_{gas} = \frac{L \cdot u}{D} \tag{3-5}$$

$$Pe_{heat} = \frac{L \cdot u}{\alpha} \tag{3-6}$$

There are many other definitions of the Péclet number, which may deliver significantly different results (Huysmans and Dassargues, 2005). It is therefore necessary to carefully select the most reasonable definition of the Péclet number for the respective problem at hand. In equations (3-5) and (3-6) the mean free path is often used as a measure for the characteristic length L. However, since the mean free path strongly varies over the course of the volatiles extraction, the mean void size is chosen as a more appropriate characteristic length for the present problem: $L = d_v$.

In the investigated scenarios it was found that $Pe \ll 1$ at all times for gas transport (Figure 3-3). Gas diffusion therefore clearly is the dominating transport mechanism, even at elevated gas pressures during short periods in the extraction process. This result is similar for the heat transport, although the Péclet number is generally higher and temporarily reaches $Pe > 1$ for periods with high pressure. This result suggests that the model would yield similar results if the convection terms, at least for the mass transport, were neglected.

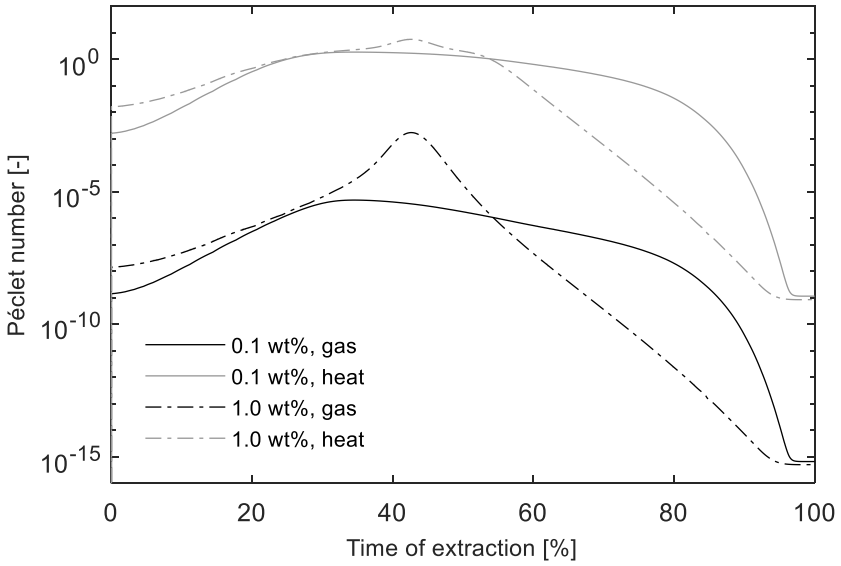

Figure 3-3: Péclet number for gas transport in the sample at different initial water contents, as calculated with the COMSOL model

A crosscheck was therefore done by computing the model with identical parameters and both with and without the convection terms for heat and mass transfer. The relative error of the maximum gas pressures for both cases is depicted in Figure 3-4. As expected from the calculated Péclet number, the error introduced by neglecting convection is very small for the sample with 0.1 wt% initial water concentration. The relative error in this case reaches a maximum of 3 % near the end of the extraction process. However, for the sample with 1.0 wt% initial water concentration, the relative error is significantly higher with 35 % near the end of the process. It could be argued that this error is still negligible because the absolute pressure is $<10^{-8}$ Pa at this point (compare Figure 3-2). Nevertheless, the relative error already temporally reaches 8 % where the absolute gas pressure reaches its maximum of 566 Pa. Interestingly the error between gas pressures without and with convection is mainly negative, indicating that the amplitude of the gas pressure is higher when considering convection. The total duration until all desorbed molecules are transported out of the sample is slightly longer (1.4 % for 1.0 wt% initial water concentration) if convection is not considered. This means that the outgassing of water from the sample happens faster with convection, creating higher pressure gradients in the sample which cause higher local peaks. However, it can principally be concluded that for a qualitative consideration such minor deviations can be neglected and that the shape of the outgassing curves do not change significantly for the investigated cases if convection is neglected.

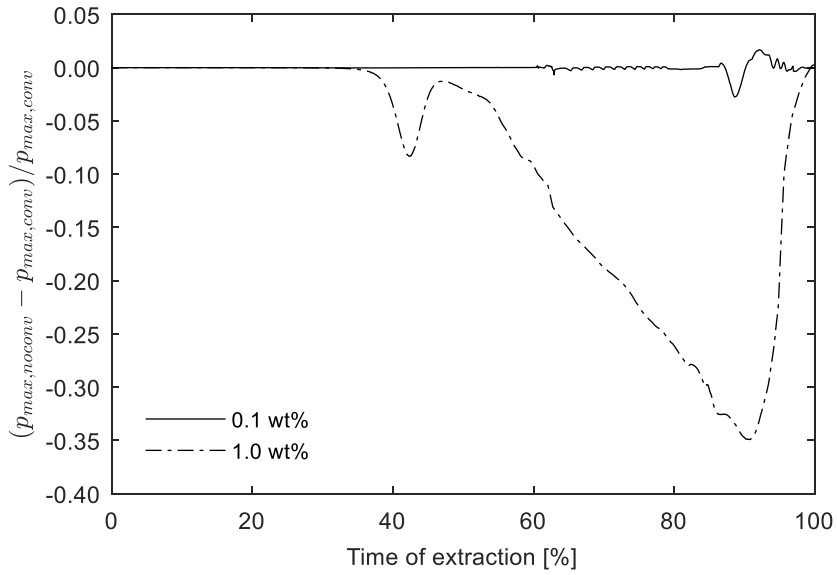

Figure 3-4: Relative error of the maximum gas pressures calculated with and without the convection terms

3.2.2 Bulk Density

The physical properties of the sample are of particular interest for the thermal diffusivity as well as the gas diffusivity and gas permeability. The bulk density is one of the major physical variables for lunar samples as it varies with location and depth. Values between approximately 1.1 g/cm³ and 2.3 g/cm³ have been determined from core samples returned by the Apollo and Luna missions (Carrier, Olhoeft and Mendell, 1991). The effect of bulk density on the gas- and thermal diffusion processes is assessed in the following.

The effective gas diffusivity determined with equation (2-40) and (2-41) directly depends on the ratio of porosity and tortuosity. Porosity is given by the relation (2-42), indicating that an increasing bulk density leads to a smaller porosity. According to the various models listed in Table 2-3, tortuosity generally increases with decreasing porosity. Figure 3-5 shows the obstruction factor, which is the quotient of porosity and tortuosity, versus bulk density. The obstruction factor is a direct measure for how the gas diffusivity scales with bulk density. Two standard models were used to calculate $\tau(\phi)$: the Millington model for spheres (Millington, 1959), and the Bruggeman model for spheres and cylinders (Tjaden *et al.*, 2016). It can be seen that the obstruction factor, or the gas diffusivity respectively, decreases by a factor of approximately 0.15 to 0.30 over the range of possible bulk properties for lunar regolith, depending on the model.

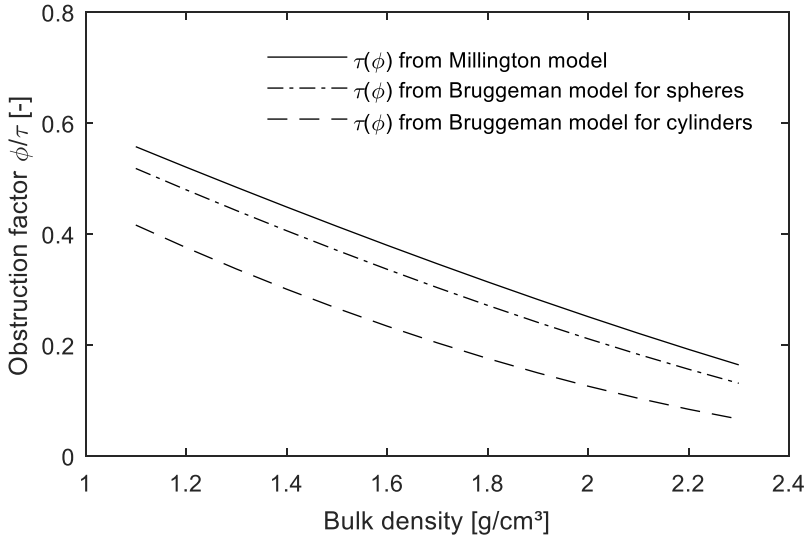

Figure 3-5: Obstruction factor versus bulk density with a particle density of 3.1 g/cm³

Bulk density also affects the thermal diffusivity. On the one hand there is a direct influence according to equation (2-33), and on the other there is an indirect influence through the thermal conductivity. The resulting dependency considering both influences is depicted in Figure 3-6. First, the thermal diffusivity decreases because the specific heat increases more strongly with temperature than the thermal conductivity. After passing the minimum, this relation is reversed, so that the thermal diffusivity increases. The positive effect of an increasing bulk density is only noticeable for low temperatures below around 200 K to 300 K. Above that the improved contact conductance that contributes to the thermal conductivity is compensated by the bulk density in the denominator of equation (2-33) and a change in bulk density has the inverse effect. This behaviour is however only visible at low gas pressures, since here the effective thermal conductivity is dominated by conductivity through the particles and the solid contact between particles (compare chapter 2.2.3). Calculated values of the thermal diffusivity by Cremers and Hsia (1974), based on the specific heat capacity determined by Hemingway, Robie and Wilson (1973), show a similar trend as depicted in Figure 3-6. It can be concluded that increasing the bulk density has a negative effect on the gas diffusivity as well as the thermal diffusivity for temperatures above approximately 300 K and at low gas pressures. Below this temperature, the thermal diffusivity increases with bulk density.

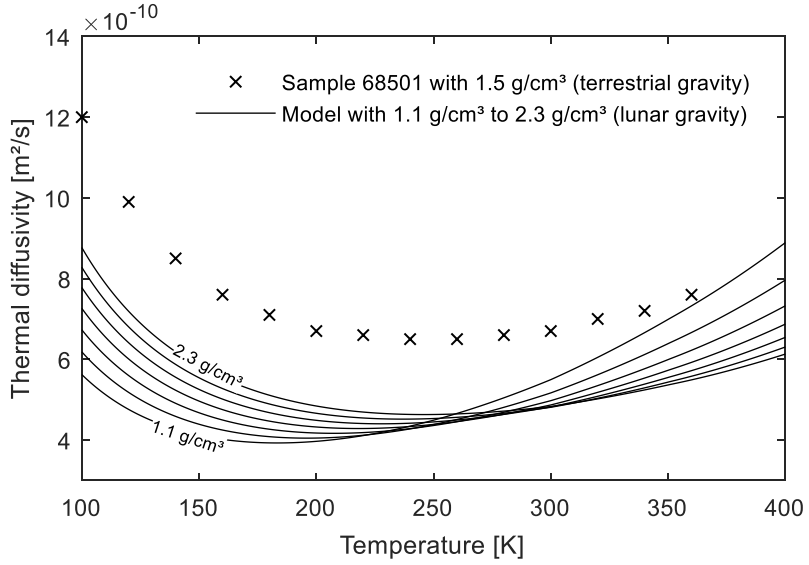

Figure 3-6: Thermal diffusivity versus temperature at 10^{-4} Pa for varying bulk densities

3.2.3 Heating Mode

The amplitude of the pressure can be reduced by reducing the heating rate to produce a more uniform temperature distribution. When changing it from 6 °C/min to 4 °C/min (a value used in experiments by Gibson and Johnson (1971)), the maximum pressure decreases by a factor of 0.76 for the 0.1 wt% initial water concentration and 0.41 for the 1.0 wt% initial water concentration. Moreover, the duration of the extraction process increases by a factor of 1.22 for the 0.1 wt% initial water concentration and 1.38 for the 1.0 wt% initial water concentration. The average temperatures in the sample decrease by a factor of 0.93 and 0.99 respectively. The shapes of the gas and temperature curves for different heating rates are provided in Figure B-3 and Figure B-4. Figure 3-7 illustrates the outgassing rate, or variation of outgassed molecules n_o over time, that would be measured by a gas analyser. The values were normalised to the maximum value at a heating rate of 6 °C/min for a more convenient interpretation. A clear shift of the outgassing peak to later times is visible for a reduced heating rate, as well as a significant lower amplitude of the outgassing rate. This is presumably because the desorbed molecules have more time to leave the voids of the sample before new molecules are desorbed to fill this space, resulting in a lower average gas pressure in the sample and hence a lower outgassing rate.

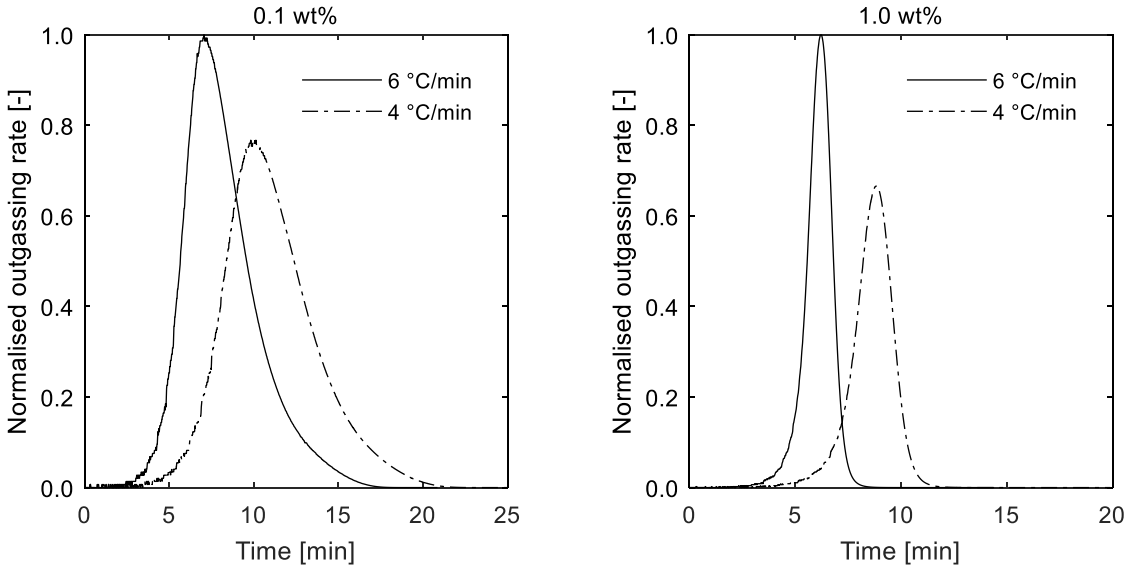

Figure 3-7: Outgassing rate for two different heating rates and different initial water contents

3.2.4 Thermal Conductivity

For small samples in the millimetre range, as comparable to the ProSPA baseline sample size, the first simulation approach might be to neglect the thermal gradients and assume a homogeneous temperature. To investigate the error of this simplification, two simulations were performed: a) using the thermal properties of lunar regolith as discussed before, and b) using an infinite thermal conductivity that produces a perfectly uniform temperature distribution in the sample. The results are presented in Figure B-3 and Figure B-4. For an ideal uniform temperature distribution compared to the realistic scenario, the maximum gas pressure increases by a factor of 2.15 for the 0.1 wt% initial water concentration but decreases by a factor of 0.42 for the 1.0 wt% water content. The extraction duration decreases by a factor of 0.42 for the 0.1 wt% initial water concentration and 0.60 for the 1.0 wt% initial water concentration (it is worth mentioning that both result in an equal absolute duration for the uniform temperature distribution). The average sample temperatures decrease by a factor of 0.81 and 0.93 respectively. The outgassing rate for both scenarios with a realistic and a uniform temperature distribution are depicted in Figure 3-8. The results illustrate that neglecting the thermal gradients in the sample mainly leads to significantly different amplitudes of the maximum pressure and different process durations. Only a minor effect is visible regarding the time of the outgassing peak. With a uniform temperature distribution the outgassing is solely dependent on the mass transfer. In the case of

the lower initial water concentration the simultaneous desorption of molecules in the entire sample volume produces higher gas pressures and subsequently the molecules are transported out of the sample faster than for a realistic temperature distribution. For the higher initial water concentration the gas pressure is already two orders of magnitude higher with a realistic temperature distribution, and hence convection has a noticeable share on the mass transfer as discussed in section 3.2.1. With the uniform temperature distribution and an accordingly simultaneous desorption in the entire sample, the gas mass transfer is even better, which leads to a reduction the maximum gas pressures in the sample. In summary, for a uniform temperature distribution the shapes of the pressure curves of the released volatiles (Figure B-3 and Figure B-4) are much more alike than for a realistic temperature distribution.

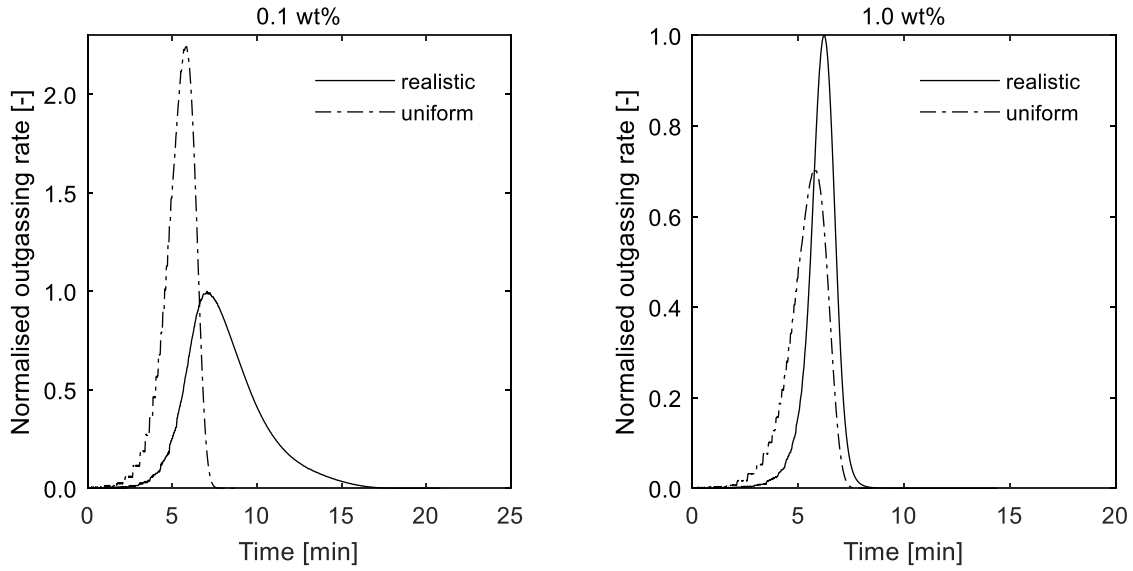

Figure 3-8: Outgassing rate for a realistic and a uniform temperature distribution and different initial water contents

4 Experimental Extraction of Volatiles

In the context of the ProSPA study a facility for the preparation and conditioning of lunar regolith analogues and the thermal extraction of volatile compounds from theses samples under low temperature and high vacuum conditions was developed. This chapter describes the development of this facility and the experimental work and research that was performed in order to achieve a proof of concept for a ProSPA-like instrument configuration and to characterise the overall process of volatiles extraction. The experiments presented here cover the evaluation of the effect of different sample conditions on the temperature-triggered outgassing of volatiles, including the variation of the initial water content of the sample, the amount of sample, its particle sizes, compaction, and different heating rates. Furthermore, preparatory tests on the sample conditioning process are presented, which were performed prior to the volatiles extraction experiments to demonstrate the feasibility of hydrating the lunar regolith simulant NU-LHT-2M.

4.1 Sample Conditioning

From the survey of possible methods to add water to lunar regolith and its analogues (chapter 1.4), it was concluded that the approach of exposing regolith to a humidified carrier gas is most promising to achieve a controlled humidification of lunar regolith simulants in the range of 0.1 wt% to 1 wt% with a manageable effort. The first question to be answered by the preparatory studies prior to the volatiles extraction demonstration was if this process is generally feasible for hydrating NU-LHT-2M and how fast the adsorption can be achieved. In a first approach, a number of tests were performed with a simple setup, as explained in the following.

In the first test series, three sample batches of NU-LHT-2M with different masses were investigated. Sample 1 was spread over a piece of aluminium foil with about 30 mm × 30 mm size and baked-out over night at 150 °C to remove atmospheric water. Samples 2 and 3 were each spread over an aluminium sheet with 40 mm × 80 mm size and heated to 150 °C for 2 h. After bake-out the samples were placed in an OHAUS Discovery DV215CD precision balance with a readability of 0.01 mg. A TFA 30.3015 sensor (accuracy: temperature ±1 °C, humidity ±3 %) was used to record temperature and humidity inside the sample compartment of the balance. The change of the sample mass was recorded by video and noted in increasing time intervals.

Figure 4-1 shows the resulting variation of sample mass, as well as temperature and humidity for all three samples. The mass gain depicted for sample 1 includes the aluminium foil where the sample was placed upon, while the mass gain depicted for sample 2 and 3 the mass of the sample holder was subtracted. The data proves the basic feasibility of the procedure and shows that for a relative humidity between 40 % and 50 % in ambient atmosphere up to 0.11 wt% of water can be adsorbed by the sample. The differences between the three measured mass gains are explained with the difficulty in determining the exact start time. When the sample was placed on the balance, an initial rapid increase of mass was observed, which presumably was due to the mechanical shock causing oscillations. After a first quasi-equilibrium was reached after a couple of seconds, the mass increased again, which was attributed to adsorption of water and hence the quasi-equilibrium was defined as the actual start time. The mass quickly increased from this point on and came to a steady-state after about 1 h. This made it practically impossible to control the amount of water in the sample via the time of exposure. The only way to achieve different levels of water content therefore was to expose a sample to different levels of relative humidity until it reaches equilibrium. In an additional test it was attempted to determine the water content at saturation by exposing the sample to a relative humidity of

80 %. The results however were inconclusive, since the readings of the precision balance were disturbed by the high amount of water in the sample compartment.

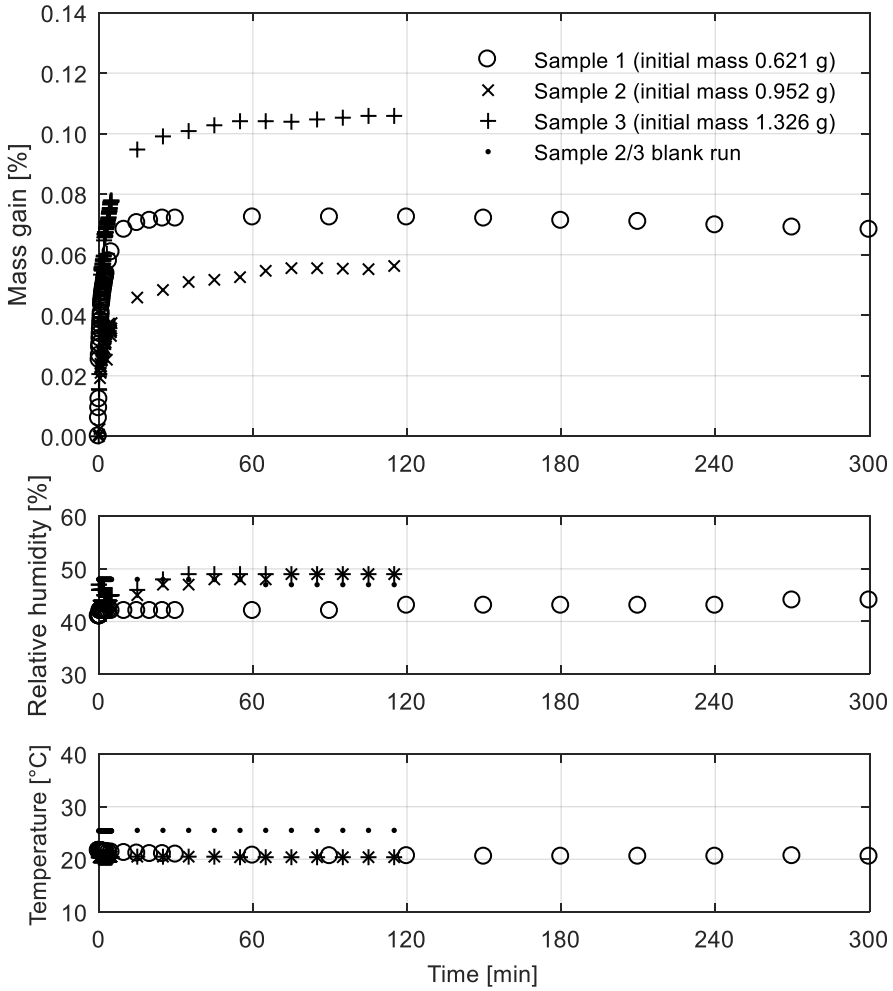

Figure 4-1: Mass change, relative humidity, and temperature during the adsorption pretests

After this initial test, a second long-term experiment was conducted where a sample was exposed to relative humidity levels between 1 % and 70 %. The same precision balance as used before was placed inside a humidity-controlled glovebox (description see chapter 4.2.1). A portion of NU-LHT-2M was spread over a stainless steel Petri dish with 75 mm diameter and baked-out in vacuum (>100 °C, ~10^{-1} mbar) for 4 h. The sample was then transferred into the humidity-controlled volume and left there for at least 12 h and up to 48 h, until it was decided that there was no further change in mass. After weighing the sample two to three times over this duration, the relative humidity was increased up to 70 % in 10 % increments. The same procedure was conducted with an empty Petri dish, where no significant mass gain could be measured (less than 0.01 wt% of the sample mass).

Figure 4-2 shows the resulting mass gain of the sample, normalised to the mass at the initial relative humidity (2.97838 g at 0.9 % relative humidity). The highest mass gain is visible between 0.9 % and 10 % relative humidity, while up to 60 % the mass gain seems to approximate saturation. However, the mass gain at 70 % relative humidity does not follow this trend but increases again. This behaviour suggests Type II adsorption (Hill, 1977), which would be in agreement with the results of Holmes and Gammage (1975), Fuller and Agron (1976), and Robens et al. (2007, 2008), as discussed in chapter 1.4. In the present case this would mean that after the formation of a monolayer of adsorbed water up to approximately 10 % to 20 % relative humidity, the adsorption continues in the form of multilayers. The amount of water for a monolayer would therefore be

in the range of 0.04 wt% to 0.08 wt%. This is about twice as much as the values found for lunar regolith (compare Table C-1), but still in the same order of magnitude. However, the temperature variations during the experiment (bottom diagram in Figure 4-2) complicate such a detailed interpretation of the mass gain and hence no clear conclusions about the types of adsorption can be drawn at this point. Nevertheless, it can be concluded that a practical and effective way of adding adsorbed water to samples of NU-LHT-2M is by storing them in a humidity-controlled atmosphere for a couple of hours, ideally more than 12 h. For the experimental studies on volatiles extraction it was therefore decided that this method is appropriate to produce samples with different water content.

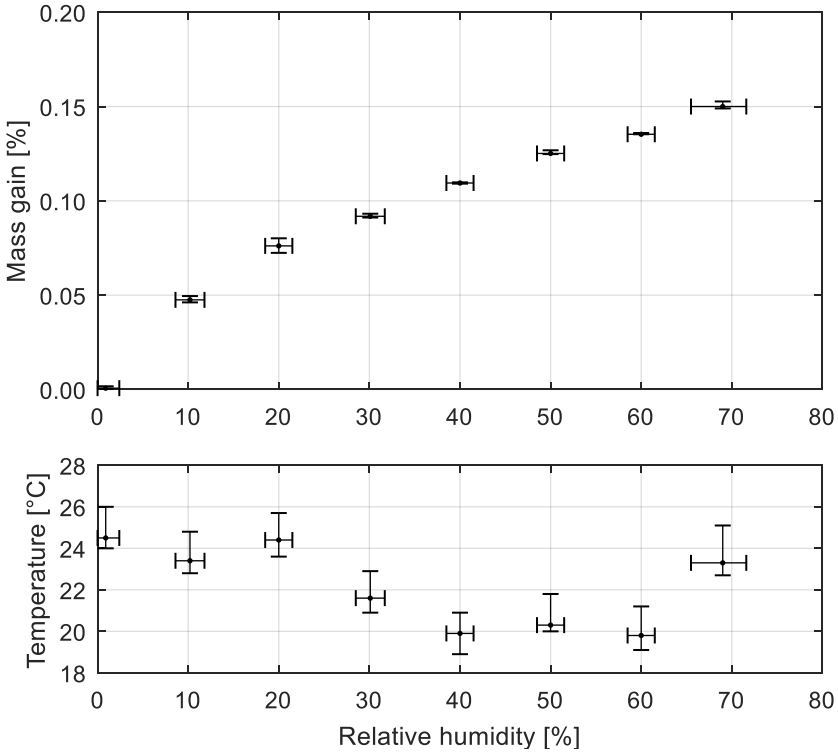

Figure 4-2: Mass gain and temperature over relative humidity for a long-time exposure of NU-LHT-2M

4.2 Extraction of Volatiles from NU-LHT-2M

4.2.1 Experimental Setup

The setup for the experiments on volatiles extraction includes a sample conditioning system for the preparation of samples and a volatiles extraction system for the actual thermal processing of the samples. Both systems are introduced in the following sections, along with a discussion of the sample cooling method that was developed and a description of the data processing approach for the volatiles extraction system.

Sample Conditioning System

The experimental setup for the preparation of lunar regolith simulants is depicted in Figure 4-3. It includes a stainless steel glovebox with a purge gas feed, humidification/dehumidification system, and an attached vacuum airlock with a separate heater setup for sample bake-out. The glovebox (Jacomex P-Box) has an internal volume of approximately 0.8 m³ and automatically maintains an overpressure to avoid inward leakage from the laboratory atmosphere. The humidification/dehumidification system (GS Glovebox Systemtechnik) uses dry nitrogen with purity 5.0 as a purge gas, which is either fed directly into the glovebox for dehumidification or guided through a bubbler with distilled water before entering the glovebox for humidification. A Vaisala HMT120 sensor installed inside the glovebox near the sample provides the measurement of temperature (range -40 °C to 80 °C, accuracy ±0.2 °C in the relevant range) and relative humidity (range 0 % to 100 %, accuracy ±1.5 % in the relevant range) for the control system. A second

sensor (ISO-certified TFA 30.3039IT Klimalogg) measures temperature (range 0 °C to 50 °C, accuracy ±1 °C), dew point, and relative humidity (range 1 % to 99 %, accuracy ±3 % from 35 %rH to 75%, otherwise ±5 %) at the sample location and transmits the data via radio to a computer. For weighing the sample, a Sartorius Excellence E 1200 S precision balance is installed in the glovebox (readability 0.001 g, standard deviation 0.001 g). The airlock is equipped with standard KF40 vacuum flanges to connect a pressure gauge, evacuation line, and a D-Sub feedthrough for a thermocouple and a power supply. The latter is used to power the heater for sample bake-out. For this purpose, the sample is placed inside a borosilicate glass container, which is mounted on top of a steel block that is heated from the inside via an inserted cartridge heater.

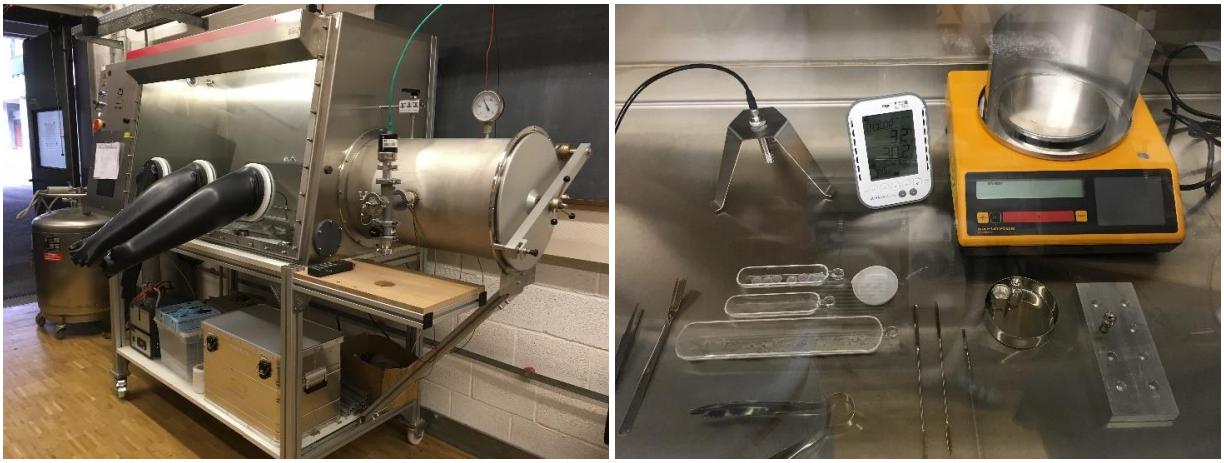

Figure 4-3: Glovebox with vacuum airlock for sample preparation (left) and equipment for sample preparation inside the glovebox (right)

Volatiles Extraction System

The experimental setup for the thermal extraction of volatiles from the sample consists of an instrumented vacuum system with two sections. Figure 4-5 and Figure 4-4 show an overview and detail view of the entire system, a schematic diagram can be found in the appendix (Figure B-5). The lower part of the system is constructed using Swagelok ¼" tubes and VCR-type fittings, can be pumped down to 10^{-5} mbar, and includes the sample holder, a purge gas feed, a Penningvac pressure gauge (Leybold PTR 90 N, 10^{-8} mbar to 10^{3} mbar), and a cooling/heating system that is applied externally to the sample holder (Figure 4-6 and Figure 4-7). The upper part consists of CF40-sized vacuum tubes, can be evacuated to 10^{-8} mbar, and contains a quadrupole mass spectrometer (Stanford Research Systems RGA 200, range 1 amu to 200 amu) and a second Penningvac PTR 90 N pressure gauge. Both sections are connected via a manual dosing valve (Swagelok SS-4BMRG-V51), which acts as an orifice to restrict the mass flow so that the RGA filament can be operated below its maximum gas pressure of 10^{-4} mbar. The entire system is evacuated using a turbomolecular pump (Leybold Turbovac SL 80) and an oil-free scroll pump (Leybold Scrollvac SC 5 D). The vacuum system is heated to 120°C using heating wires wrapped around the tubes and insulated with aluminium foil to enable a full bake-out and avoid condensation of the released water during operation. Temperature is measured at five locations throughout the system using Type K thermocouples: at the sample holder, lower crosspiece, dosing valve, upper crosspiece, and upper pressure gauge.

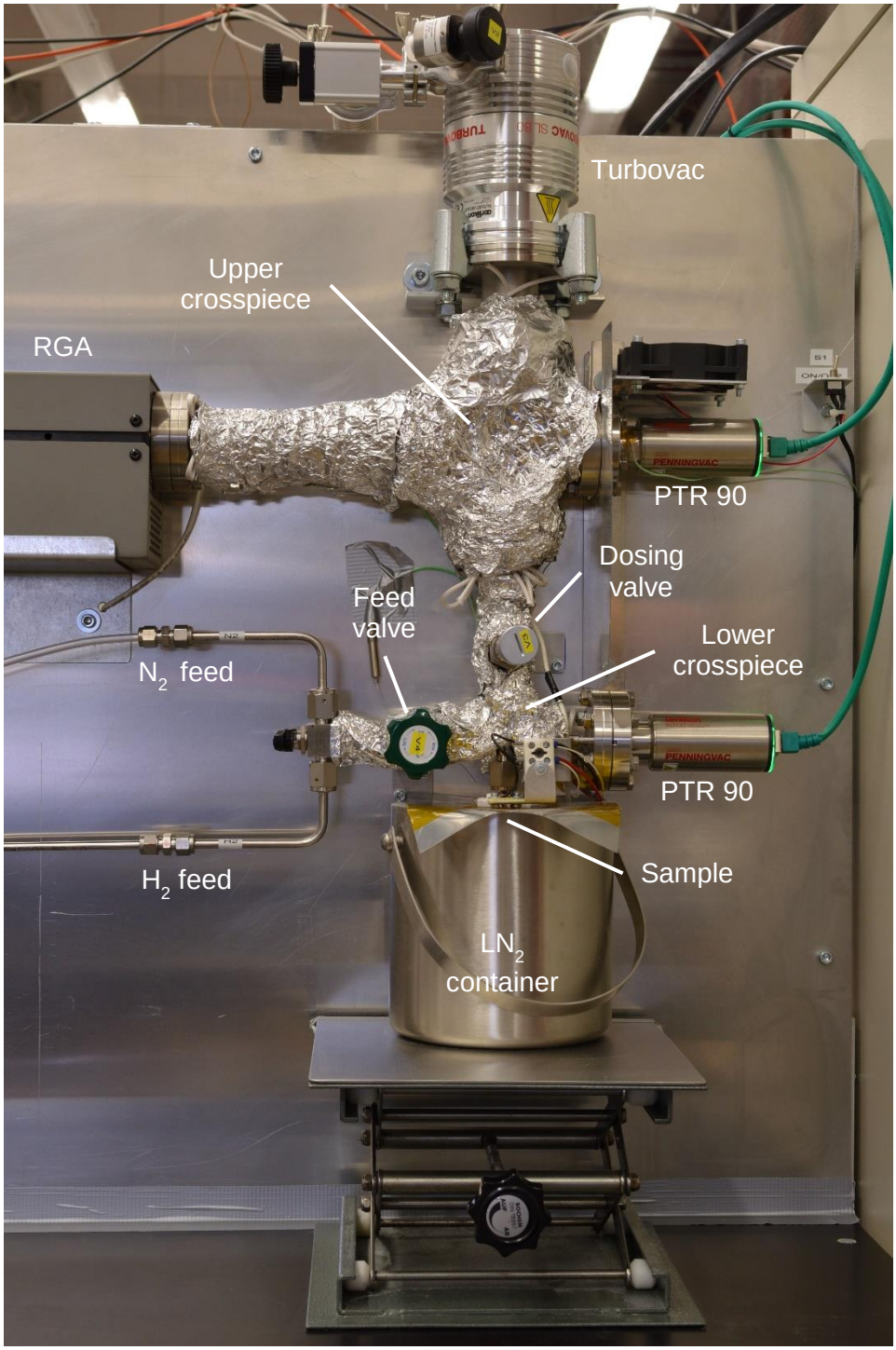

Figure 4-4: Volatiles extraction system (detail)

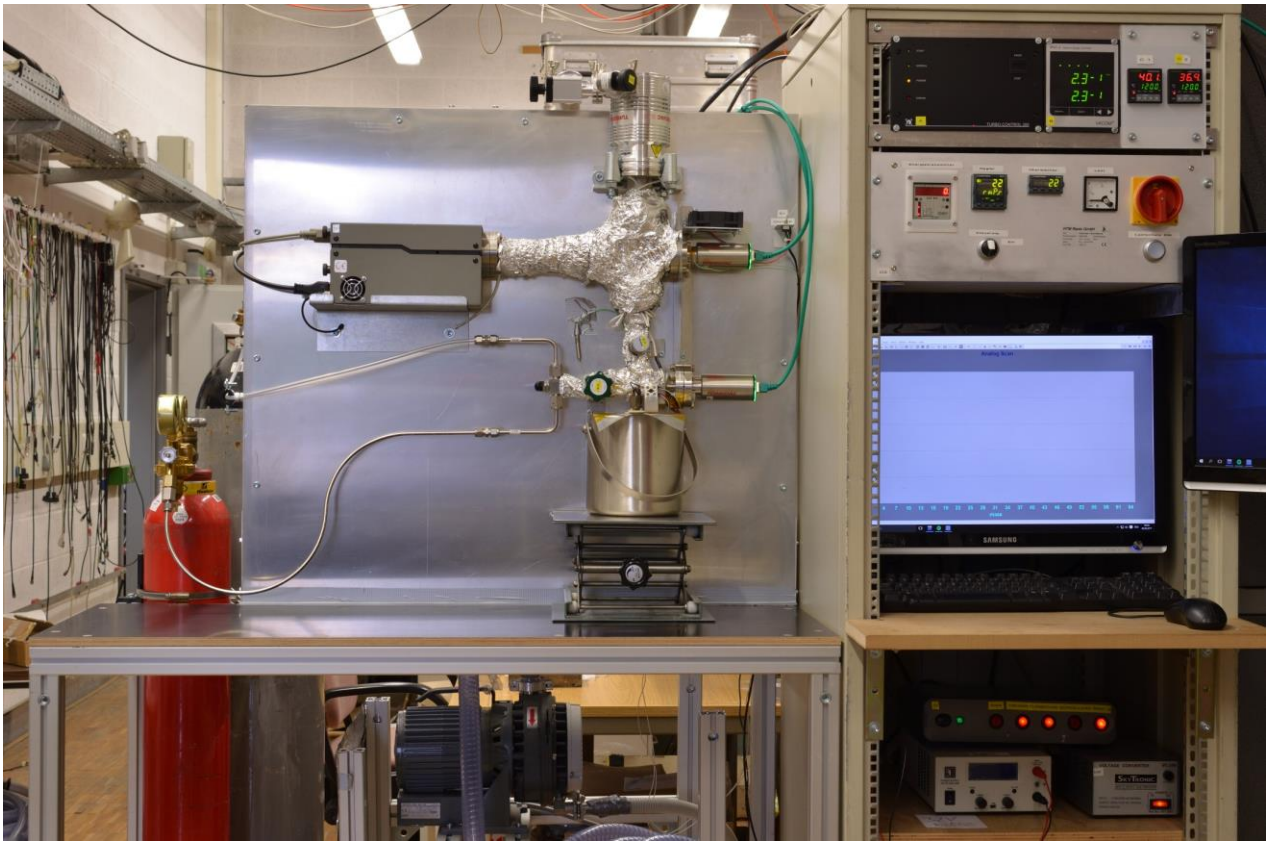

Figure 4-5: Volatiles extraction system (overview)

The sample holder is a modified stainless steel blind fitting (Figure 4-6) to accommodate a sample that is 2.8 mm in diameter and 4.5 mm in height, according to the ProSPA baseline sample size (compare chapter 1.2.4). The upper diameter of the sample holder was reduced to minimise the heat transfer from the heated tubes above (by reducing the wall thickness from 3 mm to 1 mm, the cross sectional area of the conductive heat transfer is reduced to only 23 % of the initial value). The sample holder is installed at the lower end of the extraction setup and sealed towards the lower VCR crosspiece with a steel gasket that holds a sintered filter with an average pore size of 60 µm (Swagelok SS-4-VCR-2-60M). For the design of the entire vacuum system it was taken care that the internal volume of the tubes is as small as possible while providing a sufficiently large cross section for the diffusion of molecules in high vacuum. Bends were avoided between sample holder, mass spectrometer, and vacuum pump to allow the released molecules to travel along a straight and undisturbed path.

Because the sample holder should be removed, cleaned, and stored in the glovebox between the individual test runs, a detachable heater had to be designed. Following the design developed for previous studies, a Macor ceramic heater mount was manufactured as depicted in Figure 4-6 and Figure 4-7. A Kanthal A1 heating wire with 0.2 mm diameter (32 AWG, 46.2 Ω/m, total length ~0.3 m) was wound through the ceramic holder and the ends were twisted to reduce the electrical resistance at the connection to the power supply. During the experiments it was switched to a Kanthal A1 heating wire with 0.25 mm diameter (30 AWG, 29.3 Ω/m, total length ~0.3 m) for reasons of robustness. A 0.5 mm diameter Type K mantle thermocouple was inserted along a notch at the inner side of the holder to measure the temperature of the sample holder at a location that equals half of the sample height. The ceramic heater can be attached to the sample holder after installation of the latter and secured using a ceramic washer and a splint at the bottom.

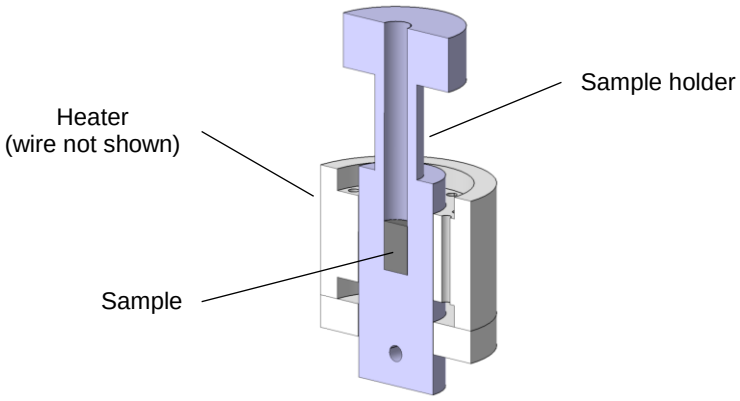

Figure 4-6: CAD model cut view of the sample holder and the ceramic heater

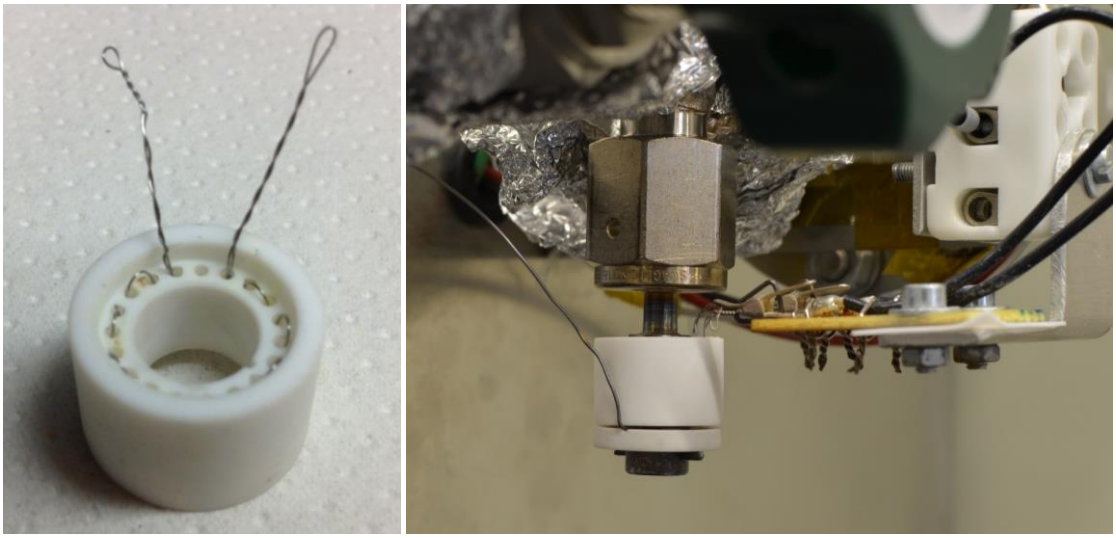

Figure 4-7: Detail view of the ceramic holder with heating wire

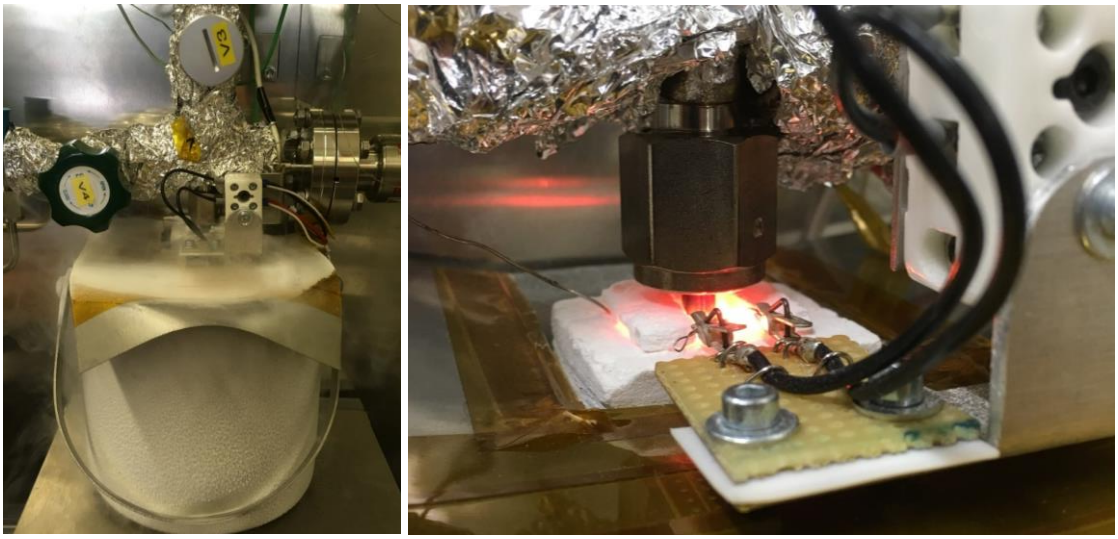

Figure 4-8: Detail view of the lower section of the volatiles extraction system illustrating the installed cooling system.

Sample Cooling

Since the goal was to start the extraction of volatiles at a temperature relevant to conditions at the lunar South Pole, the sample needed to be cooled down to approximately -150 °C prior to extraction. This was realised using liquid nitrogen, which has a boiling point of -196 °C at ambient pressure. First tests showed that simply submerging the sample holder with heater in liquid nitrogen was not applicable. The heating power required to raise the sample temperature according to the desired heating mode would have been much too high due to the large temperature difference between boiling point and desired starting temperature and the capacity of the liquid nitrogen bath. Additionally the evaporation of the nitrogen at the sample holder (Leidenfrost effect) caused an undefined heat transfer in this area which was difficult to control by the heater. When the level of liquid nitrogen sunk below the sample holder, the sample temperature immediately increased, so that even when the heater was switched off, the sample temperature could not follow the programmed heating rate. Several approaches were investigated to solve this problem and create a cooling system that can be operated reliably and predictably over the entire temperature range (Figure 4-9):

1. Submerging the sample holder in a bath of liquid nitrogen
2. Same as 1. with a glass fibre insulation around the heater
3. Same as 1. with a microporous aluminium oxide insulation around the heater
4. Same as 3. with an aluminium foil insulation around the microporous insulation
5. Same as 1. with an aluminium block below the heater
6. Same as 3. with a taller insulation block that extends to the base of the liquid nitrogen bath
7. Boiling liquid nitrogen below the sample holder with a tube that guides the gas stream around the heater
8. Blowing gaseous nitrogen through a cooling spiral submerged in liquid nitrogen and further through a tube applied to the heater

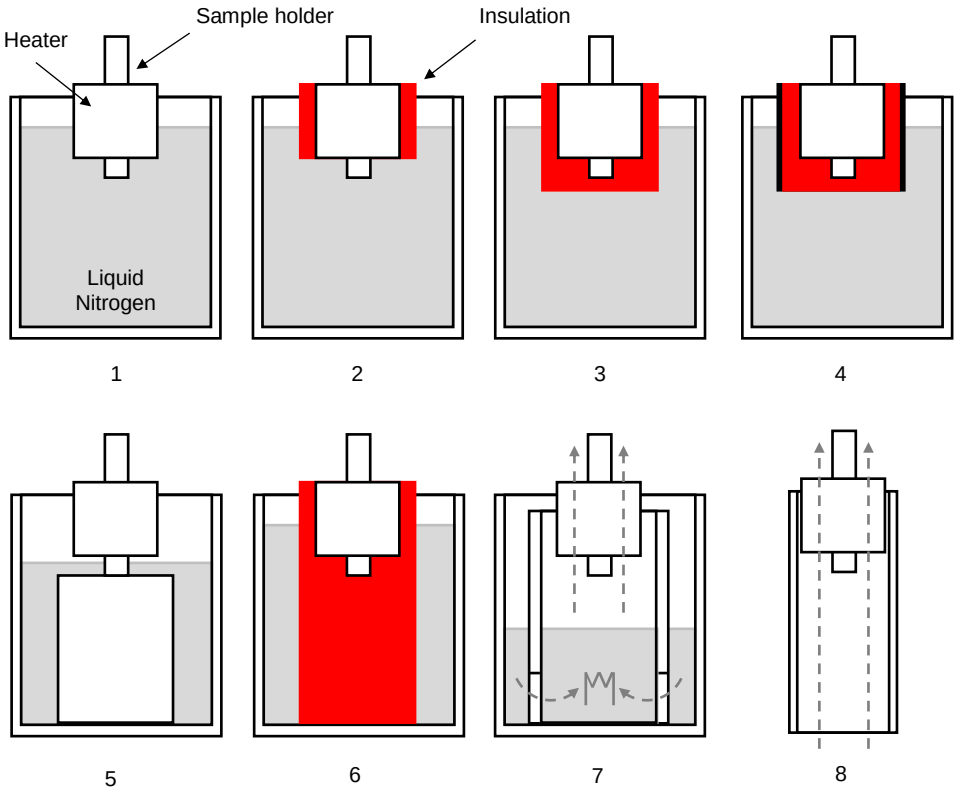

Figure 4-9: Different approaches to cool the sample in the volatiles extraction system

While solution 1 was not applicable for the aforementioned reasons, solutions 2 and 3 did not provide sufficient insulation to dampen the cooling power of the liquid nitrogen bath. Similarly to solution 1, the sample temperature significantly increased when the level of liquid nitrogen sunk below the sample holder. To reduce this effect an aluminium foil was added to the insulation (approach 4), in an attempt to prevent ambient air to enter the insulation too early and cause a strong temperature increase. Being unsuccessful with this approach, it was tried to add more thermal inertia to the system by placing an aluminium block below the sample holder (solution 5). This slightly prolonged the cooling effect of the liquid nitrogen batch even when the liquid level was low. An even more effective approach (solution 6) was to use a bigger and taller microporous insulation block that acts like a wick to draw liquid nitrogen from the bottom of the bath up to the sample holder and evaporate it in a more uniform manner. Together with a larger container for the liquid nitrogen bath, this solution achieved the best reproducibility and was therefore used for all subsequent tests. However, only small mechanical defects between the microporous insulation and the heater (as a result of attaching and detaching the very soft insulation after each test run) lead to visible oscillations of the temperature due to uneven evaporation of nitrogen near the heater. Care therefore was taken to refurbish the upper part of the cooling system when visible damage of the insulation was noticed. An additional steel plate was added to the top of the liquid nitrogen container to reduce the temperature disturbance caused by convective fluxes of the ambient air.

Another possibility to cool the sample with a gas stream was also discussed and investigated. The first approach (solution 7) was to place a cartridge heater into the liquid nitrogen bath and boil the nitrogen below the sample holder. The resulting gas stream of cold nitrogen was guided around the sample heater. This approach seemed promising at first, but had to be discarded because the sample holder could only be cooled down to -65 °C. In order to create a better heat transfer from the gas stream to the sample holder, the method was further enhanced by flowing gaseous nitrogen through a cooling spiral and guide the cooled gas stream tightly around the heater (solution 8). This allowed cooling the sample holder further down, but implied a significant consumption of gaseous nitrogen. It was discussed to design an adapter piece that fits smoothly around the sample holder and apply an outer thread to the sample holder to guide a very thin gas stream along a long path around the sample holder. However, because it would have been difficult to install both the cooling adapter and the heater around the sample holder at the same time, and because the previously described solution 6 already provided acceptable results, this major modification of the cooling system was postponed for later design improvements.

Data Processing

Data acquisition was done through a computer using special software for the RGA and National Instruments LabVIEW for the data of pressure gauges, thermocouples, power supply, and multimeter. The following data was acquired and saved during the operation of the experiments:

- Thermocouple temperatures via National Instruments SCB-68 data logger to computer
- Gas pressure in upper and lower crosspiece via VACOM vacuum gauge controller MVC-3 and RS232 interface to computer
- Heater voltage and current via Aim-TTI Instruments EX355P power supply and Fluke 8845A digital multimeter through RS232 and USB to computer
- Gas analysis data via SRS RGA 200 mass spectrometer and RS232 to computer

The data connections and power lines are illustrated in the schematic diagram in Figure B-5. The RGA and the tubes of the vacuum system were heated separately, using one manually programmable Proportional-Integral-Derivative (PID) controller each. The sample heater was connected to the computer and programmed and monitored via a custom-made LabVIEW user interface that includes a PID algorithm and limitations for voltage and current. Data was saved to text files in individual time intervals and post-processed in MATLAB. The latter includes the time synchronisation of all raw data coming from different instruments, the interpolation of pressure gauge data over the time range of the RGA data to create equally spaced time steps, and the filtering of pressure gauge signals (moving average over 10 sample points).

It was observed that the cold cathode pressure gauge in the lower section of the setup influences the RGA signal, in a way that it alters the background gas composition. This issue was traced back to the switching of the pressure gauge between two available measurement systems in the combined PTR 90 transmitter: If the absolute pressure is above $6.6 \cdot 10^{-4}$ mbar, the built-in Pirani system is used to determine the gas pressure. Below this threshold, the built-in cold cathode system is activated and used for pressure measurement. Activation and deactivation of the cold cathode system is seen by the RGA in the form of jumps in the pressure signal. For the second PTR 90 that was installed in the upper section of the experimental setup this effect was not visible, which is reasonable since this pressure gauge is located 'downstream' of the RGA. After thoroughly evaluating the phenomenon of pressure jumps, it was decided to perform experimental runs with deactivated pressure gauge in addition to the normal runs with activated pressure gauge to have one set of undisturbed data available for later interpretation. Furthermore the data affected by pressure jumps was corrected in the post-processing routine as described in the following.

Figure 4-10 shows as exemplary plot of the hydrogen partial pressure as measured by the RGA, together with the absolute gas pressure returned by the lower PTR 90 transmitter. It can be seen that the hydrogen signal abruptly drops when the absolute pressure rises above $1 \cdot 10^{-3}$ mbar (cold cathode system is switched off), and that it abruptly rises when the absolute pressure drops below $6.6 \cdot 10^{-4}$ mbar (cold cathode system is switched on). The correction of the RGA curves was done by identifying the switching events in the PTR 90 signal, finding the corresponding RGA data, and adding the difference between the RGA signal before and after this jump to the following data values. The corrected curves therefore delete the effect of the deactivated cold cathode, or in other words they ignore that the cold cathode system is being switched off. The corrected curves were compared qualitatively with the curves that were recorded with a permanently deactivated PTR 90 transmitter and found to be in accordance. However, certain smaller non-continuous pressure trends have to be taken into account at the points where the curves were joined.

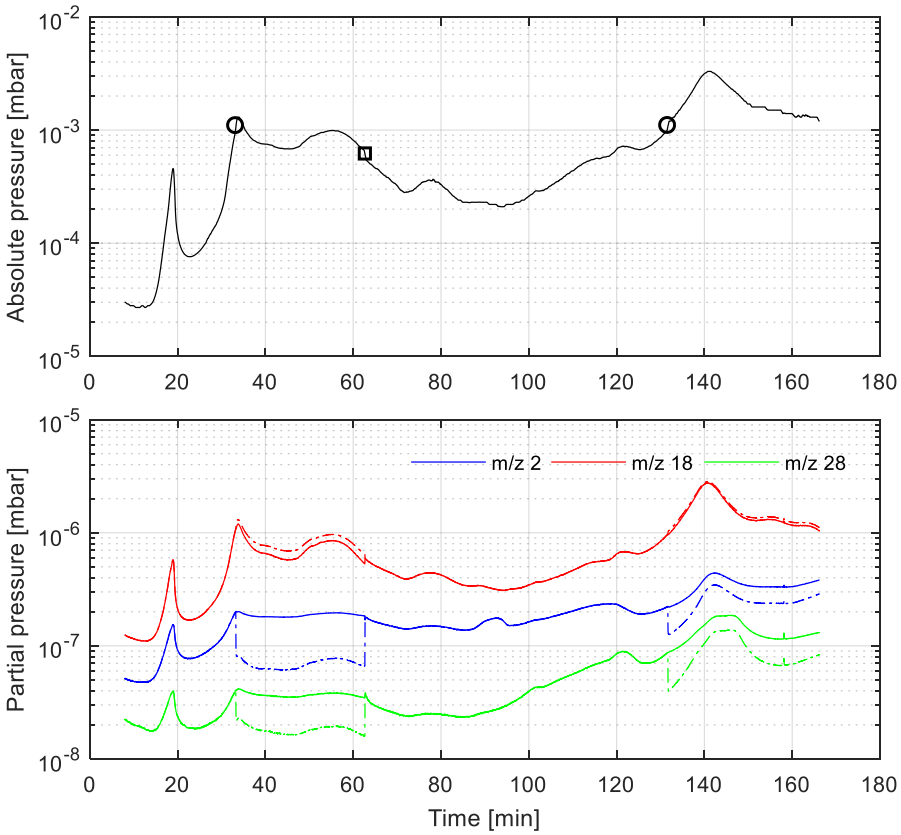

Figure 4-10: Demonstration of the pressure jump correction (top: PTR 90 signal, bottom: RGA signal). Dashed lines show the original data, solid lines show the corrected curves. Circles indicate the deactivation and squares indicate the activation of the cold cathode system.

4.2.2 Test Plan and Procedure

The volatiles extraction experiments were conducted as a parameter study, in which the conditions of the sample were varied to investigate the influence on the outgassing. This included the variation of relative humidity during the sample conditioning process, the variation of sample mass, sample particle sizes, sample compaction, and heating profile, as listed in Table 4-1. Each configuration was tested at least three times with additional reference measurements of the background outgassing without sample. This ensured that variations due to different preparation techniques or measurement errors were captured. As described previously, due to interferences of the lower pressure gauge and the RGA, test runs with deactivated pressure gauge in the lower section of the volatiles extraction system were added for each parameter combination, for one reference run as well as for one run with sample.

For all tests the highland-type lunar regolith simulant NU-LHT-2M was used. The amount of water in the sample was controlled by storing it in the previously described sample conditioning system (glovebox) at different levels of relative humidity, ranging from 1 % to 70 %. In addition, one set of samples was mixed with 15 wt% distilled water (1 ml water with 6.66 g sample) for the representation of a saturated sample, in accordance with saturation levels determined by Pitcher et al. (2016). The default sample mass for all runs was 33 mg to 36 mg, which was derived from the ProSPA baseline sample size (27.7 mm^3) and a bulk density between 1.2 g/cm^3 and 1.3 g/cm^3. In addition, a set of test runs with twice the amount of sample was also performed. The default particle size for the tests was 70 µm to 80 µm to represent the mean particle size of NU-LHT-2M. An additional set of runs with larger particles between 100 µm and 110 µm was also performed. The sample was loosely filled into the sample holder and it was made sure that all sample rested at the bottom of the holder by carefully tapping against the holder. A set of more compacted samples was also investigated, where a metal rod was used to press the sample while tapping against the sample holder. The heating modes for the tests were a temperature ramp of 6 °C/min and 4 °C/min, according to the previously established simulation model (see chapter 3) and experimental studies by Gibson and Johnson (1971) and Gibson and Moore (1972). Heating started at -190 °C and ended at 800 °C. Measurements at temperatures below -150 °C were not considered further for post-experimental analysis because such temperatures are not expected for the nominal ProSPA scenario. Furthermore the temperature control of the experiments was not as stable as desired in this range of temperatures.

Table 4-1: Test parameters for the volatiles extraction

Parameter	Values
Relative humidity for hydration	1 % / 10 % / 30 % / 50 % / 70 % / saturated
Sample mass	33-36 mg / 66-72 mg
Particle size	70-80 µm / 100-110 µm
Bulk density	loose (approx. 1.3 g/cm^3) / compacted (approx. 2.0 g/cm^3)
Heating mode	-190 °C to 800 °C at 6 °C/min / -190 °C to 800 °C at 4 °C/min

Prior to testing a regolith sample batch was sieved, filled into a borosilicate glass container, and installed inside the airlock, where it was heated between 100 °C and 200 °C under vacuum at approximately 10^{-1} mbar for at least 2 h to reduce ambient water and other atmospheric contaminants from the particles. The sample was then transferred to the glovebox and spread over a larger glass surface to allow good exposure of all particles to the glovebox atmosphere. The sample was kept in a constant atmosphere for at least 48 h to adsorb water, before it was packed inside the stainless steel sample holder (cleaned with isopropyl alcohol and heated to 200 °C to 300 °C under vacuum for at least 2 h). The sample holder was weighed before and after filling a new sample, then sealed with a fresh filter gasket and a blind fitting, and transferred through the airlock to be placed inside the volatiles extraction system.

The volatiles extraction system was evacuated for about 1 h prior to each test run, while the tubes were heated to 120 °C and the RGA was baked-out at 150 °C. At the beginning of the evacuation, before the

turbomolecular pump was activated, the system was purged with nitrogen for approximately 10 min. Prior to installation of the sample holder, the dosing valve was closed and the pressure in the lower section of the system was equalled with ambient using nitrogen to avoid ambient air to enter the system while replacing the old sample holder with the newly prepared one. After transfer to the volatiles extraction system, the sample holder was installed at the lower end of the vacuum tubing. The ceramic sample heater with thermocouple was then attached to the sample holder and connected to the power line. Finally, the prepared liquid nitrogen bath with the aluminium oxide insulation was installed and the sample was cooled down to -196 °C. After the sample temperature had stabilised for a couple of minutes, the dosing valve was opened to evacuate the lower section of the system. The RGA was turned on and its filament was activated once the pressure in the upper section of the system was $<10^{-4}$ mbar. During the remaining evacuation, a first mass spectrum was recorded from m/z 1 to m/z 200. After that, the RGA was switched to the pressure mode to track the partial pressures of selected species over time for the remainder of the experiment. The heater was activated when the pressure in the lower section reached values $<10^{-4}$ mbar. Once the final temperature of 800 °C was reached, the heater was deactivated and a second full mass spectrum was recorded with the RGA.

4.2.3 Test Results

A total of 72 test runs were performed over the course of several weeks and used for the evaluation presented in the following. During the experiments the partial pressures of selected atomic masses were recorded by the RGA in intervals of 3 s. This included m/z 2, 18, 28, 32, and 44, in order to track the following species that were found predominant in the gas mixture (major mass fragments are underlined):

- H_2O (peaks at m/z 16, 17, <u>18</u>, 19, 20), residual background of the vacuum system and volatile species in the sample, typically >70 % of the gas mixture in average over the entire process
- H_2 (peaks at m/z 1, <u>2</u>), residual background of the vacuum system, typically <10 % of the gas mixture in average over the entire process
- CO_2 (peaks at m/z 12, 16, 28, <u>44</u>, 45, 46), residual background of the vacuum system and volatile species in the sample, up to 25 % at maximum and typically <5 % in average over the entire process
- CO (peaks at m/z 12, 14, 16, <u>28</u>, 29, 30) or N_2 (peaks at m/z 14, <u>28</u>, 29), residual background of the vacuum system and volatile species in the sample, typically <5 % of the gas mixture in average over the entire process
- O_2 (peaks at m/z 16, <u>32</u>, 33, 34), residual background of the vacuum system, typically <2 % of the gas mixture in average over the entire process

Figure B-6 to Figure B-15 in the appendix show the results of all test runs summarised for each parameter combination. In all test runs no relation between time of storage in the glovebox and outgassing profile could be observed. This means that the minimum storage time of 48 h was enough to create equilibrium conditions for the water concentration in the sample, a conclusion that is supported by the results presented in chapter 4.1. Furthermore, it was noticed that for the third runs of each parameter combination, for which the lower pressure gauge was deactivated, the partial pressure curves of all species but H_2O were always lower than for the first two runs. As mentioned in section 4.2.1, this was anticipated due to the known interference between lower pressure gauge and RGA, and the RGA data were corrected accordingly during post-processing. Figure 4-11 shows an example of the partial pressure curves recorded during the experiment, with the full mass spectrum at selected times shown in Figure 4-12. Across all parameter combinations, partial pressure measurements can be divided into three distinct temperature-dependent phases, which are addressed in more detail in the following sections: An initial peak (peak A) in the temperature range from approximately -100 °C to -50 °C (phase 1), a broader feature (peak B) between approximately -50 °C and 300 °C (phase 2), and a pronounced wide peak (peak C) at temperatures above 300 °C (phase 3).

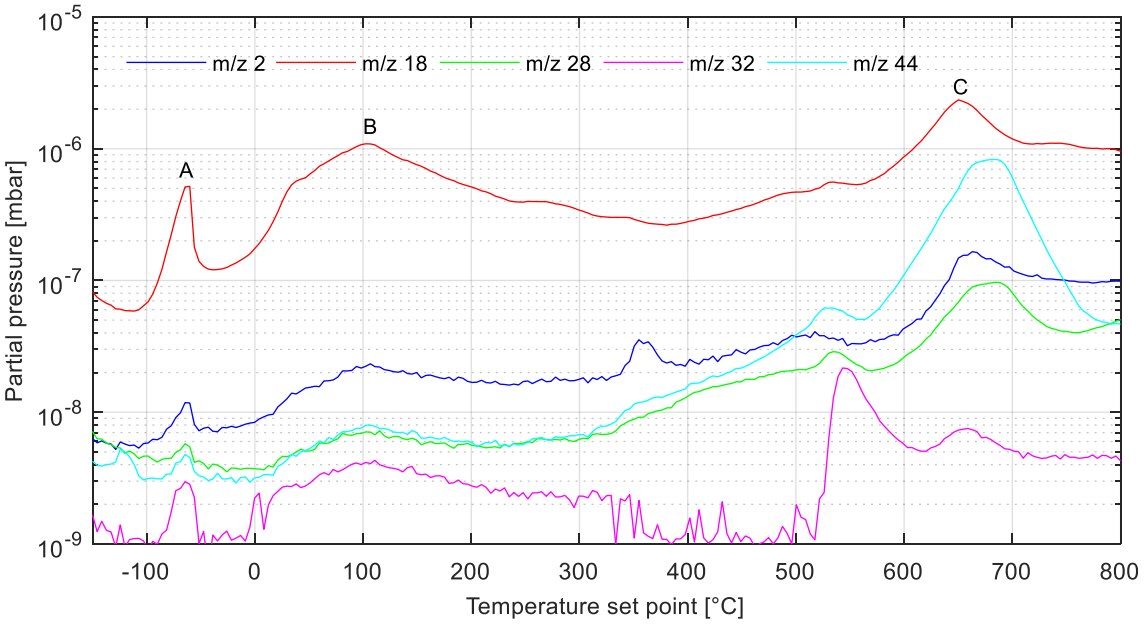

Figure 4-11: Exemplary partial pressure curves of selected species for the extraction of volatiles with 6 °C/min heating rate and a 33-36 mg, 70-80 µm, loose sample, conditioned at 30 % relative humidity

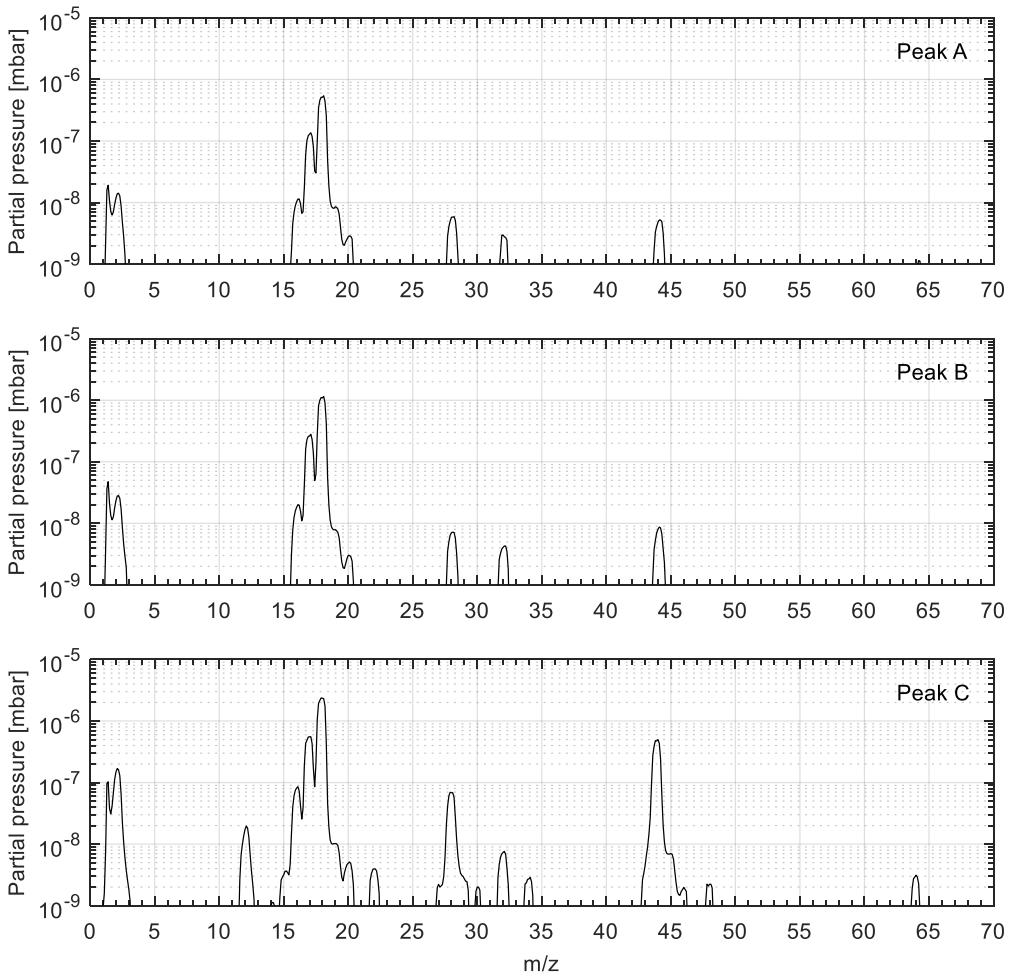

Figure 4-12: Exemplary mass spectra at selected outgassing peaks (see Figure 4-11) for the extraction of volatiles with 6 °C/min heating rate and a 33-36 mg, 70-80 µm, loose sample, conditioned at 30 % relative humidity

Phase 1: Temperature below -50 °C

The first significant peak in all outgassing curves (labelled 'A' in Figure 4-11) is attributed to loose bonds of atmospheric gases on the steel surface of the sample holder, as this feature is also visible in the reference test runs. It is noticeable that for the reference runs without sample, the initial outgassing happens later and with a larger amplitude (see for instance Figure 4-13). It is assumed that this is due to the larger exposed internal surface of the sample holder, which supports the theory that the initial peak originates from contamination of the sample holder rather than the sample. Because the reference curves do not show any other peaks besides a general increase of all partial pressures over temperature, all of the remaining peaks can be attributed to the sample. The initial desorption feature happens between -100 °C and -50 °C. However, the actual temperature at the upper part of the sample holder, which is not covered by the sample, is likely to be higher due to heat flowing down from the heated tubes. It is assumed that the contamination that causes this initial peak is residual gas from inside the glovebox. Although the glovebox was purged with nitrogen many times over the course of the experiments, smaller leaks and residuals cannot be completely removed. Other sources of contaminants can be ruled out, such as:

- Contamination in the volatiles extraction system: It is possible that the initial outgassing feature originates from the volatiles extraction system rather than the sample holder. A control run was conducted where an empty sample holder was heated twice from -190 °C to 0 °C. While in the first run the outgassing feature was clearly visible as for all other test runs, only a very minor peak (rise from $5 \cdot 10^{-8}$ mbar to $1 \cdot 10^{-7}$ mbar compared to a rise from $1 \cdot 10^{-7}$ mbar to $1 \cdot 10^{-6}$ mbar) was observed for water during the second run. All other observed species did not show any outgassing features. This leads to the conclusion that the peak observed for all other test runs must be attributed to the sample holder rather than the volatiles extraction system.
- Contamination of the filter gasket: The gaskets are cleaned by the supplier and packed in heat-sealed plastic sachets. It is not stated in the datasheets whether this is done in protective atmosphere or not. The gaskets were unpacked prior to installation on the sample holder for each test run. A separate control run with a gasket that was baked-out prior to use showed the same initial outgassing feature as the runs with untreated gaskets with only marginally lower amplitude. So did two other control runs where filterless gaskets were used.
- Contamination by ambient air during sample transfer from glovebox to vacuum system: For a short period the sample holder with filter gasket was exposed to ambient air in the laboratory, while its protective cap was removed and it was installed in the volatiles extraction system. The time of exposure typically was less than 3 s for all experiments. The volatiles extraction system was purged with nitrogen while it was opened to receive the sample holder and the purging was stopped just before the sample holder was actually installed. This procedure should in theory have reduced the risk of contamination through ambient air to a minimum. Even if some of the air constituents would have adsorbed on the gasket or inner surface of the sample holder, they should have been removed during evacuation of the system before the experiment started. Because the sample holder was cooled briefly before and longer after installation, there was a remaining risk of atmospheric contaminants to get trapped. However, a control run where cooling was not applied before the installation did not yield different results.

An additional explanation for the initial peak can be derived from Dyar, Hibbitts and Orlando (2010). They present a temperature programmed desorption measurement of water ice adsorbed on porous silicon and attribute the initial peak in the range of approximately -120 °C to -50 °C to the desorption of loosely bound multilayer (bulk) ice, rather than chemisorbed water that is released at higher temperatures. However, no additional details of this study are available, so this interpretation might not be applicable for the present experiments. It is also unlikely that the different adsorption types are distinguishable in the presented experiments, because presumably the heat and mass transport affect the outgassing curves to a stronger extent.

Phase 2: Temperature between -50 °C and 300 °C

After the initial outgassing, a second broad outgassing feature with several peaks occurs until about 200 °C to 300 °C. This is attributed to the volatile content of the sample, or all loosely adsorbed species respectively. The differences in the outgassing pressure are caused by different amounts of adsorbates and different desorption and diffusion characteristics. For large amounts of volatiles, as for the saturated sample and the sample with a mass of 66 mg to 72 mg, the first outgassing peak of the sample holder merges with this second feature (labelled 'B' in Figure 4-11). A more detailed analysis of the different outgassing features and their correlation with the different test parameters is provided in the following, with a direct comparison of selected test runs for different boundary conditions. To maintain a good readability of the following graphs, only one run for each parameter combination is represented. A certain variation within all test runs of one parameter combination as depicted in Figure B-6 to Figure B-15 in the appendix therefore needs to be considered.

Initial water concentration

The experiments showed that the different humidity levels during sample conditioning did not produce significant differences in the outgassing profiles, as illustrated in Figure 4-13. For the relative humidity levels of 30 %, 50 %, and 70 %, the peaks are of similar amplitude and at similar temperatures. While the curves deviate only little in general, they are almost identical at temperatures above 300 °C. It is therefore concluded that the outgassing of loosely bound water ends at 300 °C and further outgassing cannot be attributed to the different sample conditioning procedures. The samples stored at relative humilities of 10 % and 30 % show a higher initial peak of the sample holder outgassing than the other samples presented here. However, as it can be seen from Figure B-8, there is also strong a variation of the amplitude of this peak within the data for the samples conditioned at 30 % relative humidity. A correlation with sample mass, sample batch, or storage time could not be found. It is assumed that this variation comes from slight differences in the sample filling process which affect the amount of volatiles that remain sticking on the internal surface of the holder.

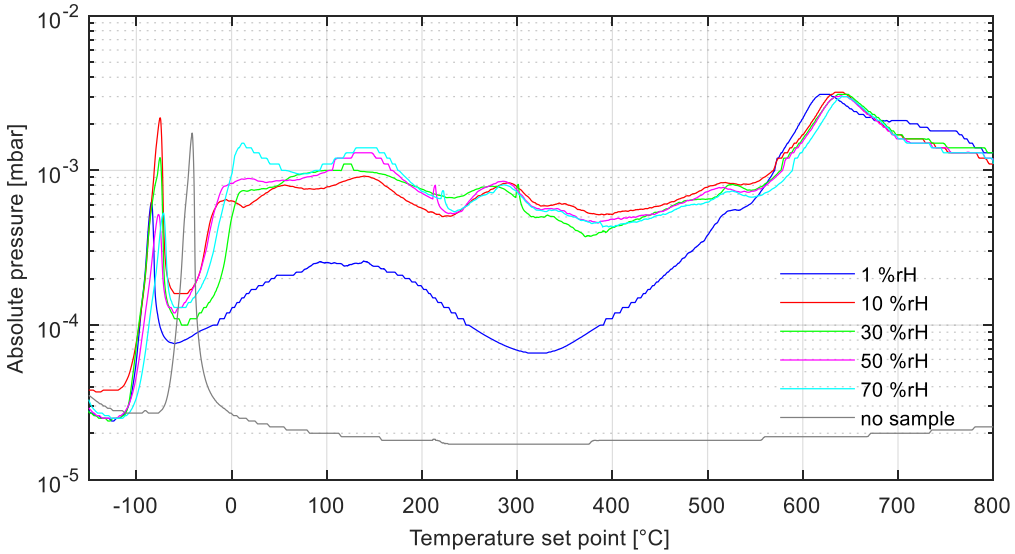

Figure 4-13: Comparison of absolute pressures (main constituent is water) near the sample for samples conditioned at different relative humidity levels

Between -50 °C and 200 °C only small differences in the outgassing pressures can be observed (Figure 4-13). After the initial sharp peak there is a rapid increase in pressure starting at -50 °C and ending around 0 °C at a pressure level that is up to one order of magnitude higher. A second distinct pressure rise happens around 50 °C to 100 °C until the pressure decreases again at 140 °C. For the samples with a relative humidity above 10 %, the curves are almost equal. Although a minimal correlation between increasing humidity level and increasing pressure might be possible, this trend is not statistically significant enough to support such a conclusion. Because the curve for the samples conditioned at 1 % relative humidity results a

much lower pressure than the rest, which is still above the pressure for an empty sample holder, it is assumed that the highest adsorption of water happens in the relative humidity range below 10 %. This result is in accordance with the preparatory tests on water adsorption described in chapter 4.1. However, the preparatory tests predicted a further increase in the amount of adsorbed water above 10 % relative humidity, which cannot be clearly identified in the results presented here.

Particle size

The outgassing of the 100 µm to 110 µm sample fraction generally shows a lower amplitude than for the smaller fraction (Figure 4-14), which was expected due to the smaller specific surface area. The curves of the larger fraction also show more pronounced peaks and more rapid pressure drops after each peak. This could be an effect of the higher gas diffusivity (higher porosity) of the sample, in a way that released volatiles are transported out of the sample faster. The most significant difference in the measured partial pressures is a big and relatively broad peak of m/z 2 around 450 °C (Figure B-12). This peak can also be observed in the other measurements of the sample conditioned at 30 % relative humidity, but is much smaller and occurs at lower temperatures around 350 °C (Figure B-8). A possible cause is the decomposition of minerals, which indicates that there is a difference in the mineral composition of both fractions of NU-LHT-2M. Another indicator for this is the shape of the m/z 44 and m/z 28 peaks between 600 °C and 700 °C. While for the smaller fraction there is a big feature with two small spikes of similar amplitude, there is a clear distinction of two different strong peaks for the larger fraction. Furthermore the absolute pressure continues to increase from 700 °C on, which could also be an indicator for a different mineral composition of the larger fraction.

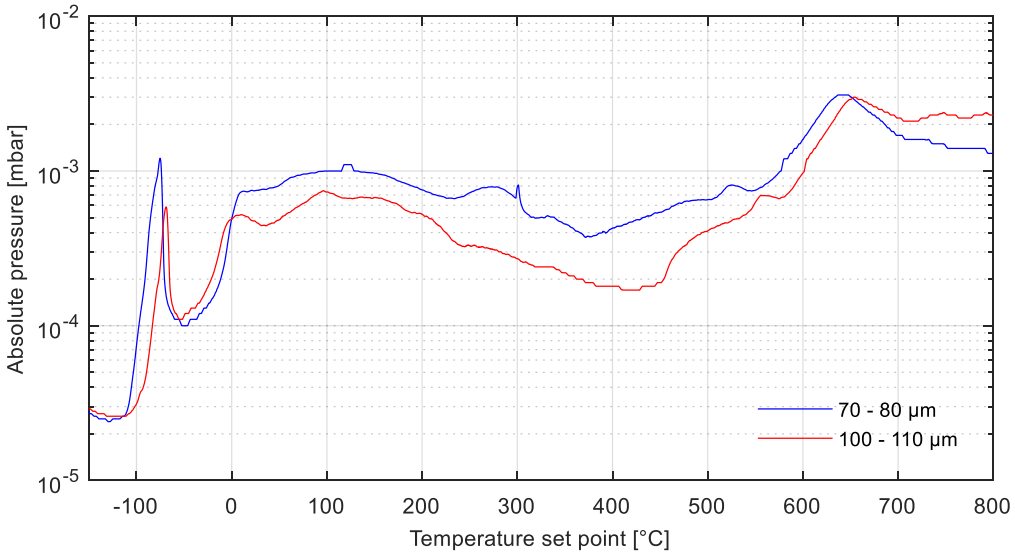

Figure 4-14: Comparison of absolute pressures near the sample for different particle sizes

Bulk density

The filling height of the compacted samples was determined by inserting a metal rod into the sample holder after compaction and marking the upper boundary on the rod. This returned a sample height of approximately 3 mm, which is two thirds of the value found for loosely poured sample. Subsequently, for a loose bulk density of 1.3 g/cm³ as determined before, the compacted density is approximately 2 g/cm³, which is close to the maximum bulk density of NU-LHT-2M determined by Zeng, He and Wilkinson (2010).

The outgassing profile of the compacted sample generally shows similar effects as the larger fraction described before with more pronounced peaks (Figure 4-15). However, the pressure level is comparable to the loose sample, presumably because the specific surface area of the particles is similar. In conclusion no clear effect of the increased bulk density is visible in the pressure curves, indicating that both heat and mass transfer through the sample are not heavily influenced by higher compaction. From the theoretical results presented in chapter 3.2, a 50 % lower gas diffusivity was predicted for this scenario. However, taking into

account the errors in determining the bulk densities, this is a worst case assumption. If, at all, a delay in the outgassing features can be observed, it is for the heavier species. From the partial pressures depicted in Figure B-13 it can be seen that m/z 28 and m/z 44 have a sharper peak at 680 °C and 685 °C respectively, which is 10 °C to 20 °C higher (or later) than for the loose sample (Figure B-8).

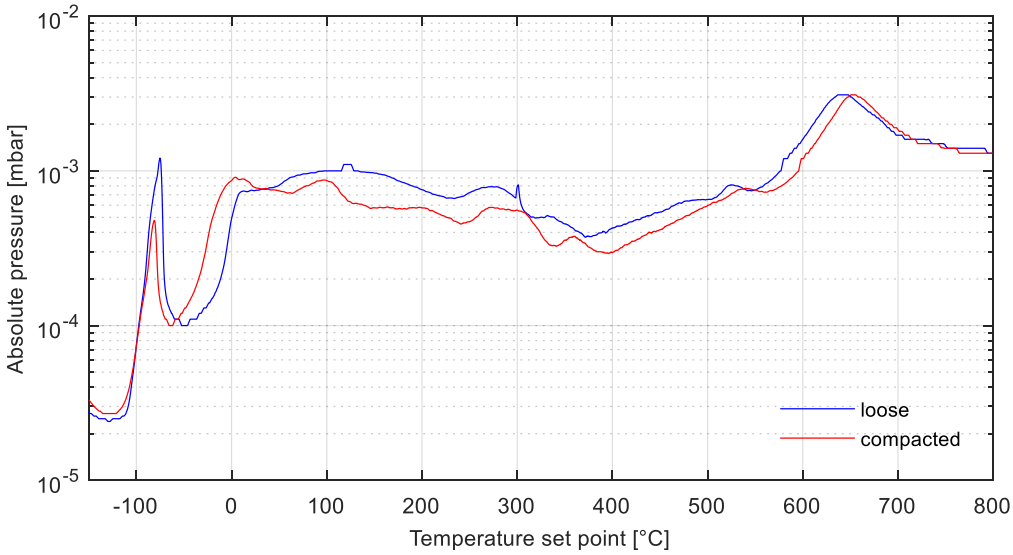

Figure 4-15: Comparison of absolute pressures near the sample for different bulk densities

Sample size

As expected, a larger sample quantity leads to a generally higher amplitude (up to two times) of the partial pressure of all species (Figure B-14) and hence the absolute pressure (Figure 4-16). For the major peaks of m/z 28 and m/z 44 there is a delay that is comparable to the one observed for the compacted sample. This is reasonable, since the distance for diffusion through the sample is twice as long. Regarding the first peak of all species a significant shift to lower temperatures is visible. It is assumed that the outgassing of the sample holder happens more rapidly because the majority of the internal surfaces is covered by the larger sample (filling height 9 mm instead of 4.5 mm). Only the uppermost part of the sample holder therefore holds adsorbed species that are exposed to vacuum and, moreover, the heat flowing down from the crosspiece. These species are desorbed just before the sample holder reaches -150 °C and therefore the initial peak is not visible in the presented pressure diagrams but only in the raw data which extends down to -190 °C.

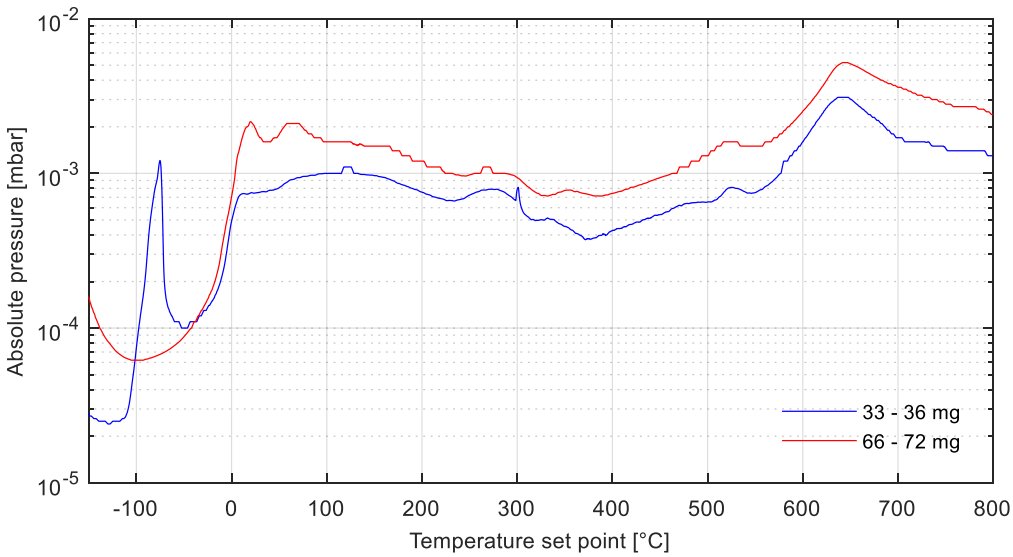

Figure 4-16: Comparison of absolute pressures near the sample for different sample sizes

Heating mode

A smaller heating rate was tested on the samples in order to investigate if this has any effect on the heat transfer into the sample or the diffusion of volatiles out of the sample. Figure 4-17 shows the resulting outgassing curve for a heating rate of 6 °C/min and 4 °C/min. The biggest difference is a significantly lower pressure over the course of the second outgassing phase for a heating rate of 4 °C/min. This could be an indicator for an improved gas transport, similar to the effect of larger particle size. It could also mean that heat is introduced more uniformly into the sample, triggering the desorption over a larger fraction of the sample. The effect of reduced pressure for a reduced heating rate was predicted in a similar way by the simulations presented in chapter 3.2.

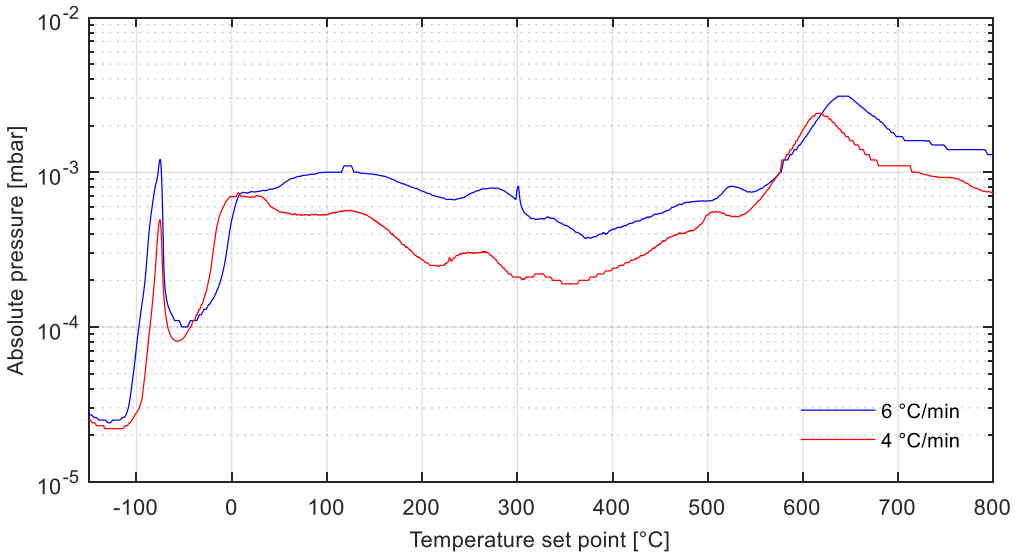

Figure 4-17: Comparison of absolute pressures near the sample for different heating modes

Volatiles yield

To evaluate the effectiveness of the sample preparation procedure, it is helpful to quantify the total amount of released volatiles. This was done using the partial pressures of all monitored species and computing the outgassing rate while assuming a continuous evacuation. The pump rate q_{pump} of the turbomolecular pump used in the experiments is 65 l/s for N_2, 60 l/s for Ar, 55 l/s for He, and 49 l/s for H_2 (Leybold GmbH, 2009). It is assumed that these values are constant at high vacuum, or the pressures measured in the RGA section of the vacuum system respectively. With the ideal gas law the amount of species removed over time $n_i(t)$ can be calculated as follows, if the gas volume is replaced with a constant pump rate:

$$n_i(t) = p_i(t) \cdot \frac{q_{pump}}{R \cdot T} \tag{4-1}$$

The partial pressures p_i are known from the RGA measurement, the temperature of the gas is assumed to be 120 °C after travelling through the heated pipes to the RGA, and the pumping speed is assumed to be constant (65 l/s) for all gases. After integrating $n_i(t)$ over time the total mass m_i of each species can be calculated by multiplication with the respective molar mass M_i:

$$m_i = M_i \int n_i(t) \tag{4-2}$$

This approach can only yield indicative values for the gas masses, since it implies major simplifications, such as a pump rate that is constant over time and uniform for all species, and the approximated temperature. However, it suffices a relative comparison of gas masses and a qualitative conclusion about the effectiveness of the sample preparation procedure. Figure B-16 to Figure B-25 (see appendix) show the calculated masses for m/z 2, 18, 28, 32, and 44 from the experiments. For each measurement the data of the corresponding

reference runs (background signal) was subtracted from the data with samples to get a net mass for the volatiles that originate from the sample. The partial pressures were integrated over the time period where the temperature set point was between -150 °C and 300 °C to account for loosely bound volatiles only and exclude gas released from mineral decomposition at higher temperatures. For the samples with 70 µm to 80 µm particle fraction, conditioned at a relative humidity between 10 % and 70 %, the mass of volatile water (m/z 18 only) released from the sample amounts to values between 0.2 wt% and 0.3 wt%. The mass of the remaining volatile species is about one order of magnitude less. For the compacted sample and the one with higher mass, the water yield up to 300 °C is slightly less (Figure B-23 and Figure B-24). This could be explained with a lower effective diffusivity, which leads to a later outgassing. For the 100 µm to 110 µm particle fraction the water yield is significantly less, between 0.1 wt% and 0.2 wt%, which can be explained with the smaller specific surface area of the particles and hence less adsorbate. Because only m/z 18 was considered for this calculation, the actual mass of water including all other mass fragments is assumed to be higher. Taking into account that m/z 18 makes up 74 % of the fragments of water, the total masses of water would be approximately 1.35 times higher than the aforementioned values.

As shown in Table C-1, the equivalent amount of water for a monolayer on comparable samples is in the range of 0.02 wt% to 0.04 wt%, or about factor ten lower than the values found in this study. This leads to the conclusion that in the presented experiments the adsorbed water was present in the form of multilayers. This suggestion is supported by the results of the preparatory tests on adsorption, described in chapter 4.1. Given the initially very low temperature of the sample, the formation of amorphous solid water is reasonable (compare chapter 2.1.1). In this context it is noteworthy that Goering et al. (2008) found three-dimensional water clusters and porous condensed water adsorbed on the similar analogue material JSC-1A. It was speculated in this study that the micron-sized sample particles act as nucleation sites for the transition to crystalline water.

The saturated sample was mixed with 15 wt% water as described before. However, the water yield calculated from the partial pressure only amounts to 6 wt% at maximum (about 8 wt% considering the remaining mass fragments of water). Furthermore, there is a big difference between the individual test runs (Figure B-21). The saturated sample was divided into three subsamples after mixture with distilled water in the glovebox. The subsamples were placed into separate glasses with an internal volume of approximately 70 ml, sealed with screw caps, and left in the glovebox for approximately 66 h. After that a 33 mg to 36 mg portion was taken from each subsample on three subsequent days for one test run per day. On the fourth day a second portion was taken from the first subsample to check if the water content within one sample changes over time. From Figure B-21 it becomes evident that there was no such variation, since the water masses for test run 1 and 4 are 6.2 wt% and 6.3 wt% respectively. Test run 2 and 3 however yielded only 3.4 wt% and 0.4 wt% water respectively. Presumably this strong variation can mainly be attributed to an inhomogeneous mixture of the sample. Another source of error is the atmosphere in the glasses, which can take up water from the sample. At saturation the internal gas volume of the glasses can take up about 2 mg of water under the given conditions (25 °C in the glovebox, water saturation pressure of 3161 Pa, as calculated with the suggested Magnus equation from Alduchov and Eskridge (1996)). For all test runs this is around 3 wt% of the sample, which partly explains the deviation from the initially measured 15 wt%. Depending on how quickly water desorbs from the sample into the glovebox atmosphere between mixing and enclosing the subsamples in the glasses, a certain loss of water into the glovebox atmosphere can also not be ruled out.

Phase 3: Temperature above 300 °C

For temperatures above 300 °C the partial pressures of the measured species show a very similar trend for all parameter variations. It is concluded that from this point on, the outgassing is caused by mineral decomposition rather than desorption of loosely adsorbed species. This is consistent with studies of Street et al. (2010), ten Kate et al. (2010), and Glavin et al. (2012), who measured a release of CO_2, SO_2, H_2S, and S between 300 °C and 600 °C, and attributed this to the breakdown of carbonate minerals and restructuring of the mineral lattice. Street et al. (2010) state that there is known hydrothermal alteration of the source material of the simulant NU-LHT-2M, which is thought to be the cause for the release of H_2O at higher

temperatures. Moreover, the same study found that there are two distinct peaks in the H_2O curve at 355 °C and 490 °C for anorthosite from the Stillwater mine, one of the main mineral constituents of NU-LHT-2M.

Around 550 °C, a significant peak in the m/z 32 signal was detected. A comparison with m/z 34 and m/z 64, which are the major fragments of H_2S (peaks at m/z 1, 32, 33, 34, 35, 36) and SO_2 (peaks at m/z 16, 24, 32, 48, 50, 64, 65, 66) confirmed the presence of mainly H_2S (Figure 4-18). While m/z 34 is also a fragment of oxygen, its relative abundance in the measured mass spectrum is much higher than to be expected for oxygen (O_2 fragments are 89 % m/z 32 and only <1 % m/z 34). Its second major fragment, m/z 16, follows much more the curves of m/z 18 and m/z 44 instead of the other oxygen fragments, suggesting that there is actually no significant amount of oxygen present. It is therefore concluded that m/z 34 is an indicator for species containing sulphur, mainly H_2S, in the gas mixture. The presence of SO_2 and H_2S was also observed by similar volatiles extraction studies (ten Kate *et al.*, 2010). A source of sulphur could possibly be the mineral pyrite (FeS_2), which is present in NU-LHT-2M. In lunar regolith, sulphur can be found in the form of the mineral troilite (FeS). Another explanation is alteration of the feedstock of NU-LHT-2M. An additional evidence for the decomposition of pyrite to H_2S is the fact that the hydrogen partial pressure drops at the same time the H_2S partial pressure rises. This could be an indicator for hydrogen reduction of pyrite, which is a well-known process (e.g. Lambert, Simkovich and Walker, 1998). Sulphur is thermally released and diffuses through the FeS_2 layer to the particle surface, where it is removed by hydrogen. This removal by hydrogen is faster than the mere desorption of sulphur and hence the overall reduction is more rapid when hydrogen is present.

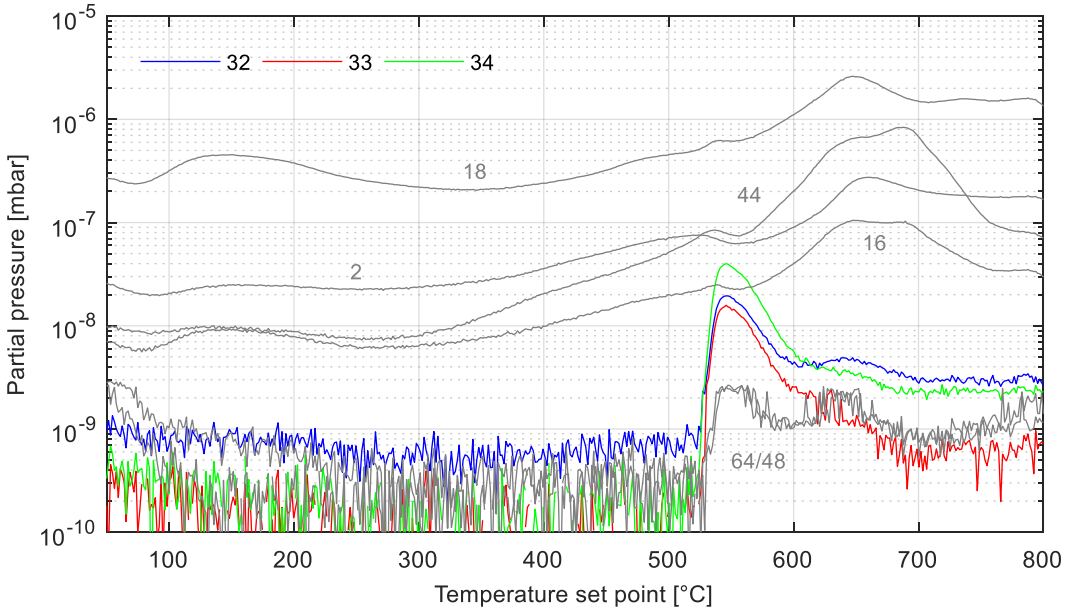

Figure 4-18: Evidence for the decomposition of sulphur-bearing minerals (Numbers indicate the m/z ratio of the depicted species, major fragments of H_2S are shown in colour)

A possible source of carbon, from which the strong carbon dioxide signal around 650 °C originates, could be calcite ($CaCO_3$), which was detected as one of the trace minerals with <0.3 vol% in the fractions <150 µm of NU-LHT-2M (Rickman and Lowers, 2012). Although its occurrence is very low, the particle area of calcite is relatively large, especially in the fraction from 75 µm to 150 µm. The origin of calcite in NU-LHT-2M is assumed to be alteration of the source material. Personal communication with D. Rickman, NASA‘s civil servant responsible for the regolith simulant development, supported this conclusion. Since the source material had to be hand-picked by geologists from a diverse feedstock in the Stillwater mine, little alteration and ‘non-lunar’ constituents in the final simulant cannot be ruled out. Separate test runs were performed with samples that were washed with distilled water and hydrochloric acid (HCl) in order to remove possible contamination or carbonates as a source of carbon dioxide. Figure 4-19 depicts the partial pressures of

relevant major fragments for an untreated sample in comparison with the H_2O-washed and HCl-washed samples.

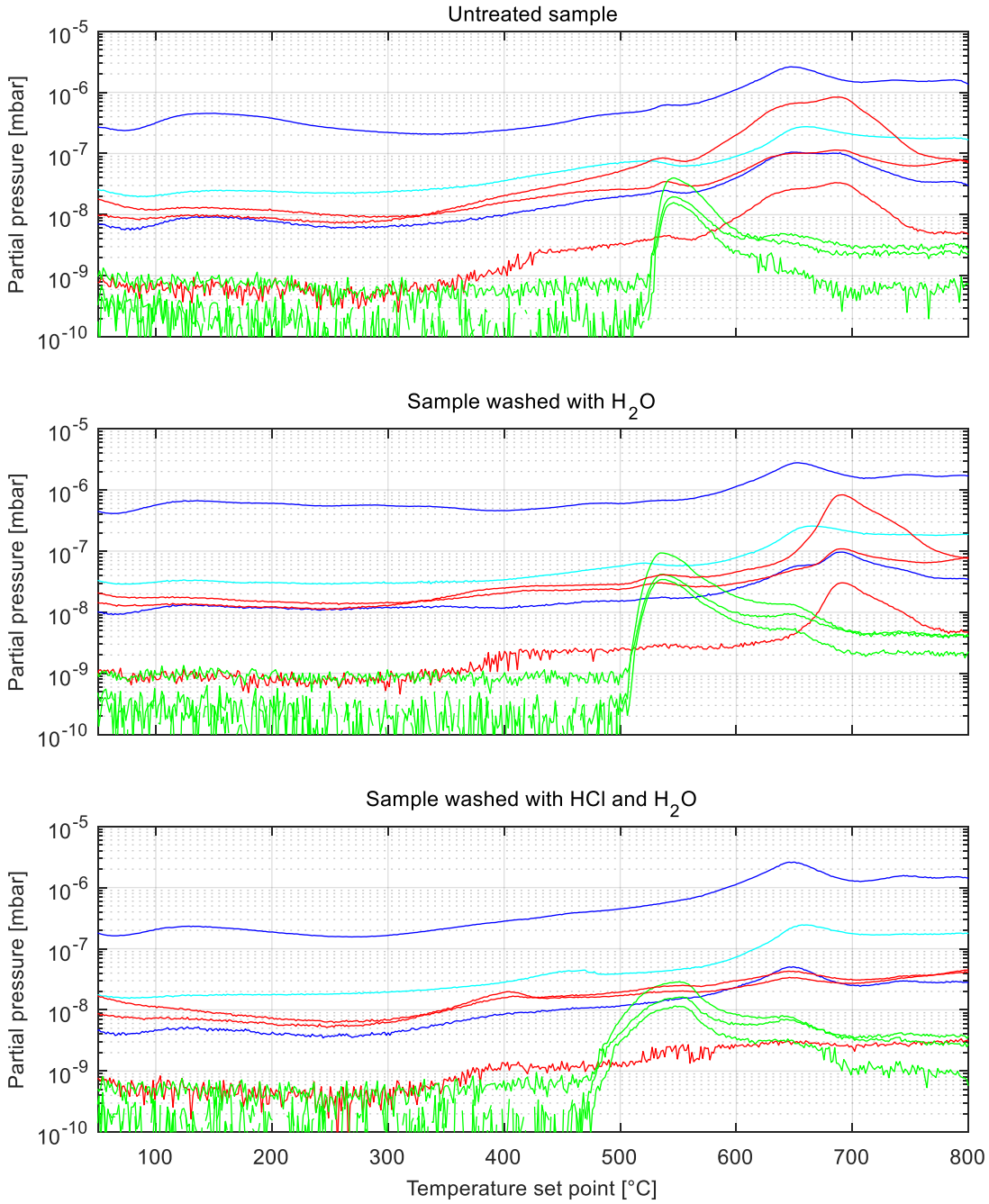

Figure 4-19: Effect of different sample treatments on the outgassing at higher temperatures, including washing with distilled water and hydrochloric acid. Selected species fragments are shown: CO_2 (red curve with m/z 12, 28, 44), H_2O (blue curve with m/z 16, 18), H_2S (green curve with m/z 32, 33, 34), and H_2 (cyan curve with m/z 2).

In the case of carbon dioxide it is evident that the HCl-wash removes nearly all of the carbon sources. However, a simple H_2O-wash also has an effect on the carbon dioxide outgassing, where the first major peak around 650 °C (which coincides with the major peak of water) is removed. Two explanations for the reduction of the carbon dioxide outgassing are suggested: a) removal of organic contamination, and b) removal of a mineral source of carbon, most likely calcite. It is presumed that most of the effect originates from the removal of carbonates, most effectively through treatment with HCl. In the case of the H_2O-wash it

might be that some of the very fine particle fractions were still present after sieving and could only be removed with the wash. Although care was taken regarding the latter (the water was pipetted from the mixture after the regolith had settled), it cannot be ruled out that some of the fine fractions were lost. An additional mixture of water and regolith was prepared to further investigate this effect. Figure 4-20 shows the mixture after the regolith had settled at the bottom of the glass container. The clouded surface of the water is clearly visible and indicates that fine-grained particles accumulated there. Dust and other environmental contamination can be ruled out because the container was thoroughly cleaned and closed with a screw cap after filling the mixture of regolith and water. The particles that were accumulated at the surface of the water were pipetted, dried, and investigated with a microscope. A large number of particles with diameter <5 µm, either single or in agglomerates, was found as depicted in Figure 4-20. The remaining regolith without these fine particles was also subjected to the volatiles extraction procedure, which produced essentially the same curve as shown in Figure 4-19 for the H_2O-washed sample. This strongly supports the hypothesis that the first carbon dioxide peak at 650 °C is caused by very fine-grained particles. This finding also leads to the conclusion that the sieving process was not ideal and that the sample fractions used in all experiments presented above probably contained some of the unwanted smaller fractions.

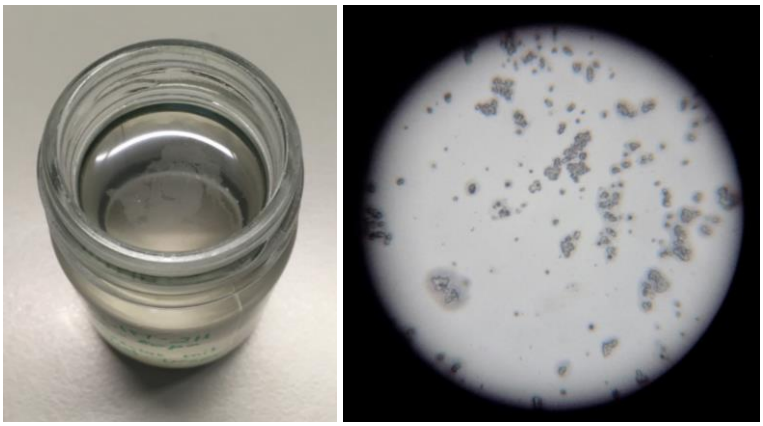

Figure 4-20: Mixture of distilled water with the 70 µm to 80 µm fraction of NU-LHT-2M with very fine-grained particles clouding the water surface (left) and microscopic image of the dried particles collected from the water surface (right, particle diameters are <5 µm)

From Figure 4-19 another apparent difference is visible in the partial pressures of the major water fragments. While there is a significant pressure decrease after the first outgassing feature at about 200 °C, the pressure remains nearly constant for the H_2O-washed sample until it matches the curve of the untreated sample above 450 °C. The HCl-washed sample shows a similarly shaped, but less pronounced pressure decrease as the untreated sample. Although the samples were all carefully dried and baked-out in vacuum, one possible explanation for the higher water abundance is that small amounts of water remained inside the pores of the regolith after washing.

4.2.4 Thermal Analysis

As pointed out in the previous chapters, it can be expected that the actual temperatures in the sample deviate from the measured temperature at the outside wall of the sample holder. This has to be taken into consideration when interpreting the previously presented outgassing curves, in particular when matching the release of the individual species to a certain temperature. A thermal model of the sample holder was therefore created to estimate the difference between temperature measured by the thermocouple that is attached to the outside of the sample holder and the temperature distribution within the sample.

The temperature at the location of the thermocouple was programmed to follow a ramp of 6 °C/min. The temperature of the lower crosspiece was ramped up from 150 °C to 190 °C over the test duration, as this temperature progression was measured with a separate thermocouple during test. The thermal conductivity of NU-LHT-2M according to chapter 2.2.4 was applied to the sample volume, while the gas pressure was

held constant at 10^{-5} mbar. Figure 4-21 shows the resulting deviation of minimum, maximum, and average sample temperature from the temperature set point (temperature of the thermocouple). At the beginning the thermal inertia of the sample leads to a large thermal gradient of up to approximately 100 °C at around 0 °C set point. The positive deviation of the maximum sample temperature is caused by radiation from the warmer upper part of the sample holder. Although the thermal gradient across the sample is then continuously reduced over time, a permanent discrepancy of approximately 30 °C to 40 °C between average sample temperature and set point remains. Near a set point temperature of 250 °C, the radiative heat loss from the sample surface and the external surfaces of the sample holder lead to an even higher temperate gradient across the sample, which further increases and reaches a maximum of approximately 150 °C at the end of the heating process.

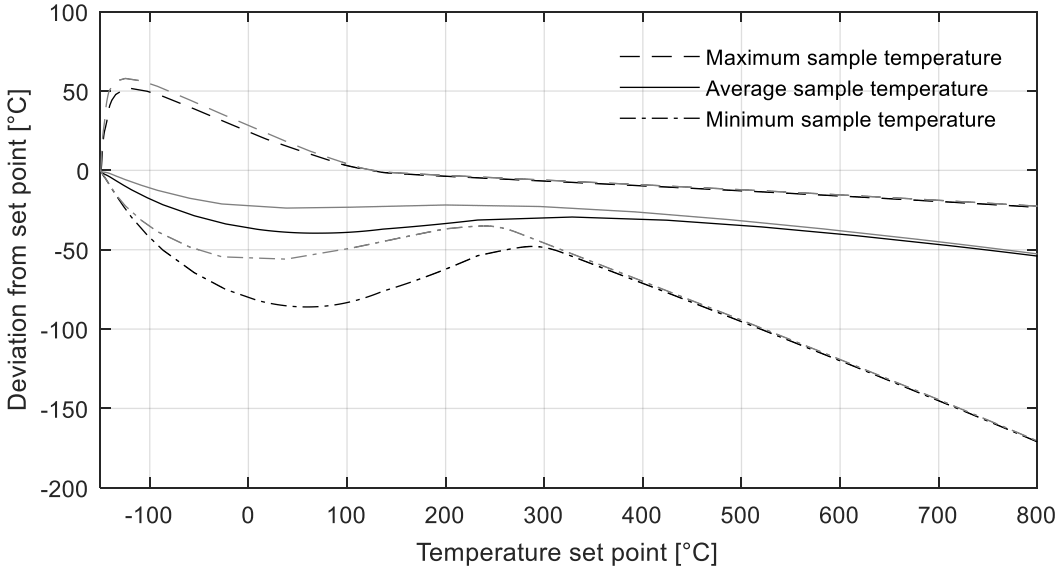

Figure 4-21: Deviation of sample temperatures from the set point for a heating rate of 6 °C/min (black) and 4 °C/min (grey)

As a result from this thermal analysis, the previously described outgassing features observed during the experiments need to be matched to temperatures that are lower than the set point temperature. Over the entire temperature range, the sample is in average about 35 °C lower than the set point. It was suspected that a slower heating rate would yield a more uniform heating of the sample because there is more time to overcome its thermal inertia. A separate simulation with a heating rate of 4 °C/min resulted in the grey curves depicted in Figure 4-21. In fact the average sample temperature is significantly closer to the set point, especially during the first half of the heating process. A more uniform temperature distribution enables a faster gas transport, which could explain the lower gas pressure and the slightly shifted outgassing curve in Figure 4-17. This conclusion is also in accordance with the simulations presented in chapter 3.2

5 Experimental Reduction with Hydrogen

In conjunction with the volatiles extraction experiments described in the previous chapter, the same experimental setup was used to demonstrate the feasibility of reducing lunar regolith analogues by using hydrogen as a reducing agent. The target specifically was to show that this chemical reduction can be done with an instrument configuration similar to ProSPA, which was not originally developed for that purpose. This circumstance is mainly highlighted by the configuration and position of the oven, which neither allows the reactant to pass through the sample, nor does it expose the sample to the reactant in any efficient way (compare chapter 2.4 for a description of the chemical process). The experiments presented here aimed at evaluating different operational modes to find the best feasible way of initiating the reaction and producing measurable results.

The setup of the volatiles extraction experiments described in the previous chapter 4.2.1 was slightly modified to enable the hydrogen reduction experiments. A second gas feed (also visible in Figure 4-5 and Figure 4-4) was added to the lower section of the system to allow the purging of the sample with hydrogen of purity 5.0. The sample cooling system was removed because for hydrogen reduction no cooling below ambient temperature was required. While for the first set of experiments (continuous gas flow) the rest of the setup was left unchanged, the second and third test series (semibatch processes) required the removal of the lower PTR 90 pressure gauge and installation of a blind flange at the right side of the lower crosspiece instead.

5.1 Test Plan and Procedure

The sample preparation was comparable with the process established for the volatiles extraction experiments as described in chapter 4.2.2. Samples were baked-out, stored in the glovebox for at least 48 h, and packed into the cleaned and baked-out sample container prior to transfer to the extraction facility. The relative humidity in the glovebox was limited to 1 % to reduce contamination with water. The samples used for the reduction with hydrogen were NU-LHT-2M in its standard particle size distribution and ilmenite ($FeTiO_3$, 93 % to 96 % pure) from the company Kenmare Moma Processing Ltd. with a mean particle size of 174 µm (Kenmare Moma Processing Ltd., 2017). A chemical analysis of both materials is provided in Table C-2 in the appendix, a microscope image of the ilmenite sample is shown in Figure 5-1.

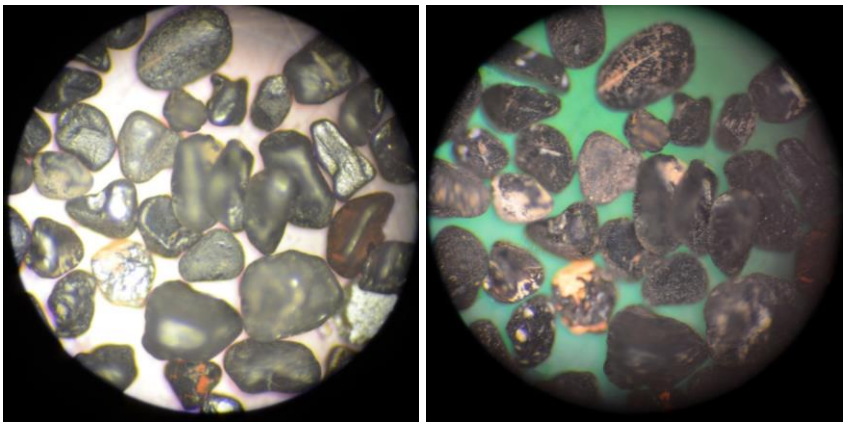

Figure 5-1: Microscope images with different filters of the ilmenite sample used for the hydrogen reduction experiments

The sample mass for all experiments was 33 mg to 36 mg. Prior to all experiments and after installation in the volatiles extraction system, the sample was heated to 800 °C in one step and held at that temperature for 30 min to release all volatile compounds. It was then left in the evacuated system to cool down to temperatures below 100 °C. Three different operational modes were investigated in the course of this study to obtain an insight into their feasibility and efficiency:

1. Continuous gas flow:

   The system was continuously purged with hydrogen and the manual valves were adjusted so that the pressure did not exceed 10^{-4} mbar in the upper section and 10^{1} mbar in the lower section. The sample was then heated to 800 °C and the evolving gas species were continuously monitored by the RGA with an analogue scan from m/z 0 to m/z 50. The temperature was kept at 800 °C for at least 3 h, or until the partial pressures of the species dropped below their initial value.

2. Semibatch process with preheating:

   The dosing valve between upper and lower section of the system was closed and hydrogen was introduced at an absolute pressure of approximately 1 bar. The purge valve was closed and the sample heated to 800 °C and held at this temperature for 30 min. With the oversupply of hydrogen it was assumed that the equilibrium reaction would have enough time to produce a significant amount of water. While the heating continued, the dosing valve was then opened so that the pressure in the upper section was approximately $1 \cdot 10^{-5}$ mbar and the gaseous reaction products leaking to the upper section were continuously analysed by the RGA as described before. To avoid damage of the lower pressure gauge caused by this relatively dense gas at high temperature, it was removed for this operational mode. This also helped to reduce leakage and analysis time and potential contamination of the reaction products.

3. Semibatch process without preheating:

   Identical to the above, the dosing valve was closed and hydrogen introduced at 1 bar. After closing the purge valve, the dosing valve was opened and the leaking gas was analysed. After a couple of mass scans were recorded by the RGA, the heating of the sample was started. This was done in order to obtain more distinguishable changes in partial pressure while monitoring the gases as they actually evolve from the reaction and therefore enable a clear comparison of the partial pressures before and after reaction.

5.2 Test Results

For the hydrogen reduction experiments, a total of 27 test runs were performed. Figure B-26 to Figure B-35 in the appendix show the results of all three modes for the ilmenite and NU-LHT-2M samples, as well as for one reference run each with an empty sample holder. For better comparability of the different modes, selected pressures for all three samples are depicted in Figure 5-2 to Figure 5-4. A plot of the ratio m/z 18 to m/z 2 is provided to illustrate the relation between the product water and the reactant hydrogen for an expected reaction according to equation (2-54), as introduced in chapter 2.4. The absolute pressures presented in the following plots were corrected for hydrogen as the main constituent in the gas mixture, according to the PTR 90 manual (Leybold GmbH, 2016).

Continuous gas flow

For the continuous gas flow process with ilmenite a clear increase in the partial pressures of m/z 18, 17, and 16 is visible in the first 60 min (Figure B-26) as the H_2O/H_2 ratio climbs from about 0.3 % up to 2 % (Figure 5-2). The pressures of m/z 2 and m/z 44 stay nearly constant over the entire process, while the pressures of m/z 28 and m/z 32 increase. This behaviour was not observed in the test runs with NU-LHT-2M and the blank run. A check of the mass scan revealed that the same increasing trend was not only visible for m/z 28 and m/z 32, but also for m/z 14 and m/z 40, which could be an indicator for a leak or trapped atmospheric gas in the hydrogen feed line. The distinct rise in the partial pressures of all water fragments suggest that water was produced by a chemical reaction. However, for the NU-LHT-2M sample no such clear evidence can be seen from the RGA data (Figure B-27). The same applies to the reference blank run, indicating that

no significant amount of water was produced in both runs (Figure B-28). For the NU-LHT-2M sample and the blank run all partial pressures show a very similar behaviour, except for m/z 32. The latter experiences a strong increase in the first 30 min for NU-LHT-2M, or 60 min for the blank run respectively, before it decreases again. The fact that this behaviour is also visible for the empty sample holder leads to the conclusion that m/z 32 originates from the vacuum system or the hydrogen feed. Because no such behaviour is seen for the other operational modes (see Figure B-29 to Figure B-35), where the purge gas valve is closed, it is suggested that the hydrogen feed line causes the increase in m/z 32. This most likely is due to contamination rather than leakage, since other atmospheric gases measured by the RGA (for instance m/z 28 and m/z 40) show a different trend.

Generally the continuous gas flow mode was very difficult to operate manually, since the purge gas valve and the dosing valve had to be adjusted very carefully. Small mechanical or thermal disturbances caused the valves to move, which affected the continuity of the gas flow and subsequently led to gas pressures in the sample section that were above the detection limit of the PTR 90 pressure gauge for hydrogen.

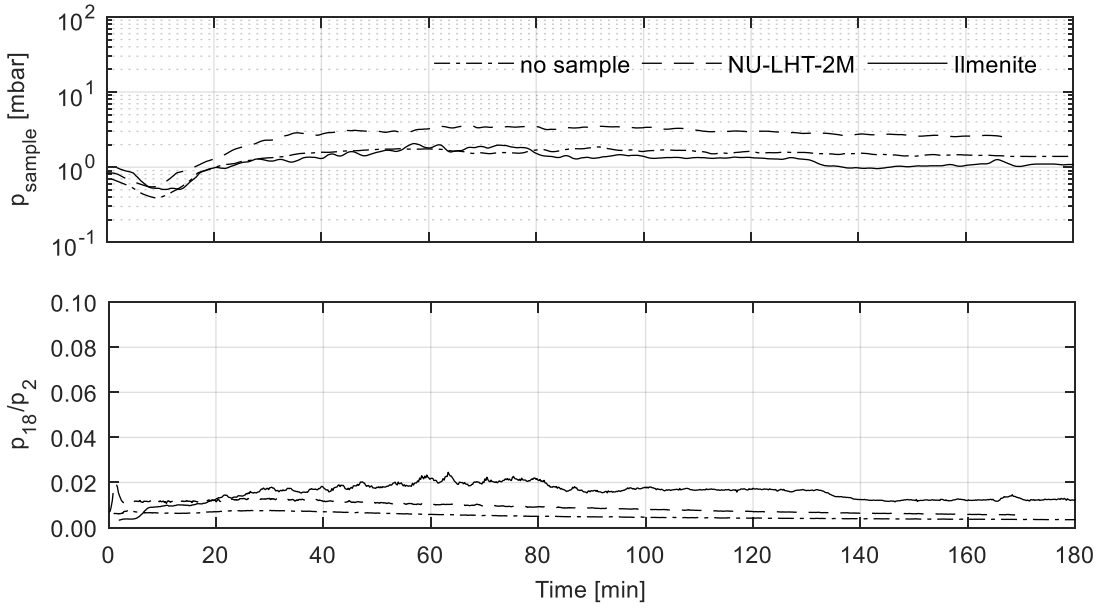

Figure 5-2: Gas pressures for the continuous gas flow process (absolute pressure was corrected for hydrogen)

Semibatch process with preheating

For the semibatch process with 30 min preheating, the partial pressures before and after opening the dosing valve need to be compared (Figure 5-3). There is a short period of approximately 20 s directly after the valve is opened, when the gas flow stabilises and all partial pressures increase slightly. In the case of ilmenite, a steep rise in the partial pressure of m/z 18 (Figure B-29) can be seen, which compared to the other observed species is disproportionately high. As illustrated in Figure 5-3, the H_2O/H_2 ratio in this case rises from about 1 % to 6 %, while for the NU-LHT-2M sample and the reference run this ratio decreases from 4 % and 2 % to both 1 % respectively. This indicates that water was produced in the case of the ilmenite sample, although due to the small differences in the H_2O/H_2 ratio no clear conclusion can be drawn.

From the partial pressures depicted in Figure B-29 to Figure B-31 another interesting observation can be made regarding m/z 28. After opening the valve the pressure of m/z 28 increases much more for the NU-LHT-2M sample and the reference run than for the ilmenite sample. A simple explanation could be that the hydrogen purge feed was contaminated with atmospheric gases, so that m/z 28 represents nitrogen. If m/z 28 represents carbon monoxide an alternative explanation could be the water gas shift reaction, described by equation (2-57). The fact that the ilmenite sample contains large quantities of Fe_2O_3 (see Table C-2),

which is a high-temperature catalyst for the water gas shift reaction (Newsome, 1980), supports this hypothesis. However, because water was also detected in concentrations similar to m/z 28 for the NU-LHT-2M sample and the reference run, it is more likely that the high partial pressure of m/z 28 is caused by contamination of the hydrogen feed with nitrogen, or atmospheric gas respectively.

It is also noticeable that the partial pressure of m/z 44 decreases more slowly after the initial rise for the ilmenite sample than for the NU-LHT-2M sample and the reference run. This could indicate that carbon monoxide acted as a reducing agent of the ilmenite to form carbon dioxide according to equation (2-56). It might also be that during preheating the reduction process with hydrogen had reached equilibrium and hence a further reduction was only possible through carbon monoxide as reactant.

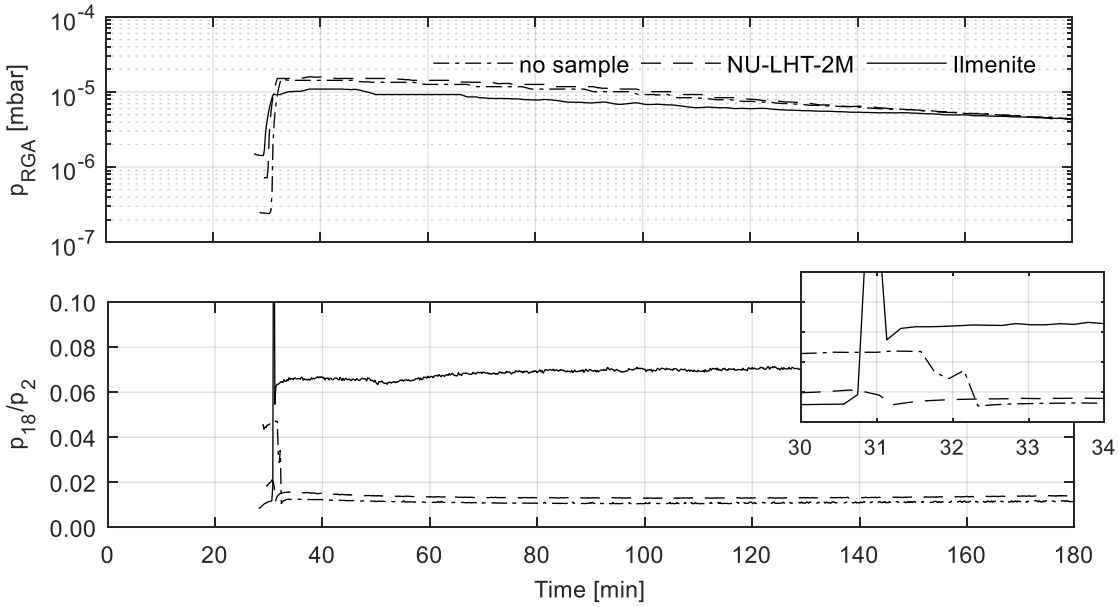

Figure 5-3: Gas pressures for the semibatch process with preheating. During the first 30 min the dosing valve was closed for batch heating and no RGA or pressure data was recorded. A detail of the valve opening process is provided in the enlarged plots.

Semibatch process without preheating

The most conclusive results are provided by the semibatch process where no preheating was applied, and where the valve for gas analysis was opened simultaneously with the start of sample heating. The partial pressures of m/z 2 and m/z 28 yield very similarly shaped curves with a continuous increase until the target temperature is reached (attributed to gas expansion only) and a subsequent constant decrease. This is most clearly visible for the ilmenite sample, see Figure B-32. With a notable time delay the pressures of the water fragments m/z 16, 17, and 18, as well as carbon dioxide with m/z 44 rise and reach a peak about 2 min after the peaks of hydrogen and carbon monoxide. As depicted in Figure 5-4, the H_2O/H_2 ratio for all runs starts between 0.4 % and 0.5 %, and reaches maximum values of 0.6 % for the reference run, 1 % for NU-LHT-2M, and almost 10 % for ilmenite. Because water is present in all three test runs in sufficiently high concentrations, the water gas shift reaction described by equation (2-57) could have caused the partial pressure of m/z 44 to rise with a time delay similar to the one of water.

Figure B-32 to Figure B-34 show a significant drop in the partial pressure of m/z 32, which is different to the other operating modes. A possible explanation is that residual oxygen in the system mixed with hydrogen to form oxyhydrogen, which combusted when the autoignition temperature was reached. Theoretically a simultaneous rise in the water partial pressure should be notable, but because the partial pressure of m/z 32 is much lower the one of water, the contribution of this reaction to the latter cannot clearly be identified.

Two control runs were done with nitrogen as reactant instead of hydrogen with the ilmenite sample to check if the small increase in carbon dioxide can clearly be attributed to the reduction with carbon monoxide. It was expected that the amount of carbon monoxide would be similar to the runs with hydrogen if it was of atmospheric origin. The resulting partial pressures in Figure B-35 show a clear decrease of water, while m/z 28 (nitrogen and carbon monoxide) remains nearly constant. On the other hand a clear increase of m/z 2 and a very small increase of m/z 44 is visible. The former could be due to thermal expansion and ineffective pumping at such low pressures and atomic masses, or due to the water gas shift reaction. The increase in m/z 44 however could be an indicator for both the reduction of ilmenite with carbon monoxide and the water gas shift reaction, although such interpretation needs to be treated with caution due to the hardly visible positive trend and the noisy signal. The results of the nitrogen control runs are therefore ambiguous and no clear conclusion can be drawn regarding the explanation of the trends of m/z 28 and m/z 44 in the test discussed above.

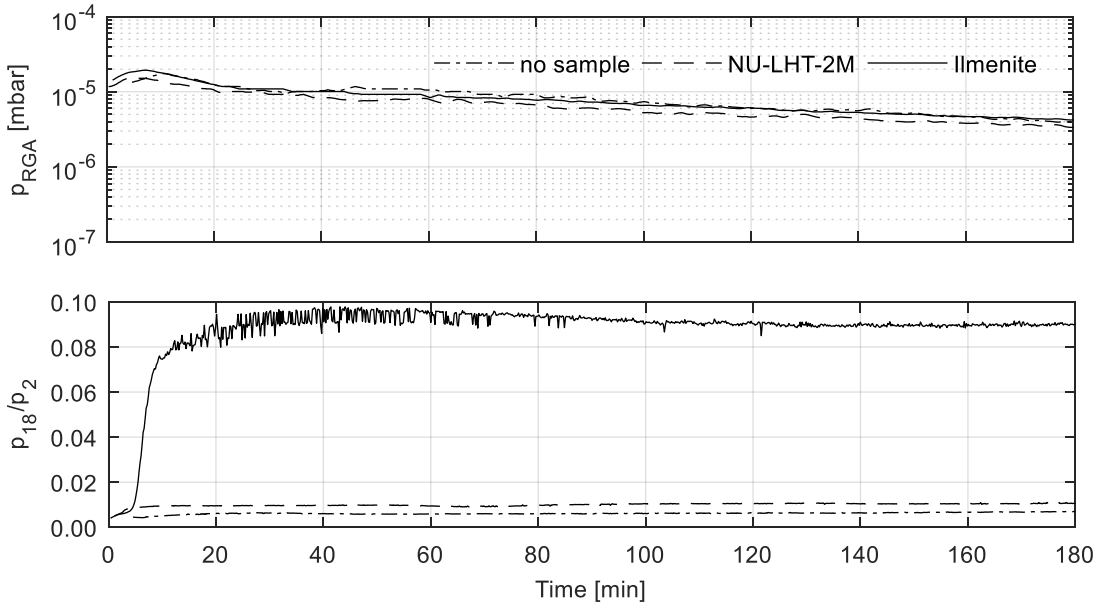

Figure 5-4: Selected partial pressure ratios for the semibatch process without preheating

For the overall process it can be concluded that the basic feasibility of the chemical production of water from ilmenite with the given setup was demonstrated. The continuous gas flow mode posed challenges in terms of handling and adjustment of the valves to maintain a constant hydrogen flow. Generally this mode would be preferred because the produced water is instantly transported away from the sample so that the reaction does not experience equilibrium conditions and subsequently stops. From an operational perspective the semibatch mode is preferred because minimum manual interaction with the experiment hardware is required. For the semibatch process without preheating and a simultaneous start of the gas analysis and the sample heating was found to be most conclusive because the interpretation of the results is most intuitive and clear. It was shown for this operational mode that the water content in the gas mixture reaches a maximum of approximately 10 %, which is in accordance with literature values (Taylor *et al.*, 1993). The initial rise of the partial pressure of water takes place within the first 30 min of heating to 800 °C for the semibatch processes. For the continuous gas flow process the partial pressure of water stagnates after approximately 60 min. In terms of water yield, the highest values were found for the ilmenite sample and the semibatch process without preheating. The calculation of the amount of water was done as for the volatiles extraction experiments described in chapter 4.2.3. The amount of m/z 18 calculated from the results is 0.2 wt% for NU-LHT-2M and 1.7 wt% for ilmenite (excluding 0.2 wt% from the background signal that was measured during the reference run), as illustrated in Figure B-36. These values are within the expected range, considering similar studies discussed in chapter 2.4.

6 Sample Oven Scalability

This chapter is an adapted and updated excerpt from Reiss et al. (2017)*, written by the author of the present thesis.*

This chapter describes the experimental studies that were conducted as a feasibility study for the design of the ProSPA sample ovens. The implications of an up-scaling of the original sample size for the thermal design of the sample ovens and the resulting temperature distributions in the sample and power demands are discussed. A review of the material compatibilities at higher temperatures is provided together with suggestions for material that can be used for the oven, insulation, and the heating wire. Finally, an experimental proof of concept for achieving higher target temperatures with a larger sample oven is presented along with the evaluation of the thermal performance of such an up-scaled sample oven.

6.1 Effects of Sample Size Scaling

During the course of the ProSPA study, an alternative design of the sample oven was discussed to accommodate a sample that is larger than the originally planned baseline sample size. The baseline was to inherit the sample ovens from the Beagle-2 GAP instrument and the Rosetta SD2 instrument (compare section 1.2.2), which accepted samples with a diameter of 2.8 mm and a height of 4.5 mm. The increased sample size under discussion for ProSPA assumed a cylindrical sample with 10 mm in diameter and 15 mm in height. This means a linear increase in both radial and vertical direction by a factor of $f \approx 4$, which has several effects on the heat transfer into the sample, heat losses to the environment, heating control and overall duration of the gas extraction process (Reiss *et al.*, 2017):

- The diameter d and the height h both scale linearly with f, so that $d_{scaled} = f \cdot d$ and $h_{scaled} = f \cdot h$. A larger diameter of the sample affects the thermal gradient between sample core and surface.
- The scaled oven surface is $A_{scaled} = f^2 \pi d h$ and thus scales quadratically with f^2. The increased surface leads to a higher heat loss via radiation to the environment. Top and bottom surface are neglected, since they interface directly with other hardware. Their contribution to the heat loss could however be considered with an additional proportionality factor.
- The scaled oven volume is $V_{scaled} = \frac{1}{4} f^3 \pi d^2 h$ and hence scales cubically with f^3. This affects the mass m and thus the heat capacity, or thermal inertia, $c_p m$.

The implications of this scaling on power demand, temperature distribution, and thermal design are discussed in the following sections

6.1.1 Power Demand

To evaluate the power increase when scaling the sample volume up from the baseline heritage concepts, a parametric simulation model was created that resembles the baseline oven design from Beagle-2/Rosetta SD2 (compare chapter 1.2.2). It consists of a hollow cylindrical oven made from platinum with an inner diameter of 2.8 mm, an inner height of 4.5 mm, and a wall thickness of 0.6 mm. The oven contains a sample modelled with the thermal conductivity of the Apollo 16 sample 68501, as described in chapter 2.2.3, and a specific heat capacity based on data by Schreiner et al. (2016), as described in chapter 2.2. The gas pressure was assumed to be in the range of 10^{-4} Pa, therefore gas conductivity was practically neglected (gas conductivity is only significant at pressures above approximately 1 Pa, as described in chapter 2.2.3 and illustrated by Figure 2-7). The density of the sample in the simulation was adapted to the experimentally measured density of 1.4 g/cm³, where a sample was loosely filled into a sample container with inner diameter

12 mm and height 18 mm up to a height of approximately 10 mm to represent the volume of a Ø10 mm × 15 mm drill core). At the outside of the oven, a white ceramic paste was modelled with a thickness of 1 mm, which was kept constant over all scaling factors. The heat load was applied to the ceramic paste, since it is used to affix the resistance wire to the surface of the oven cylinder. The environmental temperature was assumed to be 120 K, matching the temperature expected in the shaded areas at the South Pole landing site.

The results of the parametric thermal analysis are given in Figure 6-1, which shows the steady-state temperatures of the sample core as a function of the applied heating power. As described before, the optional design for ProSPA foresees oven dimensions corresponding to approximately four times the dimensions of the baseline design. In order to reach 1200 °C in the sample core, about 20 W need to be applied to the original oven. The enlarged oven with $f = 4$ however requires 244 W. The original oven takes about 240 s to reach steady state at 20 W, while at the same time for the oven with $f = 4$ the sample core temperature is just about to start increasing from the initial temperature.

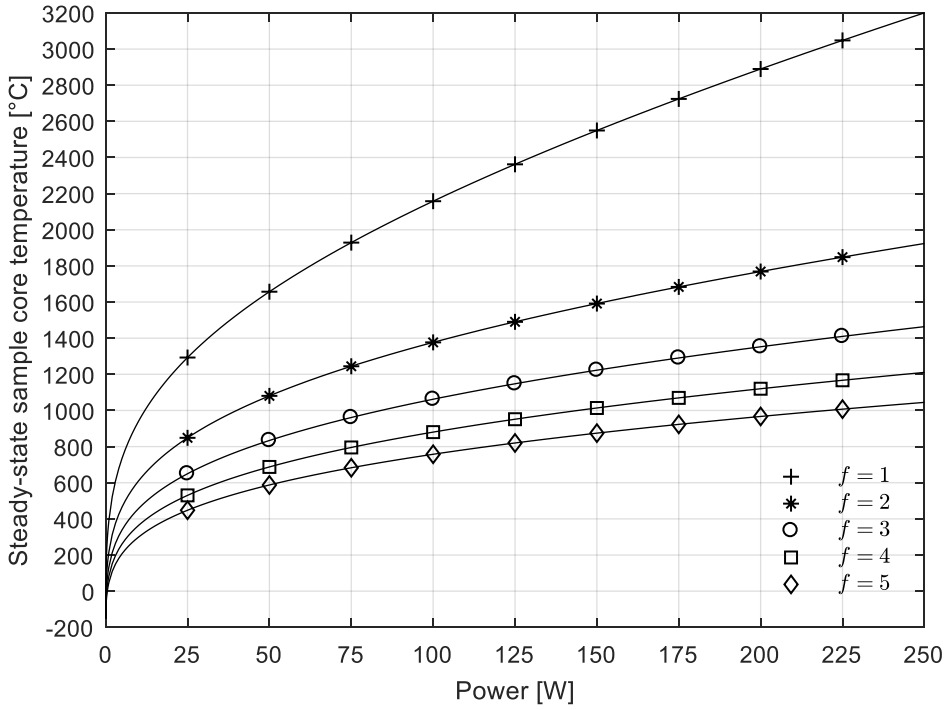

Figure 6-1: Steady-state temperature of the sample core for scaled oven dimensions

6.1.2 Temperature Distribution

Figure 6-2 shows the progression of the temperature distribution across the sample with $f = 4$ between 300 s and 3600 s for a heating power of 20 W. At the beginning the highest temperature gradient is within the first 1 mm of the sample. With increasing temperature, the thermal conductivity of the sample increases, so that the heat spreads faster. However, even after 3600 s, the temperature gradient between sample core (-34 °C) and surface (not shown in the figure) is still 518 °C. For the original sample size with a diameter of 2.8 mm, the same sample core temperature of -34 °C is reached after only 75 s. During the first seconds however, the gradient across the sample is also in the range of several hundred degrees Celsius. This can only be counteracted by reducing the heating power at the beginning of the heating process at low temperatures. The result of reducing the heating power to 10 W is shown in Figure 6-3. As expected, the gradient from sample core to the surface is smaller, with 487 °C after 3600 s. The temperature of the sample core at this time reaches -126 °C, whereas for a heating power of 20 W this temperature is reached after 2825 s. This illustrates that increasing the heating power does not help raising the sample core temperature significantly faster. In other words, doubling the heating power does not result in a doubling of the speed of

heat transfer. Furthermore the gradients at higher heating power are higher, which is not desirable for a scientific analysis of the released gases, since they cannot clearly be associated with a known uniform sample temperature. A countermeasure would be to start with low heating power at low temperatures and continuously increase the power at a higher temperature (and hence higher thermal conductivity of the sample). However, this approach comes at the cost of longer heating durations.

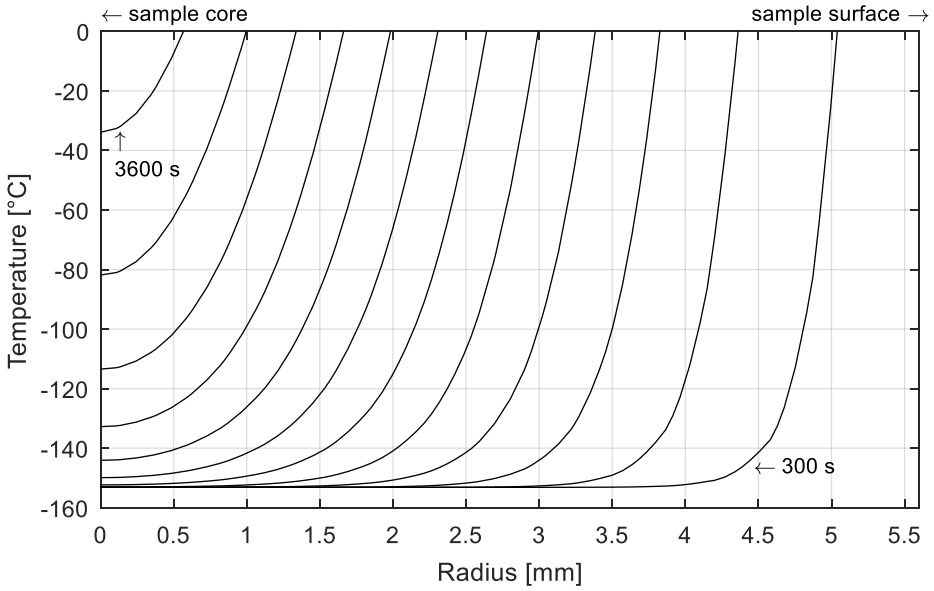

Figure 6-2: Temperature distribution over sample radius (with scaling factor $f = 4$) in steps of 300 s for a heating power of 20 W

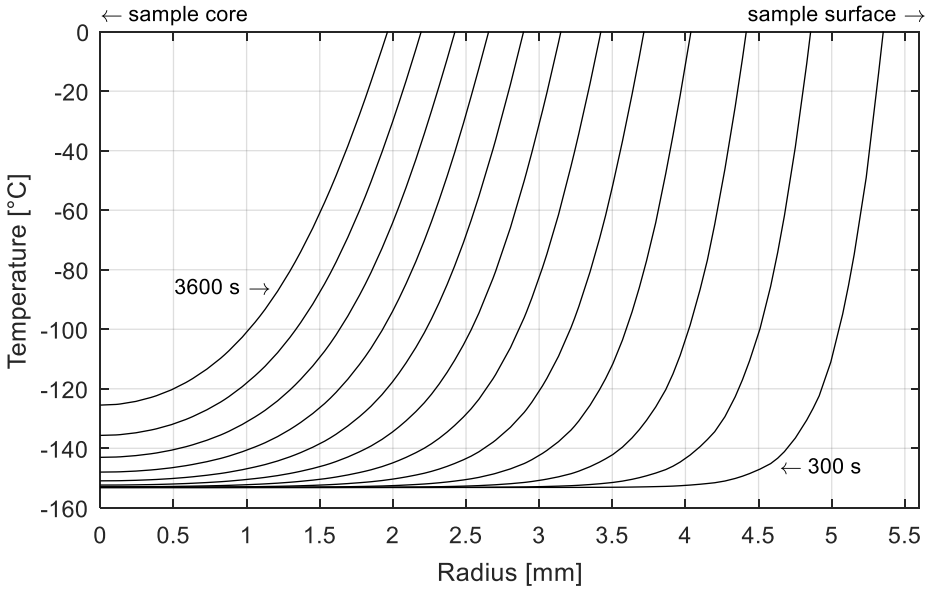

Figure 6-3: Temperature distribution over sample radius (with scaling factor $f = 4$) in steps of 300 s for a heating power of 10 W

6.1.3 Thermal Insulation

As Figure 6-1 illustrates, the heat loss via radiation has a profound effect on the achievable sample temperatures. For ovens larger than the baseline concept, additional insulation is therefore required to insulate the oven from its cold environment and the adjacent instrument hardware. This can be realised either through a set of metallic radiation shields, solid (microporous) insulation material, or a combination of

both (e.g. radiation shields in high temperature regions and microporous insulation at lower temperatures farther away from the oven). The oven also has to be insulated at its base to minimise conductive heat loss through direct hardware interfaces. Here only load-bearing materials can be considered, since the baseline instrument concept foresees a compressing sealing mechanism that exerts a force (well above 1000 N) along the vertical axis of the oven.

One of the most promising solid insulation materials found during the presented study is aerogel. It is high-temperature resistant, has a low density, and superior insulating capabilities. Amongst the aerogels, carbon aerogels generally offer the lowest thermal conductivity. Wiener et al. (2009) showed that for pyrolised carbon aerogel effective thermal conductivities between approximately 40 mW/(m·K) and 80 mW/(m·K) can be achieved between 100 °C and 1200 °C in a vacuum. The effect of such an insulation on the outer circumference of the oven is depicted in Figure 6-4, which shows the steady-state temperature of the sample core over varying insulation thickness for an oven with scaling factor $f = 4$. For the insulation the temperature-dependent effective thermal conductivity and specific heat capacitance determined by Wiener et al. (2009) were used. All other simulation parameters, such as the emissivity of the outer bound of the oven, were adapted from the model used to produce Figure 6-1 for better comparability. The results show that an insulation thickness of about 5 mm is sufficient to improve the steady-state temperature from 486 °C to the targeted maximum temperature of 1200 °C.

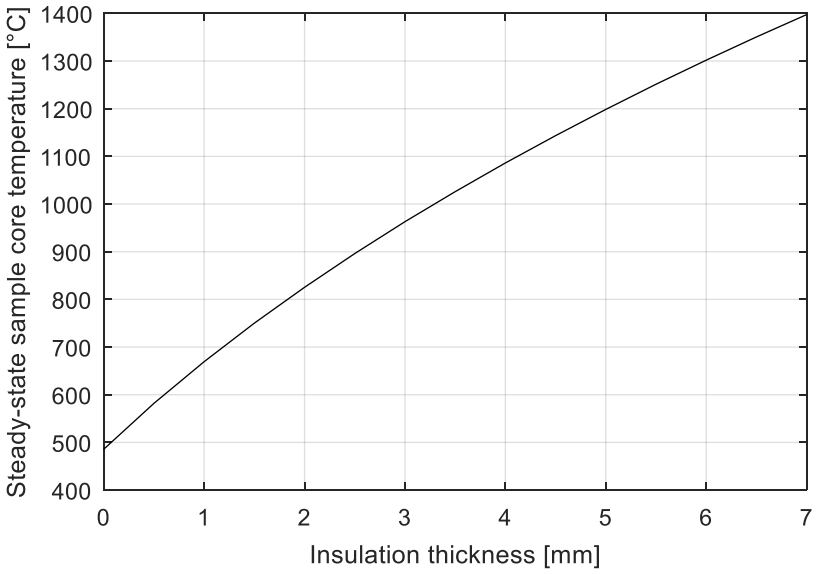

Figure 6-4: Steady-state temperature of the sample core over thickness of a carbon aerogel insulation at 20 W heating power for an oven with scaling factor $f = 4$

Different types of aerogel and other microporous materials were reviewed during this study. Multiple options from commercial suppliers were found for the insulation of the sides of the oven. A suitable insulation material for the base of the oven still has to be found. The major challenge here is to find a material that has both low thermal conductivity and high structural stability. Aerogels with a carbon or ceramic composite structural outer shell might be an option, but little information is available about such materials for the intended purpose of application. More traditional materials for such an insulation include ceramics, such as calcium silicate ceramics with thermal conductivities in the range of 200 mW/(m·K) under atmospheric pressure, or ceramic foams.

6.2 Oven and Heater Material Compatibility

The requirements for ProSPA include heating modes with a maximum temperature that is higher than the target temperatures of all other oven concepts reviewed in thesis, as described in chapter 1.2.3, except VAPoR (compare Table 1-2). Higher temperatures introduce new challenges for the material compatibility of

the sample container as well as the resistance wire used for heating. Additionally, as mentioned before, ProSPA also foresees ISRU demonstration modes that include heating the sample in the presence of a reactant gas, being either hydrogen, methane, or fluorine. An additional requirement therefore is that the sample container material withstands high temperature either in a chemically reducing or oxidising atmosphere (depending on the operational mode) and under these circumstances does not interact with the expected evolved volatile species in a way that they are chemically altered or bound to the container surface prior to reaching the analysis instruments. The structural compatibility to high temperature also applies to the heating wire. As a result of the increased power demand, an additional requirement for the heater is that it can produce sufficient power at a given supply voltage and limited current. This is only possible if the heater material has an appropriate specific resistance over the relevant temperature range. Several candidate materials for the oven and the resistance wire are reviewed in the following, including recommendations for the design of the enlarged oven for ProSPA.

6.2.1 Sample Container

Regarding the issue of material compatibility, a thorough survey was conducted that resulted in a list of over 40 relevant materials for the sample container. Table 6-1 provides a selection of the most promising oven materials along with their most relevant properties, melting point and coefficient of thermal expansion (CTE). Note that steel 1.0570 (at the bottom of Table 6-1) is not suitable for the actual flight design and only included as a reference for the experiments presented in chapter 6.3. The melting point for all relevant materials is above the maximum operation temperature of 1200 °C. The CTE is important due to the material combinations used in the design of the oven, being most relevant to the seal that is applied to one side of the oven. If the oven expands too much, the sealing force might need to be adjusted during operation, which poses a new design challenge. If the CTE is too high, the expansion of the oven could also lead to mechanical damage if it presses against other structural parts, for example a rigid ceramic insulation. Such problems can be counteracted to a certain degree by implementing CTE compensation methods, either by a modified design of the respective parts that accounts for thermal expansion, or by combining materials with different CTE.

As summarised in Table 1-2, platinum is used in most comparable instruments. It is highly inert, has high chemical and corrosion resistance and together with rhodium, platinum offers increased stress resistance and allows higher operational temperatures with good structural stability (Vaithinathan and Lanam, 2005). However, it needs to be considered that platinum is attacked by silica and silicates under reducing conditions above 1000 °C. Furthermore, iron oxides react with platinum above 1200 °C to 1250 °C , and more stable oxides, such as Al_2O_3, can lead to ignitions without attack (Stokes, 1987). Nickel generally also offers good corrosion resistance and is available in a variety of alloys with aluminium, cobalt, or chromium. The latter NiCr alloys form the Inconel series, where Inconel 693 is most suitable for high-temperature applications that require good mechanical stability and good resistance against metal dusting and corrosion. For use in vacuum, Inconel alloys require a passivating oxide layer, which can be created in an oxidising atmosphere. Gillies et al. (2007) studied the compatibility of Inconel 625 with the lunar mare type simulant JSC-1A and found that when heating both up to 1000 °C in vacuum, there is an increase in chromium in the mineral phase of the simulant. This was explained by the evaporation of chromium due to its higher vapour pressure as compared to the other constituents in Inconel 625. A common choice of material for high-temperature applications is tungsten (W). There are tungsten-rhenium (W-Re) alloys that have an improved recrystallisation temperature and creep resistance. For the application with lunar soil samples, it may be noted that tungsten reacts with Si_3N_4 at 1200 °C to form silicide. Another common material for high-temperature applications is molybdenum. However, for the potential use with the proposed reactant gases it needs to be considered that it is sensitive to oxygen and fluorine and forms molybdenum carbide with methane at 600 °C. Alloys with increased recrystallisation temperature above 1200 °C are also available (e.g. TiZrMo). The last material considered for the sample ovens is tantalum, which offers good corrosion resistance, but is susceptible to hydrogen embrittlement. Under high vacuum tantalum loses hydrogen at 800 °C and nitrogen at 1700 °C. Due to the heritage from earlier missions and its mostly superior material properties as described above, platinum is considered as baseline material for the sample container. Alternatively, a nickel alloy (e.g. Inconel) is recommended.

Table 6-1: Selection of relevant materials for the sample container and resistive wire heater

Material	Application	Melting point [°C]	CTE at room temperature [10^{-6}/°C]	Specific resistance at room temperature [Ω mm^2/m]	Specific resistance at 1200 °C [Ω mm^2/m]
Platinum	C, H	1769	9.1	0.11	~0.60
Pt90/Rh10	C, H	1850		0.20	~0.60
Nickel	C	1455	13.1	n/a	n/a
Inconel 693	C	1317 to 1367	13.0	n/a	n/a
Molybdenum	C, H	2617	5.4	0.05[a]	0.32[a]
Tungsten	C, H	3370	4.4	0.05[a]	0.33[a]
Alumina	C	2054	5.5	n/a	n/a
Tantalum	C	2996	6.5	0.13[a]	0.55[a]
(Steel 1.0570)	(E)	(1491)	(11.1)	(n/a)	(n/a)

Note: C = sample container, H = resistive heater, E = used for experiments in this study

[a]values corrected for thermal expansion, taken from Desai et al. (1984)

6.2.2 Resistive Wire Heaters

For the resistance wire the most suitable material is either molybdenum or a Pt/Rh alloy (or ZGS Pt/Rh for improved high temperature strength (McGrath and Badcock, 1987)), as used for nearly all of the heritage ovens listed in Table 1-2. The only exception is the MOMA oven, which uses a new technology to embed a thin platinum conductor in a ceramic structure. As illustrated in Table 6-1, Pt/Rh has a higher specific resistance than most other materials. This means that the diameter of the resistance wire can be larger than that of a molybdenum wire with the same total electrical resistance. The additional advantage is a higher structural strength and better fracture resistance at higher temperatures. Based on practical experience it is recommended to use a resistance wire with a diameter larger than 0.2 mm to maintain reasonable wire strength. Figure 6-5 shows the power that can be produced by different wire materials and diameters per unit length and with a typical spacecraft voltage and current that are limited to 28 V and 2 A respectively (representative values). Note that the values for the specific resistance given here are valid for room temperature only. Because the resistance and thus the achievable power increases with temperature, the curves shown here represent worst case values at start-up (ground testing), indicating the need to use active current-limiting constant current power supplies for use on the spacecraft.

Figure 6-5 illustrates that with the given constraints the Pt/Rh alloy produces its peak power at larger wire diameters than pure platinum, molybdenum, or tungsten wires. On the left side of the peak the maximum power output is constrained by the voltage limitation. On the right side of the peak, the current limitation constrains the power. Raising the voltage limitation raises the peak power and shifts it to smaller wire diameters, whereas raising the current limitation raises the peak value and shifts it to larger wire diameters. From the graph it can be seen that when selecting a wire with 0.2 mm diameter, the Pt90/Rh10 alloy is superior in terms of power output (approximately 25 W/m), while using a wire diameter of 0.1 mm moves the choice to a pure platinum wire. The latter provides substantially more power (approximately 50 W/m), but has an increased risk of structural failure at higher temperatures.

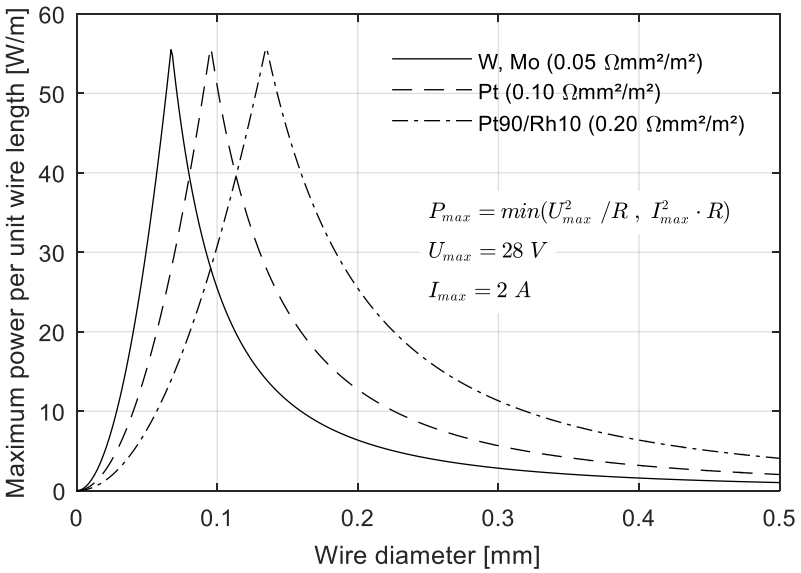

Figure 6-5: Achievable maximum heating power of relevant materials with varying wire diameters. Values for the specific resistances are valid at room temperature only (worst case). The maximum power is constrained by voltage limitation on the left side of the peak and by current limitation on the right side of the peak.

6.3 Sample Heating

Early experiments were performed for ProSPA to evaluate the general feasibility of using larger ovens instead of the baseline solution. This mainly aimed at verifying that the target temperatures as a driving requirement for the sample ovens can be reached by the different heating modes within the specified limits of power and time in a vacuum environment, and finding a design that would satisfy these requirements. The thermal simulations shown before cannot deliver conclusive results in this regard since the thermal and thermo-optical material properties, as well as the thermal contacts that are generated by assembling the parts in the actual experiment setup are not predictable in a sufficiently accurate way.

6.3.1 Experimental Setup

The experiments were performed in a thermal-vacuum chamber with an internal volume of approximately 40 cm × 40 cm × 90 cm. The thermal vacuum chamber (TVAC) is equipped with a Leybold Trivac D65B rotary vane vacuum pump and a Leybold Turbovac 600 turbomolecular vacuum pump to reach high vacuum in the range of 10^{-5} mbar, and a cooled shroud which can be controlled in the temperature range from -75 °C to +100 °C. For the experiments a sample oven was manufactured with an inner diameter of 12 mm, height 18 mm, and wall thickness 3 mm. The oven was made from structural steel grade 1.0570, which has a melting point of 1491 °C (Lindemann and Schmidt, 2002) and is easily available and workable, which is more convenient for first feasibility studies, as compared to platinum or other more exotic materials proposed for the flight design. Since the first tests targeted mainly the high-temperature capability of the setup and the feasibility of the heating modes, the use of steel rather than platinum or Inconel was deemed acceptable. For the heating wire a ceramics support structure with 36 vertical drillings in 10° spacing around the circumference for winding the heating wire up- and downwards around the sample container was developed. Thus wire lengths up to approximately 80 cm were achieved, despite the small oven dimensions. To protect the upper and lower end of the wire mount and to provide a good support for the sample container, two additional ceramic parts were designed. A cut view of the oven setup is given in Figure 6-6. The material of the wire mount was selected to be a boron-nitride ceramic (HeBoSint O120, consisting of hBN+SiC+ZrO_2), which can be easily machined due to its good structural stability and relatively high density of 2.4 g/cm³. It is stable up to a temperature of 1800 °C in vacuum and 1000 °C in an oxidising atmosphere. The new design with the HeBoSint wire mount allows for convenient and fast replacement and exchange of either sample container or heating wire due to the modular design. For heating, a pure molybdenum resistance wire with

a specific resistance of 0.053 Ω·mm²/m at room temperature (Desai *et al.*, 1984) and diameter of 0.2 mm was chosen. Other wires with higher specific resistance were not available at the time but are planned for future more refined tests to further improve the performance. The installed wire in the test setup had a resistance of 1.570 ± 0.001 Ω at room temperature, as determined via four-wire Kelvin measurement. This corresponds to approximately 1 m wire length (including the twisted lead wires outside of the mount). According to Figure 6-5, this wire can produce only 6.7 W/m at room temperature with the given voltage and current limitations. However, as the resistance increases nonlinearly to about 12 Ω/m at 1200 °C, a maximum power output of around 50 W/m could be achieved.

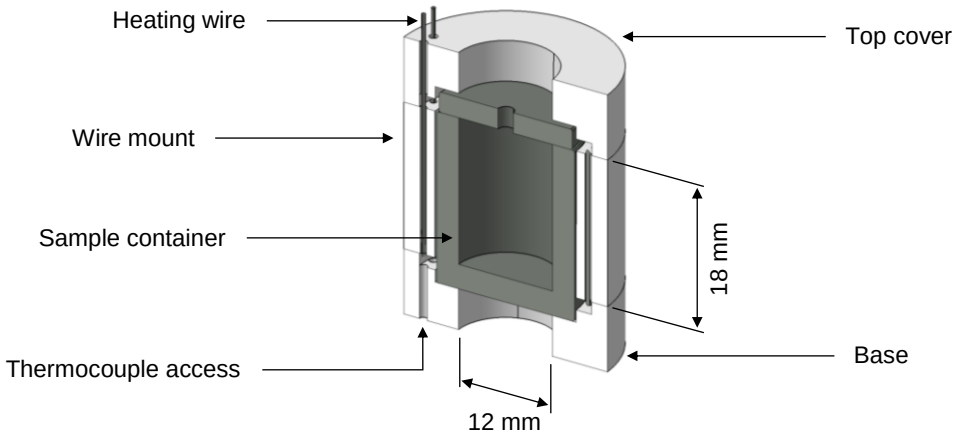

Figure 6-6: Cut view of the sample oven with ceramic wire mount

The heating wire was powered by a standard laboratory power supply with its voltage controlled by a PID controller, implemented in the software LabVIEW. However, for the tests described here only the proportional gain was set, while the integral and derivative terms were dismissed. The heater current was measured with a standard multimeter. To attain the highest heating voltage accuracy, a thin measuring line was connected to the power line as close to the heater as possible to avoid the measurement of current-induced voltage drops over the resistance of any connectors and TVAC feedthroughs. The entire setup allowed heating with constant power, while calculating the temperature-dependent resistance of the heater from the measured current and voltage across the heater terminals. The temperature of the sample oven was measured via a 0.25 mm diameter Type-K mantle thermocouple, placed inside the ceramic base structure, as depicted in Figure 6-6. The oven was insulated with four 100 mm × 100 mm layers of aluminium oxide insulation boards (Schupp Ultraboard) with a cut-out for the oven, leaving a small gap of approximately 2 mm between oven and insulation board (Figure 6-7). This insulation layer has a thermal conductivity that is about three times higher than that of the carbon aerogel discussed in section 6.1.3, which means that it represents an equivalent aerogel layer of about 10 mm. As shown before (compare Figure 6-4), a 10 mm aerogel insulation layer should be thick enough so that the power-limited design can achieve the desired target temperature of 1200 °C, even when accounting for possible thermal bridges in the test setup and the increased mass and surface of the oven including the wire mount. Figure 6-7 shows the test setup in preparation before being installed in the TVAC.

The sample material for the tests was the lunar highland-type regolith simulant NU-LHT-2M. Unsieved simulant was used to preserve the original particle distribution ranging from 1 mm down to several micrometres (compare chapter 1.3). The sample was filled loosely into the sample container up to a height of about 10 mm to match a sample volume that represents the Ø10 mm × 15 mm drill core with a volume of 1.18 cm³. The mass of the sample for all test runs was 1.6 g, as measured by weighing the empty and loaded crucible. This corresponds to a mean sample density of roughly 1.4 g/cm³, which is at the lower end of the experimentally determined bulk densities for NU-LHT-2M (Zeng, He and Wilkinson, 2010).

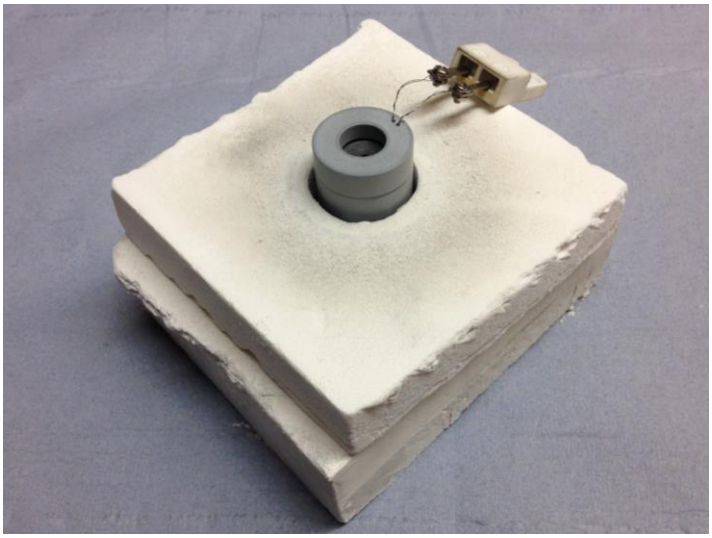

Figure 6-7: Laboratory test setup (upper insulation parts removed)

6.3.2 Heating Modes

For the experimental evaluation of the oven design, six different test modes were run. This included continuous heating to 1200 °C with a defined heating rate (heating mode 1), stepped heating to 1200 °C with a defined step and hold profile (heating mode 2), and heating up to 900 °C at the maximum heating rate (heating mode 3). All modes were run once at room temperature and once at -68 °C (as determined by the minimum TVAC temperature), both in high vacuum. The target temperatures were measured by the thermocouple which was emplaced in the heating wire mount (see Figure 6-6). For the following discussion, only the results of the low-temperature tests are presented. Table 6-2 summarises the key parameters and the required power for each experimental heating mode.

Table 6-2: Key parameters and experimentally determined power budget for heating modes 1-3

Parameter	Mode 1 (constant rate)	Mode 2 (step and hold)	Mode 3 (maximum rate)
Temperature range	-68 to 1200 °C	-68 to 1177 °C	-68 to 900 °C
Heating rate	6 °C/min	-70 to 500 °C at 60 °C/min 500 to 1210 °C at 30 °C/min	15 °C/min (average)
Temperature steps	n/a	-70, 0, 100, 220, 340, 460, 580, 700, 850, 1000, 1210 °C	-70 °C, 900 °C
Temperature holds	n/a	30 min (on each step)	3 h (at target temperature)
Duration	240 min	332 min	245 min
Average power	38 W	30 W	40 W
Peak power	68 W	68 W	51 W
Total energy	150 Wh	167 Wh	165 Wh

Heating mode 1 (constant rate of 6 °C/min)

The tests revealed that with the given setup the set maximum current of 2 A was not sufficient to reach the target temperature of 1200 °C. It was achieved only at 2.5 A, at which point 68 W (27 V at 2.5 A) was dissipated. Even then, the specified heating rate of 6 °C/min could only be maintained up to about 1100 °C, where it levelled out under the limited power supply (Figure 6-8). The Labview proportional control worked better at higher temperatures and produced maximum overshoots of 10 °C below a set point temperature of 400 °C. Above this temperature the increased radiative cooling dampened the overshoots.

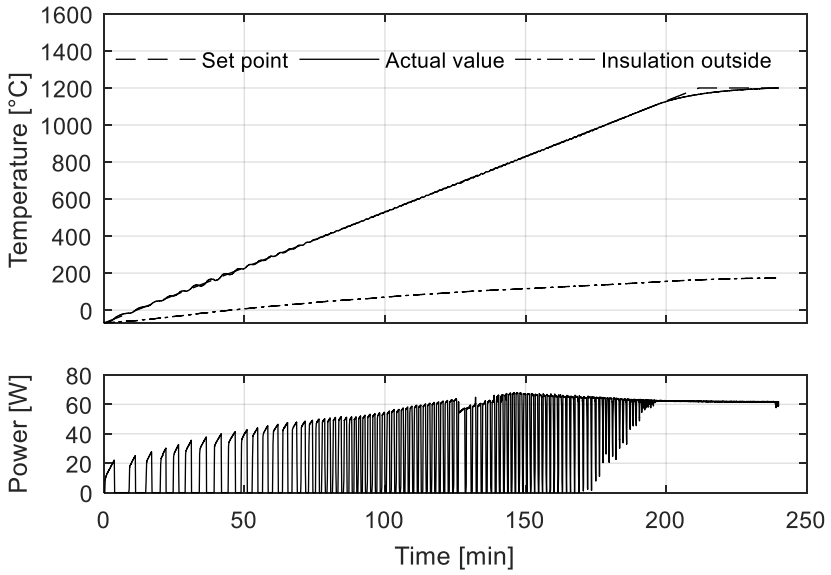

Figure 6-8: Heating results at constant heating rate (heating mode 1)

Heating mode 2 (step and hold)

Again the current had to be raised from 2 A to 2.5 A to accomplish the specified heating step profile. However, the specified heating rates could not be met at each temperature level, because the control parameters were not adapted during the test (Figure 6-9). Such an adaptive control, however, is not trivial, because of the non-linear influence of radiation losses especially at higher temperature ($\sim T^4$) and the variable resistance of the heating wire. The temperature regulation in the tests utilised a simple proportional controller with active current limit, resulting in overshoots at lower temperatures, but achieving more accurate control at elevated temperatures. The experimental setup is capable of implementing an accurate PID-control, using active current limit and active voltage control, so that the parameters can be adjusted appropriately during future experiments. At the last step of the temperature profile, the desired maximum temperature could not be reached within the given time, since the heating power was not sufficient to follow the last step from 1000 °C to 1200 °C (Figure 6-9).

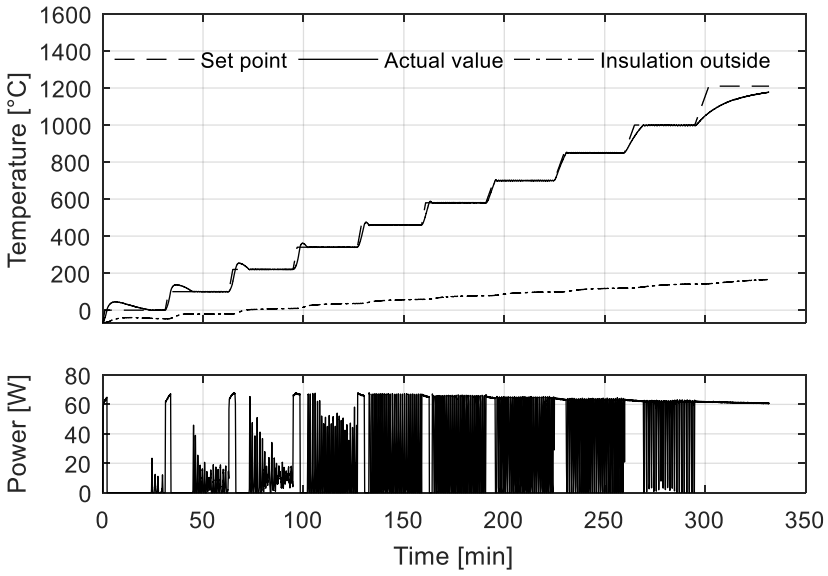

Figure 6-9: Heating results for step and hold heating (heating mode 2)

Heating mode 3 (maximum heating rate)

This test was performed with the maximum available heating rate of the setup, while maintaining a maximum supply voltage of 28 V and actively limiting the current to 2 A. The target temperature of 900 °C was achieved after 65 min, resulting in an average heating rate of 15 °C/min (Figure 6-10). Heating up from -68 °C to room temperature took only 3 min, which illustrates that the main challenge is heating at higher temperatures. The maximum power was 51 W at 2 A and 25 V. The proportional controller worked well, keeping the temperature within a tolerance band of -7/+3 °C of the target value. At the end of the test run, the resistance wire unexpectedly broke after holding its temperature at 900 °C for 3 h. As molybdenum resistance wire nominally is capable of withstanding much higher temperatures, it is assumed that oxidation processes or degradation during the previous test runs, in combination with the long duration including a high number of thermal cycles, caused the rupture. This indicates that for future tests a thicker resistance wire must be chosen (e.g. platinum or Pt-Rh wire with higher strength and higher specific resistance as described earlier).

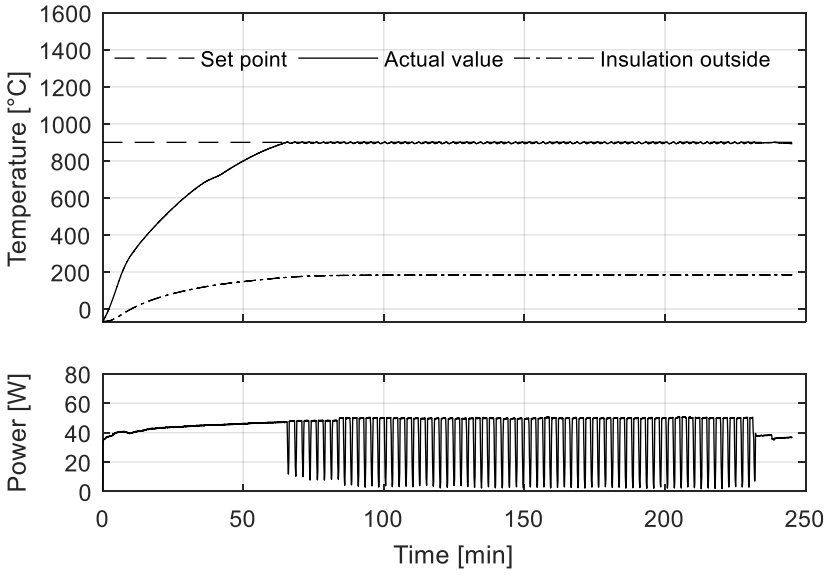

Figure 6-10: Heating results with maximum heating rate (heating mode 3)

The temperature curve in Figure 6-10 shows a dip between 700 °C and 750 °C, which has been observed before in preparatory tests. To find out whether this dip is caused by outgassing of any of the materials in the setup, or if it is caused by reversible phase changes, a separate series of test runs was performed. The oven was repeatedly heated to just over 900 °C and cooled down to 400 °C. The dip between 700 °C and 750 °C showed clearly in the first run, less significant in the second run, and almost vanished in the third run. It is therefore concluded that it is caused by outgassing and might be attributed to the ceramics or metallic components rather than the sample itself. These three test runs were performed with a sample and with comparable heating wire parameters as during the three heating modes.

Temperature measurement

As shown in Figure 6-8 to Figure 6-10, the simple proportional control method caused high power variations, thus the resistance wire experienced high stress changes. With the measured voltage and current the actual wire resistance was calculated, which is an indicator for the actual temperature of the resistance wire. With the known temperature-dependent specific resistance of the wire and using the values for the specific resistance of molybdenum taken from Desai et al. (1984), the thermocouple temperature was derived from the calculated resistance as depicted in Figure 6-11 to Figure 6-13. On average it is 200 °C to 400 °C above the temperature measured by the thermocouple but shows large cycling deviations from this average in the due to the proportional control. Towards the end of the heating process the temperature offset diminishes due to a vanishing thermal inertia. The temperature offset is also due to the fact that the thermocouple was located at 2 to 3 mm from the heating wire with direct viewing, making thermal radiation the main heat transfer mechanism between both. The relatively large temperature offset can therefore be explained with the non-optimal thermo-optical properties of wire and thermocouple, the view factor between both, and the fact that the thermocouple itself transfers heat out of the oven via conduction. The actual temperature of the sample container is assumed to lie between both curves shown in Figure 6-11 to Figure 6-13.

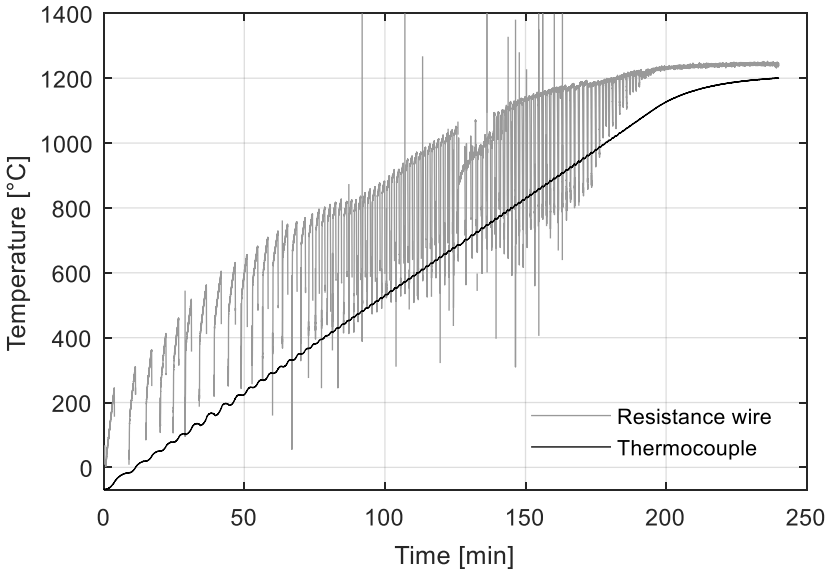

Figure 6-11: Comparison of measured thermocouple temperature and calculated temperature of the resistance wire for heating mode 1 (constant heating rate). Gaps in the calculated curve are caused by ignoring zero resistance (temperature) values at 0 V supply voltage.

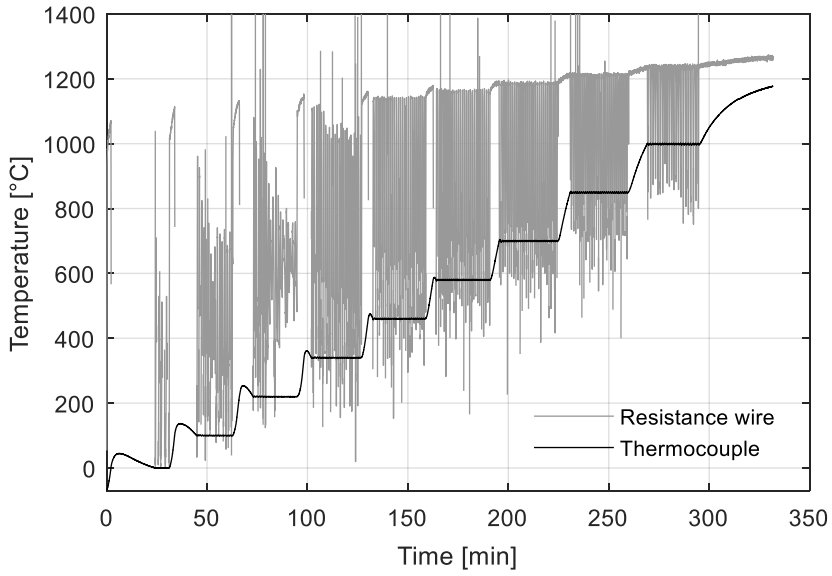

Figure 6-12: Comparison of measured thermocouple temperature and calculated temperature of the resistance wire for heating mode 2 (step and hold). Gaps in the calculated curve are caused by ignoring zero resistance (temperature) values at 0 V supply voltage.

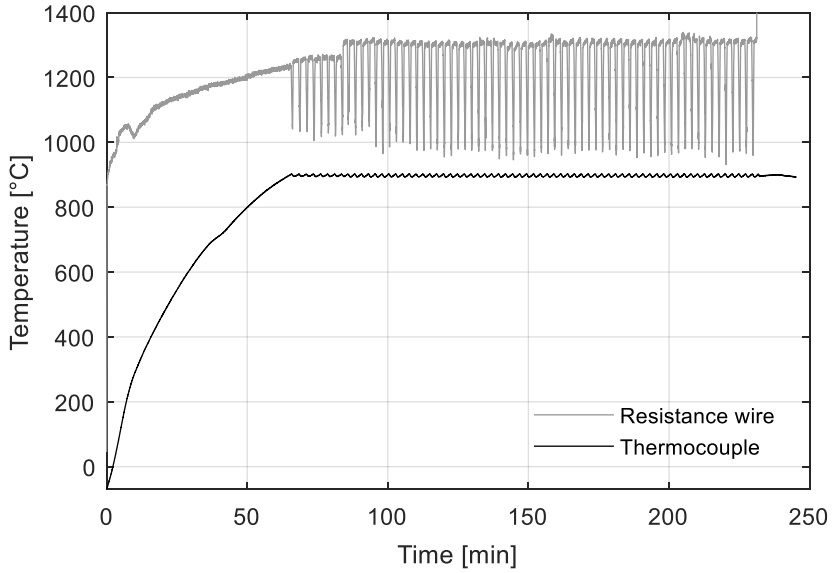

Figure 6-13: Comparison of measured thermocouple temperature and calculated temperature of the resistance wire for heating mode 3 (maximum heating rate). Gaps in the calculated curve are caused by ignoring zero resistance (temperature) values at 0 V supply voltage.

Sample transformation

As depicted in Figure 6-14, the sample experienced sintering at temperatures between 1000 °C and 1200 °C (just below the melting point of NU-LHT-2M in the range of 1200 °C to 1300 °C (U.S. Geological Survey, 2008)). When the sample was removed from the oven after experiencing a maximum temperature of 1200 °C, the following changes were observed:

- The sample container had changed in colour from dark matte to bright silvery grey both on the inside and outside.
- The regolith sample had sintered and showed different forms of deformation.
- The sample was much darker than before, indicating reduction of FeO_2 to FeO.

The sample had to be removed from the container several times because it was sintered at higher temperatures: after a series of preparatory tests (Figure 6-14), after a sequence of preparatory tests of heating mode 3 and 1 (Figure 6-15), and after the complete sequence of heating modes 3, 1, and 2, which lead to the result graphs that have been previously discussed (Figure 6-16). The first occurrence of sintering was noted after a number of different preparatory tests which included all three heating modes with different target temperatures between 900 °C and 1180 °C in variable order. The sample transformed into a single solid piece after these tests, which could easily be removed from the container. The sample had slightly shrunk, but no mass loss of either the sample container or the sample was detected (at a resolution of 0.01 g, sample mass was 1.6 g, container mass was 23.6 g). Removing the sample after a sequence of heating mode 3 and 1 with a maximum temperature of 900 °C and 1195 °C respectively showed an entirely different transformation. The volume of the sample appeared to be larger after the tests and it was not possible to remove the sample using simple mechanical means, such as scraping with a chisel. Only stronger hammer strokes revealed that the sample had formed a dark crust with a large cavity and brighter material below. A similar observation was made after the final sequence of heating modes 3, 1, and 2, with maximum temperatures of 900 °C, 1200 °C, and 1177 °C respectively (the sample was kept inside the container during the entire sequence). Here the sample appeared to have spilled over the container and lifted the top cover of the container. Again this upper crust could only be broken with hammer strokes, which revealed an even larger cavity below with residual sintered sample at the bottom of the container.

Figure 6-14: Oven after a number of preparatory tests, including heating up to 1180 °C, with significantly brighter surface and sintered regolith sample

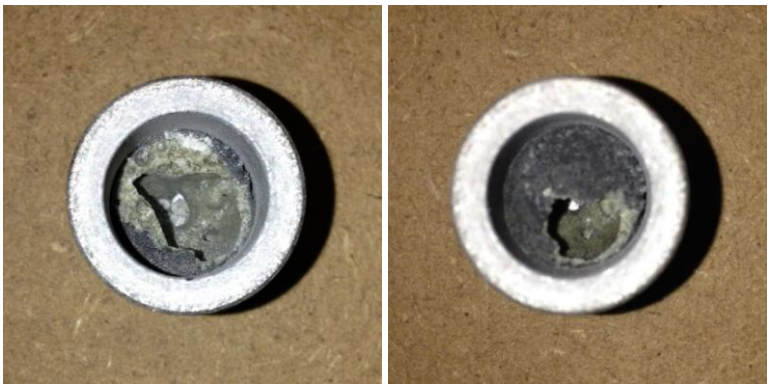

Figure 6-15: Oven after heating modes 3 and 1, showing sintered sample with cavity (after breaking the sintered crust with a hammer)

Figure 6-16: Oven after heating modes 3, 1, and 2, showing swollen and sintered sample with cavity (after breaking the sintered crust with a hammer)

It is unclear why and how this cavity structure depicted in Figure 6-15 and Figure 6-16 formed, but it is suspected that trapped gas led to the formation of the cavity, which was subsequently lodged in the crucible during crust formation through sintering temperatures above 1000 °C. The cavity could have been formed during evacuation of the oven, which allows different interpretations:

1. The evacuation of the sample took much longer than expected and occurred only just before the sintering temperature was reached. Since high vacuum was present in the TVAC before the heating was started, it is unlikely that a sufficiently high amount of gas was still trapped in the sample at this time.
2. The sample was evacuated as planned before the heating was initiated, but occurred so sudden that it formed an eruption in the sample. The simulant particles were blown up and unable to collapse back to the bottom of the sample container. Due to interlocking and arching, the cavity was maintained stable until the sintering temperature led to a solidification of the sample. Gas eruptions and arching are phenomena that have been observed before in vacuum experiments with lunar regolith simulants on larger scale (Kleinhenz, 2014; Reiss *et al.*, 2014).
3. A third explanation is that thermally released volatiles in the sample were responsible for the formation of the cavity, but it is suspected that the initial amount of volatiles in the sample was not high enough to build up such a large gas volume.
4. If the melting temperature was reached inside the sample, another phenomenon could explain the formation of the cavity. When the particles melt, their void spaces merge into a single big void in the centre of the melt. This single void is not destroyed because surface tension supports the melt. When cooling the sample down at a sufficiently high rate, the melt becomes solid leaving the central void space stable.

The difference between the cavity structures and the solid piece observed after the first sample inspection (Figure 6-14) might be explained with the different heating modes that were applied. The preparatory tests that lead to the sample transformation into a single solid piece included a series of heating modes that did not exceed 1000 °C. Only the second to last mode before sample inspection included heating to 1180 °C. It is assumed that the repeated heating to slightly lower temperatures allowed a more uniform sintering process across the sample.

6.3.3 Model Correlation

The experimental results mainly prove the feasibility of heating a larger sample to 1200 °C while consuming 30 W to 40 W in average and less than 70 W peak power. However, these numbers cannot be clearly compared to the thermal analyses presented before (see Figure 6-1 and Figure 6-2), since these were based on thermal models of a much simpler oven design. The latter serves the purpose of indicating the effect of scaling, but for the comparison with the experimental results a more detailed thermal model of the actual test setup is required. A well-tuned simulation model would enable the quick analysis of different design

modifications or environmental conditions that goes beyond the scope of the presented experiments. For this purpose, a thermal simulation model was created with the software COMSOL Multiphysics. The measured power from the experiments was imported into the thermal model and applied to the simulated resistance wire. The simulation results for the temperature of the resistance wire was then compared with the wire temperature that was calculated from the experiments, as described before. The sample was modelled with the thermal properties used to produce Figure 6-1, except for the thermal conductivity which was adapted to fit conductivity measurements of the highland simulant NU-LHT-2M that was used in the tests. Sintering and melting processes that occurred during heating alter the thermal properties of the sample. However, for the model correlation this was not reflected by the simulation model, introducing an error for the calculation of the sample temperature for values above 1000 °C.

Figure 6-17 to Figure 6-19 show the results of the thermal simulations, tuned to fit the experimental data for all three heating modes. With the help of this simulation, the actual temperature of the sample can now be illustrated. It can be seen that the sample core temperature rises much slower than the temperature at the contact between sample and crucible (‘sample surface’). How fast the two temperatures approach each other depends on the heating mode. For the stepped heating in mode 2, the simulation shows a significant mismatch between the programmed temperature profile and the actual sample temperature. Much longer heating durations are required for the lower temperature steps to achieve a steady-state in the sample. Due to the thermal inertia of the sample, also the constant heating rate in mode 1 cannot be achieved. However, for heating mode 3, steady-state in the sample is reached approximately at the same time as it is reached in the resistance wire. Another interesting finding is that for heating mode 3 the sample temperature correlates very well with the temperature of the thermocouple. This is due to similar heat losses along the path from the heat source and was not anticipated. For the other heating modes, the sample temperature is higher than the temperature of the thermocouple in the beginning and lower at the end of the process. This can partly be explained with the fact that the temperature dependency of the material properties was neglected for all materials in the simulation except the sample. In fact, the thermal conductivity of the ceramic wire mount decreases with temperature, so that in reality it becomes more insulating at higher temperature and hence helps maintaining a high sample temperature. For all three simulations, the contact conductance between the resistance wire and the wire mount had to be modified. Because the wire can move inside the mount, this contact is not well defined and can vary strongly between the tests as well as during a single test. Values used for the simulation range from 100 W/(m²·K) for heating mode 1 and 2 to 45 W/(m²·K) for heating mode 3.

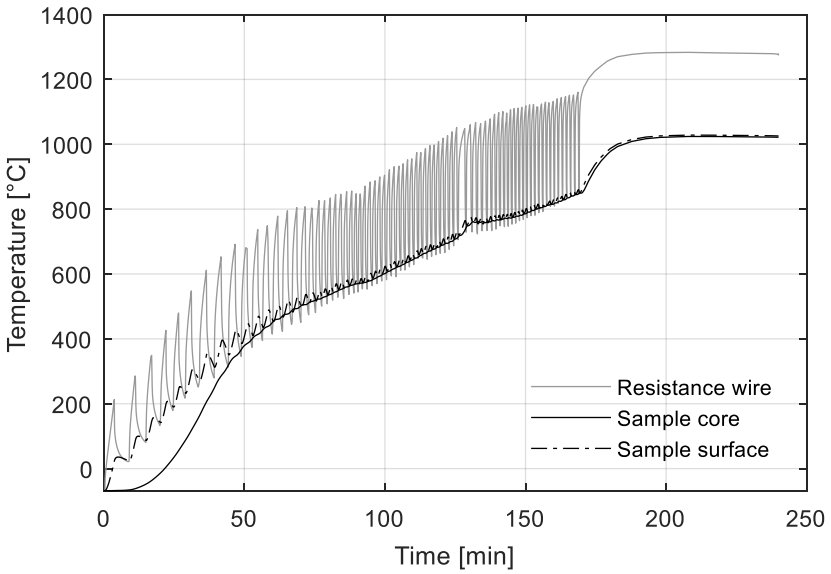

Figure 6-17: Simulated temperatures for heating mode 1 (constant heating rate)

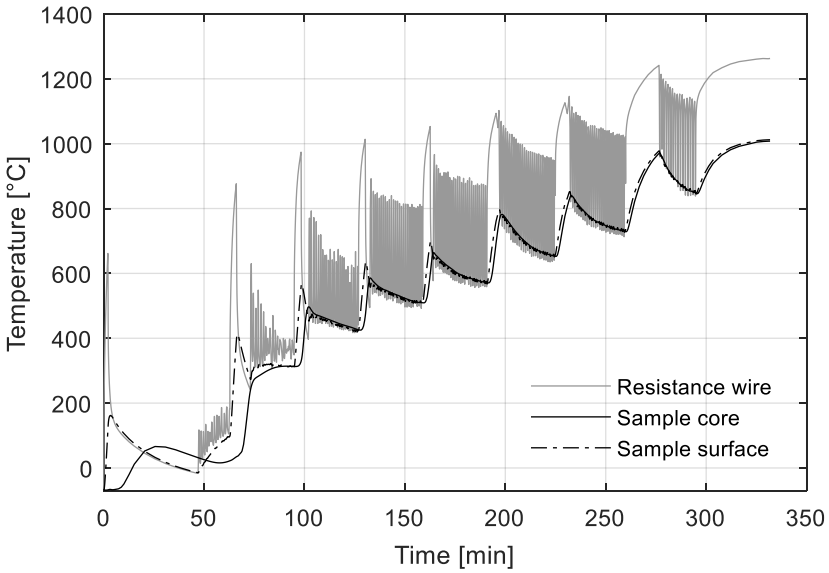

Figure 6-18: Simulated temperatures for heating mode 2 (step and hold)

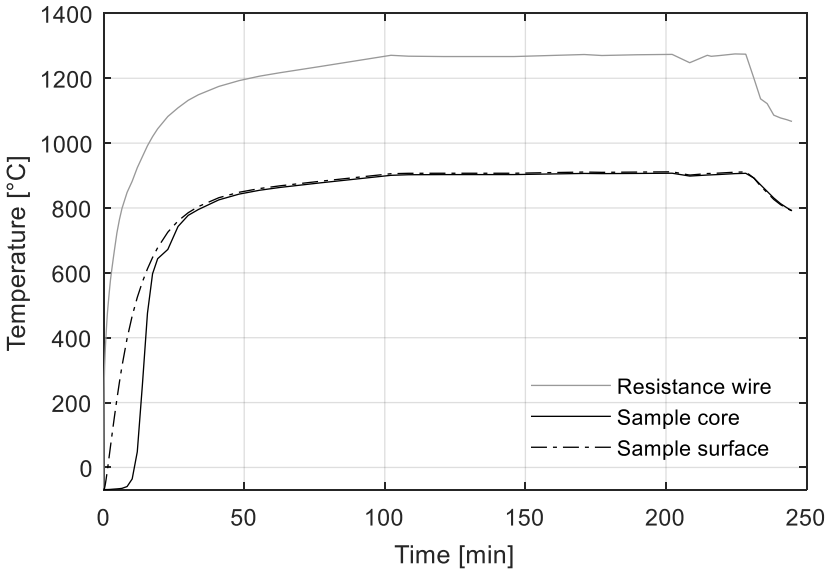

Figure 6-19: Simulated temperatures for heating mode 3 (maximum heating rate)

7 Flow Properties of Lunar Regolith Simulants

This chapter presents the theoretical basics and experimental evaluation of the effect of environmental factors on the sample transfer on the basis of a feed hopper, which is a commonly used device in relevant sample analysis instruments (compare chapter 1.2.2). The experimental work presented here includes the study on regolith flowability that was conducted as part of the second Joint European Partial-g Parabolic Flight campaign (JEPPF-2), hosted by ESA, DLR, and the Centre National d'Études Spatiales (CNES). Furthermore, several laboratory studies on the effect of gas pressure, material choice, and vibration on the flowability of lunar regolith simulants through feed hoppers are presented that complement the studies done in the frame of the partial gravity flight campaign.

7.1 Basics of Hopper Flow

The flow of granular material or powders through a silo, hopper, or similar geometry can either be characterised as mass flow or funnel flow (also known as core flow or plug flow). The former describes a state in which all of the material flows at the same time, which is generally the desired type of flow. In the case of funnel flow only the material in the centre of the hopper flows and the material near the inclined walls moves much more slowly or not at all, which is why these regions are referred to as stagnant zones. Funnel flow is caused by hopper walls that are too flat or have high friction and results in a more erratic and less uniform flow rate (Shamlou, 1988; Schulze, 2008; Ramé *et al.*, 2009). A major problem for mass flow hoppers is a phenomenon called arching, caused by interlocking and edging of coarser particles or high adhesive forces between finer particles. Mechanical arching can be avoided by using hopper outlets that are larger than several times the particle size (Shamlou, 1988; Schulze, 2008). There is a standard procedure for the design of hoppers for both mass flow and funnel flow, based on the findings of Jenike (1964), which results the required half angle and outlet size of the hopper, as depicted in Figure 7-1.

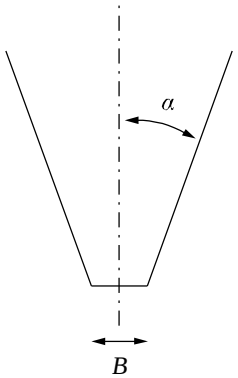

Figure 7-1: Definition of half angle α and outlet width B of a slotted hopper, inclination angle is $(90° - \alpha)$

The basis for the theoretical dimensioning of a hopper is the following statement: *'Gravity flow of a solid in a channel will take place provided the yield strength which the solid develops as a result of the action of the consolidating pressures is insufficient to support an obstruction to flow'* (Jenike, 1964, p. 31). The theory behind the dimensioning process therefore is the assumption that different soils develop different strengths for the same consolidation. The relation of strength versus consolidating pressure of each soil is called the flow function, depicted in Figure 7-2. Similarly, there is a limit of the flow function for each hopper geometry,

below which flow occurs and above which the soil is able to support its own weight and produce arching. This limiting ratio between strength and consolidation pressure is called the flow factor. The point where the flow function of the soil and the flow factor of the hopper intersect determines the critical unconfined yield strength $\sigma_{c,crit}$ of the soil, which in turn defines the minimum hopper outlet size with the following equation (Shamlou, 1988):

$$B_{min} = \frac{H(\alpha) \cdot \sigma_{c,crit}}{\rho_b g} \tag{7-1}$$

Here $\rho_b$is the bulk density and g the gravitational acceleration, α is the half angle of the hopper, measured from the vertical axis, and $H(\alpha)$ is a function that accounts for the thickness of the arch depending on the hopper geometry:

$$\frac{1}{H(\alpha)} = \left(\frac{65}{130 + \alpha}\right)^{i} \cdot \left(\frac{200}{200 + \alpha}\right)^{1-i} \tag{7-2}$$

In equation (7-2) $i = 1$ for circular and square outlets and $i = 0$ for slot outlets, the half angle α needs to be inserted in degrees.

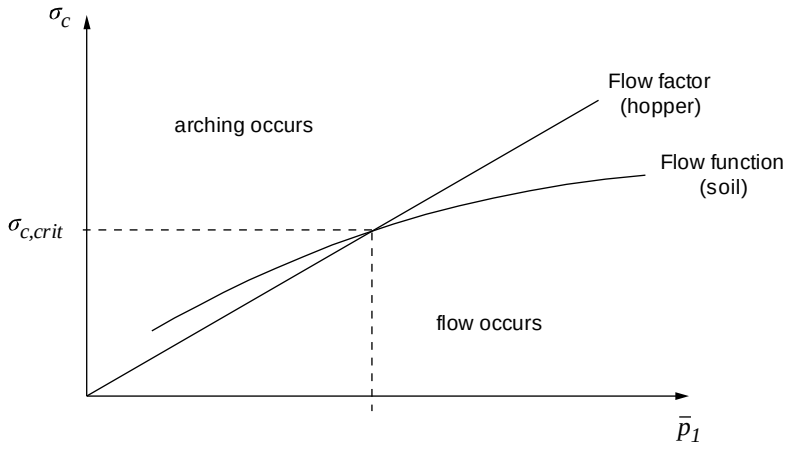

Figure 7-2: Unconfined yield strength σ_c versus major consolidating stress $\bar{p}_1$ with qualitative depiction of flow function, flow factor, and critical unconfined yield strength $\sigma_{c,crit}$, based on Shamlou (1988)

The derivation of the flow function involves the experimental determination of yield loci with a shear cell and the plot of shear stress versus normal stress, the graphical determination of unconfined yield strength and major principal stress by drawing a Mohr semicircle through the origin and the last yield locus, and finally developing the failure function from these values (Shamlou, 1988). The flow factor ff is a function of the half angle of the hopper, the kinematic angle of friction φ_w between the flowing solid and the wall, and the effective angle of friction δ, and can be determined with the following equation:

$$ff = \frac{Y \cdot (1 + sin\,\delta)}{2 \cdot (X - 1) \cdot sin(\alpha \cdot H(\alpha))} \tag{7-3}$$

with X and Y defined by:

$$X = \frac{2^i\, sin\,\delta}{1 - sin\,\delta} \cdot \left[\left(\frac{sin\,2\beta + \alpha}{sin\,\alpha}\right) + 1\right] \tag{7-4}$$

$$Y = \frac{\left(2 \cdot (1 - cos(\beta + \alpha))\right)^{i} \cdot sin(\alpha \cdot (\beta + \alpha))^{1-i} + sin\,\beta \cdot sin^{1+i}(\beta + \alpha)}{(1 - sin\,\delta) \cdot sin^{2+i}(\beta + \alpha)} \tag{7-5}$$

In order to complete the diagram depicted in Figure 7-2, the flow factor needs to be the drawn as a straight line through the origin with slope ff^{-1}. The maximum half angle for mass flow in conical hoppers can be determined independently from the aforementioned process by applying the following equation:

$$\alpha_{max} = \frac{\pi}{2} - \frac{1}{2} cos^{-1}\left(\frac{1 - sin\,\delta}{2\,sin\,\delta}\right) - \beta \tag{7-6}$$

where

$$2\beta = \varphi_w + sin^{-1}\left(\frac{sin\,\varphi_w}{sin\,\delta}\right) \tag{7-7}$$

For slot hoppers the maximum half angle is calculated with the following equation for $\varphi_w < \delta - 3$ (Shamlou, 1988):

$$\alpha_{max} = \frac{exp\left(3.75 \cdot (1.01)^{\frac{\delta-30}{10}}\right) - \varphi_w}{0.725 \cdot (tan\,\delta)^{\frac{1}{5}}} \tag{7-8}$$

For reference, the results of Ramé et al. (2009) are worth mentioning, who have performed a complete dimensioning process for the mass flow of the lunar regolith simulant JSC-1A in conical aluminium and steel hoppers. For different compaction levels with bulk densities from 1.51 g/cm³ to 2.0 g/cm³, consolidation loads from 2500 N/m² to 20000 N/m², internal friction angles from 33° to 68°, and wall friction angles from 9° to 25°, they derived half angles between 19° and 38° (or inclination angles of 52° to 71° respectively) and outlet sizes between 13 cm and 17 cm.

7.2 Reduced Gravity Experiments

This section is an adapted excerpt from Reiss et al. (2014)*, written by the author of the present thesis.*

A partial gravity parabolic flight offers the unique opportunity to repeatedly study processes that last up to approximately 30 s at reduced gravity with the possibility of manual interaction and direct observation by an operator. This opportunity was taken to experimentally study the flow of lunar regolith simulants through slot hoppers and investigate the effect of gravity and hopper geometry. A series of experiments was conducted during each of the four flight days in the frame of the JEPPF-2 campaign and 21 different hopper configurations were tested with the lunar regolith simulants JSC-1A and NU-LHT-2M under lunar and martian gravity, as presented in the following sections.

7.2.1 Experimental Setup and Procedure

The main scope of the experiments was to repeatedly observe the flow of regolith the simulants JSC-1A and NU-LHT-2M in a vacuum environment under reduced gravity. The vacuum requirement prevented the design of an open system. The sample containers were designed similar to an hourglass that can be turned upside down to initiate the material flow from the top funnel into the bottom funnel (Figure 7-3). The containers consist of a machined polyvinyl chloride (PVC) funnel geometry, covered with two polymethyl methacrylate (PMMA) plates on the front and the back side. A separate rectangular vacuum container was designed specifically for this application, using a 400 mm × 220 mm × 25 mm aluminium frame structure and a double layer of glass and polycarbonate covers on front and back side. The vacuum container carried three sample containers and was attached to a horizontal rotation axis to enable the rotation of the entire assembly. For evacuation of the container, a venting hole was included in the aluminium frame (5 mm diameter) as well as in each of the cover plates of the three sample containers (6 mm diameter each). The assembly further contains a manual valve for closing the evacuation line and a pressure sensor to monitor the pressure inside the vacuum container. To prevent the regolith simulant from being sucked through the venting line, paper filters with a pore size <10 µm were added to the venting holes of the sample containers. Two video cameras were used to record the experiment and to obtain data for the post-flight analysis. The video was recorded with a frame rate of 30 frames per second and a resolution of 1920 pixels × 1080 pixels (HD 1080p), at a

field of view angle of 170°. The samples were illuminated by a LED array placed behind the sample container in order to increase the contrast for the video cameras.

Twelve sample containers were manufactured, each having two opposite two-dimensional funnels with different inclination angles and outlet widths. The angles were 55°, 60°, 65°, 70°, and 75°, measured from the horizontal. Two asymmetrical funnels were also produced with inclination angles 55° and 75°, as well as 60° and 70°. Three outlet widths were investigated with all funnels, namely 8 mm, 13 mm, and 18 mm. An exemplary schematic depiction of two sample containers is given in Figure 7-4. The minimum outlet width of 8 mm was chosen in compliance with Schulze (2008), where a width of at least 3 to 7 times the maximum grain size is suggested to prevent arching due to interlocking and wedging of particles (both samples used in the experiments have particles <1 mm). The depth of the sample containers (15 mm, without cover plates) also fulfils this requirement. The design of all hoppers is similar the design envelope of the Dosing Station used within the SPDS of the ExoMars rover (Schulte *et al.*, 2010; Richter *et al.*, 2013; Paul *et al.*, 2017) (compare chapter 1.2.2). The motive for using the asymmetrical funnels was to determine whether any improvement is possible with such configuration for the application with small sample quantities. Schulze (2008) describes that the asymmetrical hoppers generally have no advantages and should only be used if the space around the hopper required this geometrical shape. However, like other aforementioned design principles this might only be valid for larger hoppers and silos. In total, the experiment setup provided 21 different combinations inclination angles and outlet widths.

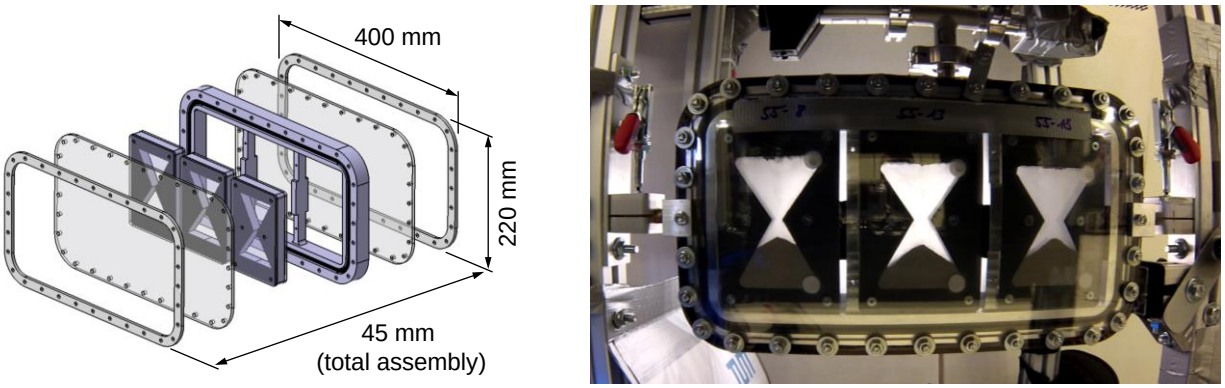

Figure 7-3: Schematic depiction of the vacuum container assembly (left) and picture of the final integration in the aircraft (right), taken by the onboard experiment cameras

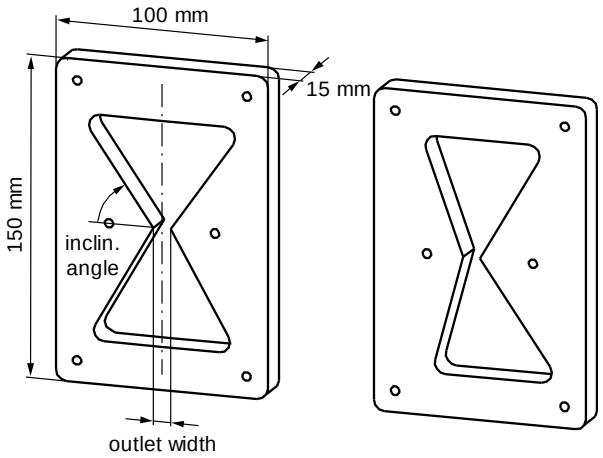

Figure 7-4: Schematic depiction of two exemplary sample containers. Left: symmetrical version with 55° and 60° inclination angle. Right: asymmetrical version with 55°/75° and 60°/70° inclination angle.

On each flight two vacuum containers were used, both equipped with three sample containers having the same inclination angles but varying outlet widths. Prior to flight, the regolith simulant was filled into the containers and each sample mass was determined by weighing. The sample containers were then installed in the vacuum containers and evacuated over night. The pressure was measured before and after each flight to determine the approximate leak rate. The onboard use of a vacuum pump was technically and safety-wise not feasible for this experimental setup. During the parabolic flight campaign four flights were conducted, each including 30 parabolas. The flight sequence consisted of one Mars-*g* test parabola, two sets of 6 Mars-*g* parabolas, followed by two sets of 6 Moon-*g* parabolas, and one set of 6 zero-*g* parabolas. This sequence was repeated in the same order on all four flights. The duration of the reduced gravity phase varied from approximately 22 s for zero-*g* parabolas, over 26 s for Moon-*g* parabolas, to 33 s for Mars-*g* parabolas. The two vacuum containers were exchanged between each parabola set because only one could be examined at a time. In that way each hopper configuration could be tested under all gravity levels. The zero-*g* phase was not used for this experiment. During the hyper-*g* phase in the beginning and the end of each parabola the vacuum container was locked to prevent unintended rotation around the horizontal axis. During the reduced gravity phase the container was manually turned by the operator to be aligned with the gravity vector. No additional tapping or vibration was applied to the container to produce an undisturbed flow driven by gravity only. Depending on the flow rate of the sample, the container was turned multiple times during a single parabola. This procedure allowed a minimum of three repetitions for each combination of sample material, hopper configuration, and gravity level.

The main objective of the experiments was the determination of sample flow rates. For post-flight analysis the flow duration was measured visually from the video data taken by the onboard cameras. Start and end time of the flow was obtained with a resolution of 1/30 s at a frame rate of 30 frames per second. The start of flow was defined as the moment when the sample containers were rotated by 90°, meaning that the containers were in horizontal position. The end of flow was defined as the moment when the material entirely left the upper funnel (not including material that remained sticking to the upper funnel walls). The respective flow rate was then determined by dividing the sample mass in each container by the flow duration. The following evaluation is based on 925 values for sample flow rates in total, attributed to different gravity levels and hopper configurations, as summarised in Table 7-1. For each evaluation type (flow rate versus hopper configuration, flow rate versus gravity, flow rate versus outlet width), the mean values and standard deviation were determined. Values that exceed a deviation of twice the standard deviation from the mean value were defined as outliers and therefore excluded from the following analyses.

Table 7-1: Overview of all partial gravity measurements

Gravity	Sample material	Number of measurements	Values considered for further analysis
Earth (1 *g*)	JSC-1A	105	105
Mars (0.38 *g*)	JSC-1A	210	203
Moon (0.16 *g*)	JSC-1A	50	49
Earth (1 *g*)	NU-LHT-2M	105	105
Mars (0.38 *g*)	NU-LHT-2M	324	310
Moon (0.16 *g*)	NU-LHT-2M	131	128

7.2.2 Initial Observations

During preparatory testing of the experiment hardware in the laboratory, several observations were made that influenced the design of the flight hardware. These mainly were the impact of ambient pressure on the material flow, as well as the electrostatic charging of particles and its consequences for the experiment.

Under ambient pressure (approximately 1 bar), the gas inclusions in the regolith restricted the material flow. Interlocking between the particles of the sample, combined with counter-flowing residual air, lead to the creation of arches. As the arch partly broke off, the included gas was released and caused ‘dust fountains’, as depicted in Figure 7-5. In a test series the ambient pressure was reduced stepwise to detect the pressure level at which this phenomenon could no longer be observed. The dust fountains did not occur at pressure levels below approximately 1 mbar to 2 mbar. For the parabolic flight experiment it was therefore decided to aim for maintaining pressures below this level inside the vacuum container.

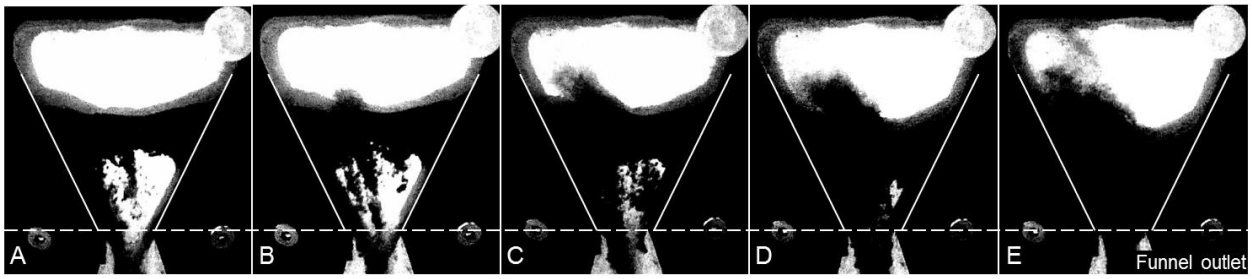

Figure 7-5: Arching and abrupt release of gas inclusions in the regolith lead to the formation of dust fountains. A: arching at maximum stress, B: arch collapses, C: air permeates through the arch to the upper funnel volume, D: material continues flowing, E: continuation of mass flow. To improve the visibility of the sample particles, the original video stills were converted into monochromatic images and the contrast was increased. The filter covering the venting hole is visible in the upper right corner of each image.

Besides the residual gas, humidity also impacts the flowability of the sample material and increases the probability of arching. The gas pressure of water at room temperature (15 °C) is approximately 17 mbar, hence it was assumed that most of the water would be outgassed at the aforementioned pressure level after a pre-flight evacuation over night of approximately 12 h. The exact moisture content of the samples at the time of experiment could not be determined inside the sealed containers, but was assumed sufficiently low due to the vacuum exposure.

Another factor for the flowability of the sample is the electrostatic charging that results from friction between the particles and between particles and the sample container. The sample containers for the experiment were made from PVC and PMMA. Depending on the amount of electrostatic charge that can be accumulated, this charging can lead to perturbations in the granular flow. Anderson et al. (2009) and Berkebile and Gaier (2012) suggest that these effects are mainly to be considered in an ultra-high vacuum where discharging through residual moisture or gas collisions cannot occur. Hence, electrostatic charging is less a significant factor for the flowability in the low vacuum environment of this experiment. However, electrostatic charging has another more obvious effect on the test setup. In preliminary laboratory tests it was observed that smaller dust particles adhere to the PMMA cover plate and lead to an obscured view. This effect was much stronger for the simulant JSC-1A than for NU-LHT-2M. Additionally the mare simulant JSC-1A is significantly darker than the highland simulant, which increased the obscuring effect on the transparent cover. Gaier, Street and Gustafson (2010) determined the solar absorptance of both simulants to be 0.817 for JSC-1AF and 0.556 for NU-LHT-2M, along the investigated variants of both types the mare simulants generally have a higher absorptance than the highland type. Such adherent particles could only be removed mechanically with a brush or by rinsing with water. Both solutions were not applicable for the evacuated sample containers. To improve the visibility for the cameras through the obscured cover plate, a backlighting setup was added to the experiment as described before (Figure 7-3).

During operation of the experiment, several problems were encountered regarding the sample flow, whereas some problems occurred only occasionally or only during the Moon-*g* phase:

1. Residual sample material stuck to the upper wall of the sample container.
2. Residual sample material stuck to the inclined walls of the sample container.
3. The volume of the sample increased (resulting a lower bulk density) over the capacity of the lower funnel at lower gravity and prevented further material flow.

4. The sample flow lasted longer than the available duration of the reduced gravity phase (only during Moon-*g*, where the reduced gravity phases lasted approximately 26 s).
5. Material got completely stuck in the upper funnel (only during Moon-*g*).

The most unanticipated and perturbing problem was that the consolidation (or bulk density) of the sample under reduced gravity was significantly lower than under Earth-*g*. This lead to a 10 % to 14 % increased material volume of depending on the gravity and the type of simulant (Reiss and Walter, 2013), and subsequently to an increased size of the heap in the lower funnel. In some cases this prevented further material flow from the funnel above. After the first flight day, this problem was solved by reducing the quantity of sample material in the sample containers. It was expected that the hyper-*g* phase (approximately 1.8 *g*) before each parabola would lead to higher consolidation of the sample. However, this would only have affected the first rotation of the sample container during each parabola. The post-flight analysis showed that the effect on the sample flow is negligible or smaller than the measurement accuracy. Additional evaluation proved that the hyper-*g* phase had no visible impact on the sample compaction (Reiss and Walter, 2013).

The problem of material sticking to one of the container walls occurred more often for the sample NU-LHT-2M, although the quantity of residual material in the upper funnel was small compared to the total sample mass. In all experiments the sample flow could be characterised as mass flow. Although the flow got significantly slower and less continuous with smaller gravity, the inclination angles of all hoppers were steep enough to prevent funnel flow. Nevertheless, with smaller gravity the risk of arching increased, which lead to flow rate restrictions and the aforementioned formation of dust fountains. Arching is known to be a main problem in the mass flow regime (compare chapter 7.1) and was also the most often observed phenomenon during the partial-*g* experiments. Due to the sufficiently large hopper outlet (minimum 8 times the largest particle size), the observed arching is assumed to be mainly caused by the cohesive strength of the sample material. Another factor for the observed arching is counter-flowing residual air from the lower funnel.

During the experiments the ambient pressure in the sample containers was kept in the range of 0.07 mbar to 6.10 mbar. The pressure was measured prior to flight and directly after flight, which was about 5 h to 6 h later. Besides leakage in the assembly, the pressure increase over flight time was explained with outgassing of the plastic materials and residues in the sample material. Regarding gravity level the requirement of the flight operator was to maintain a tolerance band of ±0.05 *g* during all parabolas. According to the flight acceleration data provided by the flight operator Novespace, this requirement was met for almost all of the flight manoeuvres. Only 13 out of 100 partial-*g* parabolas included minor (below 0.05 *g*) deviations from this tolerance band.

The number of flow repetitions for each hopper configuration ranged from 2 to 9 per parabola, depending on the duration of the reduced gravity phase and the flow rate. The sample masses in the hoppers ranged from 27 g to 46 g, depending on the available volume in the sample containers. The stress on a sample depends on its consolidation, which mainly is a function of the sample mass. However, since the sample masses did not vary strongly in the experiments, it is assumed that the different pre-consolidation created by the weight of the samples did not affect their flow rates significantly.

7.2.3 Flight Results

The results of the parabolic flight experiments are presented and discussed in the following regarding the sample flow rate and the influence of gravity, outlet width, inclination angle, and sample material.

Sample Flow Rate

Figure 7-6 to Figure 7-8 show an overview of the resulting mean flow rates for different hopper configurations and sample materials. During benchmark measurements under Earth-*g*, mean flow rates of up to 101 g/s for JSC-1A (75° inclination, 18 mm outlet) and 109 g/s for NU-LHT-2M (70° inclination, 18 mm outlet) were measured. Under Mars-*g* the maximum values were 40 g/s for JSC-1A (75° inclination, 18 mm outlet) and 40 g/s for NU-LHT-2M (55°/75° inclination, 18 mm outlet). Under Moon-*g* the maximum flow rates were 21 g/s for JSC-1A (70° inclination, 18 mm outlet) and 22 g/s for NU-LHT-2M (75° inclination, 18 mm outlet). In general, the standard deviations of flow rates for the thinner funnels with 8 mm outlet width are smaller

compared to the wider funnels. For some configurations no data was collected during Moon-*g* parabolas due to the aforementioned problems (larger sample volume leads to overflow in the lower funnel, clogging of the sample, or because the duration of the reduced gravity phase was too short to empty the upper funnel).

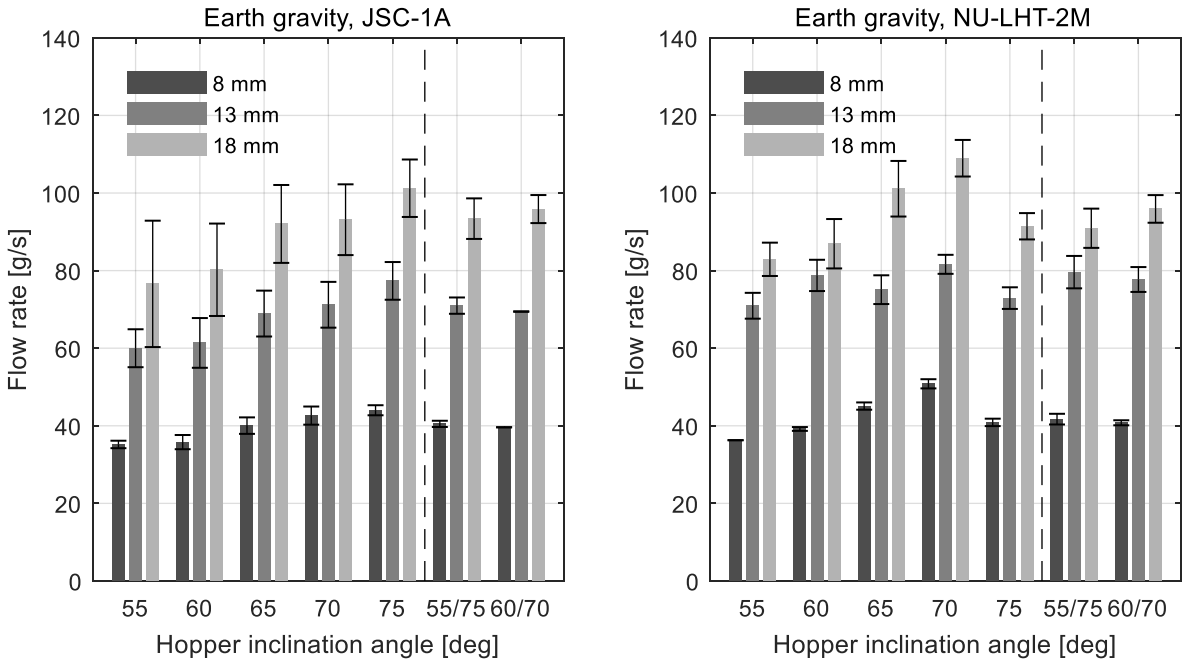

Figure 7-6: Flow rates (mean value and standard deviation) under Earth-*g* in hoppers with varying inclination angles and outlet widths

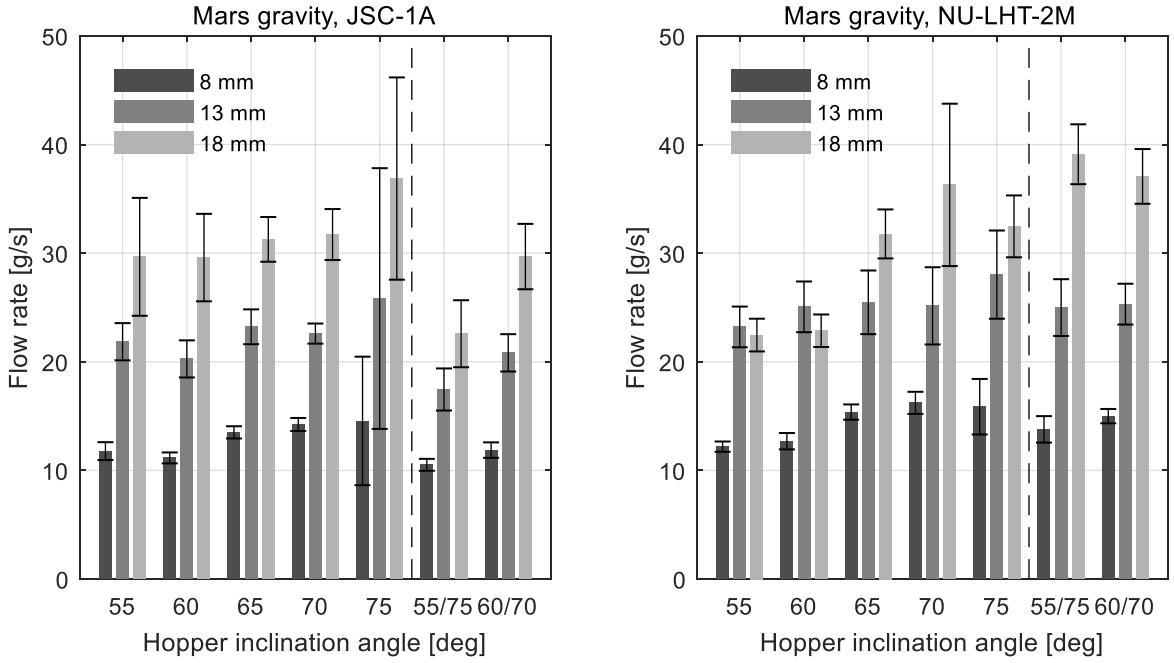

Figure 7-7: Flow rates (mean value and standard deviation) under Mars-*g* in hoppers with varying inclination angles and outlet widths

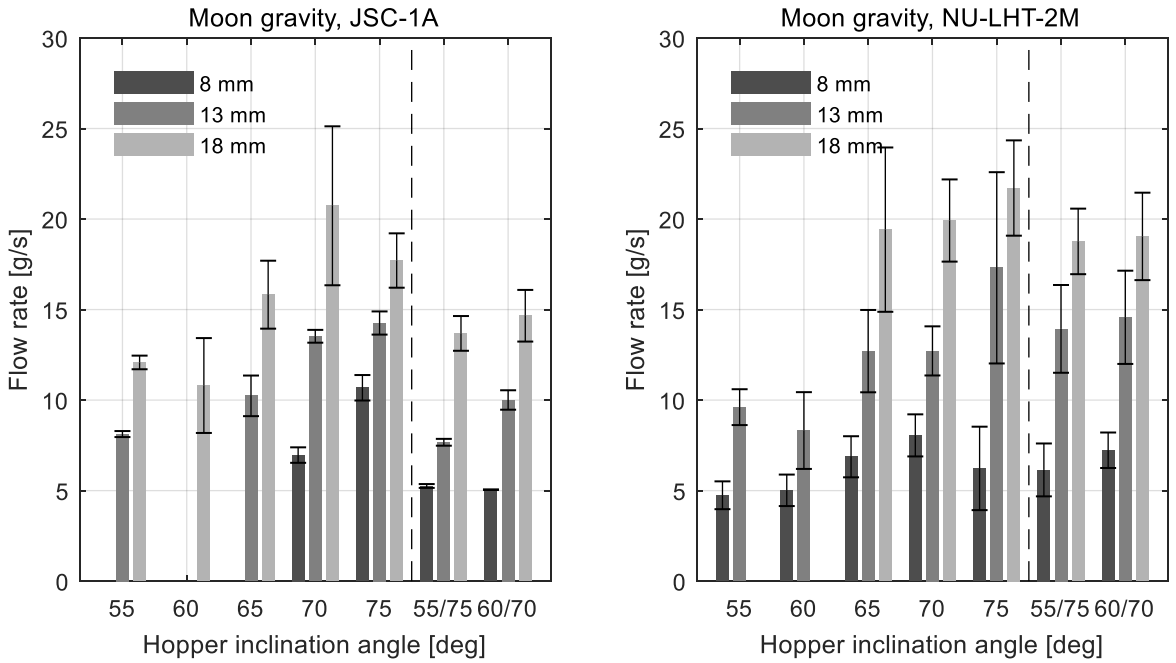

Figure 7-8: Flow rates (mean value and standard deviation) under Moon-*g* in hoppers with varying inclination angles and outlet widths

Influence of Gravity

As expected, the flow rates decrease with lower gravity, which also means that the experiment could be repeated more often during Mars-*g* than during Moon-*g* parabolas. Plotting the mean flow rates of each of the 21 different hoppers versus gravity clearly shows this behaviour (Figure 7-9). In an attempt to determine the character of the relation between gravity and flow rate, different regression curves were fitted to the mean values of each hopper with the method of least squares. Table C-3 and Table C-4 in the appendix summarise the coefficients for a linear and square fit in the form $y = a \cdot x + b$ and $y = a \cdot x^2 + b$, both with $b \neq 0$ and $b = 0$. To evaluate the quality of the curve fit, the coefficient of determination R^2 is provided. Although there are different optimum fit types for each hopper, the linear fit generally results in a better R^2 value. For most hoppers the best fit is achieved by the linear regression with $b \neq 0$. In most cases b is negative, which physically means that the sample flow stops before the gravity is zero (negative flow rates are neglected). One explanation for this effect is that the cohesive force exceeds the gravitational force and hence the sample flow comes to a halt. However, to characterise the exact flow behaviour close to zero gravity, more data in this area is required. The square regression curve in all cases returns a relatively high positive value for b, which physically makes no sense. Although the coefficient of determination for some square fits is better than for the linear fit, they are not considered further due to the suggested positive flow rate at zero gravity. Figure 7-9 shows the linear regression fits with $b \neq 0$.

To determine the relative proportionality between flow rate and gravity, the mean flow rates of each hopper were normalised to the mean value at Earth-*g* and plotted versus gravity normalised to Earth-*g* (Figure 7-10). The plot shows that the relative values are distributed around the dotted line that represents direct proportionality. A decrease of gravity from 1 *g* to 0.38 *g* (Mars) leads to a decrease of flow rates by a factor of 0.24 to 0.39 for JSC-1A and 0.26 to 0.43 for NU-LHT-2M. A decrease from 1 *g* to 0.16 *g* (Moon) leads to a decrease of flow rate by a factor of 0.11 to 0.24 for both JSC-1A and NU-LHT-2M. The parameters outlet width and inclination angle do not influence the scaling significantly in the presented experimental setup.

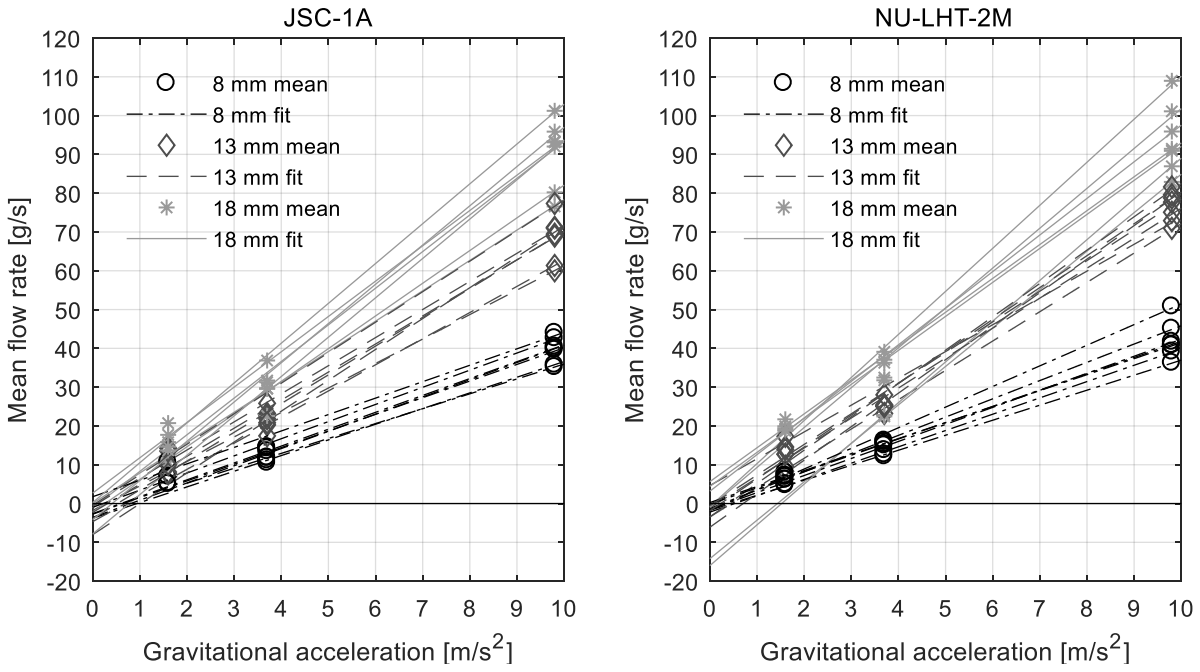

Figure 7-9: Mean flow rates of each hopper with inclination angles from 55° to 75° and outlet widths from 8 to 18 mm, a linear fit in the form $y = a \cdot x$ was applied to the mean values using the method of least squares

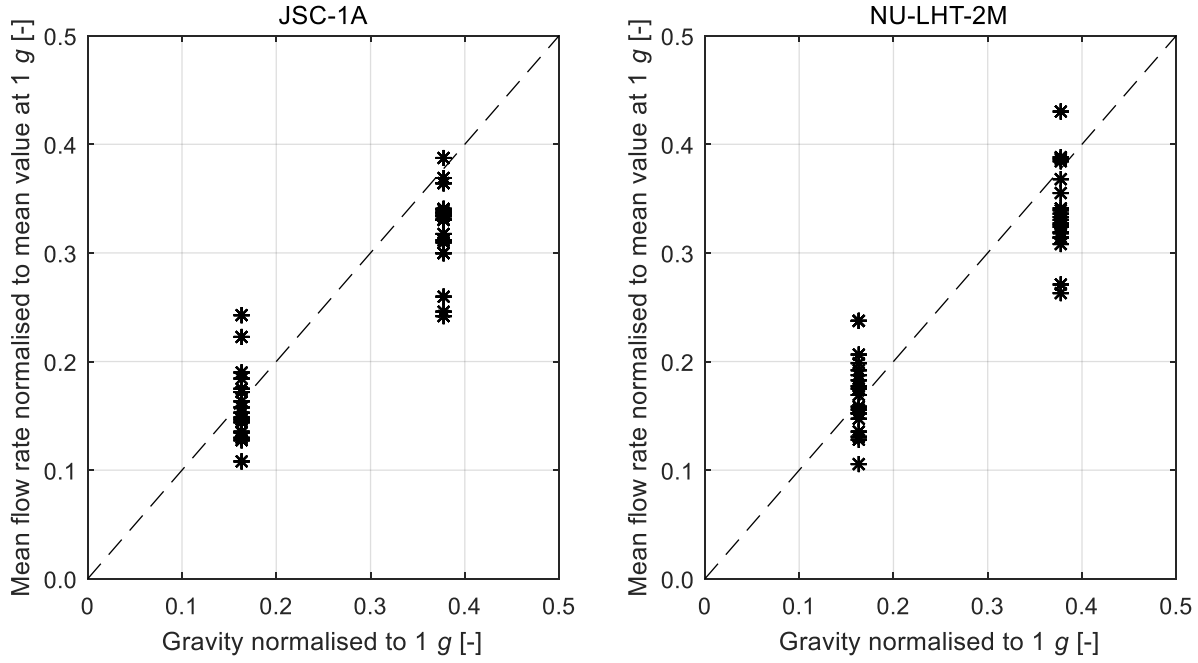

Figure 7-10: Mean flow rates of each hopper normalised to mean values under Earth-g versus normalised gravity

Influence of Outlet Width

In almost all examined hopper configurations the enlargement of the outlet lead to an increased flow rate. The only exception to this rule was observed during Mars-*g* parabolas where the simulant NU-LHT-2M showed either only a small increase or a decrease of flow rate when comparing the 13 mm with the 18 mm outlet width. It is assumed that the flow rates discussed here directly depend on the cross-section area of the hopper outlet, similar to conventional silo guidelines (Schulze, 2008). In the experiments the outlet was

rectangular with a fixed depth, so that in this case there would be a direct dependence between flow rate and outlet width. To verify this, the mean flow rates of each hopper were normalised to the values measured with the respective 18 mm outlet width. The results were plotted against the normalised outlet width in Figure 7-11. It can be seen that the values group around the dotted line, which represents a direct proportionality. When scaling the outlet from 18 mm down to 13 mm by a factor of 0.72, the mean flow rate decreases by a factor of 0.56 to 0.81 for JSC-1A and 0.64 to 0.91 for NU-LHT-2M. When decreasing the outlet width from 18 mm to 8 mm by a factor of 0.44, the mean flow rate decreases by a factor of 0.34 to 0.60 for JSC-1A and 0.29 to 0.56 for NU-LHT-2M respectively. Gravity and inclination angle did not show a significant influence on the relation between flow rate and outlet width.

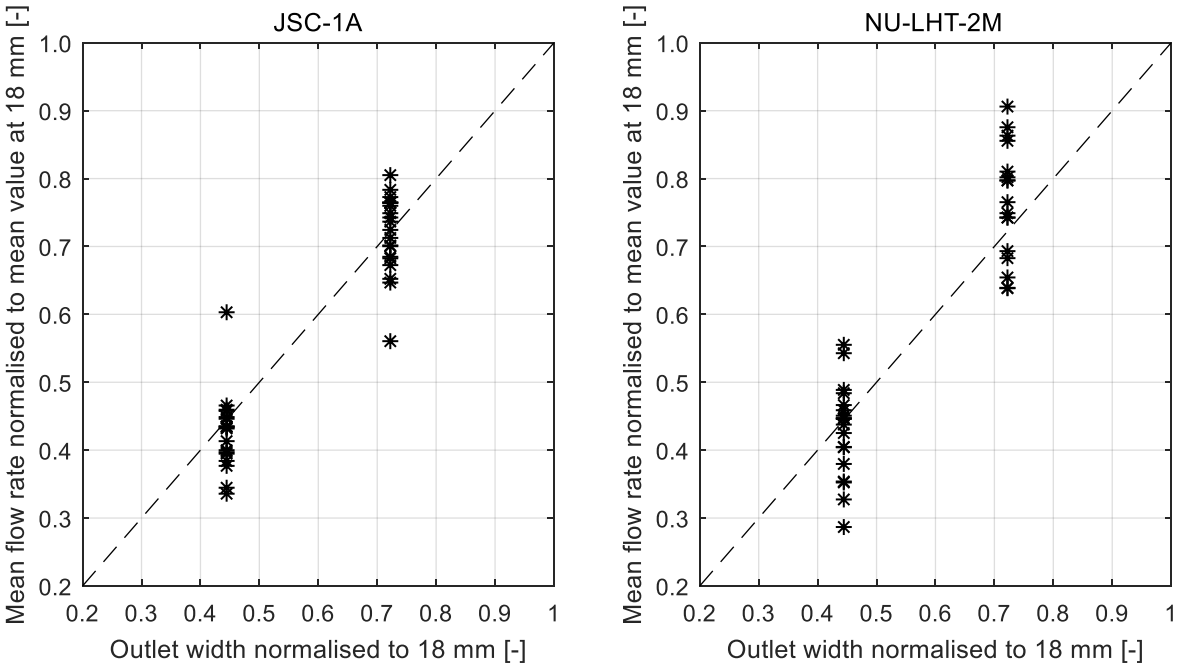

Figure 7-11: Mean flow rates for each hopper normalised to values measured with 18 mm outlet width, versus normalised outlet width

Correlation between the Influence of Gravity and Outlet Width

As introduced earlier, the stress of the sample at the outlet, which determines the material flow, is directly dependent on the outlet width and gravity (Schulze, 2008). This tendency can also be derived from the experiment results, as previously shown. When designing a hopper for laboratory tests on Earth, these relations can help to scale the hopper for simulating different gravity environments. If a lunar application shall be simulated, the hopper outlet would have to be reduced by a factor of 0.16 in order to produce the same flow rate as it would on the Moon (following a direct proportionality). Figure 7-12 exemplarily shows the mean flow rates of the hopper with 70° inclination angle, depending on gravity and outlet width. The linear fit allows the extrapolation of the measured data to a certain extent. It was chosen to force the regression through the origin to avoid positive flow rates for an outlet width of zero, which would be created for some of the optimum regression curves. For the 70° hopper it can be seen that to reach a flow rate of for instance 20 g/s under Moon-*g*, the hopper outlet would have to be 19 mm wide. The same flow rate under Earth-*g* could be produced with the same hopper inclination, but a smaller outlet of about 3 mm to 4 mm. However, one must be careful with extrapolation of the given data, especially for very small outlet widths near the maximum grain size of the sample and near zero gravity. Here other effects, such as cohesion, might affect the proportional dependence between these parameters.

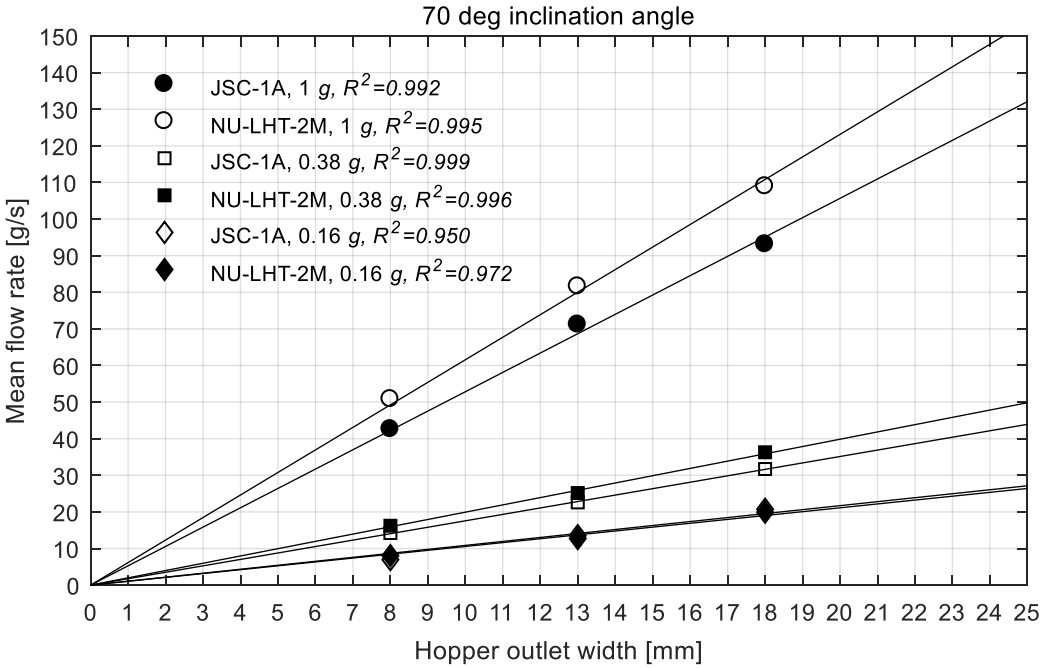

Figure 7-12: Mean flow rate over outlet width for an exemplary symmetrical hopper with 70° inclination angle. A linear fit through the origin with the method of least squares is provided together with the coefficient of determination R² for each fit.

Influence of Inclination Angle

When increasing the inclination angle from 55° to 70°, an increase of flow rate was observed for nearly all combinations of sample material, outlet width, and gravity (see Figure 7-6 to Figure 7-8). However, some configurations, especially under reduced gravity, did not follow this trend. In some cases the flow rate produced by the 75° inclination was unexpectedly lower than for the smaller inclination angles. The asymmetrical combinations of 55°/75° and 60°/70° in most cases showed no absolute improvement of the flow rate. However, for the sample NU-LHT-2M, this configuration of two different angles yielded higher flow rates than the symmetrical configurations with the same angles, for instance 55°/55° or 60°/60°. Especially for the Moon-*g* phase the asymmetrical design allowed material flow where the symmetrical design lead to clogging.

Influence of Sample Material

The experiment data did not reveal any clear relation between flow rate and sample material that could be regarded as generally valid. However, the highland simulant NU-LHT-2M showed a slightly more cohesive behaviour. Small fractions of residual material always remained sticking to the upper wall of the top funnel, which was not the case for JSC-1A. Another observation was the release of smaller dust particles during operation. The JSC-1A samples apparently contained more visible dust particles than NU-LHT-2M, since the transparent cover of the experiment containers was significantly more clouded for the former.

7.3 Gas Pressure Experiments

As described in the previous section, a significant hindrance of the regolith flow was observed due to arching and partial blocking in the funnel (compare Figure 7-5). It was assumed that this phenomenon was caused by restricted gas flow from the lower to the upper funnel and hence is also gas pressure dependent. To address this problem, a series of isolated tests with the 75° funnels and NU-LHT-2M was performed after the parabolic flight campaign in the frame of a semester thesis (Tattusch, 2013), initiated and supervised by the author of the present thesis. The containers were filled with a similar amount of regolith as in the parabolic flight experiments and placed into a vacuum chamber with a mechanical feedthrough that allowed rotation

of the containers from outside the chamber. The vacuum chamber was evacuated to pressures $<5 \cdot 10^{-3}$ mbar before the vacuum pump was separated from the chamber by closing a manual valve. The leak rate was then adjusted through a leak valve to reach a pressure increase of approximately 0.1 mbar/s. During the pressure rise in the chamber, the containers were rotated to initiate the flow of the sample. When a significant hindrance of the flow occurred, the according gas pressure in the chamber was noted. The following three distinct phases of flow hindrance were observed for all three containers with 75° inclination angle and outlet widths 8 mm, 13 mm, and 18 mm:

1. Phase 1 'Dust fountains'

   This first phase was defined as the beginning of visible dust fountains before the sample passes the outlet, similar to the ones observed during the parabolic flight experiments. However, the dust eruptions were not always visible as fountains, but more as a cloud of dust above the sample. Figure 7-13 shows a more distinguished example of this phase.

2. Phase 2 'Stagnating flow'

   As pressure increases, the dust fountains become more clearly visible with higher amplitude and earlier occurrence in the flow process. Subsequently this leads to a partially blocked flow, which marks the second phase. As depicted in the image sequence Figure 7-13, the flow stagnates and the filling height in the upper funnel remains nearly constant (images 1-3 in the series). Because the lower part of the sample continues to flow, a cavity is visible (image 4) before the mass flow suddenly continues with an eruption (image 5-6).

3. Phase 3 'Arching'

   At higher gas pressures the flow starts to be completely blocked. Figure 7-13 shows the formation of an arch that prevents further flow. In most cases however this arch is unstable and collapses after a short time.

Figure 7-14 shows an overview of all three phases with the respective gas pressure at which each phase was observed. The tendency is the same for all three funnels, while the larger outlets were not as susceptible to arching as the smaller outlets. This might be because the distance between both inclined walls is too large to allow the formation of a semi-stable arch, but it could also be addressed to an improved gas circulation from the lower to the upper funnel and hence an improved flow.

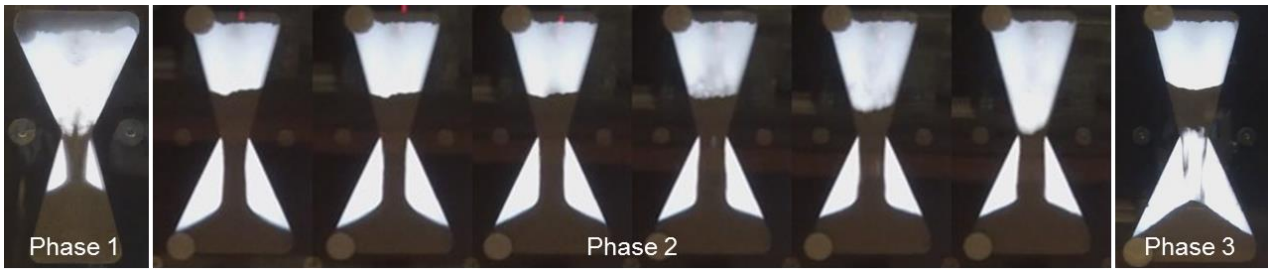

Figure 7-13: Three phases of the observed flow hindrance due to residual gas pressure, based on Tattusch (2013)

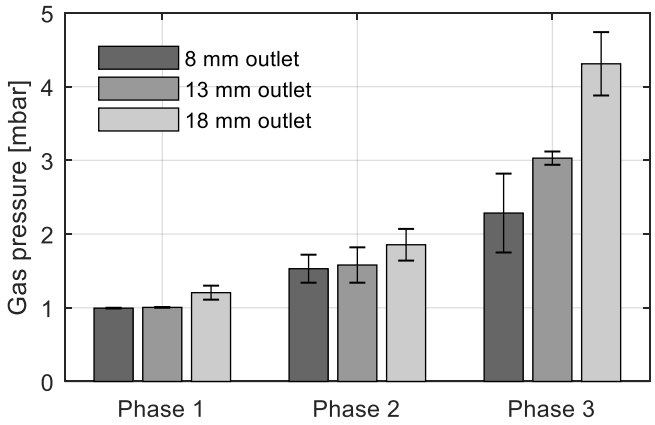

Figure 7-14: Gas pressure for flow hindrance phenomena observed for the 75° funnel with mean values and ranges of two measurements per outlet width

To check whether an improved gas circulation from lower to upper funnel would lead to an improved sample flow, an enhanced version of the sample containers from the parabolic flight was developed (Figure 7-15). This version has the same outside dimensions but includes an air duct next to the inclined walls and fixation points for vibration motors near the four corners of the container (not visible in the picture). The latter were added because the positive effect of vibration on the material flow should also be investigated with this setup. The frame structure of the container was made from aluminium and the front cover from PMMA. In order to investigate the effect of triboelectric charging, the back plate and the inclined walls were designed exchangeable and made from three different materials: PVC, aluminium, and steel. For the gas pressure tests presented here, only the PVC version was considered. Again the container was filled with NU-LHT-2M, while care was taken that the filling height of the lower container was low enough to not block the air ducts. The first test with 27.3 g of sample under ambient pressure showed none of the aforementioned flow hindrances. A second test with 40.7 g of sample delivered the same results, which was a clear indication that the restricted gas flow in the original containers was the reason for the observed dust fountains and flow blocking. To further confirm this, the air ducts were blocked using paper rolls and polyimide tape. Additionally all of the venting holes were also blocked. This measure then lead to the aforementioned Phase 2 type flow behaviour at ambient pressure. Since no more evidence of the functionality of the air ducts was required at this point, the originally planned tests under vacuum where discarded.

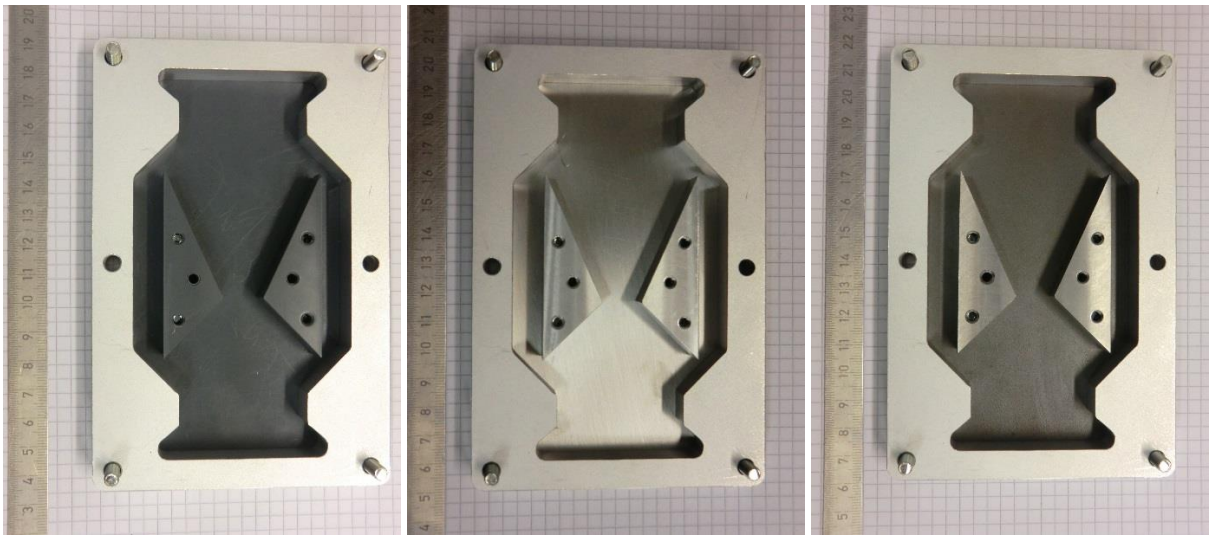

Figure 7-15: Pictures of the enhanced versions of the sample container with different materials for back plate and inclined walls (from left to right: PVC, aluminium, steel) (Tattusch, 2013)

7.4 Vibration Experiments

Because mechanical agitation, for instance through vibration, is a common measure to improve granular flow, its effects on the previously described hopper setup were also investigated by Tattusch (2013) in the frame of a semester thesis initiated and supervised by the author of the present thesis. Four electric motors with unbalanced masses, which were originally designed for vibrating mechanisms in mobile phones, were installed inside the frame of the improved sample container (Figure 7-15) with their rotation axis being in the same orientation as the rotation axis of the sample container. The latter was again installed in the vacuum chamber as described in the previous section and evacuated to pressures where the aforementioned Phase 3 flow behaviour occurs (Figure 7-14), since originally it was intended to investigate the effect of vibration on arching. Because with the air ducts arching did no longer occur, it was decided to investigate the effect of vibration on the discharge times of the funnel instead. This was done at excitation frequencies of 0 Hz, 30 Hz, 45 Hz, 60 Hz, 75 Hz, 90 Hz, 105 Hz, 120 Hz, and 135 Hz. From the results presented in Table 7-2 and Figure 7-16, it is difficult to conclude on a general trend, since the resulting discharge times are fairly similar. However, it appears that frequencies between 60 Hz and 105 Hz tend to have a positive effect on the discharge times. Measurement errors have a relatively large effect on the results, since the experiment was operated manually and discharge times were determined through visual inspection of video footage. In an attempt to rule out the influence of varying rotation times, the duration of discharge was exemplarily plotted against the duration of rotation in Figure 7-17. It is obvious that there is no visible relation between the two, which is why at least this source of error can be neglected.

Table 7-2: Discharge times for different excitation frequencies, based on Tattusch (2013)

Excitation frequency [Hz]	Mean discharge time [s]	Standard deviation [s]	Number of measurements
0	2.039	0.230	16
30	1.987	0.248	21
45	2.018	0.256	29
60	1.925	0.152	27
75	1.880	0.180	29
90	1.813	0.158	19
105	1.837	0.149	19
120	1.981	0.183	13
135	2.086	0.121	8

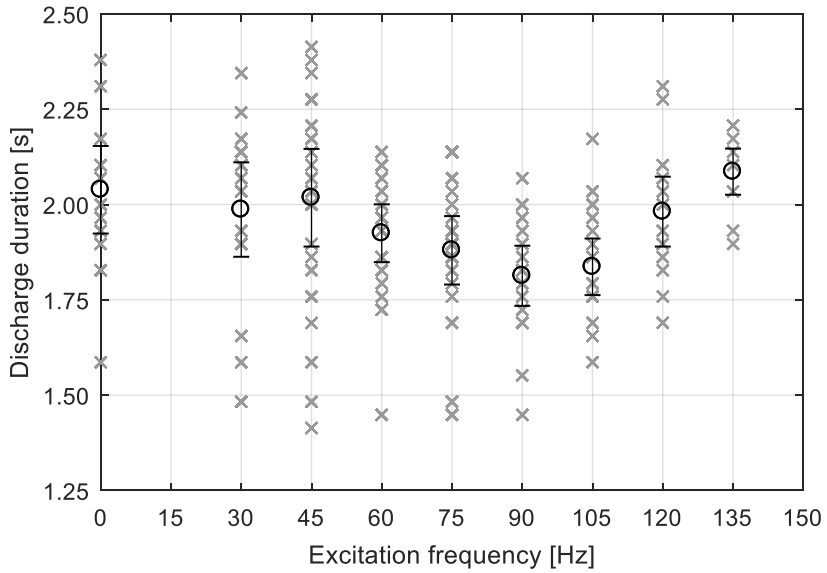

Figure 7-16: Discharge times versus excitation frequencies for the enhanced sample container, with mean values and standard deviation, based on Tattusch (2013)

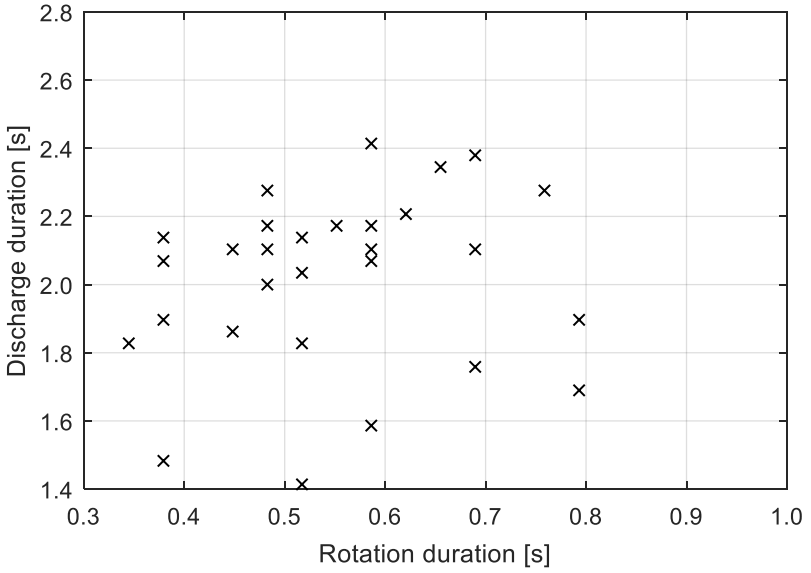

Figure 7-17: Discharge times versus rotation times at an exemplary excitation frequency of 45 Hz, based on Tattusch (2013)

8 Conclusion and Outlook

8.1 Summary

The primary objective of this thesis was to enable a better understanding of the process of volatiles extraction from lunar regolith as a whole. This included a thorough research about the involved physical processes and an analysis of their interdependencies. The theoretical foundations developed in chapter 2 are considered complete regarding the most relevant and dominating phenomena for the volatiles extraction process. This includes the mechanisms of desorption, gas transport through a porous lunar regolith sample, resorption within the sample, and heat transfer. Since lunar regolith and its analogues are a complex mixture of different particle shapes and sizes with different chemical composition, each of the physical processes involves a number of unknowns that are difficult to determine when using the bulk material. However, for an in-situ extraction of volatiles from lunar regolith it is the bulk material that is relevant. The present thesis discusses effects that arise from the interplay of different micro-scale heat and mass transfer processes within the sample and are measurable with in-situ instrumentation on a larger scale. This includes sample temperatures, gas pressures, process duration, and power demands. An analysis of the combined effects of heat and mass transfer on the release of volatiles from a regolith sample was made possible through the implementation of the theoretical basics into a combined simulation model and subsequent parameter studies (chapter 3). The latter include the variation of initial water concentrations in the sample, its particle size fraction, bulk density, and applied heating rate.

A variety of experimental studies was performed in the frame of this thesis to address the various aspects of volatiles extraction from lunar regolith samples. To verify the simulation results regarding the release of volatiles and test the effect of different sample conditioning methods, an experimental setup and according procedures were established to enable the controlled hydration of the lunar regolith simulant NU-LHT-2M, the thermal extraction of volatiles from this simulant, and their subsequent analysis at Moon-like ambient conditions. The effect of initial water content, particle size, bulk density, sample mass, and heating mode on the outgassing of different volatile species was investigated through experimental studies with this setup (chapter 4). The resulting characterisation of the volatiles extraction process depending on different influence factors and boundary conditions helps to understand and interpret future in-situ measurements that will be made by gas analysis instruments. Furthermore, a number of new findings regarding the volatile content released from NU-LHT-2M at higher temperatures were made, which will inform future laboratory studies with this simulant. The same experimental setup as used for the volatiles extraction demonstration was used to study the possibility of chemically reducing the oxides of lunar regolith simulants to produce water. A proof of concept for different operational modes of reduction in a hydrogen atmosphere was achieved and the production of water was demonstrated (chapter 5). The achievement of this ISRU-style process in the present context highlights the potential of volatile-bearing lunar regolith as a resource and shows the additional capabilities of an instrument setup that was originally only designed for the thermal extraction and analysis of volatile species. In the context of current instrument developments, the scalability of sample ovens for volatiles extraction was investigated theoretically and through experimental studies (chapter 6). The results highlight the problem of significant thermal gradients even in very small samples, scaling issues regarding power demand and insulation requirements, temperature compatibility of materials for both sample oven and heater, as well as the problem of measuring sample temperature. Regarding the transport of lunar regolith samples, a separate study on the flow properties of lunar regolith was addressed in the frame of this thesis (chapter 7). The results of different experimental studies, mainly conducted in a reduced gravity environment, help to notice and understand the challenges in sample transport and provide useful findings for the design of any sampling chain that involves lunar regolith in a Moon-like environment.

8.2 Conclusion

The most important and relevant findings of this thesis in different areas can be summarised as follows.

Simulation of heat and mass transfer

- Gas diffusivity in the sample is up to six orders of magnitude higher than thermal diffusivity and only in a similar range near low temperatures and atmospheric pressure. Thermal gradients in the sample can reach significant values up to several tens of degrees when the gas pressure is below approximately 0.1 Pa to 1 Pa.
- An initial water concentration in the sample of 1.0 wt% develops a higher gas pressure inside the sample over time with a more pronounced peak, compared to an initial concentration of 0.1 wt%. Additionally, the time required for the extraction of the water is shorter for the higher initial concentration.
- At high-vacuum conditions a higher bulk density of an Apollo 16 type regolith sample leads to a higher thermal diffusivity for temperatures below approximately -50 °C. Above approximately 0 °C this relation is reverse.
- The reduction of the heating rate from 6 °C/min to 4 °C/min leads to a significantly lower gas pressure inside the sample, a lower outgassing rate, and a longer duration of the extraction process for the investigated initial water concentrations of 0.1 wt% and 1.0 wt%.
- Assuming a uniform temperature distribution in the sample leads to an overestimated gas pressure in the sample for the 0.1 wt% water concentration and an underestimated gas pressure for the 1.0 wt% water concentration. With a realistic temperature distribution the gas pressure developed by the desorption of water in the sample is more distinguishable for different initial water concentrations.

Experimental extraction of volatiles

- NU-LHT-2M can be hydrated by storing a sample in a humidity-controlled nitrogen atmosphere for at least 12 h. Up to 0.15 wt% are gained at a relative humidity of 70 %, while the relation between relative humidity and mass gain is nonlinear. Thermal extraction of the adsorbed volatile water is achieved at sample boundary temperatures between -50 °C and 300 °C. Water concentrations above 10 wt% are not distinguishable by their outgassing pressure.
- Outgassing of volatiles produces higher gas pressures for a smaller particle fraction (70-80 µm instead of 100-110 µm), a larger sample (66-72 mg instead of 33-36 mg), and a higher heating rate (6 °C/min instead of 4 °C/min).
- NU-LHT-2M contains pyrite (FeS_2), which decomposes above 550 °C and produces mainly H_2S. It also contains calcite ($CaCO_3$), which decomposes above 650 °C and produces CO_2. Furthermore, NU-LHT-2M particles contain water trapped in the mineral lattice, probably caused by hydrothermal alteration, which is released at temperatures above 300 °C.

Experimental reduction with hydrogen

- Ilmenite can be chemically reduced with hydrogen at temperatures around 800 °C with a ProSPA-like setup that is not optimised for this chemical reaction. Water partial pressures of up to 10 % in the gas mixture can be produced after approximately 30 min, yielding up to approximately 2 wt% of water after 3 h. NU-LHT-2M shows no clear sign of water production under the given boundary conditions.

Experimental studies on regolith flow

- The flow rate of JSC-1A and NU-LHT-2M in a two-dimensional feed hopper is proportional to gravity (as investigated at 0.16 *g*, 0.38 *g*, and 1 *g*) and outlet width (as investigated at 8 mm, 13 mm, and 18 mm). Higher inclination angles in feed hoppers tend to lead to higher flow rates. Gas inclusions in the regolith inhibit the material flow but can be counteracted by including air ducts for pressure equalisation.
- The volume of loosely poured JSC-1A and NU-LHT-2M under lunar gravity increases by up to 10 % and 14 % respectively.

In conclusion, the present thesis is seen as a first step towards a more profound and practical understanding of the overall process of sample transport, sample heating, thermal extraction and transport of volatiles within the sample, potential chemical reactions, outgassing of volatiles, and subsequent gas analysis. The single parts of this overall process in combination are mainly relevant to instruments that are developed to be operated in-situ on the Moon, such as ProSPA. With this application in mind, the present thesis approaches all of the above topics from both an engineering and a science perspective in order to bridge the gap between the mere instrument design that enables the operation and the actual scientific interest that justifies the instrument development. In this regard it can help to optimise existing instrument concepts in terms of design, for instance by providing suggestions for improved heating approaches and hence energy savings, as it was demonstrated for the instrument ProSPA. With the enhanced knowledge about heat transfer in lunar regolith, new instrument concepts can even be developed with a focus on sample heating, as shown by developments of the research projects associated to this thesis, LUISE and LUVMI. The presented work can also help to increase the science output from in-situ measurements, because it enables the discussion of gas analysis data in the light of the overall system configuration and complex micro-scale processes that take place within the sample. The considerations regarding heat and mass transfer in the sample are not only relevant to the intended thermal treatment of a sample to extract volatiles, but also to the unintended loss of volatiles that can occur during sample transfer. The simulation model developed within this thesis can therefore also be applied to assess the effects of sample manipulation on the volatile content and hence optimise the overall system to maximise the scientific output of instruments such as ProSPA. Problems caused by regolith flow in reduced gravity, as studied in this thesis, apply for current instrument developments that rely on hoppers and similar devices for sample transfer. This is partly relevant to the ExoMars SPDS Dosing Station, and even more for larger scale systems for ISRU-style applications that will be developed in the near future.

8.3 Future Work

Over the course of the studies performed within the scope of this thesis, several aspects were either neglected for the sake of simplicity or because they were considered not essential to the fulfilment of the thesis objectives. Some of the suggestions for future research are given in the following.

Modelling of heat and mass transfer

A theoretical assessment of resorption of volatile species in the sample was developed in this thesis (chapter 2.1.2). Due to increased computational complexity, the uncertainties in the theoretical model, and insufficient empirical data, it was not implemented in the presented COMSOL simulation model and hence is a major simplification of the latter. Future work could address this topic and implement a simple approach to include resorption. This could be done through using a solely temperature-dependent sticking coefficient for free molecules in the sample and neglecting the surface characteristics of the sample particles. A sensitivity study should give a first indication of how sensible the mass transfer is with respect to resorption.

Another improvement regarding the COMSOL model would be to include the simulation of molecular flow from the sample surface to the RGA, while considering the geometry of the vacuum system that connects both. Especially for systems with very thin cross sections and long distances between sample and gas analyser, the diffusion of outgassed molecules from the sample to the gas analyser could take substantially longer than expected, resulting in a significantly delayed signal. COMSOL offers a software extension that can be coupled with the existing model to account for molecular flow in the vacuum system.

Further to the above, the existing model could be expanded to include chemical reactions, such as the reduction of iron oxide with hydrogen. This would enable the in-depth analysis of ISRU-style processes and could reveal interesting correlations between temperatures, gas pressures, and reduction rates across the sample volume. The basic feasibility of including such reactions was demonstrated in this thesis for the conversion of adsorbed into desorbed species.

Regolith heating

A recurring problem with the heating of highly thermally insulating regolith is the temperature measurement. As highlighted multiple times in the present thesis, there is a significant mismatch between the temperature

that can be measured and the temperature that would be measured without the disturbance introduced by a temperature sensor. For the studies presented here, very thin mantle thermocouples with either 0.25 mm or 0.50 mm diameter were utilised to reduce the thermal disturbance. A further improvement in this regard can only be made when using the bare thermocouple wires without any metal sheath or other type of insulation. The two welded wires of each thermocouple could be drawn through the sample so that the weld lies at the position that shall be measured. The positive and negative wire would be guided out of the sample where they could be insulated and then connected to a terminal. Depending on the materials of the thermocouple wires and the applied stress, diameters well below 0.1 mm could theoretically be installed this way to reduce their thermal disturbance of the sample. Further experimental work on this topic is recommended to reduce measurement errors in future experiments.

As it was demonstrated through work in this thesis, it is difficult to achieve a uniformly heated regolith sample with common approaches, even if the sample has dimensions of only a few millimetres. A promising approach to improve heat transfer would be to mechanically agitate the sample so that its particles are constantly mixed. This could be achieved by applying vibration and hence generating a vibrofluidised sample. First tests on this matter were conducted within this thesis, but temporarily discarded because no clear results could be generated in the little time dedicated for this side activity. It is however still considered relevant and promising especially for small ProSPA-like samples in a ‘static’ oven. Furthermore, the exerted vibration could be used to shake loose volatile compounds in the sample prior to heating or determine the mechanical properties of a sample through measurement of the responding vibration frequencies.

Experimental extraction of volatiles

The work covered in the present thesis provides a basis for future studies on lunar regolith analogues with loosely adsorbed volatile water. During the development of the experimental setup several hardware issues were encountered and new questions arose that should be addressed in future studies. As an improvement of the test setup for low temperature experiments, the cooling system should be reworked. While the current system performs well with the heating profiles applied so far, other profiles such as stepped heating with temperature holds have larger control errors that cannot be accepted, especially at low temperature. A suggestion for improvement was presented in chapter 4.2.1 and it is recommended to modify the current test setup accordingly for future studies.

An issue that was not addressed in the frame of the presented studies is the sample disturbance through evacuation and venting of the vacuum system, such as discussed in chapter 6 in another context. For the experiments on volatiles extraction and hydrogen reduction it was assumed that no significant eruptions of the loose sample would have taken place because of very slow evacuation and venting using manual valves and a comparably small amount of sample. However, it cannot be ruled out that there was such disturbance even under these circumstances, which would in turn affect the heat and mass transfer through the sample significantly. Parts of the sample could have been swirled up, possibly remain sticking on the surface of the sample holder or filter gasket or leaving gas channels in the rest of the sample. The only way to investigate such sample movements is to enable visual inspection, for instance through using a transparent sample holder. This could be done using a welded glass tube with an appropriate fitting to the vacuum system. The latter would probably be an elastomer seal which cannot be exposed to such extreme temperatures and would not have the same tightness as the knife-edge seals used so far. However, for the mere investigation of sample disturbance such a design would be sufficient.

A slight modification of the current test setup could be done to enable the isolated evaluation of gas transport in the sample. An approach described in chapter 1.4 could be modified and implemented for this purpose, for instance by filling a reservoir with hydrated salt, placing it at the bottom end of sample holder, and thermally releasing the bound water at a defined temperature. Depending on the tortuosity of the sample, the released water would travel through the sample more or less quickly and would subsequently be measured by the RGA with a certain delay. A variation of the particle size fraction or the compaction could then be correlated to the time that is required for the water to be transported through the sample.

In the experimental studies presented in this thesis, many outgassing features were attributed to the decomposition of minerals in the sample. However, because there are some uncertainties in the

measurement of temperature, time of desorption, and actual species in the mass spectrum, a completely unambiguous interpretation of the mass spectra is almost never possible. It is therefore recommended for future studies to perform X-ray diffraction (XRD) analysis of a heated sample in addition to the mass spectrum analysis done so far. This would allow to observe phase changes and mineral decomposition in-situ while heating. Such measurements would complement the mass spectrometry and help to understand the mineral processes that take place within the sample.

Chemical reduction of lunar regolith analogues

For a more complete evaluation of the success or degree of the reduction process, it would be valuable to inspect the reduced sample particles using Scanning Electron Microscopy (SEM). For ilmenite, a distinct picture of spheroidal iron cores with TiO_2 in the form of vein-like arrangements should be visible, as mentioned in chapter 2.4. It would be of particular interest to investigate a depth profile of the reacted sample to see if the upper layers of the sample were subject to a higher degree of reduction than the lower layers, due to hindered hydrogen diffusion or differences in the chemical equilibrium across the sample. Another indicator to determine the success of the reduction could be included in future experiments by adding a microbalance that detects mass loss during the reduction of the sample.

In addition to the hydrogen reduction experiments, different reactants could be investigated in future studies. This includes the utilisation of carbon monoxide, pure as well as mixed with hydrogen, to investigate the slowing effect of carbon monoxide due to the water gas shift reaction.

Regolith flow

A logical next step on the basis of the presented experiments would be to perform similar systematic studies on three-dimensional hoppers and investigate if the same observations can be made. This could be done in conjunction with investigating the effect of different hopper materials and surface finishes or coatings on the flowability and the sticking of residual material on the hopper walls. Future studies should also address the effect of vibration on the sample flow in more detail. This should include the analysis of directionality, amplitude, and shape of the oscillation. Finally, it was noted that many of the flow hindrances can be attributed to residual gas pressure, which is why future experiments should be conducted at a higher vacuum than the ones presented in this thesis, ideally well below 1 mbar.

9 References

9.1 References

Adar, F. (2011) ‘Analytical vibrational spectroscopy: NIR, IR, and Raman’, *Spectroscopy*. Available at: http://www.spectroscopyonline.com/analytical-vibrational-spectroscopy-nir-ir-and-raman.

Alduchov, O. A. and Eskridge, R. E. (1996) ‘Improved Magnus form approximation of saturation vapor pressure’, *Journal of Applied Meteorology*, 35(4), pp. 601–609. doi: 10.1175/1520-0450(1996)035<0601:IMFAOS>2.0.CO;2.

Allen, C. C. (1997) *Oxygen extraction from lunar samples*, *NASA Astromaterials Acquisition & Curation Office, Lunar News No. 60*. Available at: https://curator.jsc.nasa.gov/lunar/lnews/lnmar97/oxygen.htm (Accessed: 19 December 2017).

Allen, C. C., Morris, R. V. and McKay, D. S. (1996) ‘Oxygen extraction from lunar soils and pyroclastic glass’, *Journal of Geophysical Research*, 101(E11), p. 26085. doi: 10.1029/96JE02726.

Anderson, R. C. *et al.* (2009) ‘Particle transport and distribution on the Mars Science Laboratory mission: Effects of triboelectric charging’, *Icarus*, 204(2), pp. 545–557. doi: 10.1016/j.icarus.2009.07.006.

Andreas, E. L. (2007) ‘New estimates for the sublimation rate for ice on the Moon’, *Icarus*, 186(1), pp. 24–30. doi: 10.1016/j.icarus.2006.08.024.

Barber, S. J. *et al.* (2017) ‘ProSPA: the science laboratory for the processing and analysis of lunar polar volatiles within PROSPECT’, *Lunar and Planetary Science Conference XLVIII*, p. 2171.

Bardi, G., Gozzi, D. and Stranges, S. (1987) ‘High temperature reduction kinetics of ilmenite by hydrogen’, *Materials Chemistry and Physics*, 17(4), pp. 325–341. doi: 10.1016/0254-0584(87)90085-X.

Barmatz, M. *et al.* (2014) ‘3D microwave print head approach for processing lunar and Mars regolith’, *Proceedings of the 45th Lunar and Planetary Science Conference*, p. 1137. Available at: http://adsabs.harvard.edu/abs/2014LPI....45.1137B.

Barmatz, M. B. *et al.* (2013) ‘Microwave heating studies and instrumentation for processing lunar regolith and simulants’, *Proceedings of the 44th Lunar and Planetary Science Conference*, p. 1223.

Bayerisches Zentrum für Angewandte Energieforschung (2015) *Determination of thermal resistance by means of guarded hot plate*. Available at: https://www.zae-bayern.de/fileadmin/web_data/downloads/ausstattung/THA/THA_GHP_en.pdf.

Beck, P. *et al.* (2010) ‘Kinetics of water adsorption on minerals and the breathing of the Martian regolith’, *Journal of Geophysical Research*, 115(E10), p. E10011. doi: 10.1029/2009JE003539.

Berkebile, S. and Gaier, J. R. (2012) ‘Adhesion in a vacuum environment and its implications for dust mitigation techniques on airless bodies’, *Proceedings of the 42nd International Conference on Environmental Systems*, p. AIAA 2012-3465.

Biemann, K. *et al.* (1977) ‘The search for organic substances and inorganic volatile compounds in the surface of Mars’, *Journal of Geophysical Research*, 82(28), pp. 4641–4658. doi: 10.1029/JS082i028p04641.

Boynton, W. V. *et al.* (2001) ‘Thermal and Evolved Gas Analyzer: part of the Mars Volatile and Climate Surveyor integrated payload’, *Journal of Geophysical Research: Planets*, 106(E8), pp. 17683–17698. doi: 10.1029/1999JE001153.

Brecher, A. *et al.* (1975) ‘The effects of heating and subsolidus reduction on lunar materials - an analysis by magnetic methods, optical, Moessbauer, and X-ray diffraction spectroscopy’, *Proceedings of the 6th Lunar Science Conference*, pp. 3091–3109.

Briggs, R. a. and Sacco, A. (1991) ‘Hydrogen reduction mechanisms of ilmenite between 823 and 1353 K’,

Journal of Materials Research, 6(03), pp. 574–584. doi: 10.1557/JMR.1991.0574.

Briggs, R. A. and Sacco, A. (1988) 'Oxidation and reduction of ilmenite; application to oxygen production on the lunar surface', *Abstracts of papers presented to the Second Conference on Lunar Bases and Space Activities of the 21st Century*, p. 34.

Buch, A. *et al.* (2011) 'In situ analysis of organic compounds on Mars by gas chromatography-mass spectrometry onboard ExoMars (MOMA)', *European Planetary Science Congress*. EPSC Abstracts, p. EPSC-DPS2011-1722-2.

Buck, A. L. (1981) 'New Equations for Computing Vapor Pressure and Enhancement Factor', *Journal of Applied Meteorology*, 20(12), pp. 1527–1532. doi: 10.1175/1520-0450(1981)020<1527:NEFCVP>2.0.CO;2.

Cadenhead, D. A., Brown, M. G. and Rice, D. K. (1977) 'Some surface area and porosity characterizations of lunar soils', *Proceedings of the 8th Lunar Science Conference*, pp. 1291–1303.

Caps, R., Fricke, J. and Reiss, H. (1985) 'Radiative heat transfer in anisotropic scattering fiber insulations', *High Temperatures - High Pressures*, 17(3), pp. 303–309.

Carpenter, J. D. *et al.* (2017) 'PROSPECT: ESA's package for resource observation and in situ prospecting for exploration, commercial exploitation and transportation', *Proceedings of the Lunar and Planetary Science Conference XLVIII*, p. 2514.

Carrier, W. D., Bromwell, L. G. and Martin, R. T. (1973) 'Behavior of returned lunar soil in vacuum', *Journal of the Soil Mechanics and Foundations Division*, 99(11), pp. 979–996.

Carrier, W. D., Olhoeft, G. R. and Mendell, W. (1991) 'Physical properties of the lunar surface', in *Lunar Sourcebook*, pp. 475–594. Available at: http://scholar.google.co.uk/scholar?hl=en&q=physical+properties+of+the+lunar+surface&btnG=&as_sdt=1,5&as_sdtp=#0.

Chase, M. W. (1998) 'NIST-JANAF Thermochemical Tables, 4th Edition', *Journal of Physical and Chemical Reference Data, Monograph 9*, p. 1952. doi: citeulike-article-id:12140840.

Choate, R. *et al.* (1969) 'Lunar Surface Mechanical Properties', in *Surveyor Program Results*. National Aeronautics and Space Administration, pp. 129–169.

Ciadamidaro, A. (2017) *Experimental determination of the tortuosity of the lunar regolith simulant NU-LHT-2M*. Technical University of Munich.

Clark, R. N. (2009) 'Detection of adsorbed water and hydroxyl on the Moon', *Science*, 326(5952), pp. 562–564. doi: 10.1126/science.1178105.

Clifford, S. M. and Hillel, D. (1986) 'Knudsen diffusion: The effect of small pore size and low gas pressure on gaseous transport in soil', *Soil Science*, 141(4), pp. 289–297. doi: 10.1097/00010694-198604000-00006.

Clifford, S. M. and Marshall, J. (1999) 'Characterization of Regolith Volatile Transport and Storage Properties by The MECA Payload on the MSP 2001 Lander', *Proceedings of Lunar and Planetary Science XXX*, p. 1985.

Colaprete, A. *et al.* (2010) 'Supporting online material for: Detection of water in the LCROSS ejecta plume', *Science*, 330(6003), pp. 463–468. doi: 10.1126/science.1186986.

Coutelieris, F. A. and Delgado, J. (2012) *Transport processes in porous media*. Berlin, Heidelberg: Springer Berlin Heidelberg (Advanced Structured Materials). doi: 10.1007/978-3-642-27910-2.

Cowley, A. *et al.* (2016) 'In-situ resource driven approaches to additive manufacturing using lunar regolith simulant', *Annual Meeting of the Lunar Exploration Analysis Group*, p. 5038.

Crawford, I. A. *et al.* (2012) 'Back to the Moon: the scientific rationale for resuming lunar surface exploration', *Planetary and Space Science*, 74(1), pp. 3–14. doi: 10.1016/j.pss.2012.06.002.

Cremers, C. J. (1971) 'A thermal conductivity cell for small powdered samples', *Review of Scientific Instruments*, 42(11), pp. 1694–1696. doi: 10.1063/1.1684970.

Cremers, C. J. (1972a) 'Thermal conductivity of Apollo 14 fines', *Proceedings of the Thrid Lunar Science Conference*, pp. 2611–2617.

Cremers, C. J. (1972b) 'Thermal conductivity of Apollo 14 fines at low density', *Abstracts of the Lunar and Planetary Science Conference*.

Cremers, C. J. and Birkebak, R. C. (1971) 'Thermal conductivity of fines from Apollo 12', *Proceedings of the Second Lunar Science Conference*, pp. 2311–2315.

Cremers, C. J., Birkebak, R. C. and Dawson, J. P. (1970) 'Thermal conductivity of fines from Apollo 11', *Proceedings of the Apollo 11 Lunar Science Conference*, pp. 2045–2050.

Cremers, C. J. and Hsia, H. S. (1973) 'Thermal conductivity and diffusivity of Apollo 15 fines at low density', *Proceedings of the Fourth Lunar Science Conference*, pp. 2459–2464.

Cremers, C. J. and Hsia, H. S. (1974) 'Thermal conductivity of Apollo 16 lunar fines', *Proceedings of the Fifth Lunar Science Conference*, pp. 2703–2708.

Crotts, A. P. S. and Hummels, C. (2009) 'Lunar outgassing, transient phenomena & the return to the Moon II: predictions and tests for outgassing/regolith interactions', *The Astrophysical Journal*, 707(2), pp. 1506–1523. doi: 10.1088/0004-637X/707/2/1506.

Dang, J., Zhang, G. and Chou, K. (2015) 'Kinetics and mechanism of hydrogen reduction of ilmenite powders', *Journal of Alloys and Compounds*, 619(January), pp. 443–451. doi: 10.1016/j.jallcom.2014.09.057.

Delgado, J. M. P. Q. (2008) 'A simple experimental technique to measure tortuosity in packed beds', *The Canadian Journal of Chemical Engineering*, 84(6), pp. 651–655. doi: 10.1002/cjce.5450840603.

Desai, P. D. *et al.* (1984) 'Electrical resistivity of selected elements', *Journal of Physical and Chemical Reference Data*, 13(4), pp. 1069–1096. doi: 10.1063/1.555723.

Do, D. D. (1998) *Adsorption analysis: equilibria and kinetics*. London: Imperial College Press.

Dyar, M. D., Hibbitts, C. A. and Orlando, T. M. (2010) 'Mechanisms for incorporation of hydrogen in and on terrestrial planetary surfaces', *Icarus*, 208(1), pp. 425–437. doi: 10.1016/j.icarus.2010.02.014.

European Space Agency (2015a) 'ESA space exploration strategy'. Available at: http://esamultimedia.esa.int/multimedia/publications/ESA_Space_Exploration_Strategy/.

European Space Agency (2015b) *The MOMA instrument during development tests*. Available at: http://exploration.esa.int/mars/47876-moma-during-testing/ (Accessed: 11 February 2017).

European Space Agency (2017) *ExoMars 2018 test campaign journal: #01 - ExoMars rover sample preparation and distribution system tested under martian conditions*. Available at: http://exploration.esa.int/mars/51986-journal-01-exomars-rover-sample-preparation-and-distribution-system-tested-under-martian-conditions/ (Accessed: 11 February 2017).

Fateri, M., Meurisse, A. and Sperl, M. (2017) 'Solar sintering for additive manufacturing on the Moon', *EPSC Abstracts*.

Feldman, W. C. *et al.* (1998) 'Fluxes of fast and epithermal neutrons from Lunar Prospector: evidence for water ice at the lunar poles', *Science*, 281(5382), pp. 1496–1500. doi: 10.1126/science.281.5382.1496.

Finzi, a. E. *et al.* (2007) 'SD2 – how to sample a comet', *Space Science Reviews*, 128(1–4), pp. 281–299. doi: 10.1007/s11214-006-9134-6.

Fuller, E. L. and Agron, P. A. (1976) *The reactions of atmospheric vapors with lunar soil*.

Gaier, J. R., Street, K. W. and Gustafson, R. J. (2010) 'Measurement of the solar absorptance and thermal emittance of lunar simulants', *Proceedings of the 40th International Conference on Environmental Systems*, p. AIAA-2010-6025.

Gibson, E. K. and Hubbard, N. J. (1972) 'Thermal volatilization studies on lunar samples', *Proceedings of the Third Lunar Science Conference*, pp. 2003–2014.

Gibson, E. K. and Johnson, S. M. (1971) 'Thermal analysis-inorganic gas release studies of lunar samples', *Proceedings of the Second Lunar Science Conference*, pp. 1351–1366.

Gibson, E. K. and Moore, G. W. (1972) 'Inorganic gas release and thermal analysis study of Apollo 14 and 15 soils', *Proceedings of the Third Lunar Science Conference*, pp. 2029–2040.

Gibson, M. A. *et al.* (1994) 'Reduction of lunar basalt 70035: oxygen yield and reaction product analysis', *Journal of Geophysical Research*, 99(E5), p. 10887. doi: 10.1029/94JE00787.

Gibson, M. A. and Knudsen, C. W. (1985) 'Lunar oxygen production from ilmenite', in Mendel, W. W. (ed.) *Lunar Bases and Space Activities of the 21st Century*, pp. 543–550.

Gillies, D. *et al.* (2007) 'Poisoning of heat pipes', *Space Technology and Applications International Forum*. Albuquerque: AIP Publishing. Available at: http://ntrs.nasa.gov/search.jsp?R=20070018820 (Accessed: 16 November 2015).

Glavin, D. P. *et al.* (2012) 'Volatile analysis by pyrolysis of regolith for planetary resource exploration', *Proceedings of the 2012 IEEE Aerospace Conference*. Big Sky, Montana: IEEE, pp. 1–11. doi: 10.1109/AERO.2012.6187065.

Goering, J. P. *et al.* (2008) *Adsorption of water on simulated Moon dust samples*.

Goesmann, F. *et al.* (2007) 'COSAC, the cometary sampling and composition experiment on Philae', *Space Science Reviews*, 128(1–4), pp. 257–280. doi: 10.1007/s11214-006-9000-6.

Goesmann, F. *et al.* (2017) 'The Mars Organic Molecule Analyzer (MOMA) instrument: characterization of organic material in martian sediments', *Astrobiology*, 17(6–7), pp. 655–685. doi: 10.1089/ast.2016.1551.

Griesinger, A., Spindler, K. and Hahne, E. (1999) 'Measurements and theoretical modelling of the effective thermal conductivity of zeolites', *International Journal of Heat and Mass Transfer*, 42(23), pp. 4363–4374. doi: 10.1016/S0017-9310(99)00096-4.

Gunn, R. D. and King, C. J. (1969) 'Mass transport in porous materials under combined gradients of composition and pressure', *AIChE Journal*, 15(4), pp. 507–514. doi: 10.1002/aic.690150409.

Gustafson, R. *et al.* (2010) 'Demonstrating the solar carbothermal reduction of lunar regolith to produce oxygen', *48th AIAA Aerospace Sciences Meeting Including the New Horizons Forum and Aerospace Exposition*. Reston, Virigina: American Institute of Aeronautics and Astronautics. doi: 10.2514/6.2010-1163.

Hager, P. B. *et al.* (2015) 'Transient thermal envelope for rovers and sample collecting devices on the Moon', *Advances in Space Research*, 55(5), pp. 1477–1494. doi: 10.1016/j.asr.2014.12.012.

Haskin, L. and Warren, P. (1991) 'Lunar chemistry', in *Lunar Sourcebook*, pp. 357–474.

Hayne, P. O. *et al.* (2015) 'Evidence for exposed water ice in the Moon's south polar regions from Lunar Reconnaissance Orbiter ultraviolet albedo and temperature measurements', *Icarus*, 255, pp. 58–69. doi: 10.1016/j.icarus.2015.03.032.

Haynes, D. R., Tro, N. J. and George, S. M. (1992) 'Condensation and evaporation of water on ice surfaces', *The Journal of Physical Chemistry*, 96(21), pp. 8502–8509. doi: 10.1021/j100200a055.

He, W. *et al.* (2013) 'Gas transport in porous electrodes of solid oxide fuel cells: A review on diffusion and diffusivity measurement', *Journal of Power Sources*, 237, pp. 64–73. doi: 10.1016/j.jpowsour.2013.02.089.

He, W., Lv, W. and Dickerson, J. (2014) *Gas transport in solid oxide fuel cells*. Cham: Springer International Publishing (SpringerBriefs in Energy). doi: 10.1007/978-3-319-09737-4.

Hemingway, B. S., Robie, R. A. and Wilson, W. H. (1973) 'Specific heats of lunar soils, basalt, and breccias from the Apollo 14, 15, and 16 landing sites, between 90 and 350°K', *Proceedings of the Fourth Lunar Science Conference*, pp. 2481–2487.

Hibbitts, C. A. *et al.* (2011) 'Thermal stability of water and hydroxyl on the surface of the Moon from temperature-programmed desorption measurements of lunar analog materials', *Icarus*, 213(1), pp. 64–72. doi: 10.1016/j.icarus.2011.02.015.

Hill, C. G. (1977) *An introduction to chemical engineering kinetics & reactor design*. John Wiley & Sons, Inc.

Ho, C. K. and Webb, S. W. (2006) *Gas transport in porous media*. Edited by C. K. Ho and S. W. Webb. Springer Netherlands (Theory and Applications of Transport in Porous Media). doi: 10.1007/1-4020-3962-X.

Holmes, H. F. and Gammage, R. B. (1975) 'Interaction of gases with lunar materials: revised results for Apollo 11', *Proceedings of the sixth Lunar Science Conference*, pp. 3343–3350.

Hoogschagen, J. (1955) 'Diffusion in porous catalysts and adsorbents', *Industrial & Engineering Chemistry*, 47(5), pp. 906–912. doi: 10.1021/ie50545a016.

Horai, K. (1981) 'The effect of interstitial gaseous pressure on the thermal conductivity of a simulated Apollo 12 lunar soil sample', *Physics of the Earth and Planetary Interiors*, 27(1), pp. 60–71. doi: 10.1016/0031-9201(81)90087-X.

Hudson, T. L. *et al.* (2007) 'Water vapor diffusion in Mars subsurface environments', *Journal of Geophysical Research*, 112(E5), p. E05016. doi: 10.1029/2006JE002815.

Hudson, T. L., Aharonson, O. and Schorghofer, N. (2009) 'Laboratory experiments and models of diffusive emplacement of ground ice on Mars', *Journal of Geophysical Research*, 114(E1), p. E01002. doi: 10.1029/2008JE003149.

Huysmans, M. and Dassargues, A. (2005) 'Review of the use of Péclet numbers to determine the relative importance of advection and diffusion in low permeability environments', *Hydrogeology Journal*, 13(5–6), pp. 895–904. doi: 10.1007/s10040-004-0387-4.

ISECG (2013) 'The global exploration roadmap'. Available at: https://www.nasa.gov/sites/default/files/files/GER-2013_Small.pdf.

Jackson, K. A. (2010) *Kinetic processes: crystal growth, diffusion, and phase transitions in materials*. 2nd edn. Wiley-VCH.

Jaumann, R. *et al.* (2012) 'Geology, geochemistry, and geophysics of the Moon: status of current understanding', *Planetary and Space Science*, 74(1), pp. 15–41. doi: 10.1016/j.pss.2012.08.019.

Jenike, A. W. (1964) 'Storage and flow of solids', *Bulletin of the University of Utah*.

Kaganer, M. G. (1969) *Thermal Insulation in Crygenic Engineering*. Jerusalem: Israel Program for Scientific Translations.

Kast, W. and Hohenthanner, C.-R. (2000) 'Mass transfer within the gas-phase of porous media', *International Journal of Heat and Mass Transfer*, 43(5), pp. 807–823. doi: 10.1016/S0017-9310(99)00158-1.

ten Kate, I. L. *et al.* (2010) 'VAPoR – Volatile Analysis by Pyrolysis of Regolith – an instrument for in situ detection of water, noble gases, and organics on the Moon', *Planetary and Space Science*, 58(7–8), pp. 1007–1017. doi: 10.1016/j.pss.2010.03.006.

Kenmare Moma Processing Ltd. (2017) 'Material safety data sheet Kenmare Moma ilmenite'. Available at: http://www.kenmareresources.com/sales-and-marketing/material-safety-data-sheets.aspx.

Kennard, E. H. (1938) *Kinetic theory of gases*. McGraw-Hill Book Company Inc.

Kleinhenz, J. (2014) 'Lunar polar environmental testing: regolith simulant conditioning', *Proceedings of the 7th Symposium on Space Resource Utilization*. AIAA SciTech, p. AIAA 2014-0689. Available at: http://ntrs.nasa.gov/search.jsp?R=20140012567.

Kleinhenz, J. E. *et al.* (2009) 'Design and implementation of a reactor for extracting resources from lunar regolith', *Proceedings of the AIAA SPACE 2009 Conference & Exposition*, p. AIAA 2009-6473.

Kleinhenz, J. E., Sacksteder, K. R. and Nayagam, V. (2008) 'Lunar Resource Utilization: development of a reactor for volatile extraction from regolith', *Proceedings of the 46th AIAA Aerospace Sciences Meeting and Exhibit*. doi: 10.2514/6.2008-1415.

Kleinhenz, J. and Linne, D. (2013) 'Preparation of a frozen regolith simulant bed for ISRU component testing in a vacuum chamber', *51st Aerospace Science Conference*. Available at: http://ntrs.nasa.gov/search.jsp?R=20130009566.

Krishna, R. and Wesselingh, J. A. (1997) 'The Maxwell-Stefan approach to mass transfer', *Chemical Engineering Science*, 52(6), pp. 861–911. doi: 10.1016/S0009-2509(96)00458-7.

LaMarche, C. Q., Curtis, J. S. and Metzger, P. T. (2011) 'Permeability of JSC-1A: a lunar soil simulant', *Icarus*, 212(1), pp. 383–389. doi: 10.1016/j.icarus.2010.12.015.

Lambert, J. M., Simkovich, G. and Walker, P. L. (1998) 'The kinetics and mechanism of pyrite-to-pyrrhotite transformation', *Metallurgical and Materials Transactions B*, 29B, pp. 385–396.

Lee, K. A. *et al.* (2013) 'The ROxygen project: outpost-scale lunar oxygen production system development at Johnson Space Center', *Journal of Aerospace Engineering*, 26(1), pp. 67–73. doi: 10.1061/(ASCE)AS.1943-5525.0000230.

Leybold GmbH (2009) 'Turbovac SL 80 incorporation declaration & operating instructions

130000760_002_A1'.

Leybold GmbH (2016) 'Penningvac-Transmitter PTR 90 N Gebrauchsanleitung 300544657_001_C1'.

Lindemann, A. and Schmidt, J. (2002) 'Thermal analytical investigations of metals including the melting range', *International heat transfer conference*. Societe Francaise de Thermique.

Lobo, V. M. M., Ribeiro, A. C. F. and Verissimo, L. M. P. (1998) 'Diffusion coefficients in aqueous solutions of potassium chloride at high and low concentrations', *Journal of Molecular Liquids*, 78(1–2), pp. 139–149. doi: 10.1016/S0167-7322(98)00088-9.

Lucey, P. G. (2009) 'A Lunar Waterworld', *Science*, 326(5952), pp. 531–532. doi: 10.1126/science.1181471.

Mahaffy, P. (2008) 'Exploration of the habitability of Mars: development of analytical protocols for measurement of organic carbon on the 2009 Mars Science Laboratory', *Space Science Reviews*, 135(1–4), pp. 255–268. doi: 10.1007/s11214-007-9223-1.

Mahaffy, P. R. *et al.* (2012) 'The Sample Analysis at Mars investigation and instrument suite', *Space Science Reviews*, 170(1–4), pp. 401–478. doi: 10.1007/s11214-012-9879-z.

Malvern Instruments (2007) *Measurements of particle size distribution by wet & dry laser diffraction*. Available at: https://isru.msfc.nasa.gov/lib/Documents/particlesize/LHT-1M/Malvern/Size/LHT-1Msize_Malvern2102_Report.pdf.

Masel, R. I. (1996) *Principles of adsorption and reaction on solid surfaces*. Wiley.

Mason, E. A., Malinauskas, A. P. and Evans, R. B. (1967) 'Flow and diffusion of gases in porous media', *The Journal of Chemical Physics*, 46(8), pp. 3199–3216. doi: 10.1063/1.1841191.

Matar, E. *et al.* (2010) 'Gas temperature dependent sticking of hydrogen on cold amorphous water ice surfaces of interstellar interest', *The Journal of Chemical Physics*, 133(10), p. 104507. doi: 10.1063/1.3484867.

McGrath, R. B. and Badcock, G. C. (1987) 'New dispersion strengthened platinum alloy', *Platinum Metals Review*, 31(1), pp. 8–11.

Mellon, M. T., Jakosky, B. M. and Postawko, S. E. (1997) 'The persistence of equatorial ground ice on Mars', *Journal of Geophysical Research: Planets*, 102(E8), pp. 19357–19369. doi: 10.1029/97JE01346.

Millington, R. J. (1959) 'Gas diffusion in porous media', *Science*, 130(3367), pp. 100–102. doi: 10.1126/science.130.3367.100-a.

Morris, M. A., Bowker, M. and King, D. A. (1984) 'Kinetics of adsorption, desorption and diffusion at metal surfaces', in Bamford, C. H., Tipper, C. F. H., and G., C. (eds) *Comprehensive chemical kinetics*. Vol. 19, pp. 1–179. doi: 10.1016/S0069-8040(08)70099-2.

Morris, R. V. *et al.* (1983) *Handbook of lunar soils*.

Morse, A. D. *et al.* (2012) 'The lunar volatile resources analysis package', *European Lunar Symposium*.

Mueller, R. P. and Townsend, I. (2009) 'Effects of regolith simulant properties on an experiment: ROxygen phase I input hopper reduced gravity flight', *Lunar Regolith / Simulant Workshop*.

Murphy, D. M. and Koop, T. (2005) 'Review of the vapour pressures of ice and supercooled water for atmospheric applications', *Quarterly Journal of the Royal Meteorological Society*, 131(608), pp. 1539–1565. doi: 10.1256/qj.04.94.

Mylswamy, A. *et al.* (2012) 'Chandrayaan-2: India's first soft-landing mission to Moon', *39th COSPAR Scientific Assembly*.

Neal, C. R. (2009) 'The Moon 35 years after Apollo: what's left to learn?', *Chemie der Erde - Geochemistry*, 69(1), pp. 3–43. doi: 10.1016/j.chemer.2008.07.002.

Newsome, D. S. (1980) 'The water-gas shift reaction', *Catalysis Reviews*, 21(2), pp. 275–318. doi: 10.1080/03602458008067535.

Nozette, S. *et al.* (1996) 'The Clementine bistatic radar experiment', *Science*, 274(5292), pp. 1495–1498. doi: 10.1126/science.274.5292.1495.

O'Hanlon, J. F. (2003) *A user's guide to vacuum technology*. John Wiley & Sons, Inc. doi: 10.1002/0471467162.

Orbital Technologies Corporation (2007) *Material safety data sheet JSC-1A*.

Pant, L. M., Mitra, S. K. and Secanell, M. (2012) 'Absolute permeability and Knudsen diffusivity measurements in PEMFC gas diffusion layers and micro porous layers', *Journal of Power Sources*, 206, pp. 153–160. doi: 10.1016/j.jpowsour.2012.01.099.

Parzinger, S. (2014) *Analytische Modellierung der temperatur- und gasdruckabhängigen effektiven Wärmeleitfähigkeit von Pulvern*. Dr. Hut.

Paul, R. *et al.* (2017) 'Sample flow and implications on design and testing for the SPDS mechanism chain on the Exomars 2020 rover', *14th Symposium on Advanced Space Technologies in Robotics and Automation (ASTRA)*.

Paz, A. *et al.* (2013) 'RESOLVE OVEN field demonstration unit for lunar resource extraction', *Proceedings of the 51st AIAA Aerospace Sciences Meeting*. Available at: http://ntrs.nasa.gov/search.jsp?R=20130000835.

Pieters, C. M. *et al.* (2009) 'Character and spatial distribution of OH/H2O on the surface of the Moon seen by M3 on Chandrayaan-1', *Science*, 326(5952), pp. 568–572. doi: 10.1126/science.1178658.

Pitcher, C. *et al.* (2016) 'Investigation of the properties of icy lunar polar regolith simulants', *Advances in Space Research*, 57(5), pp. 1197–1208. doi: 10.1016/j.asr.2015.12.030.

Pollack, J. B., Toon, O. B. and Khare, B. N. (1973) 'Optical properties of some terrestrial rocks and glasses', *Icarus*, 19(3), pp. 372–389. doi: 10.1016/0019-1035(73)90115-2.

Poston, M. J. *et al.* (2013) 'Water interactions with micronized lunar surrogates JSC-1A and albite under ultra-high vacuum with application to lunar observations', *Journal of Geophysical Research: Planets*, 118(1), pp. 105–115. doi: 10.1029/2012JE004283.

Pullan, D. *et al.* (2004) *Beagle 2: the exobiological lander of Mars Express*, *European Space Agency Special Publication*.

Ramé, E. *et al.* (2009) *Flowability of JSC-1a*.

Ramé, E., Aguí, J. and Wilkinson, A. (2010) *Flowing and sifting lunar soil simulant in lunar gravity*.

Reinecke, S. a. and Sleep, B. E. (2002) 'Knudsen diffusion, gas permeability, and water content in an unconsolidated porous medium', *Water Resources Research*, 38(12), pp. 16-1-16–15. doi: 10.1029/2002WR001278.

Reiss, H. (1985) *Radiative transfer in disperse non-transparent media*. Brown, Boveri & Cie AG.

Reiss, P. *et al.* (2014) 'Flowability of lunar regolith simulants under reduced gravity and vacuum in hopper-based conveying devices', *Journal of Terramechanics*, 55, pp. 61–72. doi: 10.1016/j.jterra.2014.04.005.

Reiss, P. *et al.* (2017) 'Implications of sample size for the thermal extraction of volatiles from lunar regolith with the PROSPECT instrument package', *Journal of Aerospace Engineering*, 30(3), p. 04016088. doi: 10.1061/(ASCE)AS.1943-5525.0000688.

Reiss, P. (2018) 'A combined model of heat and mass transfer for the in situ extraction of volatile water from lunar regolith', *Icarus*, 306, pp. 1–15. doi: 10.1016/j.icarus.2018.01.020.

Reiss, P., Hoehn, A. and Henn, N. (2015) 'Stamp-heater instrument concept for mobile in-situ extraction and analysis of lunar volatiles', *European Lunar Symposium*.

Reiss, P. and Walter, U. (2013) 'Compaction of lunar regolith simulants under reduced gravity', *European Planetary Science Congress*, pp. EPSC2013-431–2.

Reschetilowski, W. (2015) *Einführung in die Heterogene Katalyse*. Springer Berlin Heidelberg. doi: 10.1007/978-3-662-46984-2.

Richter, L. *et al.* (2013) 'Technologies for automated sample handling and sample distribution on planetary landing missions', *Proceedings of the 12th Symposium on Advanced Space Technologies in Automation and Robotics*.

Rickman, D. L. and Lowers, H. A. (2012) *Particle shape and composition of NU-LHT-2M*.

Robens, E. *et al.* (2007) 'Investigation of surface properties of lunar regolith: Part I', *Applied Surface Science*, 253(13 SPEC. ISS.), pp. 5709–5714. doi: 10.1016/j.apsusc.2006.12.098.

Robens, E. *et al.* (2008) 'Investigation of surface properties of lunar regolith - Part II', *Journal of Thermal Analysis and Calorimetry*, 94(3), pp. 627–631. doi: https://doi.org/10.1007/s10973-008-9352-0.

Robie, R. A., Hemingway, B. S. and Wilson, W. H. (1970) 'Specific heats of lunar surface materials from 90 to 350 degrees Kelvin', *Science*, 167(3918), pp. 749–750. doi: 10.1126/science.167.3918.749.

Satterfield, C. N. (1970) *Mass transfer in heterogeneous catalysis*. MIT Press.

Sauerborn, M. (2005) *Pyrolyse von Metalloxiden und Silikaten unter Vakuum mit konzentrierter Solarstrahlung Dissertation*. Rheinische Friedrich-Wilhelms-Universität Bonn.

Schorghofer, N. and Taylor, G. J. (2007) 'Subsurface migration of H2O at lunar cold traps', *Journal of Geophysical Research*, 112(E2), p. E02010. doi: 10.1029/2006JE002779.

Schrader, C. M. *et al.* (2010) *Lunar regolith simulant user's guide*.

Schreiner, S. S. *et al.* (2016) 'Thermophysical property models for lunar regolith', *Advances in Space Research*, 57(5), pp. 1209–1222. doi: 10.1016/j.asr.2015.12.035.

Schulte, W. *et al.* (2010) 'Design and testing of the ExoMars sample preparation and distribution system', *Proceedings of the International Symposium on Artificial Intelligence, Robotics and Automation in Space*, pp. 7–14.

Schulze, D. (2008) *Powders and bulk solids*, *New York*. Springer Berlin Heidelberg. doi: 10.1007/978-3-540-73768-1.

Schwandt, C. *et al.* (2012) 'Oxygen from lunar regolith', in Badescu, V. (ed.) *Moon*. Springer Heidelberg New York Dordrecht London, pp. 165–187.

Schwister, K. and Leven, V. (2014) *Verfahrenstechnik für Ingenieure*, *Verfahrenstechnik für Ingenieure*. München: Carl Hanser Verlag GmbH & Co. KG. doi: 10.3139/9783446440012.

Senior, C. L. (1993) 'Lunar oxygen production by pyrolysis', in Lewis, J. S., Matthews, M. S., and Guerrieri, M. L. (eds) *Resources of near-Earth space*. University of Arizona Press, pp. 179–197.

Shamlou, P. A. (1988) *Handling of bulk solids - theory and practice*. Butterworth & Co.Ltd.

Siegler, M. A. *et al.* (2011) 'Laboratory measurements of thermal properties of icy regolith analogs', *EPSC Abstracts*. European Planetary Science Congress, p. EPSC-DPS2011-1695. Available at: http://meetingorganizer.copernicus.org/EPSC-DPS2011/EPSC-DPS2011-1695.pdf.

Smoluchowski, R. (1968) 'Mars: retention of ice', *Science*, 159(3821), pp. 1348–1350. doi: 10.1126/science.159.3821.1348.

Special Metals Corporation (2005) *INCONEL alloy 693 - excellent resistance to metal dusting and high temperature corrosion*. Available at: http://www.specialmetalswiggin.co.uk/pdfs/products/INCONEL alloy 693.pdf.

Sridharan, R. *et al.* (2010) '"Direct" evidence for water (H2O) in the sunlit lunar ambience from CHACE on MIP of Chandrayaan I', *Planetary and Space Science*, 58(6), pp. 947–950. doi: 10.1016/j.pss.2010.02.013.

Stebbins, J. F., Carmichael, I. S. E. and Moret, L. K. (1984) 'Heat capacities and entropies of silicate liquids and glasses', *Contributions to Mineralogy and Petrology*, 86(2), pp. 131–148. doi: 10.1007/BF00381840.

Stokes, J. (1987) 'Platinum in the glass industry', *Platinum Metals Review*, 31(2), pp. 54–62.

Street, K. W. *et al.* (2010) 'Thermal properties of lunar regolith simulants', *Earth and Space 2010*. Reston, VA: American Society of Civil Engineers, pp. 266–275. doi: 10.1061/41096(366)28.

Sunshine, J. M. *et al.* (2009) 'Temporal and spatial variability of lunar hydration as observed by the Deep Impact spacecraft', *Science*, 326(5952), pp. 565–568. doi: 10.1126/science.1179788.

Swimm, K. *et al.* (2009) 'Gas pressure dependence of the heat transport in porous solids with pores smaller than 10 μm', *International Journal of Thermophysics*, 30(4), pp. 1329–1342. doi: 10.1007/s10765-009-0617-z.

Tattusch, T. (2013) *Impact of ambient pressure and electrostatic charging on the flow properties of a lunar regolith simulant*. Technical University of Munich.

Taylor, L. A. *et al.* (1993) 'Production of O2 on the Moon: a lab-top demonstration of ilmenite reduction with hydrogen', *Proceedings of the 24th Lunar and Planetary Science Conference*, pp. 1411–1412.

Taylor, L. A. and Carrier, W. D. (1993) 'Oxygen production on the Moon: an overview and evaluation', in Lewis, J., Matthews, M. S., and Guerrieri, M. L. (eds) *Resources of near-Earth space*. The University of Arizona Press, pp. 69–108.

Taylor, L. a. and Meek, T. T. (2005) 'Microwave sintering of lunar soil: properties, theory, and practice', *Journal of Aerospace Engineering*, 18(3), pp. 188–196. doi: 10.1061/(ASCE)0893-1321(2005)18:3(188).

Taylor, L. A. and Meek, T. T. (2004) 'Microwave processing of lunar soil', *International Lunar Conference / International Lunar Exploration Working Group 5*. Available at: http://web.utk.edu/~lataylor/pub-list/microwave1.pdf.

Taylor, L. A., Pieters, C. M. and Britt, D. (2016) 'Evaluations of lunar regolith simulants', *Planetary and Space Science*, 126, pp. 1–7. doi: 10.1016/j.pss.2016.04.005.

Thomas, N. H. *et al.* (2017) 'ChemCam survey of volatile elements in the Murray formation, Gale crater, Mars', *Proceedings of the Lunar and Planetary Science XLVIII*.

Tjaden, B. *et al.* (2016) 'On the origin and application of the Bruggeman correlation for analysing transport phenomena in electrochemical systems', *Current Opinion in Chemical Engineering*, 12, pp. 44–51. doi: 10.1016/j.coche.2016.02.006.

Toutanji, H. *et al.* (2012) 'Gas permeability and flow characterization of simulated lunar regolith', *Advances in Space Research*, 49(8), pp. 1271–1276. doi: 10.1016/j.asr.2012.02.002.

U.S. Geological Survey (2008) *Material safety data sheet NU-LHT-2M*.

Vaithinathan, K. and Lanam, R. (2005) *Features and benefits of different platinum alloy*, *Technical Articles: Alloys, Platinum Guild International*. Iselin, NJ, USA. Available at: www.platinumguild.com/files/pdf/v13n3_features_benefits.pdf.

Vaniman, D. *et al.* (1991) 'The lunar environment', in Heiken, G. H., Vaniman, D. T., and French, B. M. (eds) *Lunar Sourcebook*. Cambridge University Press, pp. 27–60.

Vaniman, D. T., Meek, T. T. and Blake, R. D. (1986) 'Fusing lunar materials with microwave energy. Part II: melting of a simulated glassy Apollo 11 soil', *Proceedings of the Lunar and Planetary Science Conference XVII*, pp. 911–912.

Verein Deutscher Ingenieure (2010) *VDI heat atlas*. 2nd edn. Springer Berlin Heidelberg. doi: 10.1007/978-3-540-77877-6.

Verein Deutscher Ingenieure (2013) *VDI-Wärmeatlas*. 11th edn. Springer Berlin Heidelberg. doi: 10.1007/978-3-642-19981-3.

Vijay, P. L., Venugopalan, R. and Sathiyamoorthy, D. (1996) 'Preoxidation and hydrogen reduction of ilmenite in a fiuidized bed reactor', *Metallurgical and Materials Transactions B*, 27(5), pp. 731–738. doi: 10.1007/BF02915601.

Vosteen, H.-D. and Schellschmidt, R. (2003) 'Influence of temperature on thermal conductivity, thermal capacity and thermal diffusivity for different types of rock', *Physics and Chemistry of the Earth, Parts A/B/C*, 28(9–11), pp. 499–509. doi: 10.1016/S1474-7065(03)00069-X.

Wagner, W., Saul, A. and Pruss, A. (1994) 'International equations for the pressure along the melting and along the sublimation curve of ordinary water substance', *Journal of Physical and Chemical Reference Data*, 23(3), pp. 515–527. doi: 10.1063/1.555947.

Walton, O. (2012) 'Challenges in transporting, handling and processing regolith in the lunar environment', in Badescu, V. (ed.) *Moon*. Springer Berlin Heidelberg, pp. 267–293. doi: 10.1007/978-3-642-27969-0.

Watson, K. (1964) *I. The thermal conductivity measurements of selected silicate powders in vacuum from 150 - 350 K. II. An interpretation of the Moon's eclipse and lunation cooling as observed through the Earth's atmosphere from 8-14 microns.*

Watson, K., Murray, B. C. and Brown, H. (1961) 'The behavior of volatiles on the lunar surface', *Journal of Geophysical Research*, 66(9), pp. 3033–3045. doi: 10.1029/JZ066i009p03033.

Webb, S. W. (1996) *Gas-phase diffusion in porous media - evaluation of an advective-dispersive formulation*

and the dusty-gas model including comparison to data for binary mixtures, *Sandia Report*.

Wiener, M. *et al.* (2009) 'Carbon aerogel-based high-temperature thermal insulation', *International Journal of Thermophysics*, 30(4), pp. 1372–1385. doi: 10.1007/s10765-009-0595-1.

Wiens, R. C. *et al.* (2005) 'Joint analyses by laser-induced breakdown spectroscopy (LIBS) and Raman spectroscopy at stand-off distances', *Spectrochimica Acta Part A: Molecular and Biomolecular Spectroscopy*, 61(10), pp. 2324–2334. doi: 10.1016/j.saa.2005.02.031.

Williams, M. M. R. (1977) 'The mathematics of diffusion', *Annals of Nuclear Energy*, 4(4–5), pp. 205–206. doi: 10.1016/0306-4549(77)90072-X.

Wilson, A. H. (1948) 'V. A diffusion problem in which the amount of diffusing substance is finite', *The London, Edinburgh, and Dublin Philosophical Magazine and Journal of Science*, 39(288), pp. 48–58. doi: 10.1080/14786444808561166.

Wright, I. P. *et al.* (2007) 'Ptolemy – an instrument to measure stable isotopic ratios of key volatiles on a cometary nucleus', *Space Science Reviews*, 128(1–4), pp. 363–381. doi: 10.1007/s11214-006-9001-5.

Wright, I. P. *et al.* (2012) 'L-VRAP - a lunar volatile resources analysis package for lunar exploration', *Planetary and Space Science*, 74(1), pp. 254–263. doi: 10.1016/j.pss.2012.08.014.

Wright, R. A. *et al.* (1986) 'Fusing lunar materials with microwave energy. Part I: studies of doping media', *Proceedings of the Lunar and Planetary Science Conference XVII*, pp. 958–959.

Yoshida, H. *et al.* (2000) 'Experimental study on water production by hydrogen reduction of lunar soil simulant in a fixed bed reactor', *Second Space Resources Roundtable*.

Zeng, X., He, C. and Wilkinson, A. (2010) 'Geotechnical properties of NU-LHT-2M lunar highland simulant', *Journal of Aerospace Engineering*, 23(4), pp. 213–218. doi: 10.1061/?ASCE?AS.1943-5525.0000026 CE.

Zhao, Y. and Shadman, F. (1993) 'Production of oxygen from lunar ilmenite', in Lewis, J. S., Matthews, M. S., and Guerrieri, M. L. (eds) *Resources of Near-Earth Space*. The University of Arizona Press, pp. 149–178.

Zoth, G. and Haenel, R. (1988) 'Appendix', in Haenel, R., Stegena, L., and Rybach, L. (eds) *Handbook of Terrestrial Heat-Flow Density Determination*. Kluwer Academic Publishers, pp. 449–466.

9.2 List of Publications

First author publications

Reiss, P. and Hager, P. (2013) 'Investigation of the flow characteristics of lunar regolith simulants under reduced gravity and vacuum on a partial-g parabolic flight', EGU General Assembly, p. EGU2013-7741-2.

Reiss, P., Hager, P. and Hoehn, A. (2013) 'Hopper-flow of lunar regolith simulants in reduced gravity and vacuum', *7th Regional Americas Conference of the International Society of Terrain-Vehicle Systems*.

Reiss, P. and Walter, U. (2013) 'Compaction of lunar regolith simulants under reduced gravity', *European Planetary Science Congress*. EPSC Abstracts, p. EPSC2013-431-2.

Reiss, P. *et al.* (2014) 'Technological challenges for in-situ investigation of lunar resources', *European Lunar Symposium*.

Reiss, P. *et al.* (2014) 'Flowability of lunar regolith simulants under reduced gravity and vacuum in hopper-based conveying devices', *Journal of Terramechanics*, 55, pp. 61–72. doi: 10.1016/j.jterra.2014.04.005.

Reiss, P. and Hoehn, A. (2014) 'Evaluation of small-scale penetrators for lunar subsurface investigation', *European Lunar Symposium*.

Reiss, P., Hoehn, A. and Henn, N. (2015) 'Stamp-heater instrument concept for mobile in-situ extraction and analysis of lunar volatiles', *European Lunar Symposium*.

Reiss, P. *et al.* (2016) 'In-situ thermal extraction and analysis of lunar volatiles with the Lunar Volatiles Scouting instrument', *European Lunar Symposium*, p. 60.

Reiss, P. (2017) 'Simulation and demonstration of the extraction of water from lunar regolith analogues for

the ProSPA sample analysis instrument', *European Lunar Symposium*.

Reiss, P. *et al.* (2017) 'Implications of sample size for the thermal extraction of volatiles from lunar regolith with the PROSPECT instrument package', *Journal of Aerospace Engineering*, 30(3), p. 4016088. doi: 10.1061/(ASCE)AS.1943-5525.0000688.

Reiss, P. (2018) 'A combined model of heat and mass transfer for the in situ extraction of volatile water from lunar regolith', *Icarus*, 306, pp. 1–15. doi: 10.1016/j.icarus.2018.01.020.

Reiss, P. *et al.* (2018) 'In-situ hydrogen reduction of lunar polar regolith: from proof of concept experiments with ProSPA to larger scale ISRU demonstrators', *European Lunar Symposium*.

Reiss, P., Grill, L. and Barber, S. (2018) 'Demonstration of volatiles extraction from NU-LHT-2M with the ProSPA instrument breadboard', *European Lunar Symposium*.

Co-author publications

Barber, S. J. *et al.* (2015) 'ProsPA : a miniature chemical laboratory for in-situ assessment of lunar volatile resources', *European Lunar Symposium*.

Barber, S. *et al.* (2016) 'ProSPA: the chemical laboratory for in-situ assessment of lunar volatile resources within ESA's PROSPECT package', *European Lunar Symposium*, p. 47.

Barber, S. J. *et al.* (2017) 'ProSPA: the science laboratory for the processing and analysis of lunar polar volatiles within PROSPECT', *Lunar and Planetary Science Conference XLVIII*, p. 2171.

Barber, S. *et al.* (2017) 'PROSPECTing for lunar polar volatiles: the ProSPA miniature in-situ science laboratory', *European Lunar Symposium*.

Barber, S. *et al.* (2018) 'ProSPA: analysis of lunar polar volatiles and ISRU demonstration on the Moon', *49th Lunar and Planetary Science Conference*, p. 2172.

Barber, S. *et al.* (2018) 'ProSPA: an instrument for lunar polar volatiles prospecting and in situ resource utilization proof of concept', *European Lunar Symposium*.

Biswas, J. *et al.* (2017) 'Application of the LVS subsurface probe on the LUVMI rover for a lunar volatiles exploration mission', *European Lunar Symposium*.

Biswas, J. *et al.* (2018) 'Mobile in-situ exploration of lunar volatiles with the LVS on LUVMI', *European Lunar Symposium*.

Carpenter, J. D. *et al.* (2014) 'Accessing and assessing lunar resources with PROSPECT', *Annual Meeting of the Lunar Exploration Analysis Group*. Laurel, Maryland.

Deiml, M. *et al.* (2015) 'Development and evaluation of thermal model reduction algorithms for spacecraft', *Acta Astronautica*, 110, pp. 168–179. doi: 10.1016/j.actaastro.2015.01.018.

Fisackerly, R. *et al.* (2015) 'Accessing, drilling and operating at the lunar south pole: status of European plans and activities', *13th Symposium on Advanced Space Technologies in Robotics and Automation*. Noordwijk.

Gancet, J. *et al.* (2017) 'LUVMI: a concept of low footprint lunar volatiles mobile instrumentation', *13th Symposium on Advanced Space Technologies in Robotics and Automation*.

Hager, P. and Reiss, P. (2013) 'Verification of a thermal simulation tool for moving objects on the lunar surface', *EGU General Assembly*, p. 9434.

Killian, M. and Reiss, P. (2015) 'Investigating thermal aspects of lunar traverses for scientific exploration', *European Lunar Symposium*.

Pitcher, C. *et al.* (2018) 'Volatile extraction and detection from frozen lunar regolith simulants in preparation for the LUVMI rover', *European Lunar Symposium*.

Richter, L. *et al.* (2017) 'OHB instruments development for volatile scouting on the Moon', Proceedings of the *68th International Astronautical Congress*, p. 40120.

Sargeant, H. *et al.* (2018) 'Hydrogen reduction of ilmenite in a static system for a lunar ISRU demonstration', *European Lunar Symposium*.

Urbina, D. *et al.* (2017) 'LUVMI : an innovative payload for the sampling of volatiles at the lunar poles', Proceedings of the *68th International Astronautical Congress*, p. 41392.

9.3 List of Supervised Theses

Barz, D. (2015) ‘Dichtungskonzepte für Probeöfen zur Verwendung unter lunaren Bedingungen’. RT-BA 2015/04, Bachelor Thesis, Technical University of Munich.

Biswas, J. (2016) ‘Drive mechanism design and verification for the LUISE lunar subsurface probe’. RT-MA 2015/11, Master Thesis, Technical University of Munich.

Boden, R. (2014) ‘Development, simulation and testing of temperature sensors for the attitude determination of the MASCOT asteroid lander’. RT-MA 2013/03, Master Thesis, Technical University of Munich.

Bulla, B. (2013) ‘Concept development for the in-situ heating of regolith samples on the Moon’. RT-BA 2013/12, Bachelor Thesis, Technical University of Munich.

Ciadamidaro, A. (2017) ‘Experimental determination of the tortuosity of the lunar regolith simulant NU-LHT-2M’. RT-SA 2017/07, Semester Thesis, Technical University of Munich.

Deiml, M. (2013) ‘Entwicklung eines Tools zur Modellreduktion von Thermalmodellen’. RT-SA 2013/13, Semester Thesis, Technical University of Munich.

Edelhäuser, M. (2015) ‘Entwicklung einer Visualisierungsfunktion für die CubeSat-Thermalsoftware TherMACS’. RT-BA 2015/17, Technical University of Munich.

Helfrich, E. (2014) ‘Thermal simulation of an antiproton-detector for BEXUS and CubeSats’. RT-BA 2014/18, Technical University of Munich.

Hering, T. (2014) ‘Experimentelle Bestimmung des Ausgasverhaltens von Mondregolith bei Erwärmung durch unterschiedliche Heizer-Konfigurationen’. RT-BA 2014/34, Bachelor Thesis, Technical University of Munich.

Hertel, D. (2015) ‘Reduktion von Störeinflüssen für die experimentelle Bestimmung des Aufheizverhaltens von Mondregolith’. RT-SA 2015/04, Semester Thesis, Technical University of Munich.

Koop, A. (2013) ‘Simulation of the mechanical load on lunar regolith caused by sample acquisition and transport’. RT-BA 2013/10, Bachelor Thesis, Technical University of Munich.

Lösch, C. (2016) ‘Modification of the LUISE-instrument for the application with the Nanokhod-rover’. RT-BA 2016/06, Bachelor Thesis, Technical University of Munich.

Matz, M. (2014) ‘Konstruktion eines Testaufbaus zur Aufheizung von Mondregolith unter Vakuum-bedingungen’. RT-BA 2014/23, Bachelor Thesis, Technical University of Munich.

Nudelis, N. (2015) ‘Bestimmung der Gasdurchlässigkeit von Mondregolith in Abhängigkeit von Dichte und Druck’. RT-BA 2015/03, Bachelor Thesis, Technical University of Munich.

Schrenk, L. (2015) ‘Development of an ISRU sizing model to analyze the impact of In Situ Resource Utilization on space mission performance’. RT-MA 2015/12, Master Thesis, Technical University of Munich.

Tattusch, T. (2013) ‘Impact of ambient pressure and electrostatic charging on the flow properties of a lunar regolith simulant’. RT-SA 2013/15, Semester Thesis, Technical University of Munich.

Tattusch, T. (2014) ‘Optimization of the vibration and shock mechanism for the Crushing Station of ESA's ExoMars rover’. RT-MA 2014/06, Master Thesis, Technical University of Munich.

Appendix A List of Figures and Tables

A.1 List of Figures

A.2 List of Tables

Appendix B Supplementary Figures

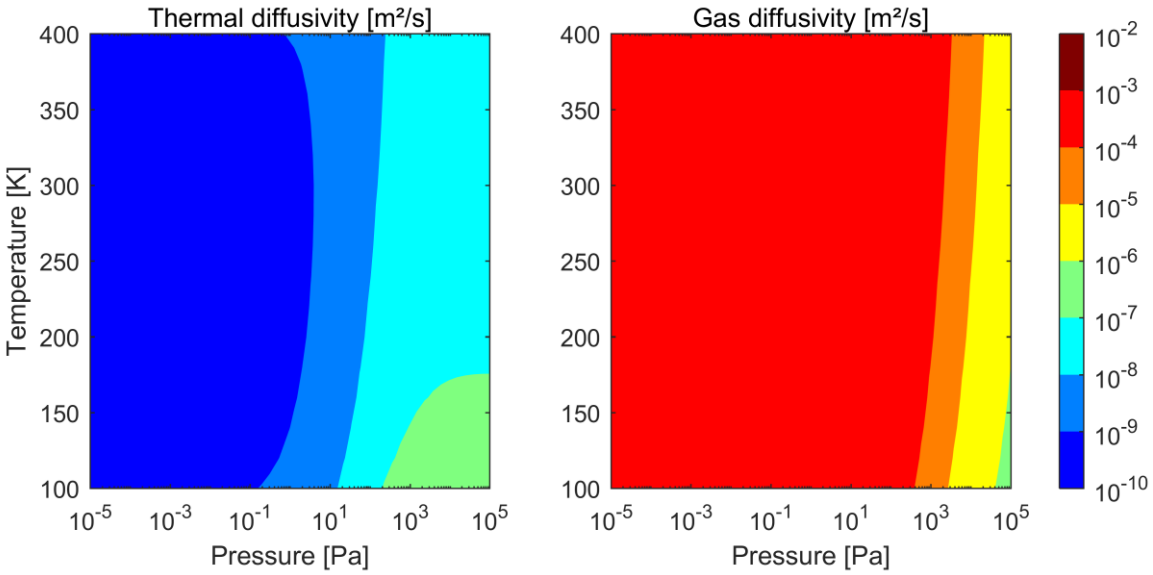

Figure B-1: Thermal diffusivity and gas diffusivity for a lunar regolith sample

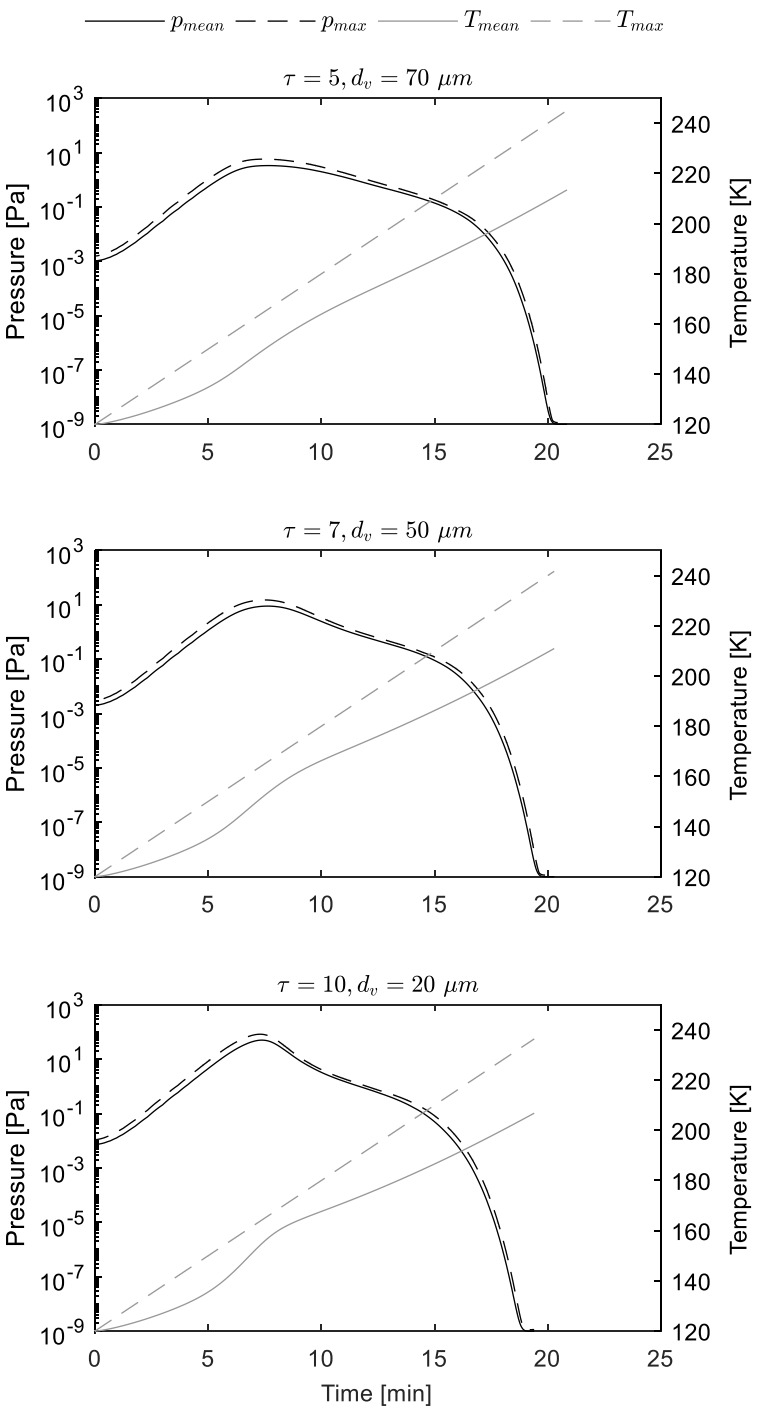

Figure B-2: Gas pressure and sample temperature for the sample with 0.1 wt% initial water content, as produced with the COMSOL simulation model. Tortuosity τ and mean diameter of the voids d_v were varied as indicated in the titles of the diagrams.

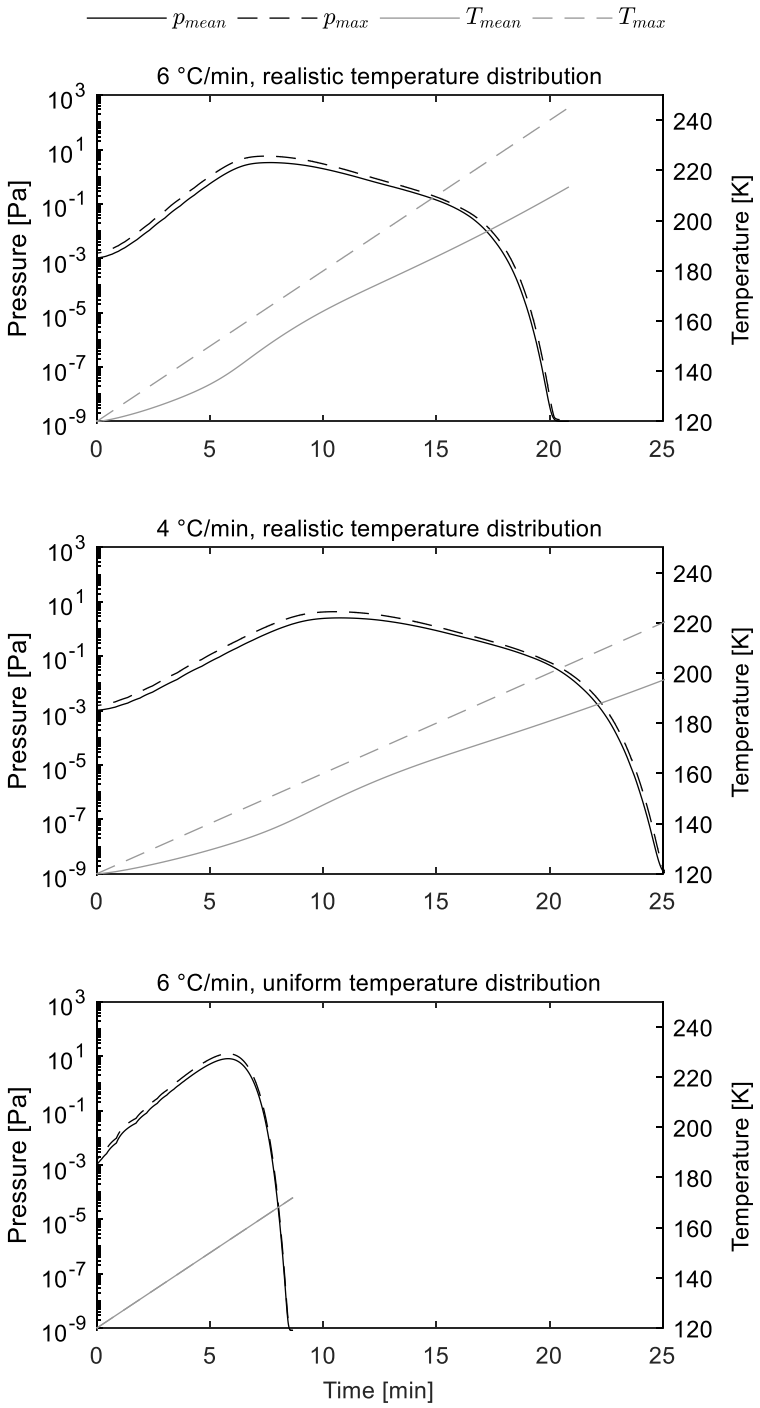

Figure B-3: Gas pressure and sample temperature for the sample with 0.1 wt% initial water content, as produced with the COMSOL simulation model. Heating rate and temperature distribution were varied as indicated in the titles of the diagrams.

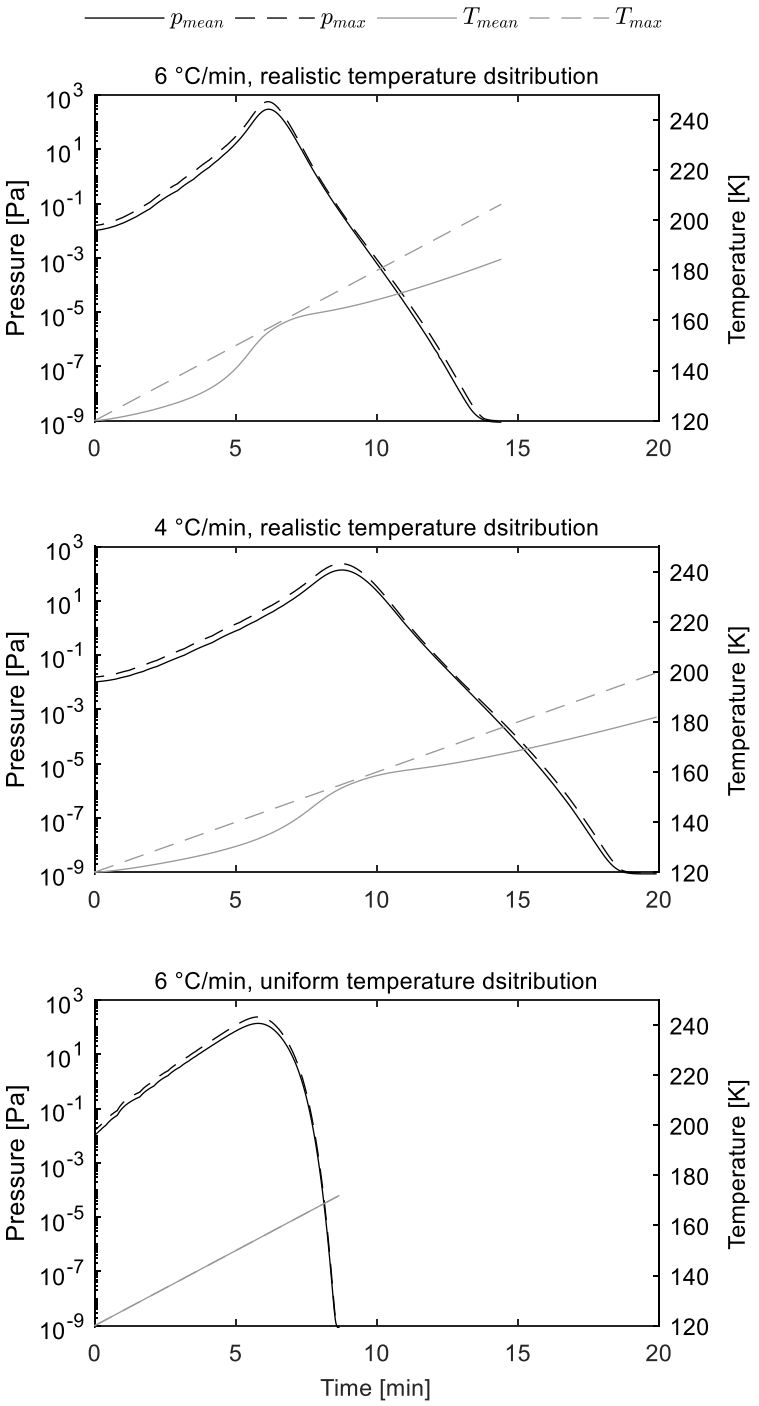

Figure B-4: Gas pressure and sample temperature for the sample with 1.0 wt% initial water content, as produced with the COMSOL simulation model. Heating rate and temperature distribution were varied as indicated in the titles of the diagrams.

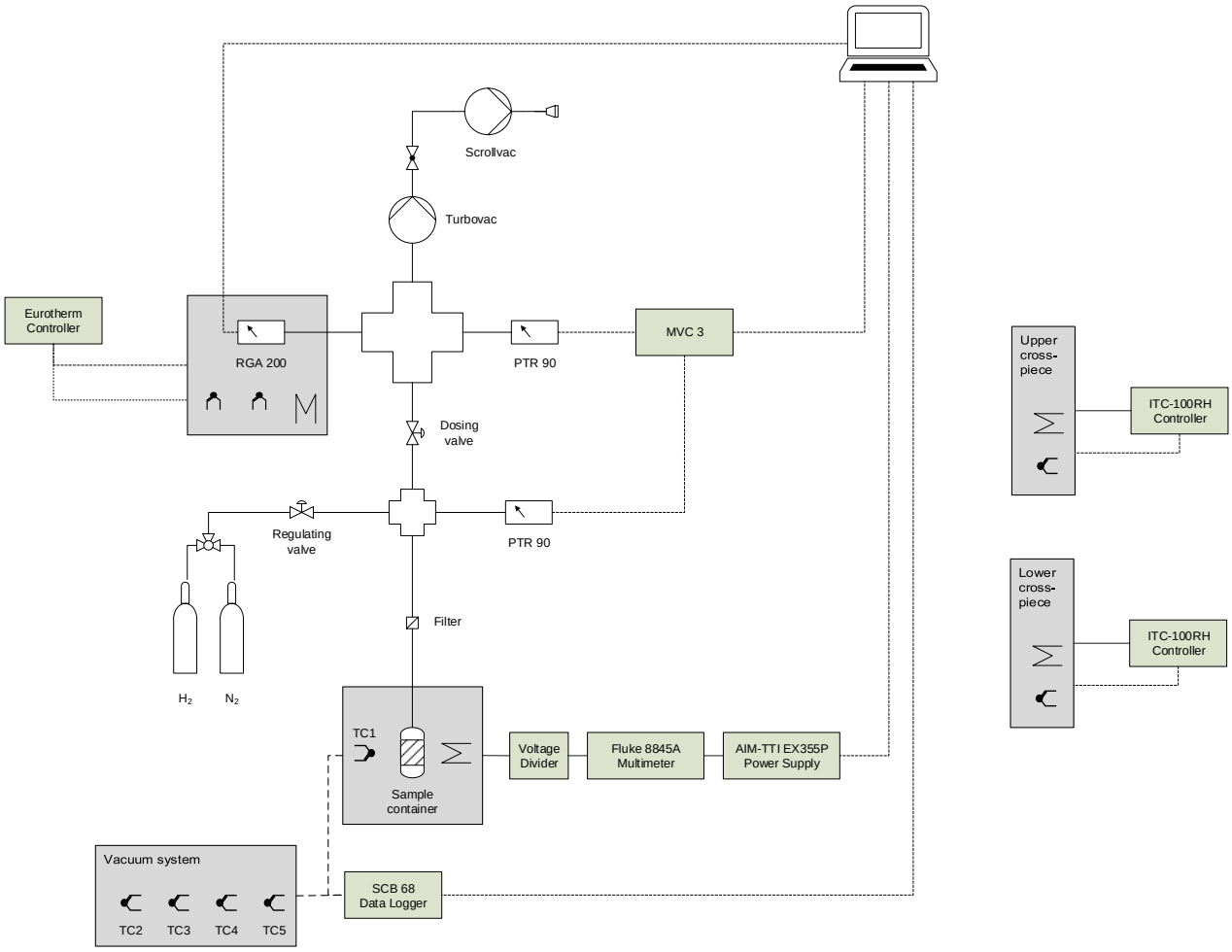

Figure B-5: Schematic diagram of the volatiles extraction setup (power lines are dotted, data lines are dashed)

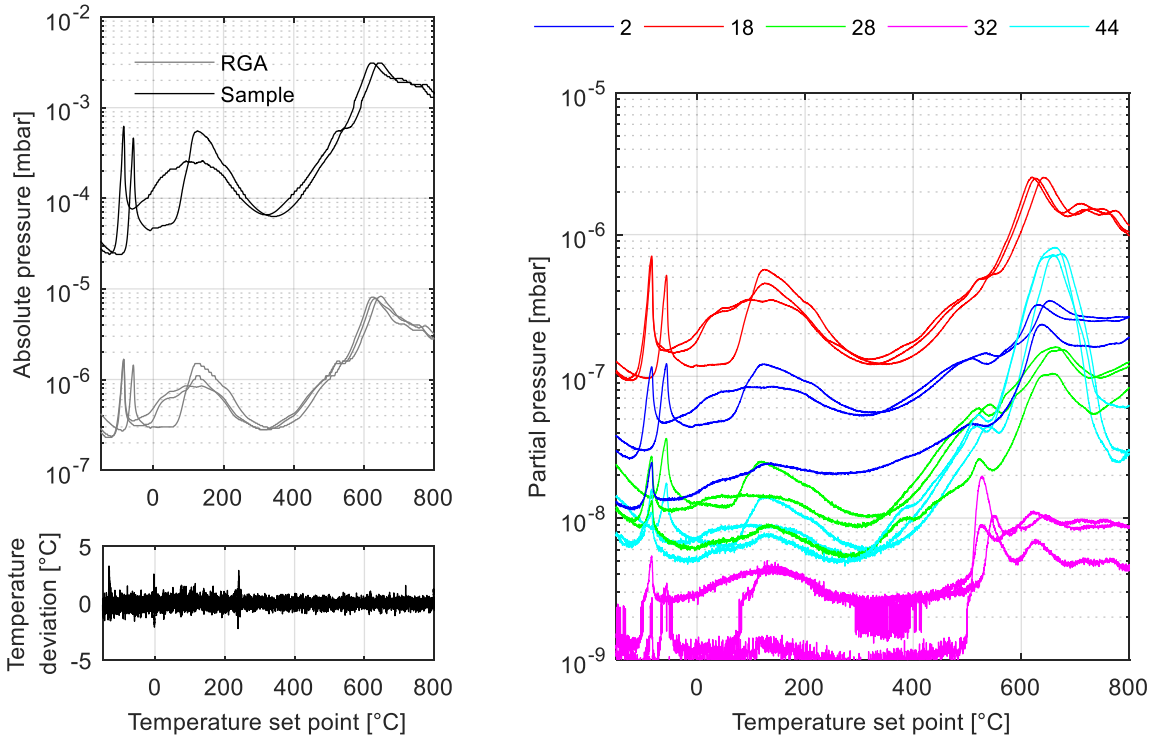

Figure B-6: Results for the 1 % rel. hum., 33-36 mg, 70-80 µm, loose sample at 6 °C/min (m/z ratios of depicted species are provided in the legend)

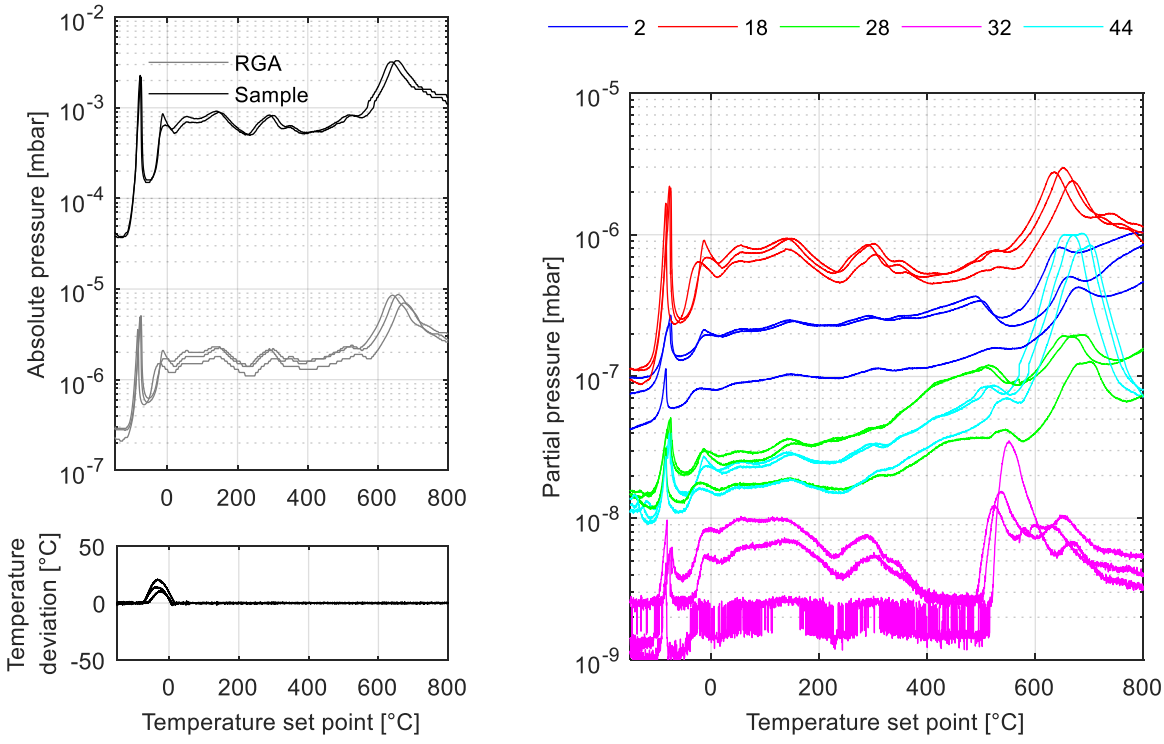

Figure B-7: Results for the 10 % rel. hum., 33-36 mg, 70-80 µm, loose sample at 6 °C/min (m/z ratios of depicted species are provided in the legend)

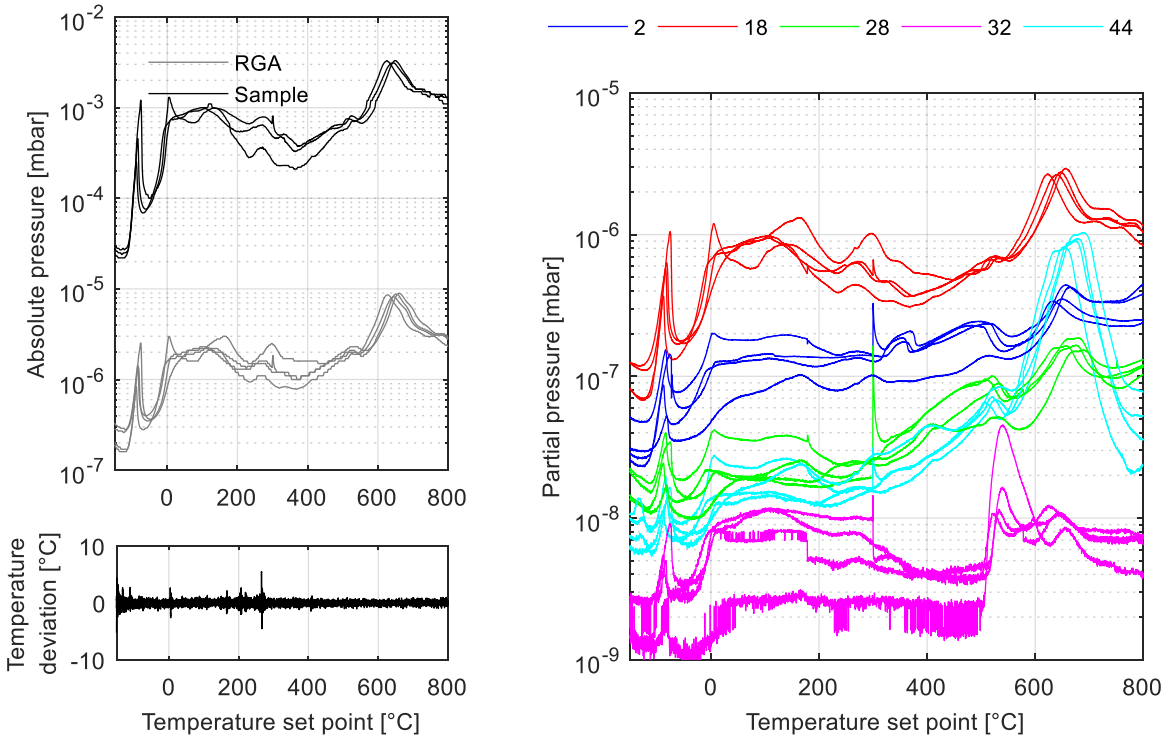

Figure B-8: Results for the 30 % rel. hum., 33-36 mg, 70-80 µm, loose sample at 6 °C/min (m/z ratios of depicted species are provided in the legend)

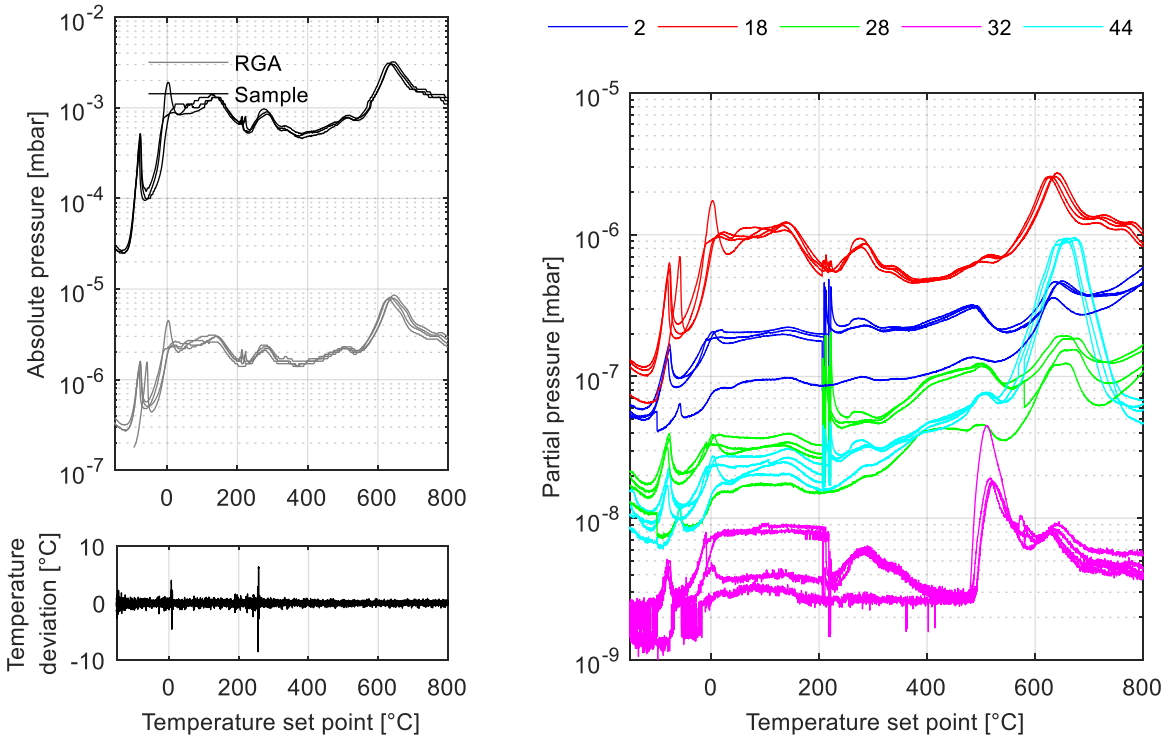

Figure B-9: Results for the 50 % rel. hum., 33-36 mg, 70-80 µm, loose sample at 6 °C/min (m/z ratios of depicted species are provided in the legend)

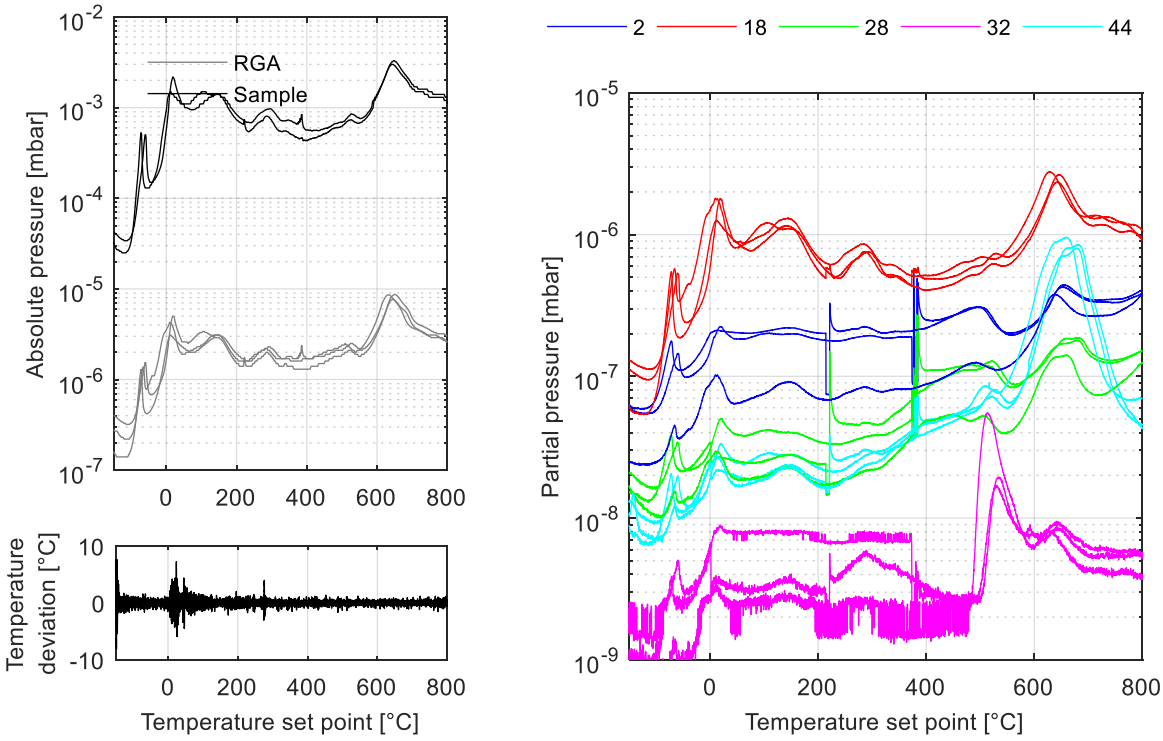

Figure B-10: Results for the 70 % rel. hum., 33-36 mg, 70-80 µm, loose sample at 6 °C/min (m/z ratios of depicted species are provided in the legend)

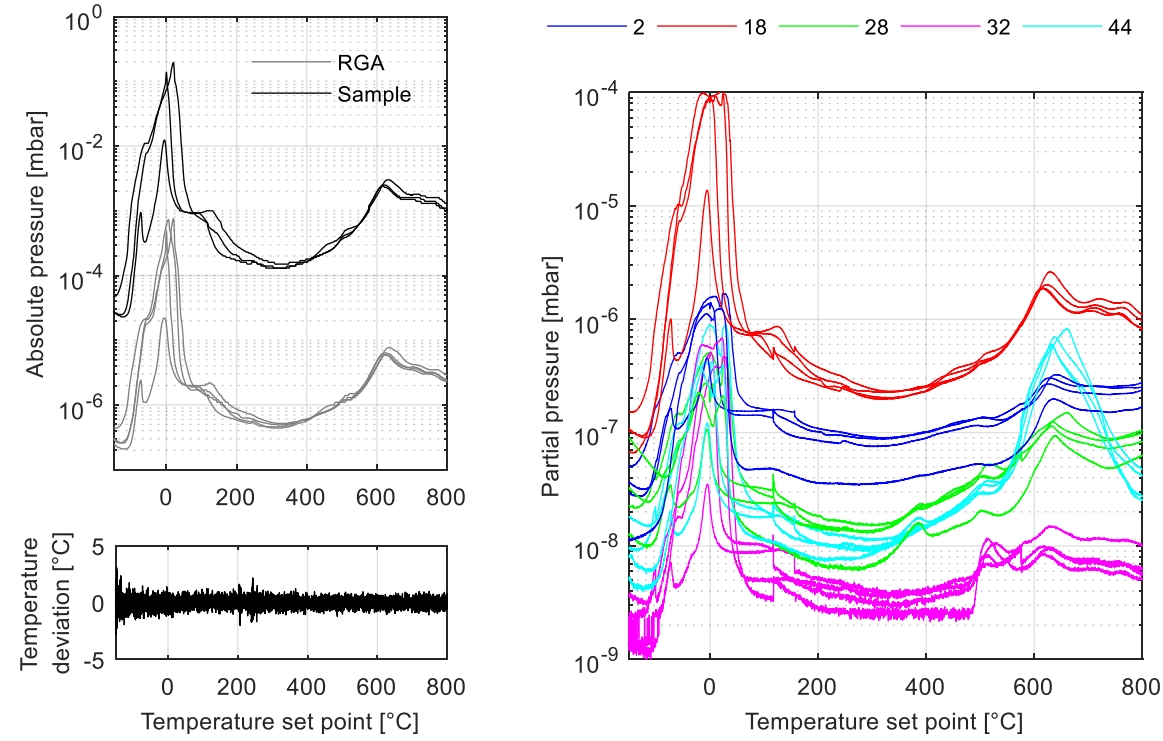

Figure B-11: Results for the saturated, 33-36 mg, 70-80 µm, loose sample at 6 °C/min (m/z ratios of depicted species are provided in the legend)

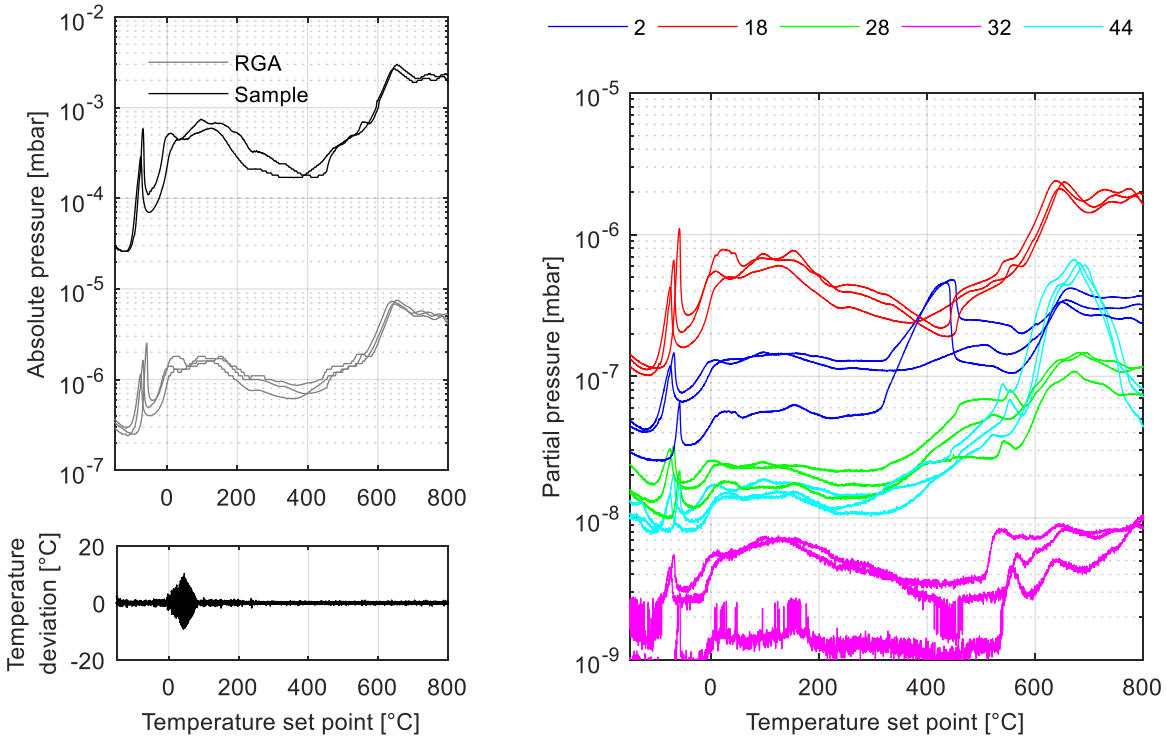

Figure B-12: Results for the 30 % rel. hum., 33-36 mg, 100-110 µm, loose sample at 6 °C/min (m/z ratios of depicted species are provided in the legend)

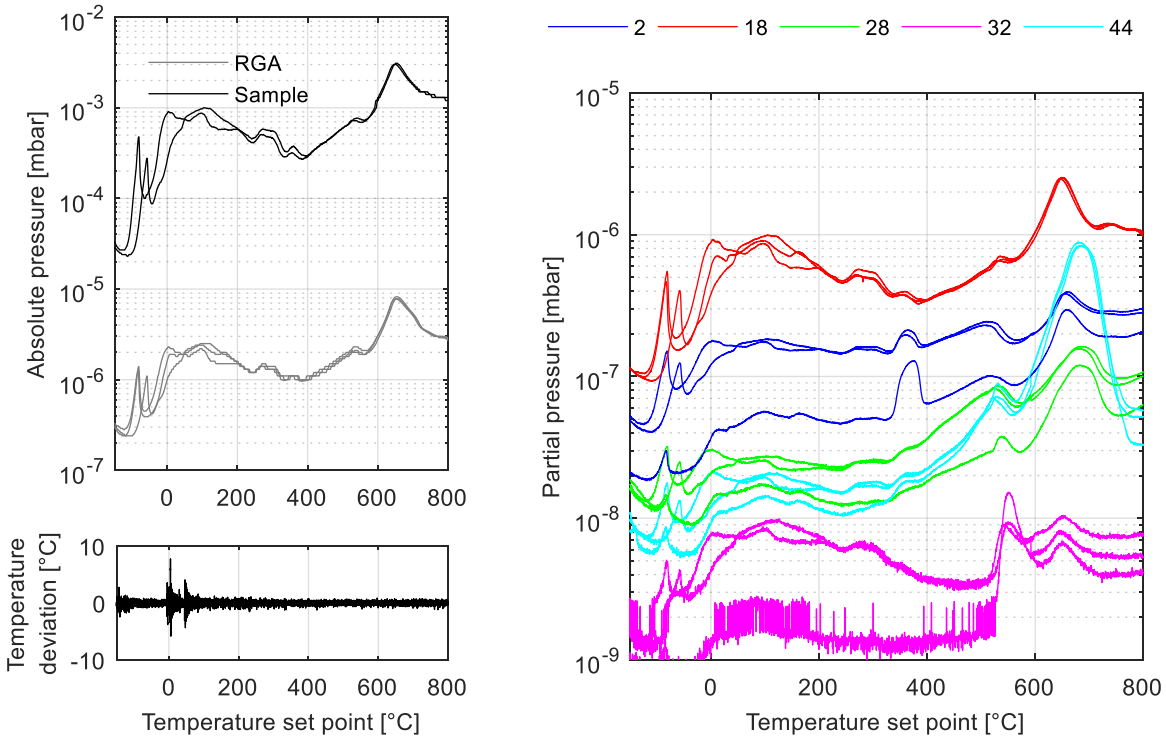

Figure B-13: Results for the 30 % rel. hum., 33-36 mg, 70-80 µm, compacted sample at 6 °C/min (m/z ratios of depicted species are provided in the legend)

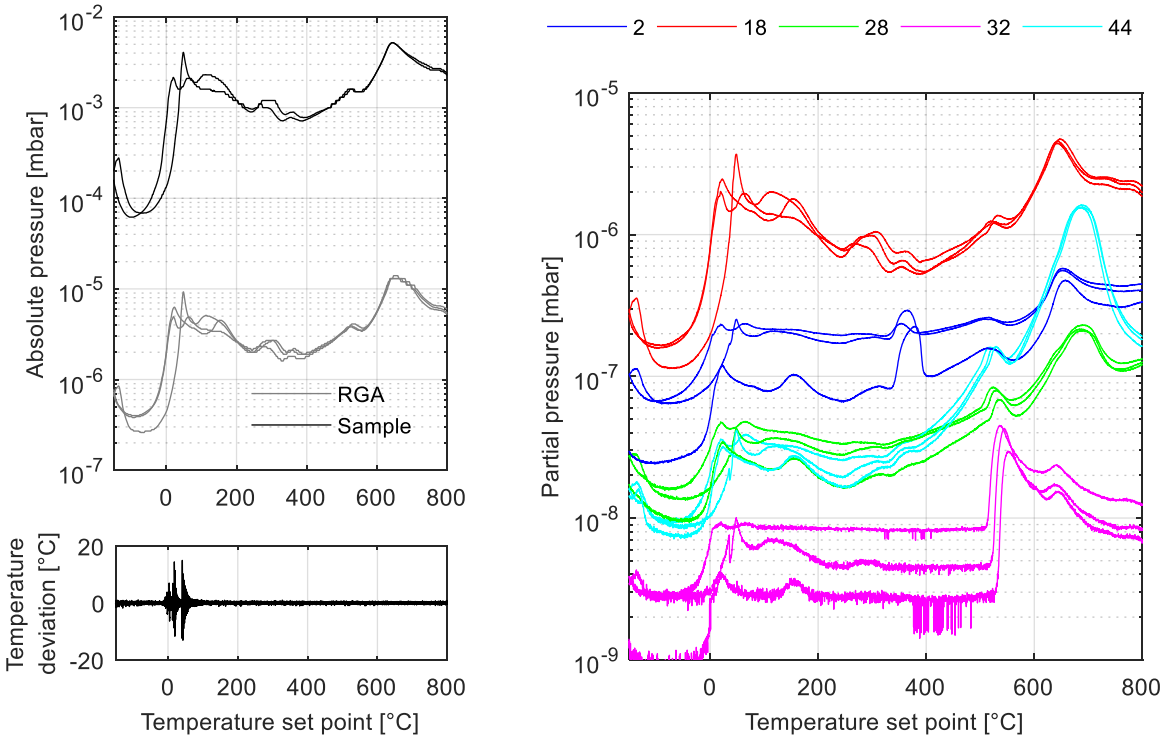

Figure B-14: Results for the 30 % rel. hum., 66-72 mg, 70-80 µm, loose sample at 6 °C/min (m/z ratios of depicted species are provided in the legend)

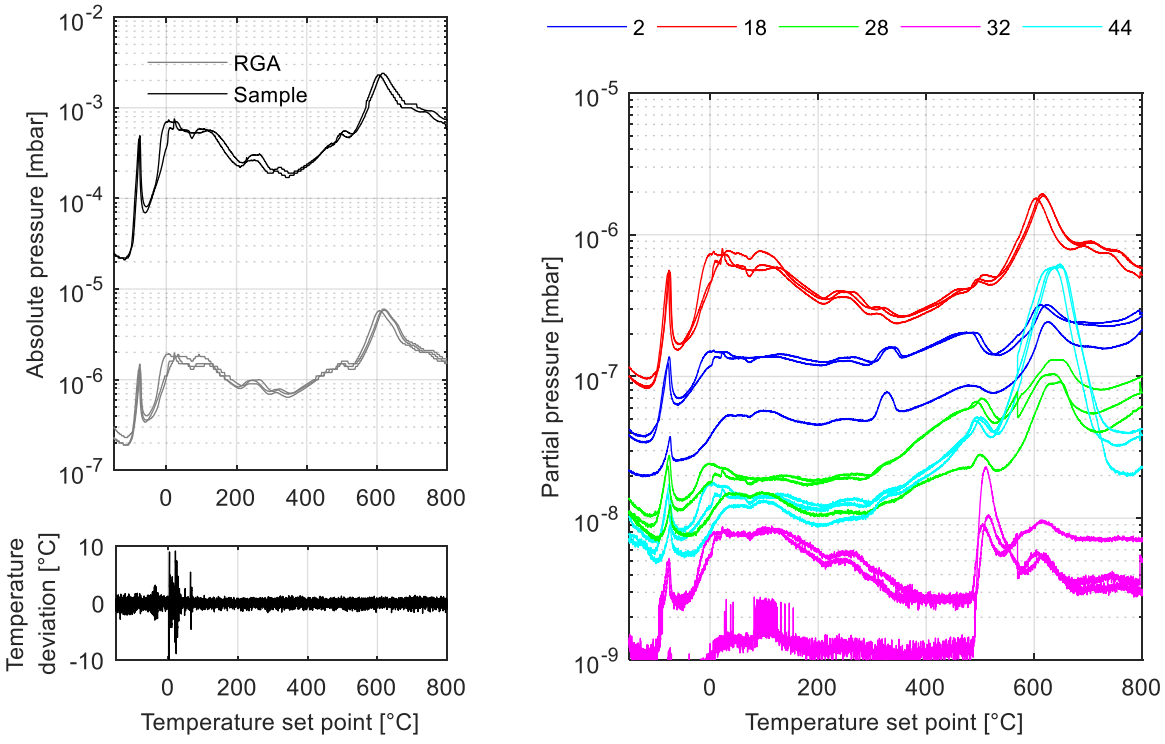

Figure B-15: Results for the 30 % rel. hum., 33-36 mg, 70-80 µm, loose sample at 4 °C/min (m/z ratios of depicted species are provided in the legend)

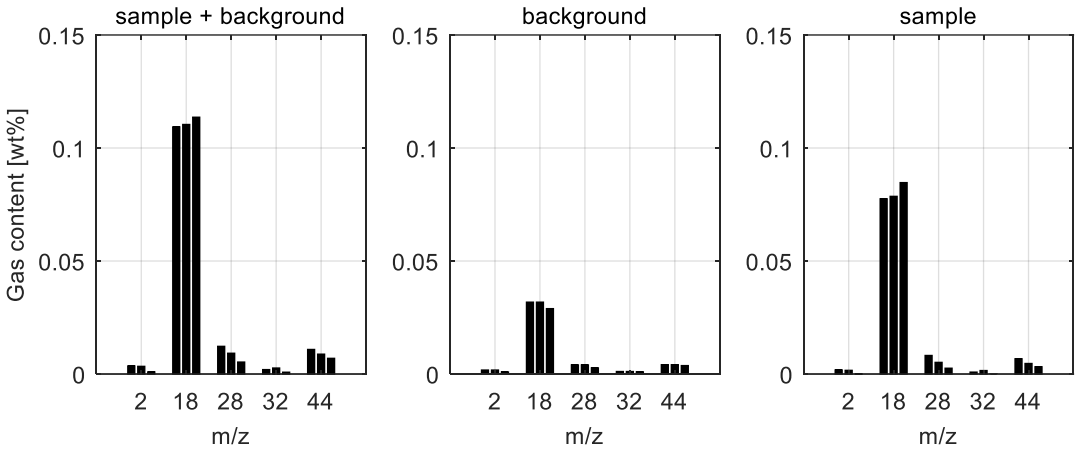

Figure B-16: Gas masses for the 1 % rel. hum., 33-36 mg, 70-80 µm, loose sample at 6 °C/min

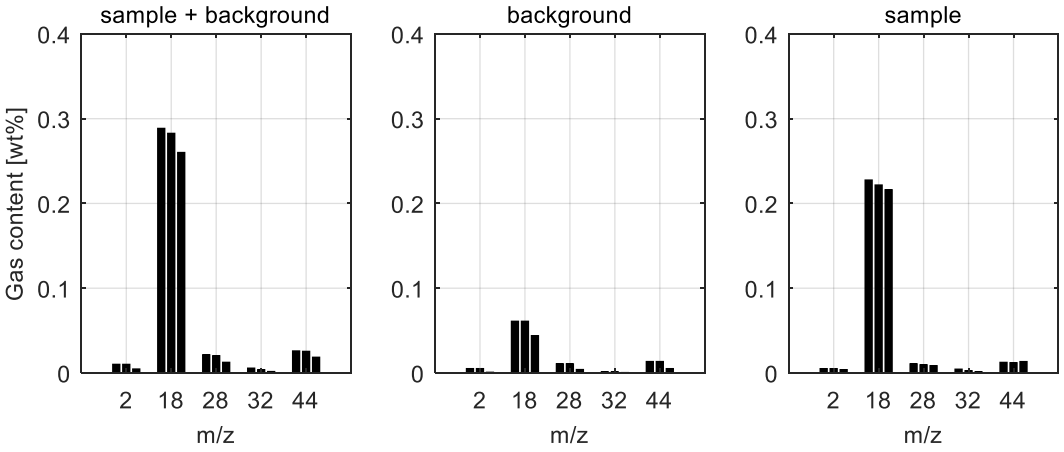

Figure B-17: Gas masses for the 10 % rel. hum., 33-36 mg, 70-80 µm, loose sample at 6 °C/min

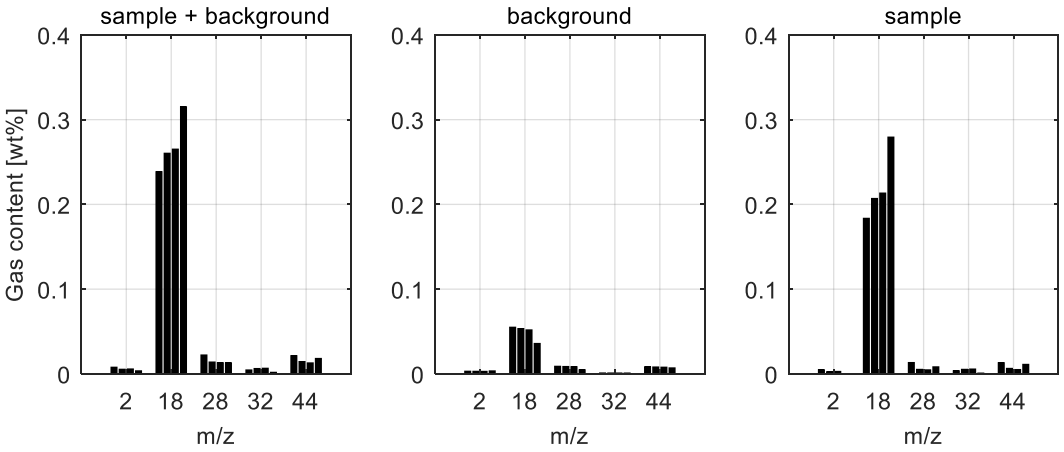

Figure B-18: Gas masses for the 30 % rel. hum., 33-36 mg, 70-80 µm, loose sample at 6 °C/min

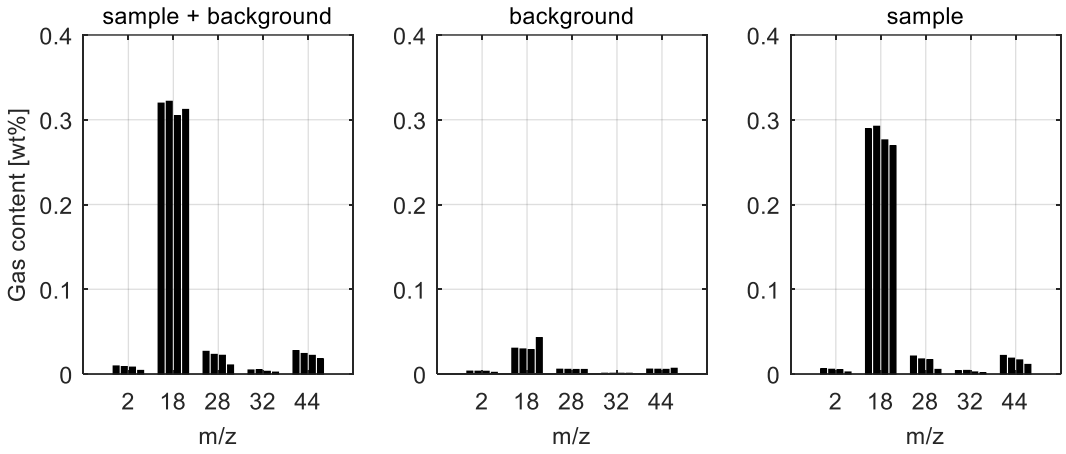

Figure B-19: Gas masses for the 50 % rel. hum., 33-36 mg, 70-80 µm, loose sample at 6 °C/min

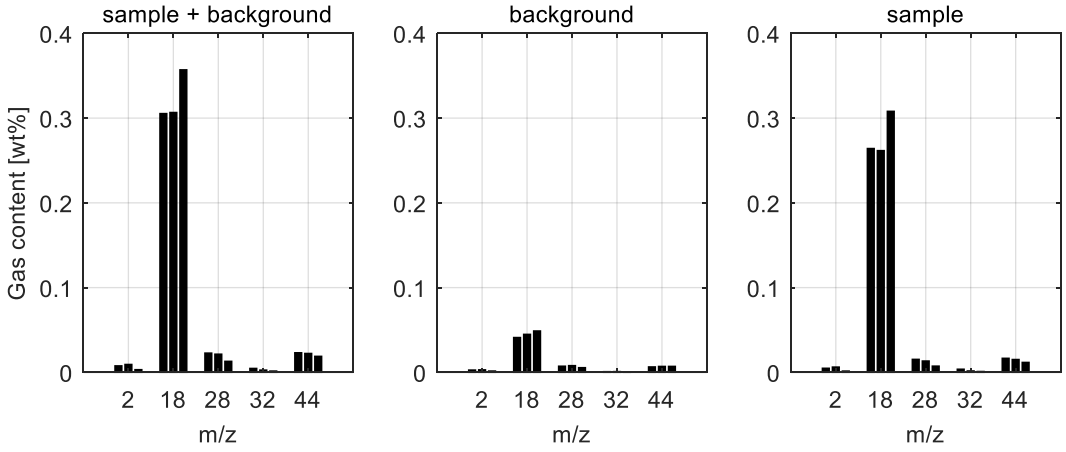

Figure B-20: Gas masses for the 70 % rel. hum., 33-36 mg, 70-80 µm, loose sample at 6 °C/min

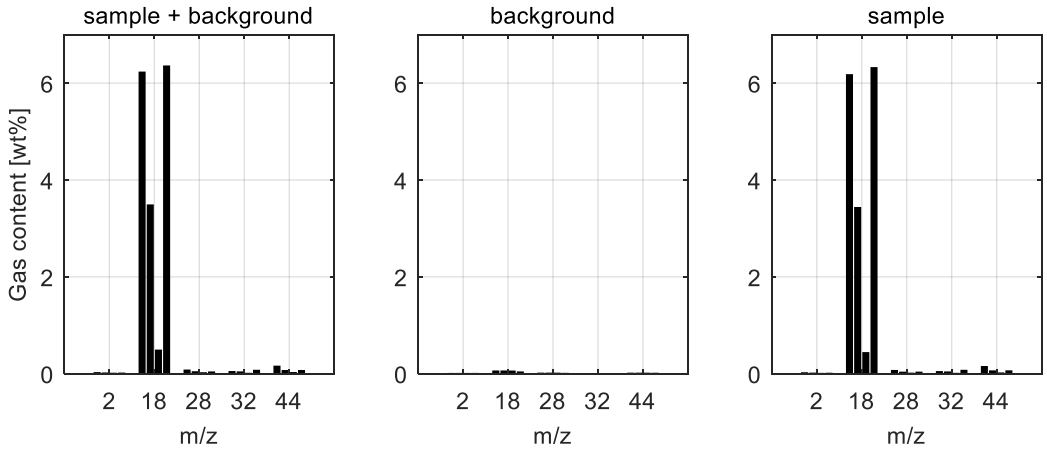

Figure B-21: Gas masses for the saturated, 33-36 mg, 70-80 µm, loose sample at 6 °C/min

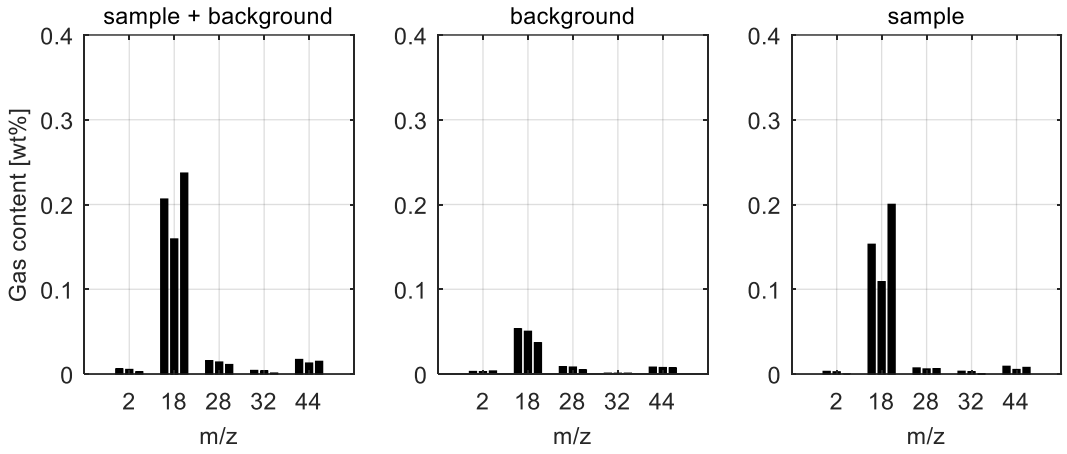

Figure B-22: Gas masses for the 30 % rel. hum., 33-36 mg, 100-110 µm, loose sample at 6 °C/min

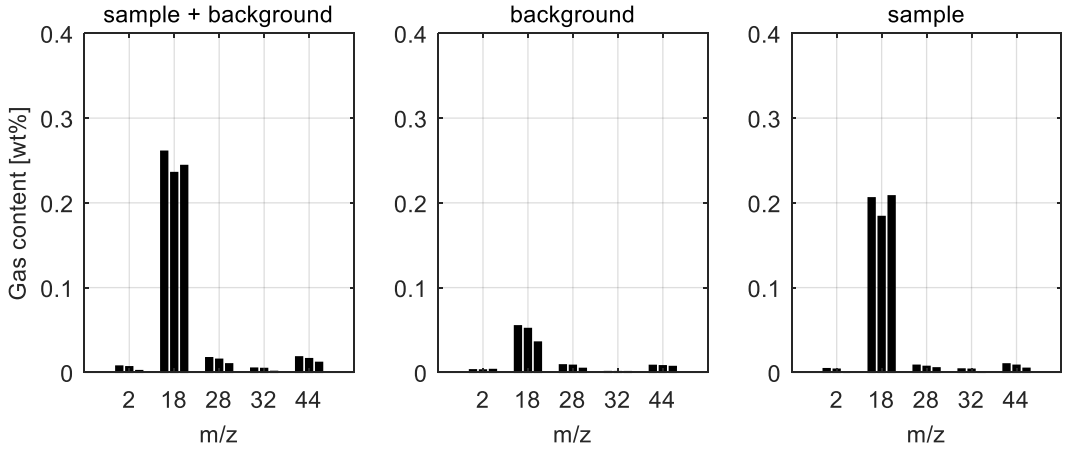

Figure B-23: Gas masses for the 30 % rel. hum., 33-36 mg, 70-80 µm, compacted sample at 6 °C/min

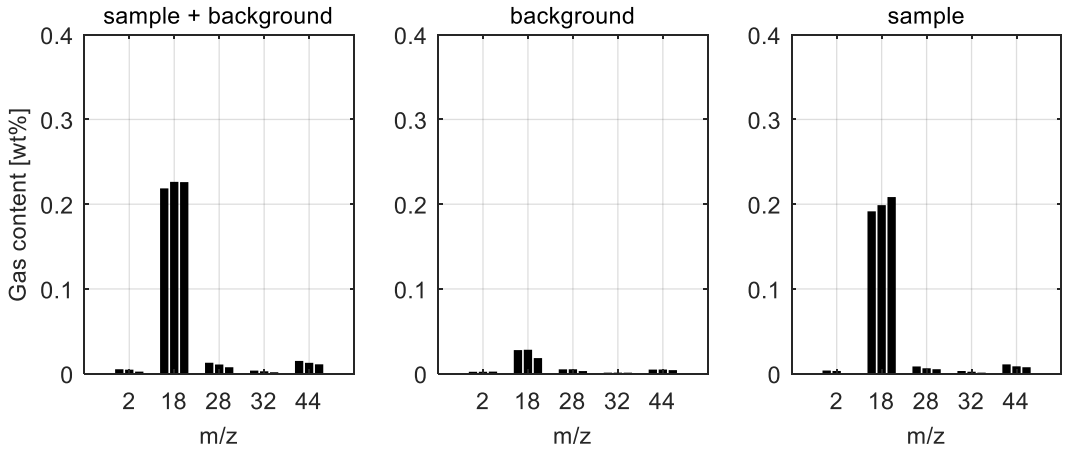

Figure B-24: Gas masses for the 30 % rel. hum., 66-72 mg, 70-80 µm, loose sample at 6 °C/min

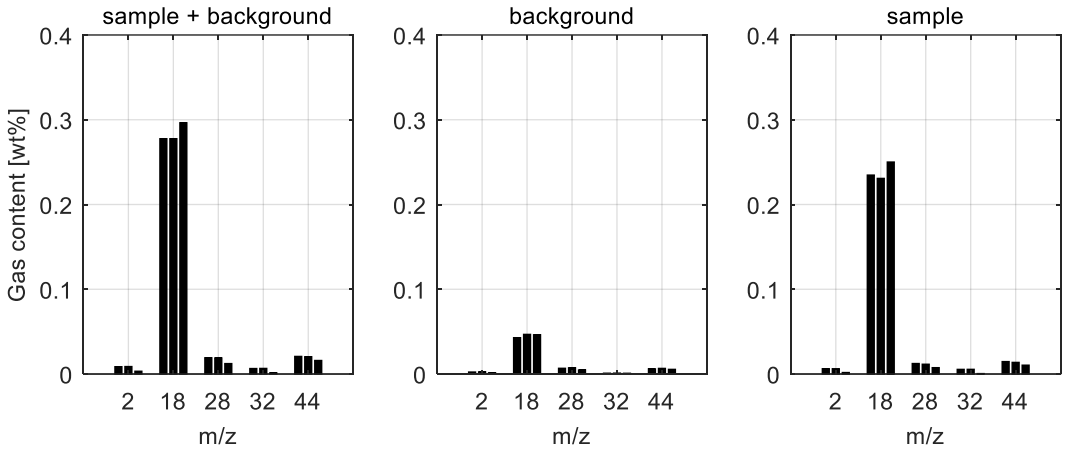

Figure B-25: Gas masses for the 30 % rel. hum., 33-36 mg, 70-80 µm, loose sample at 4 °C/min

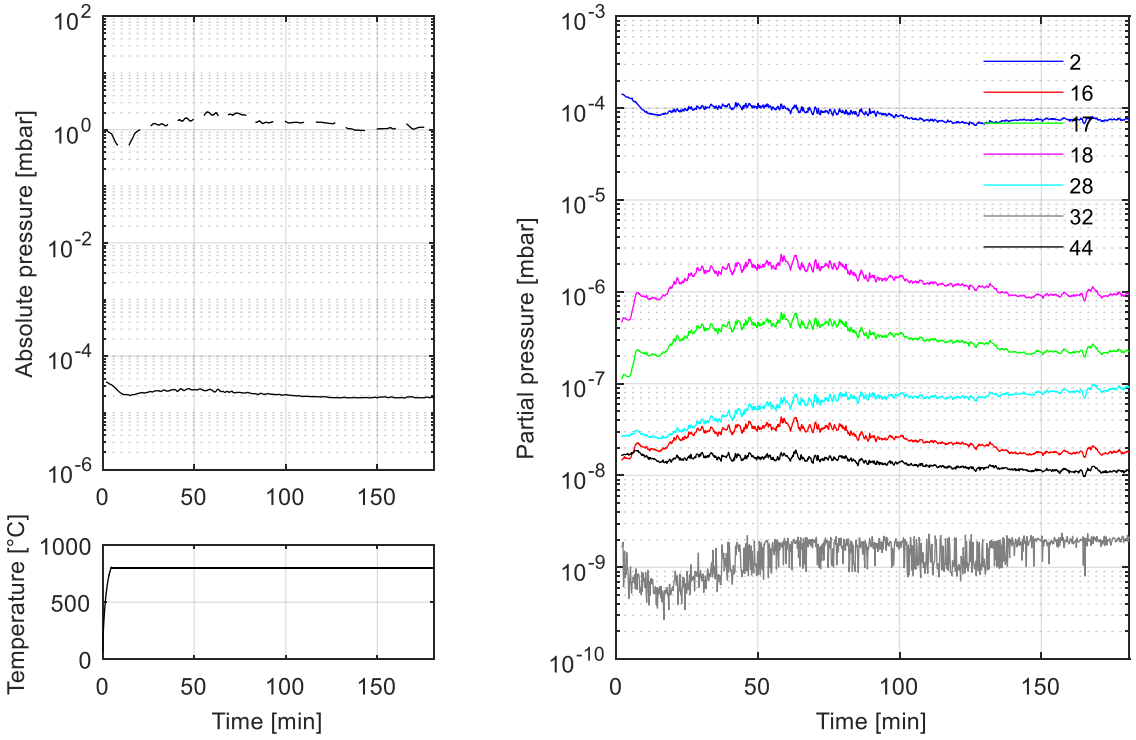

Figure B-26: Results of the continuous gas flow process for ilmenite (dashed line is for sample section, m/z ratios of depicted species are provided in the legend)

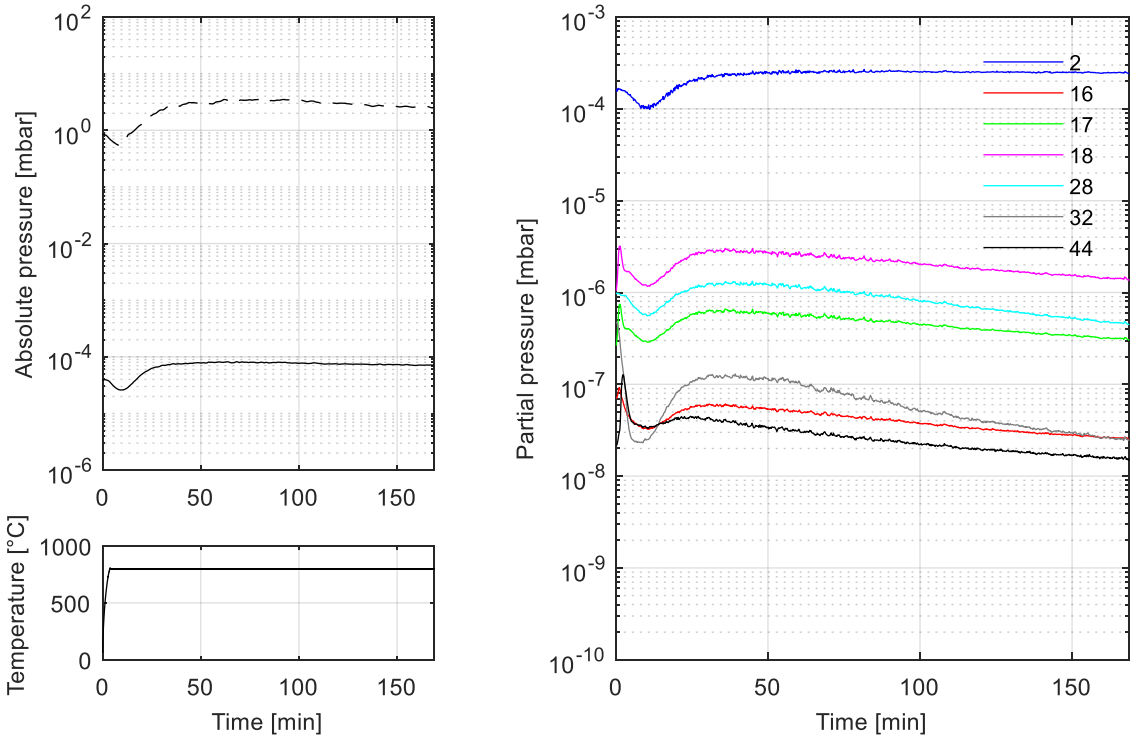

Figure B-27: Results of the continuous gas flow process for NU-LHT-2M (dashed line is for sample section, m/z ratios of depicted species are provided in the legend)

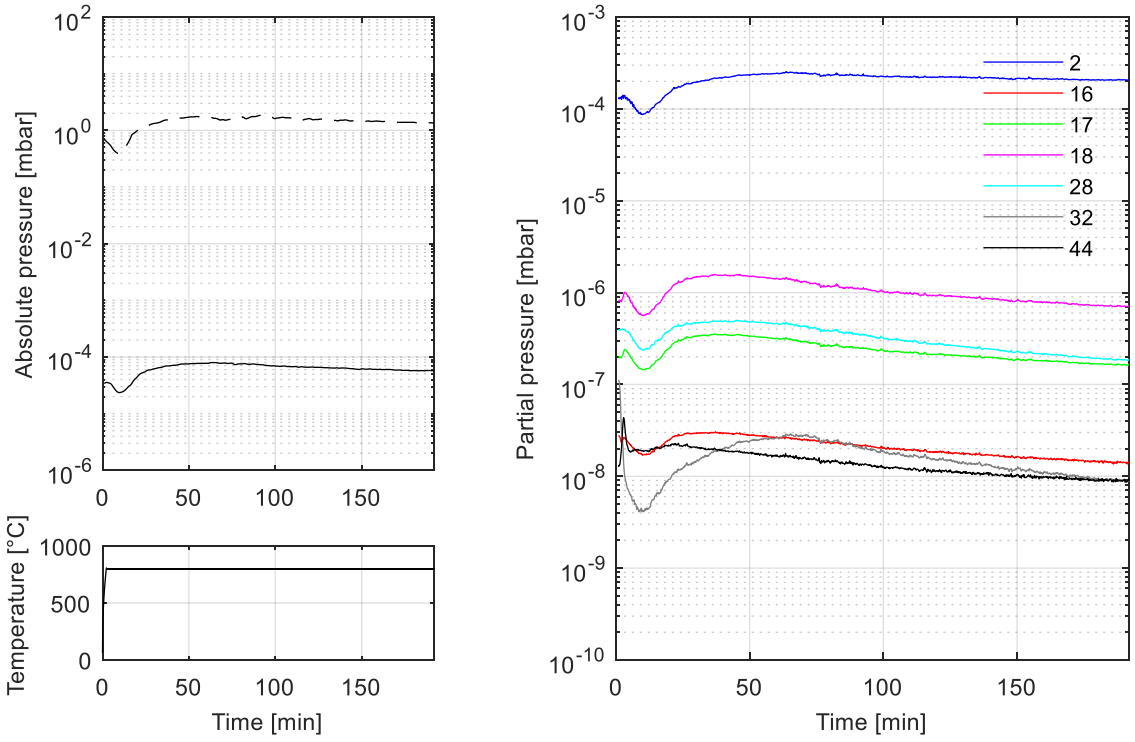

Figure B-28: Results of the continuous gas flow process for the blank run (dashed line is for sample section, m/z ratios of depicted species are provided in the legend)

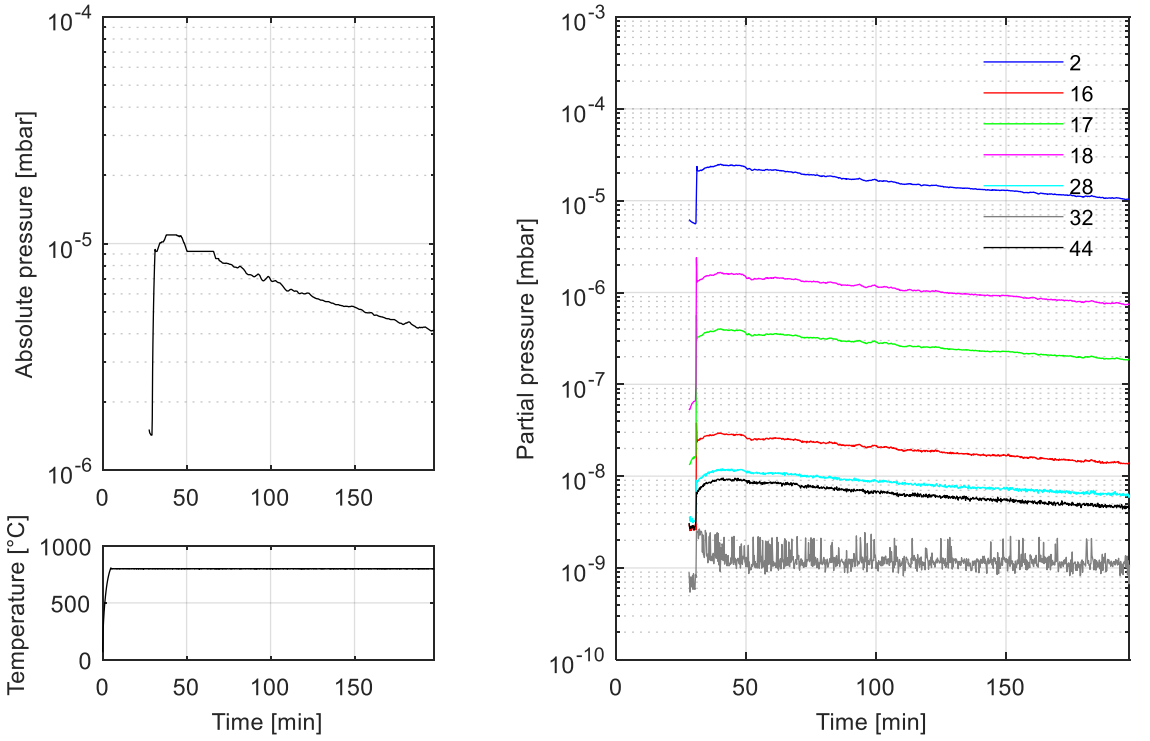

Figure B-29: Results of the semibatch process with preheating for ilmenite (m/z ratios of depicted species are provided in the legend)

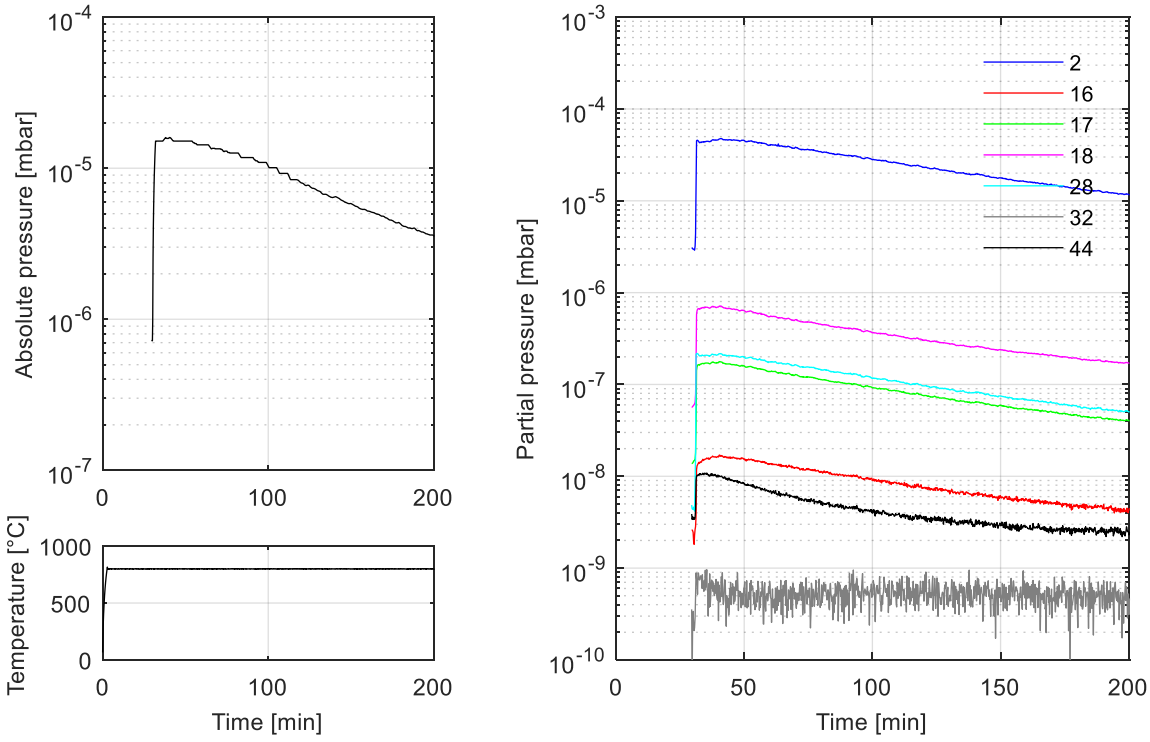

Figure B-30: Results of the semibatch process with preheating for NU-LHT-2M (m/z ratios of depicted species are provided in the legend)

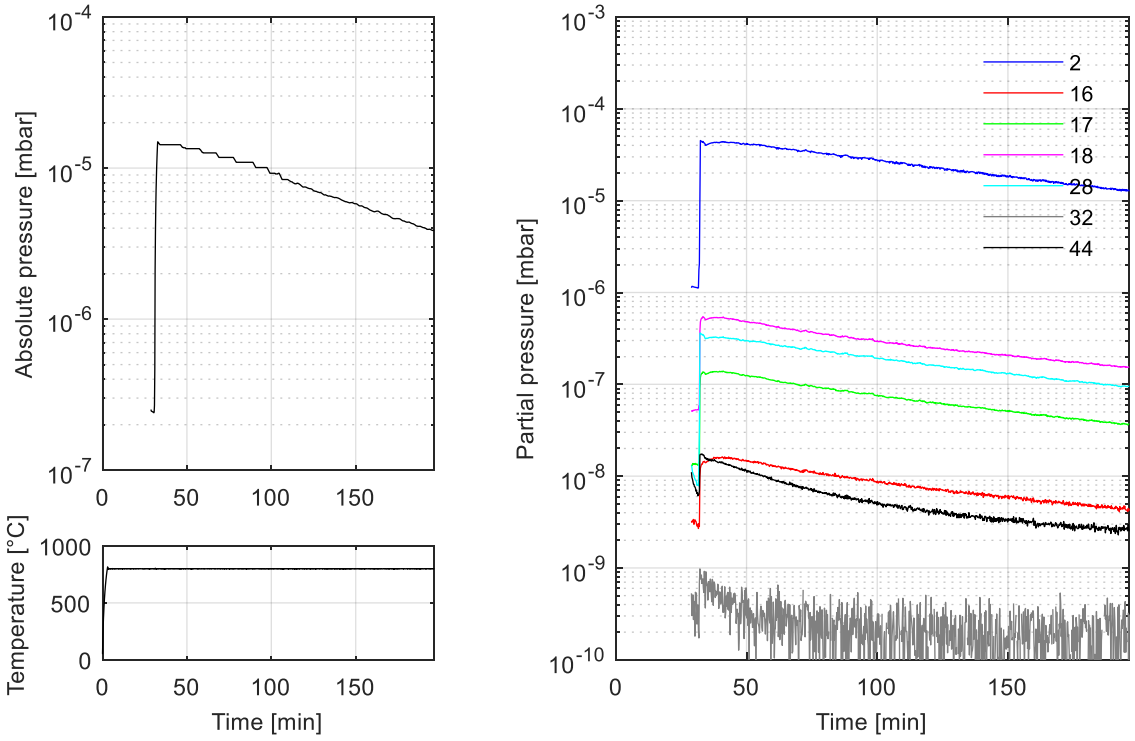

Figure B-31: Results of the semibatch process with preheating for the blank run (m/z ratios of depicted species are provided in the legend)

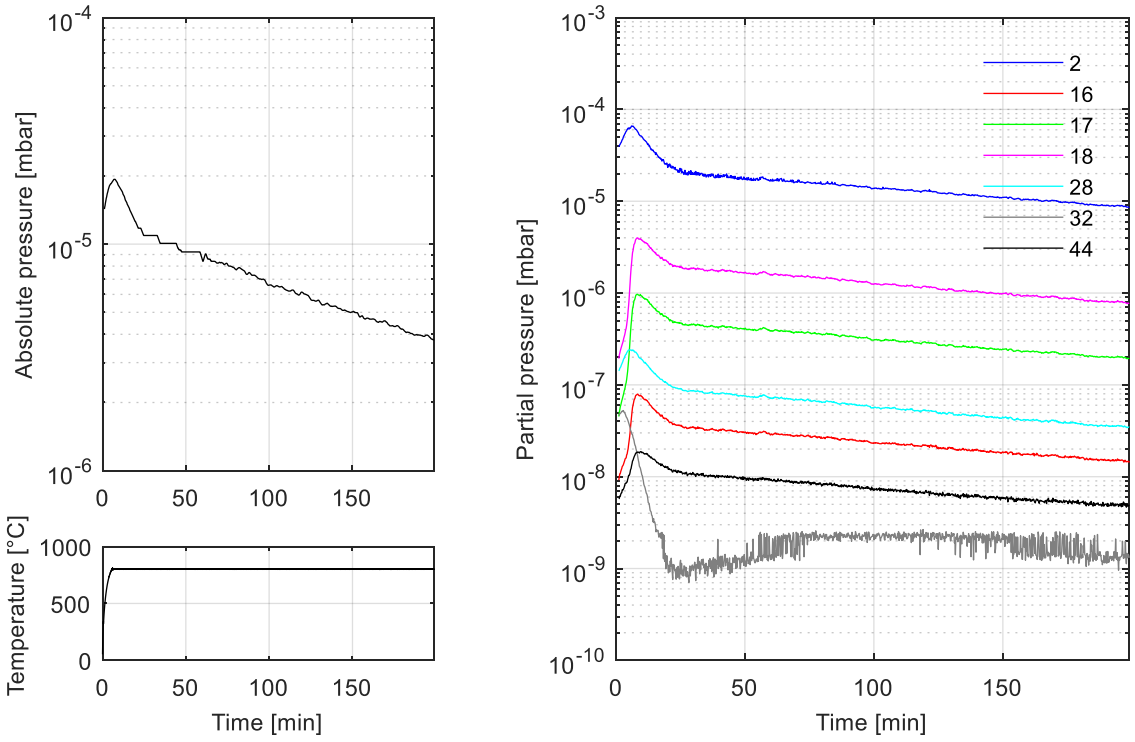

Figure B-32: Results of the semibatch process without preheating for ilmenite (m/z ratios of depicted species are provided in the legend)

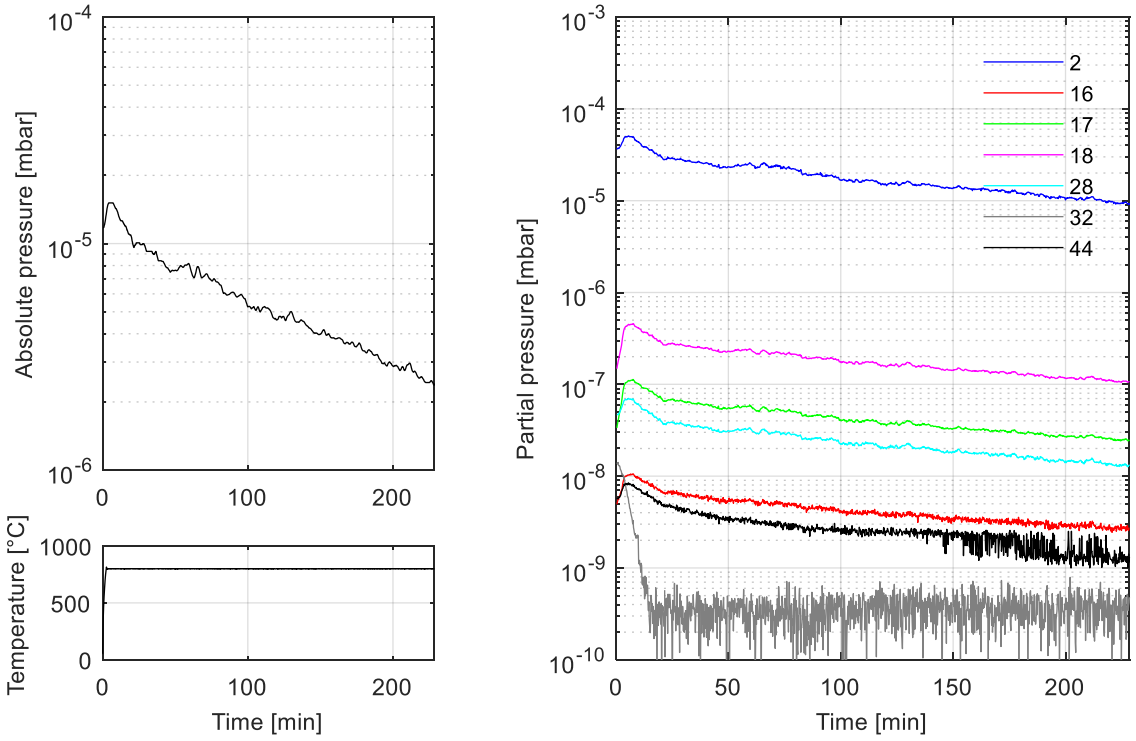

Figure B-33: Results of the semibatch process without preheating for NU-LHT-2M (m/z ratios of depicted species are provided in the legend)

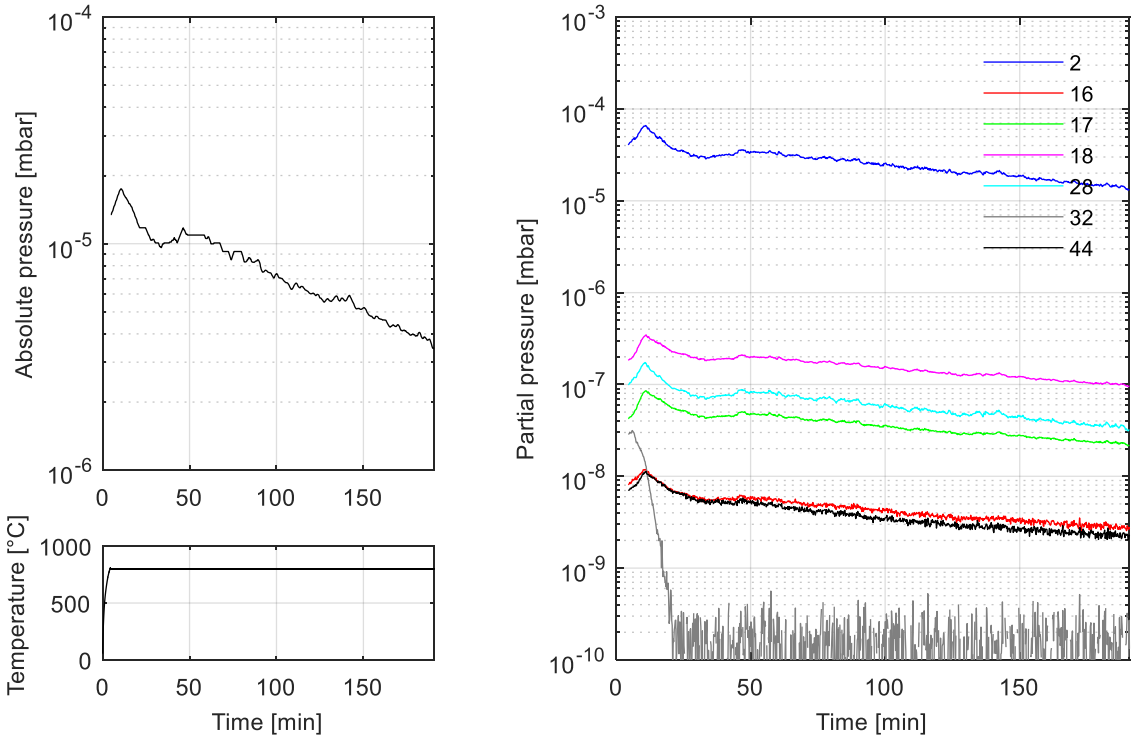

Figure B-34: Results of the semibatch process without preheating for the blank run (m/z ratios of depicted species are provided in the legend)

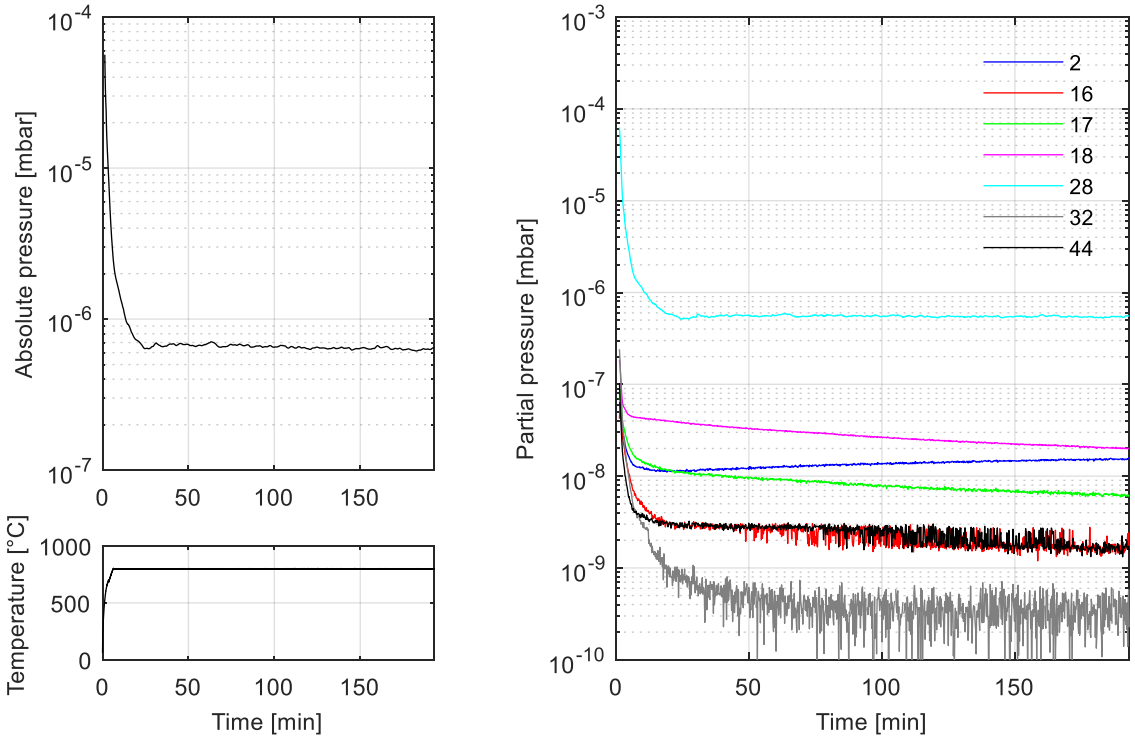

Figure B-35: Results of the semibatch process without preheating for ilmenite and nitrogen instead of hydrogen (m/z ratios of depicted species are provided in the legend)

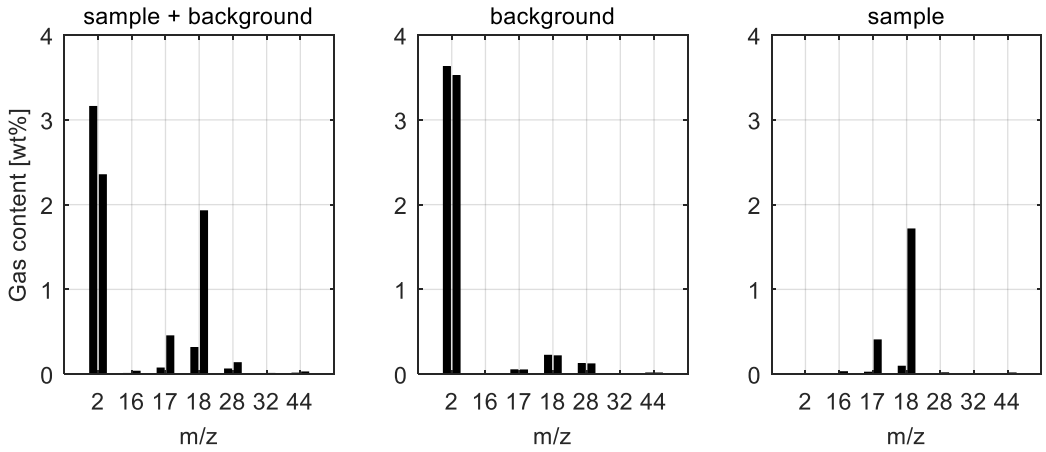

Figure B-36: Gas masses for the semibatch process without preheating (first bar is for NU-LHT-2M, second bar is for ilmenite)

Appendix C Supplementary Tables

Table C-1: Specific surface area and water concentration for a monolayer of water molecules for relevant lunar regolith materials, based on (Cadenhead, Brown and Rice, 1977; Malvern Instruments, 2007; Poston *et al.*, 2013)

Material/Sample	Mean particle size [μm]	Specific surface area [m^2/g]	Calculated monolayer-equivalent water concentration	
			[10^{-6} mol/g]	[wt%]
JSC-1A (micronized)	0.25	8	223.7	0.403
NU-LHT-1M	147	0.121	3.4	0.006
NU-LHT-1M	139	0.233	6.5	0.012
NU-LHT-1M	120	0.255	7.1	0.013
Typical lunar regolith	68	0.50	14.0	0.025
10084 (Apollo 11)	52	0.59	16.5	0.030
12033 (Apollo 12)	97	0.02	0.6	0.001
12070 (Apollo 12)	n/a	0.57	15.9	0.029
14003 (Apollo 14)	99	0.51	14.3	0.026
14163 (Apollo 14)	56	0.21	5.9	0.011
14259 (Apollo 14)	63	0.61	17.1	0.031
15101 (Apollo 15)	n/a	0.65	18.2	0.033
15301 (Apollo 15)	n/a	0.68	19.0	0.034
15401 (Apollo 15)	61	0.48	13.4	0.024
15401 (Apollo 15)	61	0.40	11.2	0.020
61221 (Apollo 16)	68	0.78	21.8	0.039
61241 (Apollo 16)	72	0.72	20.1	0.036
63321 (Apollo 16)	87	0.43	12.0	0.022
63341 (Apollo 16)	80	0.42	11.7	0.021
74220 (Apollo 17)	41	0.42	11.7	0.021
74220 (Apollo 17)	41	0.46	12.9	0.023
75081 (Apollo 17)	67	0.50	14.0	0.025

Table C-2: Major oxides in Kenmare Moma ilmenite and NU-LHT-2M

Oxide	Kenmare Moma ilmenite (Kenmare Moma Processing Ltd., 2017)		NU-LHT-2M certificate of information		NU-LHT-2M (U.S. Geological Survey, 2008)	
	Average [wt%]	Standard deviation [wt%]	Average [wt%]	Standard deviation [wt%]	Average [wt%]	Standard deviation [wt%]
SiO_2	0.5 - 1.5	n/a	47.62	0.21	46.70	0.11
Al_2O_3	0.5 - 1.5	n/a	27.4	0.48	24.40	0.07
CaO	0.01 - 0.1	n/a	13.6	0.41	13.60	0.05
MgO	0.3 - 0.7	n/a	8.50	0.48	7.90	0.04
FeO	-	-	2.15	0.09	-	-
Fe_2O_3	30 - 48	n/a	-	-	4.16	0.03
TiO_2	50 - 60	n/a	0.33	0.02	0.41	0.02
MnO	1.3 - 1.8	n/a			0.07	<0.005
Cr_2O_3	0.03 - 0.6	n/a			n/a	n/a
ZrO_2	0.05 - 0.5	n/a			n/a	n/a
V_2O_3	0.1 - 0.25	n/a			n/a	n/a
P_2O_5	0.02 - 0.2	n/a			0.15	0.01

Table C-3: Comparison of different fits (method of least squares) for the relation between mean flow rate and gravity with JSC-1A (Reiss *et al.*, 2014)

Hopper angle [deg] and outlet [mm]	Fit type and coefficient of determination R^2											
	a) $y = ax + b$			b) $y = ax^2 + b$			Best fit for b = 0	c) $y = ax$		d) $y = ax^2$		Best fit for b ≠ 0
	a	b	R2	a	b	R2		a	R2	a	R2	
55-8	3.8	-2.2	1.000	27.2	8.0	1.000	a), b)	34.7	0.993	36.2	0.829	c)
55-13	6.3	-1.8	1.000	50.0	10.5	0.979	a)	59.5	0.998	62.0	0.852	c)
55-18	7.9	0.1	0.998	61.9	15.4	0.966	a)	77.0	0.998	79.6	0.790	c)
60-8	4.0	-3.4	1.000	28.5	7.3	1.000	a), b)	35.1	0.986	36.7	0.871	c)
60-13	6.7	-4.7	1.000	48.0	13.3	1.000	a), b)	60.3	0.990	63.0	0.849	c)
60-18	8.4	-1.6	0.999	66.2	14.8	0.971	a)	80.0	0.998	83.2	0.828	c)
65-8	4.4	-2.6	1.000	31.0	9.0	1.000	a), b)	39.5	0.993	41.1	0.834	c)
65-13	7.2	-2.3	0.999	57.7	11.6	0.990	a)	67.9	0.996	71.0	0.872	c)
65-18	9.4	-0.9	0.998	75.3	17.2	0.992	a)	91.2	0.997	95.0	0.840	c)
70-8	4.4	-1.0	0.997	35.3	7.5	0.993	a)	42.0	0.995	43.9	0.862	c)
70-13	7.2	-0.5	0.991	58.2	13.2	0.998	b)	70.1	0.989	73.3	0.848	c)
70-18	9.1	2.7	0.988	73.4	19.9	0.999	b)	92.7	0.984	96.2	0.783	c)
75-8	4.2	1.8	0.980	34.3	9.7	1.000	b)	43.8	0.973	45.4	0.764	c)
75-13	7.9	-0.4	0.994	63.1	14.5	0.996	b)	76.4	0.993	79.7	0.841	c)
75-18	10.2	1.7	1.000	80.6	21.4	0.979	a)	101.8	0.999	105.2	0.776	c)
55/65-8	4.4	-3.6	0.988	35.7	4.8	0.999	b)	38.7	0.970	41.3	0.946	c)
55/65-13	8.0	-8.0	0.989	64.1	7.0	0.999	b)	67.4	0.962	72.1	0.964	d)
55/65-18	10.1	-7.8	0.979	82.2	11.2	1.000	b)	89.0	0.962	95.0	0.946	c)
50/70-8	4.3	-2.7	0.996	34.3	5.5	0.994	a)	38.4	0.985	40.6	0.921	c)
50/70-13	7.4	-3.9	0.994	59.4	10.2	0.996	b)	67.5	0.986	71.2	0.910	c)
50/70-18	10.1	-4.2	0.994	81.1	15.1	0.996	b)	93.6	0.989	98.4	0.895	c)
Mean			0.994			0.993			0.988		0.858	

Table C-4: Comparison of different fits (method of least squares) for the relation between mean flow rate and gravity with NU-LHT-2M (Reiss *et al.*, 2014)

Hopper angle [deg] and outlet [mm]	Fit type and coefficient of determination R^2											
	a) $y = ax + b$			b) $y = ax^2 + b$			Best fit for b = 0	c) $y = ax$		d) $y = ax^2$		Best fit for b ≠ 0
	a	b	R2	a	b	R2		a	R2	a	R2	
55-8	3.9	-1.7	1.000	0.3	5.8	0.985	a)	3.6	0.995	0.4	0.881	c)
55-13	7.6	-3.4	0.999	0.6	10.9	0.990	a)	7.1	0.992	0.8	0.895	c)
55-18	9.9	-14.2	1.000	0.7	12.4	1.000	a), b)	8.2	0.963	0.9	0.939	c)
60-8	4.2	-2.2	0.999	0.3	6.0	0.988	a)	3.9	0.992	0.4	0.895	c)
60-13	8.6	-6.1	1.000	0.7	10.4	0.987	a)	7.8	0.985	0.8	0.921	c)
60-18	10.5	-16.0	1.000	0.8	11.9	1.000	a), b)	8.5	0.956	0.9	0.951	c)
65-8	4.7	-1.3	0.999	0.4	7.9	0.988	a)	4.5	0.997	0.5	0.860	c)
65-13	7.7	-1.1	0.997	0.6	13.7	0.993	a)	7.6	0.997	0.8	0.849	c)
65-18	10.3	-1.0	0.988	0.9	18.8	0.999	b)	10.2	0.989	1.1	0.847	c)
70-8	5.3	-1.7	0.995	0.4	8.4	0.995	a), b)	5.1	0.993	0.5	0.880	c)
70-13	8.6	-3.4	0.994	0.7	13.4	0.997	b)	8.1	0.989	0.9	0.885	c)
70-18	11.1	-0.8	0.994	0.9	21.0	0.997	b)	11.0	0.993	1.2	0.831	c)
75-8	4.2	-0.1	0.999	0.3	8.6	0.961	a)	4.2	0.996	0.4	0.764	c)
75-13	6.9	4.6	0.996	0.6	19.2	0.985	a)	7.6	0.979	0.8	0.621	c)
75-18	8.8	4.4	0.989	0.7	22.5	0.994	b)	9.5	0.984	1.0	0.687	c)
55/65-8	4.4	-1.6	0.998	0.4	6.8	0.992	a)	4.2	0.994	0.4	0.884	c)
55/65-13	8.2	-1.9	0.992	0.7	13.6	0.998	b)	8.0	0.989	0.9	0.875	c)
55/65-18	8.7	5.7	0.999	0.7	23.3	0.971	a)	9.5	0.985	1.0	0.640	c)
50/70-8	4.1	0.3	0.999	0.3	8.2	0.987	a)	4.2	0.999	0.4	0.805	c)
50/70-13	7.9	-0.6	0.992	0.7	14.3	0.998	b)	7.8	0.991	0.8	0.850	c)
50/70-18	9.4	3.2	0.999	0.8	21.4	0.986	a)	9.9	0.996	1.0	0.751	c)
Mean			0.997			0.990			0.988		0.834	